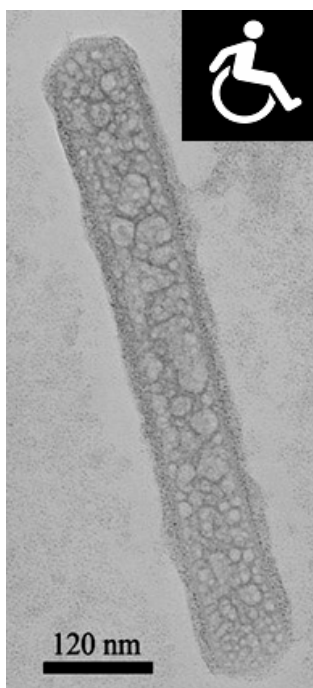




Nadia Khaled Zurba

Luminescência persistente de nanotubos, nanoarames e cápsulas de $\text{SrAl}_2\text{O}_4:\text{Ce(III)}$, Dy, Eu para pessoas com deficiências: *nano-emergência*

Persistent luminescence of $\text{SrAl}_2\text{O}_4:\text{Ce(III)}$, Dy, Eu nanotubes, nanowires and core-shells for people with disabilities: *nano-emergency*





Nadia Khaled Zurba

Luminescência persistente de nanotubos, nanoarames e cápsulas de $\text{SrAl}_2\text{O}_4:\text{Ce(III)}$, Dy, Eu para pessoas com deficiências: *nano-emergência*

Persistent luminescence of $\text{SrAl}_2\text{O}_4:\text{Ce(III)}$, Dy, Eu nanotubes, nanowires and core-shells for people with disabilities: *nano-emergency*

Tese submetida à Universidade de Aveiro em cumprimento aos requisitos para a obtenção do grau de Doutor em Ciência e Engenharia de Materiais, sob orientação do Doutor José Maria da Fonte Ferreira, Professor Associado com Agregação do Departamento de Engenharia Cerâmica e do Vidro da Universidade de Aveiro.

Thesis submitted to the University of Aveiro in fulfillment of the requirements for the degree of Doctor of Philosophy in Materials Science and Engineering, under the supervision of Doctor José Maria da Fonte Ferreira, Associated Professor with Agregation of the Department of Ceramic and Glass Engineering of the University of Aveiro.

Doctoral Fellowship from the
Research Institute - Rectory of
University of Aveiro PORTUGAL
(BDUA\RECTORY\2698\2006-2010)
Ministry of Science, Technology and
High Education (MCTES)

«Prémio Maria Cândida da Cunha 2009»
PhD Thesis Awarded € 6,000
National Institute for Rehabilitation, INR
Ministry of Work and Social Solidarity
GOVERNMENT OF PORTUGAL

the jury

president

Doutor Nelson Fernando Pacheco da Rocha

Professor Catedrático da Universidade de Aveiro

Doutor Joaquim Carlos Neto Murta

Professor Associado com Agregação da Faculdade de Medicina da Universidade de Coimbra

Doutora Ana Maria Bastos da Costa Segadães

Professora Associada com Agregação da Universidade de Aveiro

Doutor José Maria da Fonte Ferreira

Professor Associado com Agregação da Universidade de Aveiro (Orientador)

Doutor Luís Filipe da Silva dos Santos

Professor Auxiliar do Instituto Superior Técnico da Universidade Técnica de Lisboa

Doutora Paula Campos Pinto

Investigadora do 'York Institute for Health Research' de Toronto, Canadá

acknowledgments

The author is very grateful for advice and assistance from the Professor Doctor José Maria da Fonte Ferreira, from the Department of Ceramic and Glass Engineering, University of Aveiro.

The team is grateful for assistance, advice and suggestions from the:

National Institute for Industrial Property (INPI), Portugal.

National Institute for Rehabilitation (INR), Portugal.

Unity of Technology Transfer of University of Aveiro (UATEC), namely to Vice-Rector Prof. Dr. Fernando Tavares Rocha, Dr. Mafília Condesso, Dr. José Paulo Rainho, MSc. Ana Teresa Pinto, and Lic. Lúcia Oliveira.

Centre for Research in Ceramic and Composite Materials (CICECO).

Ceramic and Glass Engineering Department, especially to Eng. Maria Conceição and Eng. Célia Miranda, and Ms. Luísa Costa.

To Prof. Dr. Luís Dias Carlos group from Physics Department for the support in luminescence spectra acquisitions.

To Prof. Dr. Andrei Kholkin and Dr. Igor BdiKin, for their attention in AFM measurements.

To Dr. Marc-Georg Willinger for his work on acquisition of HR-TEM images.

To Prof. Dr. Dmitri Golberg from International Center for Materials Nanoarchitectonics (MANA), National Institute for Materials Science (NIMS), Japan, for the critical revision about the nanotube topic.

To Dr. Ophthalmologist Manuel dos Santos Mariano, Medical Director of the Sector of Ophthalmology, Infante Dom Pedro Hospital, Aveiro.

To Prof. Dr. António Arsénio Nogueira, Department of Biology, University of Aveiro.

To Prof. Dr. Eugénio O. B. Leite from Leite & Leite Ocular Microsurgery, Coimbra, Portugal.

To Humanitarian Society of Voluntary Firemen, Bombeiros-Velhos of Aveiro.

To the corporations Lanxi Minhui Photoluminescent Pigments Co., China, Cinkarna S.A., Slovenia, Esmalticer Esmaltes Cerâmicos Lda., Portugal, and Eliane Ceramic Tiles S.A., Brazil, for the technical collaborations.

To all members of the jury for their productive contributions.

To professionals, colleges and friends that contributed direct or indirectly for the finalization of this work.

To all Zurba family that offered a stable outlook during this stage, namely to my mother and to my sister Leila Zurba Ribeiro.

At last, the author is very thankful for the four years of the entire financial support under a Doctoral Fellowship from the Research Institute of University of Aveiro, for the teaching activities and the knowledge acquired during this doctoral program that will be useful for future works. ■

*In Memoriam of my dear father
Mr. Khaled Rashid Hasan Zurba (1932-2008†).
To my mother.*

This work is dedicated for all persons with disabilities

palavras-chave

Luminescência persistente, estrôncio, cério (III), lantanídeos, nanotubos, nanoarames, nanocápsulas, pessoas com deficiências.

resumo

Este estudo transversal está focado na propriedade de luminescência persistente do aluminato de estrôncio co-dopado com cério (III), disprósio (III) e európio (II), $\text{SrAl}_2\text{O}_4:\text{Ce}^{3+}, \text{Dy}^{3+}, \text{Eu}^{2+}$, em sistemas de sinalização de áreas de risco e emergências para pessoas com deficiências.

Na área da ciência e engenharia dos materiais, foram desenvolvidos novos materiais com características nanométricas, nanotubos, nanoarames e nanobastões luminescentes de $\text{SrAl}_2\text{O}_4:\text{Ce}^{3+}, \text{Dy}^{3+}, \text{Eu}^{2+}$ para aplicações na área da reabilitação e acessibilidade de pessoas com deficiências. Os nanotubos foram obtidos a partir de micro- e nano-partículas precursoras sintetizadas por reação do estado-sólido e tratamento térmico de recozedura (1273-1473 K). Os nanoarames e nanobastões foram preparados por moagem, sonificação e recozedura (373 K).

Novas nanocápsulas de aluminatos luminescentes dopados com cério (III) e encapsulados com TiO_2 foram criadas de modo a obter-se materiais multifuncionais, designadamente com ação fotocatalítica antimicrobiana, antibacteriana e resistência à água. Tais aluminatos podem ser amplamente aplicados como superfícies higiênicas, auto-limpantes, em biomateriais, no domínio de medicamentos antibióticos, na formulação de vacinas, e com ênfase à aplicação em cerâmicas fotoluminescentes.

As metodologias de obtenção de tais nanoestruturas de aluminato de estrôncio dopado com cério (III) e do seu encapsulamento, desenvolvidas no âmbito desta tese, são aplicáveis a diversos aluminatos dopados com outros íons lantanídeos (Ln consiste em La, Ce, Pr, Nd, Pm, Sm, Eu, Gd, Tb, Dy, Ho, Er, Yb, Tm ou Lu) com a fórmula $\text{M}_{(1-x-y)}\text{N}_2\text{O}_4:\text{Ce}_x\text{Ln}_y$, onde M é Be, Mg, Ca, Sr ou Ba.

Na área da oftalmologia, foi desenvolvido um equipamento médico para o diagnóstico de bifuncionalidade das células retiniais fotoreceptoras, e como suporte à telemedicina oftalmológica. Este equipamento foi utilizado para realizar testes de visão cromática FM100HUE em fundo branco/preto para a personalização de materiais luminescentes. Os resultados demonstraram uma biofuncionalidade celular à visibilidade fotópica das cores em fundo preto superior no grupo de tratamento, composto por pessoas com retinopatia diabética (n=38), em comparação ao grupo de referência (n=38). Estes resultados sugerem a recomendação de materiais com fotoluminescência persistente ($\lambda_{\text{em}}=485-555 \text{ nm}$), incluindo $\text{SrAl}_2\text{O}_4:\text{Ce}^{3+}, \text{Dy}^{3+}, \text{Eu}^{2+}$, para o referido grupo de tratamento, em sinalização de emergência e em ambientes de baixa iluminação.

Na área da arquitectura, foi proposta uma nova aplicação dos referidos nanomateriais luminescentes à base de $\text{SrAl}_2\text{O}_4:\text{Ce}^{3+}, \text{Dy}^{3+}, \text{Eu}^{2+}$ em cerâmica de revestimento, tendo em vista a sua boa visibilidade e uso por pessoas com deficiências. Novos pavimentos, cerâmicos, fotoluminescentes, foram desenhados com propriedades multisensoriais (contraste táctil, sonoro e visual) e antimicrobianas, para pessoas portadoras de deficiências utilizarem, no escuro, com a prioridade de salvar vidas em emergências. Tais pisos, com relevos, podem ser combinados de modo a compor um sistema exclusivo de sinalização fotoluminescente multisensorial que possibilita a rápida evacuação mediante o uso de auxílios de mobilidade (e.g. bengala, cadeira de rodas, andadores, muletas).

A solução integrada de tais inovações que potencializa a propriedade de luminescência persistente de $\text{SrAl}_2\text{O}_4:\text{Ce}^{3+}, \text{Dy}^{3+}, \text{Eu}^{2+}$ de modo acessível para as pessoas com deficiências, pode contribuir para salvar vidas, no escuro, em emergências. ■

keywords

Persistent luminescence, strontium, cerium (III), lanthanide, nanotubes, nanowires, core-shells, people with disabilities.

abstract

This transversal study is focused on the persistent luminescence property of the strontium aluminate co-doped with cerium (III), dysprosium (III) and europium (II), $\text{SrAl}_2\text{O}_4:\text{Ce}^{3+}, \text{Dy}^{3+}, \text{Eu}^{2+}$, in signalling systems of risk areas and emergencies for people with disabilities.

In the area of materials science and engineering, new nanostructured luminescent materials were developed, $\text{SrAl}_2\text{O}_4:\text{Ce}^{3+}, \text{Dy}^{3+}, \text{Eu}^{2+}$ nanotubes, nanowires and nanorods, for applications in rehabilitation and accessibility for people with disabilities. The nanotubes were obtained from precursor micro- and nano-particles as-synthesized by solid-state reaction and under thermal treatment of post-annealing (1273-1473 K). The nanowires and nanorods were prepared by grinding, sonification and post-annealing (373 K).

New luminescent core-shells of strontium aluminate doped with cerium (III) and encapsulated with TiO_2 were created in order to obtain multifunctional materials, especially with photocatalytic activity, antimicrobial, antibacterial and water resistance. Such aluminates can be widely applied as hygiene surface, self-cleaning, in biomaterials, in the field of antibiotic drugs, in the formulation of vaccines, with emphasis on application in photoluminescent ceramics.

The methods of obtaining such strontium aluminate nanostructures doped with cerium (III) and its encapsulation process developed in this thesis are applicable to various aluminates doped with other lanthanide ions (Ln is La, Ce, Pr, Nd, Pm, Sm, Eu, Gd, Tb, Dy, Ho, Er, Yb, Tm or Lu) with the formula $\text{M}_{(1-x-y)}\text{N}_2\text{O}_4:\text{Ce}_x, \text{Ln}_y$, where M is Be, Mg, Ca, Sr or Ba.

In the field of ophthalmology, medical equipment was developed for the diagnosis of biofunctionality of retinal photoreceptor cells, and for to support the ophthalmic telemedicine. This equipment was used for testing colour vision FM100HUE in white/black backgrounds for personalization of luminescent materials. The results showed a superior cellular biofunctionality to the photopic visibility of colours on a black background in treatment trials with diabetic retinopathy (n=38) than compared with references subjects (n=38). These results suggest the recommendation of persistent luminescent materials ($\lambda_{em}=485-555$ nm), including $\text{SrAl}_2\text{O}_4:\text{Ce}^{3+}, \text{Dy}^{3+}, \text{Eu}^{2+}$, specifically to the said people with diabetes, in emergency signalling and for a better life quality in low lighting environments.

In the field of architecture, we proposed a new application of these $\text{SrAl}_2\text{O}_4:\text{Ce}^{3+}, \text{Dy}^{3+}, \text{Eu}^{2+}$ based-nanomaterials in ceramic tiles, in view to the superior persistent luminescence visibility and use by disable persons. New floors, photoluminescent-warning ceramic tiles were designed with multi-sensory (tactile, sonorous and visual contrast) and antimicrobial properties, for people with disabilities use them in the dark, with the priority of saving lives in emergencies. Such floors, with reliefs, can be combined to compose a unique multisensory photoluminescent signalization that enables a rapid evacuation through the use of mobility aids (e.g. canes, wheelchairs, walkers, crutches).

The integrated solution of such innovations that enhances the persistent luminescence property of $\text{SrAl}_2\text{O}_4:\text{Ce}^{3+}, \text{Dy}^{3+}, \text{Eu}^{2+}$ accessible for people with disabilities, can help save lives in the dark in an emergency. ■

mots-clés

Luminescence persistante, strontium, cerium (III), lanthanide, nanotubes, nanofils, capsules, personnes handicapées.

résumé

Cette étude transversale se concentre sur des propriétés de luminescence persistante liées à l'aluminate de strontium dopé par cerium (III), dysprosium (III) et europium (II), $\text{SrAl}_2\text{O}_4:\text{Ce}^{3+}$, Dy^{3+} , Eu^{2+} , dans les systèmes de signalisation des zones de risques ou d'urgences pour les personnes handicapées.

Dans le domaine de la science et ingénierie des matériaux, a développé de nouveaux matériaux luminescents à l'échelle nanométrique, $\text{SrAl}_2\text{O}_4:\text{Ce}^{3+}$, Dy^{3+} , Eu^{2+} nanotubes, nanofils et nanotiges, pour les applications dans la réhabilitation et l'accessibilité des personnes handicapées. Les nanotubes ont été obtenus à partir de micro- et nano-particules précurseurs par synthèse à l'état solide suivie d'un traitement thermique de post-recuisson (1273-1473 K). Les nanofils et nanotiges ont été préparés par broyage, traitement aux ultrasons et post-recuits (373 K).

Les capsules luminescentes originales, basées sur les aluminates dopés au cérium (III) et encapsulés avec le TiO_2 , ont été créés afin d'obtenir des matériaux multifonctionnels avec une activité photocatalytique, y compris les antimicrobiens, antibactériens et des propriétés de résistance à l'eau. Ces aluminates peuvent être largement appliqués en tant que surface d'hygiène, d'auto-nettoyage, dans les biomatériaux, dans le domaine des antibiotiques, dans la formulation des vaccins, en mettant l'accent sur l'application de la céramique photoluminescente.

Les méthodes pour obtenir ces nanostructures à l'aluminate de strontium dopé au cérium (III) et de son encapsulation, développé dans cette thèse, sont applicables aux différents aluminates dopés avec d'autres ions lanthanides (Ln est La, Ce, Pr, Nd, Pm, Sm, Eu, Gd, Tb, Dy, Ho, Er, Yb, Tm ou Lu) avec la formule $\text{M}_{(1-x-y)}\text{N}_2\text{O}_4:\text{Ce}_x\text{Ln}_y$, où M est Be, Mg, Ca, Sr ou Ba.

Dans le domaine de l'ophtalmologie, un équipement médical a été développé pour le diagnostic de biofonctionnalité des cellules photoréceptrices de la rétine et le soutien de la télé-médecine en ophtalmologie. Ce équipement a été utilisé pour tester la vision des couleurs FM100HUE en blanc/noir fond pour la personnalisation de matériaux luminescents. Les résultats montrent une biofonctionnalité cellulaire supérieure à la visibilité photopique de couleurs sur un fond noir chez les personnes atteintes de rétinopathie diabétique (n=38) que par rapport aux sujets de référence (n=38). Ces résultats suggèrent la recommandation de matériaux photoluminescents ($\lambda_{\text{em}} = 485-555 \text{ nm}$), y compris $\text{SrAl}_2\text{O}_4:\text{Ce}^{3+}$, Dy^{3+} , Eu^{2+} , à ces personnes atteintes de diabète, dans la signalisation d'urgence et pour une meilleure qualité de vie dans l'éclairage faible.

Dans le domaine de l'architecture, nous avons proposé une nouvelle application de ces nanomatériaux luminescents basée sur $\text{SrAl}_2\text{O}_4:\text{Ce}^{3+}$, Dy^{3+} , Eu^{2+} , en carreaux céramiques, en vue de la bonne visibilité pour les personnes ayant des déficiences visuelles. Nouveaux pavements, céramiques, photoluminescents, ont été conçus avec des propriétés multi-sensorielle et antimicrobiennes, dans des conditions d'obscurité pour les personnes handicapées, et dans le but de sauver des vies dans les situations graves d'urgence. Ces pavements, en reliefs, peuvent être combinés pour composer un signal unique photoluminescent multisensoriel qui permet une évacuation rapide grâce à l'utilisation des aides à la mobilité (par exemple, cannes, fauteuils roulants, des déambulateurs).

La solution intégrée de ces innovations améliore la propriété de luminescence persistante de $\text{SrAl}_2\text{O}_4:\text{Ce}^{3+}$, Dy^{3+} , Eu^{2+} nanomatériaux accessible aux personnes handicapées et peut aider à sauver des vies, dans l'obscurité, dans une situation d'urgence. ■

Contents

Chapter 1	General Introduction	1
1.1	Luminescence Field for People with Disabilities	3
1.2	Background Research: People with Disabilities	4
	1.2.1. Pilot Project for Urban Accessibility	4
	1.2.2. Ceramic Tiles for Accessibility	5
	1.2.3. Rehabilitation Background	6
1.3	Scope of Work, Motivation and Contribution	6
1.4	Legal Postulations	7
1.5	Objectives	9
1.6	Overview and Document Structure	10
Chapter 2	Tools	12
	Part I – Theoretical Tools	13
2.1	Conceptual Background	13
	2.1.1. Luminescent materials	13
	2.1.2. Standards & Legislations of photoluminescent materials and products	20
	2.1.3. Human factors for emergency photoluminescent signalling	24
	2.1.3.1. Visual system	24
	2.1.3.2. Illuminance	33
	2.1.3.3. Mobility time for evacuation	34
	2.1.3.4. Preferential pedestrian pathway	35
	Part II – Experimental Tools	36
2.2	Characterization Techniques	36
	2.2.1. AFM	36
	2.2.2. SEM	36
	2.2.3. TEM	37
	2.2.4. XRD	37
	2.2.5. XRF	38
	2.2.6. ICP-MS	38
	2.2.7. RAMAN	38
	2.2.8. NMR	39
	2.1.9. Zeta potential	39
	2.1.10. Particle size distribution	40
	2.1.11. Thermal analysis	40
	2.1.12. Photoluminescence spectroscopy	40
2.3	Materials	41
	2.3.1. Baseline material : SrAl ₂ O ₄ :Ce ³⁺ , Dy ³⁺ , Eu ²⁺ micro- and nano-particles	42
	2.3.2. Porcelain stoneware ceramic substrate	44
	2.3.3. Materials and reagents for encapsulating the luminescent particles	44
	2.3.4. Transparent frit for covering the multilayered luminescent samples	44
	2.3.5. Characterizations of starting materials	44
2.4	Processing	46
	2.4.1. Mechanical deposition, dry-pressing and/or post-annealing	46
	2.4.2. Grinding and/or ultrasonification	46

Chapter 3	Afterglow phenomenon of luminescent SrAl₂O₄:Ce³⁺, Dy³⁺, Eu²⁺ nanotubes	47
	Part I – Nanotubes growth	48
3.1	SrAl ₂ O ₄ nanotube growth	48
3.2	Synthesis process of luminescent nanotubes growth	49
	3.2.1. Utilization of SrAl ₂ O ₄ :Ce ³⁺ , Dy ³⁺ , Eu ²⁺ micro- and nano-particles	49
	3.2.2. Lattice defects and rolling up mechanism	49
3.3	Luminescent SrAl ₂ O ₄ :Ce ³⁺ , Dy ³⁺ , Eu ²⁺ nanotube growth	54
	3.3.1. Luminescent nanotubes	54
	3.3.2. Intercrystalline distances of SrAl ₂ O ₄ :Ce ³⁺ , Dy ³⁺ , Eu ²⁺ polymorphs	56
	Part II – Intercrystalline distal-effect	58
3.4	Photoluminescence of α, β and γ-nanotube phases	58
	3.4.1. Photoluminescence excitation and emission	58
	3.4.2. Afterglow lifetime	61
3.5	Afterglow modifications from polymorphism	63
	3.5.1. Trap model of energy transfer mechanism	63
	3.5.2. Spatial separation of DAPs	64
3.6	Intercrystalline distal-effect on the afterglow phenomenon	65
3.7	Conclusion	68
Chapter 4.	Luminescent SrAl₂O₄:Ce³⁺, Dy³⁺, Eu²⁺ nanowires and nanorods	69
4.1	Formation of SrAl ₂ O ₄ nanowires and nanorods	70
4.2	Ultrasonic method of manufacturing nanostructures	71
	4.2.1. Processing of alkaline-earth aluminates doped with cerium (III)	71
	4.2.2. Grinding of precursor particles	71
	4.2.3. Ultrasonification of particles	72
	4.2.4. Post-annealing of milled and sonicated particles	72
4.3	Luminescent M _(1-x-y) N ₂ O ₄ :Ce _x , Ln _y nanowires/nanorods	73
	4.3.1. Structure of nanowires/nanorods	73
	4.3.2. Morphology of nanowires/nanorods	74
	4.3.3. Chemical characterization of nanowires/nanorods	75
	4.3.4. Photoluminescence of nanowires/nanorods	76
4.4	Potential utilizations of nanowires and nanorods	77
4.5	Conclusion	78
Chapter 5.	Photocatalytic core-shells of SrAl₂O₄:Ce³⁺, Dy³⁺, Eu²⁺@TiO₂ nanotubes	79
5.1	Hydrolysis of the crystalline host lattice	80
5.2	Encapsulation process	85
	5.2.1. Na ₂ TiO ₃ approach for the synthesis of core-shells	85
	5.2.2. Formation of a film of hybrid strontium aluminate co-doped	85
	5.2.3. Encapsulation of SrAl ₂ O ₄ :Ce ³⁺ , Dy ³⁺ , Eu ²⁺ @TiO ₂ core-shells	85
5.3	Encapsulation process analysis	87
5.4	Core-shells: biocompatible nanoprobe	88
	5.4.1. TiO ₂ nanotubes shell	88
	5.4.2. ¹³ C and ²⁷ Al MAS NMR of core-shells	91
	5.4.3. Photocatalytic core-shells	93
	5.4.4. Aqueous resistance of core-shells	94
	5.4.5. Antiseptic, antimicrobial and antibacterial core-shell nanoprobe	96
5.5	Conclusion	96

Chapter 6.	Biometric personalization of SrAl₂O₄:Ce³⁺, Dy³⁺, Eu²⁺ colour emission	97
	Part I – EYE-BIO-VIS Telemedical Workstation	98
6.1.	Pre-clinical colour vision FM100-HUE test	98
6.2.	Designing an ophthalmic medical equipment	99
	6.2.1. Construction and spatial configuration of the medical equipment	99
	6.2.2. Components of the medical equipment	100
	6.2.3. General instructions for use the medical equipment	100
6.3.	Biometric personalization of materials by retinal diagnostic	101
	6.3.1. Interactive testing eyes	101
	6.3.2. Retinal diagnoses of biofunctionality from the end user(s) in space	104
	6.3.3. Biometric data conversion via ocular neural network	105
	6.3.4. Personalized materials	106
	Part II – Personalization of luminescence emission	107
6.4.	Retinal diagnostic test for personalization of photoluminescent materials	107
6.5.	Biostatistical analysis	111
	6.5.1. Descriptive statistics	111
	6.5.2. ANOVA with covariates (intergroup analysis)	117
	6.5.3. Paired T-test (intragroup analysis)	121
6.6.	Personalized SrAl ₂ O ₄ :Ce ³⁺ , Dy ³⁺ , Eu ²⁺ colour emission	122
6.7.	Conclusion	127
Chapter 7.	Designing photoluminescent-warning ceramic tiles for risk areas and emergency	128
	Part I – Designing for accessibility	129
7.1.	Multisensory systems for accessibility	129
	7.1.1. Warning detectable tiles	129
	7.1.2. Photoluminescent products for safety	130
7.2.	Designing with SrAl ₂ O ₄ :Ce ³⁺ , Dy ³⁺ , Eu ²⁺ nanomaterials	131
7.3.	PL-WCT — Photoluminescent-warning ceramic tiles	132
	7.3.1. PL-WCT typologies	132
	7.3.2. Transversal characterization in emergency	134
	7.3.3. Principles of Universal Design in emergency signalling	135
7.4.	PL-WCT sunlight energy upconversion and emission	136
7.5.	PL-WCT architectural applications	140
	Part II – Manufacturing PL-WCT	144
7.6.	Ceramic process	144
	7.6.1. Moulding and pressing the ceramic substrate	145
	7.6.2. Sintering the ceramic substrate at 1473 K	145
	7.6.3. Photoluminescent layer onto the ceramic substrate	146
	7.6.4. Transparent glass frit deposition onto photoluminescent layer	147
	7.6.5. Post-annealing at 923 K	147
	7.6.6. Predicting the technical characteristics of PL-WCT	148
	Part III – Multilayered system	149
7.7.	Photoluminescent multilayered system	149
	7.7.1. Samples preparation	149
	7.7.2. Thermal behaviour of PL-multilayered system	150
	7.7.3. Alternative solutions for the PL-multilayered system	150
7.8.	Conclusion	151

Chapter 8. General Conclusion	152
8.1. Conclusion	153
8.2. Perspectives of future works in related fields	155
Bibliography.	156
Glossary.	166

Publications

Oral communication

Deutschen UNESCO-Kommission - Fördern durch Spielmittel - Bethel, Bielefeld, Deutschland (2006)

Humanism by (Bio) Materials – An Introduction for Accessibility and Rehabilitation

N. K. Zurba

Book

Deutschen UNESCO-Kommission, Fördern durch Spielmittel, Wissen Media Verlag (2007) 1, 12,

ISBN 978-3-577-10200-1. In: <http://www.unesco.de>

UNESCO Spielkulturen – Bauen - Spielen - Lernen

N. K. Zurba (Citation): A. Heinzemann, C. Sonntag, R. Elbracht (Editors)

Prize

«Prémio Maria Cândida de Cunha 2009»

National Institute for Rehabilitation, INR, I.P.

Ministry of Work and Social Solidarity, MTSS



NANO-EMERGÊNCIA: Luminescência Persistente de $SrAl_2O_4:Ce^{3+}$, Dy^{3+} , Eu^{2+} para Pessoas com Deficiências

Patents

National Patent, PI105107 (2010) *Ultrasonic method of manufacturing luminescent aluminates nanowires and nanorods doped with cerium (III) and nanostructured composites*, N. K. Zurba, J. M. F. Ferreira

National Patent, Div. PI104801 (2010) *Luminescent antibacterial dental paste from aluminates doped with cerium (III) encapsulated with TiO_2* , N. K. Zurba, J. M. F. Ferreira

National Patent, PI104801 (2009) *Encapsulation process of beryllium, magnesium, strontium, calcium and barium aluminates doped with cerium (III) coated with TiO_2 and respective utilizations*, N. K. Zurba, J. M. F. Ferreira

International Patent, PCT/PT2009/000070/PI104486 (2009) *Luminescent beryllium, magnesium, strontium, calcium and barium aluminate nanotubes doped with cerium (III) and co-doped with other lanthanide ions, $M_{(1-x-y)}N_2O_4:Ce_x, Ln_y$* , N. K. Zurba

National Patent, PI103919 (2008) *Medical equipment and Method of personalization of materials by retinal diagnostic of photoreceptor cells in space*, N. K. Zurba, M. Fernandes, E.O. B. Leite, A. A. Nogueira, P. T. Fiadeiro, M. C. Fredel (Concession still 2028)

National Patent, PI103915 (2007) *Photoluminescent-Warning Ceramic Tiles for Risk Areas and Emergency of People with Special Needs*, N. K. Zurba, M. Fernandes, E. O. B. Leite, M. C. Fredel

Article

Nanotechnology (2010) 21, 32, doi:10.1088/0957-4484/21/32/325707, *Intercrystalline distal-effect on the afterglow phenomenon in photoluminescent $SrAl_2O_4:Ce(III)$, Ln nanotube growth*

N. K. Zurba, I. Bdiqin, A. Kholkin, D. Golberg, J. M. F. Ferreira

Trademarks

National Trademark, INPI, 446679 (2009) Concession still 2019

PL-BaNT :Ce³⁺, Ln Photoluminescent-Barium Aluminate Nanotube®

N. K. Zurba

National Trademark, INPI, 446680 (2009) Concession still 2019

PL-CaNT :Ce³⁺, Ln Photoluminescent-Calcium Aluminate Nanotube®

N. K. Zurba

National Trademark, INPI, 446681 (2009) Concession still 2019

PL-MgNT :Ce³⁺, Ln Photoluminescent-Magnesium Aluminate Nanotube®

N. K. Zurba

National Trademark, INPI, 446682 (2009) Concession still 2019

PL-SNT :Ce³⁺, Ln Photoluminescent-Strontium Aluminate Nanotube®

N. K. Zurba

National Trademark, INPI, 446683 (2009) Concession still 2019

PL-NT :Ce³⁺, Ln Nanoröhren mit Photolumineszenz®

N. K. Zurba

National Trademark, INPI, 446684 (2009) Concession still 2019

PL-BeNT :Ce³⁺, Ln Photoluminescent-Beryllium Aluminate Nanotube®

N. K. Zurba

National Trademark, INPI, 458140 (2009) Concession still 2019

Biotitania TiO₂ Nanocoating Ce³⁺ Phosphor®

N. K. Zurba, J. M. F. Ferreira

National Trademark, INPI, 460961 (2010) Concession still 2020

PL-NW :Ce³⁺, Ln Photoluminescent-Nanowires®

N. K. Zurba, J. M. F. Ferreira

National Trademark, INPI, 460962 (2010) Concession still 2020

PL-NR :Ce³⁺, Ln Photoluminescent-Nanorods ®

N. K. Zurba, J. M. F. Ferreira

National Trademark, INPI, 425983 (2007) Concession still 2017

PL-WCT Photoluminescent-Warning Ceramic Tiles®

N. K. Zurba, M. Fernandes, E. O. B. Leite, M. C. Fredel

National Trademark, INPI, 425984 (2007) Concession still 2017

PL-WCT Keramikfliesen mit Photolumineszenz für Gefahren- und Notfallstellen®

N. K. Zurba, M. Fernandes, E. O. B. Leite, M. C. Fredel

National Trademark, INPI, 425985, 425986 (2007) Concession still 2017

EYE-BIO-VIS Telemedical Workstation®

N. K. Zurba, M. Fernandes, E. O. B. Leite, M. C. Fredel

Abbreviations

ADAAG	Americans with Disabilities Act Accessibility Guidelines
AFM	Atomic force microscopy
AMD	Age-related macular degeneration
ANSI	American National Standard Institute
ASTM	American Society for Testing Materials
CB	Conduction band
cGMP	Cyclic guanosine monophosphate
CIE	<i>Commission Internationale de L'Eclairage</i>
CNT	Carbon nanotube
CRT	Cathode ray-tube
CTA	Ceramic tiles for accessibility
DAPs	Donors and acceptors pairs
DCCT	Diabetes control and complications trial
DGS	Directorate General of Health
DIN	<i>Deutsches Institut für Normung</i>
DTA	Differential thermo gravimetric analysis
EDX	Energy dispersive X-ray spectroscopy
ENC	Encapsulated sample
ET	Energy transfer
EUROSTAT	European Commission Statistical Committees
EWGS	Emergency way finding guidance system
FM100-HUE	Farnsworth-Munsell 100-HUE
HRTEM	High-resolution transmission electronic microscopy
IBGE	Brazilian Institute of Geography and Statistics
ICP-MS	Inductively coupled plasma-mass spectroscopy
IEP	Isoelectric point
INE	National Institute of Statistics
IOL	Intra-ocular lens
ISO	International Organization for Standardization
ITDS	Integrated Thermodynamic Databank System
Ln	Lanthanide
MAS	Magic angle spinning
NF	French Norm
NMR	Nuclear magnetic resonance
PEG	Poly(ethylene glycol)
PL	Photoluminescence
PMMA	Poly(methyl methacrylate)
PNPA	National Plan for the Promotion of Accessibility
PSPA	Photoluminescent Safety Products Association
SAED	Selected area electron diffraction
SEM	Scanning electronic microscopy
TEC	Thermal expansion coefficient
TEM	Transmission electronic microscopy
TG	Thermo gravimetry
TRE	Time-resolved emission spectroscopy
WHO	World Health Organization
XRD	X-ray diffraction

List of Figures

Chapter 1

1-1. a) Urban landscape of warning tiles applied at Álvaro de Carvalho and Esteves Júnior Streets, in the Historical Centre of Florianópolis, Brazil; b-c) alert typology in concrete material with relative low mechanical resistance and durability for high pedestrian traffic in open spaces [6, 7].	4
1-2. Multisensory assistive devices on surfaces of the Ceramic Tiles for Accessibility [9] with: a) alert, b) stopped, c) guide, and d) crossing typologies. A sensorial test was realized by a blind using a walking stick.	5
1-3. Elderly using assistive devices in the rehabilitation centre, at Bethel Altenhilfe Institution, Germany.	6
1-4. Persistent luminescence approach for emergency signalling visually accessible, upon illuminance <25 lux: activation of the afterglow phenomenon.	10

Chapter 2

2-1. Dieke diagram with Ln^{3+} energy levels observed in LaCl_3 [27a].	16
2-2. Optical features of SrAl_2O_4 and ZnS co-doped phosphors [23f].	17
2-3. Energy transfer mechanism between sensitizer and activator.	18
2-4. Kelvin temperature conversion of the $\text{SrO}-\text{Al}_2\text{O}_3$ phase diagram [40].	19
2-5. Luminance parameters of DIN 67510 [14] and PSPA [16] for emergency applications.	21
2-6. Ophthalmic colour vision test Farnsworth Munsell 100-HUE: a) first generation with coloured caps; b) second generation with electronic score results; and c) third generation with computational test.	25
2-7. Retinal response in dark adaptation from hyperpolarization to depolarization of photoreceptor cone-cells via cGMP electron transmission [56].	26
2-8. Dark-adapted retinal response vs. time in the dark, which dark adaptation is determined in part by the time required to build up the rhodopsin stores and for optimal adaptation of rod function [55]: (a) The time-limit (10 min) valid for our experimental of FM100-HUE colour vision test from photopic (cone cells) biofunctionality response for luminescent materials.	27
2-9. Spectral sensitivity of the colour vision under the Purkinje effect [59], supporting the selection of photoluminescent materials for emergency.	29
2-10. a) Trigonometric forces generated during the walking [65]; b) and c) dimensional space of a person in wheelchair [50a].	34
2-11. Preferential pedestrian pathway with a photoluminescent signalling, according to the New York City's Building Code [48] upon day light illumination (left side), and in darkness (right side).	35
2-12. Assembly of AFM Multimode, Nanoscope IIIA, DI.	36
2-13. In left, a schematic functionalization of the spectrophotometer: (1) Xenon lamp; (2) excitation monochromator; (3) support and the sample; (4) the emission monochromator, photomultiplier, computer and data control. In right, IS-SPECWIN software.	41
2-14. Yellow-green emission spectra of $\text{SrAl}_2\text{O}_4:\text{Ce}^{3+}, \text{Dy}^{3+}, \text{Eu}^{2+}$ starting material upon different wavelength of excitation: a) $\lambda_{\text{ex}} = 300$ nm, b) $\lambda_{\text{ex}} = 320$ nm, and c) $\lambda_{\text{ex}} = 360$ nm (UV-lamp).	42
2-15. SEM and Coulter analyses of the particles size distribution of $\text{SrAl}_2\text{O}_4:\text{Ce}^{3+}, \text{Dy}^{3+}, \text{Eu}^{2+}$ precursor micro- and nano- particles and 65% SiO_2 —21% Al_2O_3 —14% alkali oxides.	45
2-16. Pressed samples: a) laboratorial moulding; and b) typical pallet samples of the $\text{SrAl}_2\text{O}_4:\text{Ce}^{3+}, \text{Dy}^{3+}, \text{Eu}^{2+}$ precursor micro- and nano-particles phosphor (starting material) applied onto (65% SiO_2 —21% Al_2O_3 —14% alkalis) ceramic substrates.	46

Chapter 3

3-1. TEM images of SrAl_2O_4 : (a)-(d) the roll-up layers to form nanoscrolls during hydrothermal synthesis at 393 K; (e) nanotubes [70].	48
3-2. TEM image of a precursor α -monoclinic $\text{SrAl}_2\text{O}_4:\text{Ce}^{3+}, \text{Dy}^{3+}, \text{Eu}^{2+}$ isolated nanoparticle with linear lattice defects (arrowed) having a) isotropic distribution, and b) anisotropic lamellar distribution; c-h) crystallographic arrangement and rolling-up mechanism of (α,β) phases \rightarrow γ -nanotubes transition under a solid-state synthesis and post-annealing at 1473 K [75].	50
Figure 3-3. SEM analysis of post-annealed $\text{SrAl}_2\text{O}_4:\text{Ce}^{3+}, \text{Dy}^{3+}, \text{Eu}^{2+}$ samples. From 573 to 873 K the α -type present nanoparticles grouped and dispersed (1-D < 70 nm). At 973 K, the limit of phase transformation temperature, the α - β transition was characterized by planar defects and the starting of polymorphic hexagonal phase. From 1073 to 1373 K, the material presents micro and nano crystals with β -type structures. Scale bar= 500 nm.	51
3-4. Crystallographic arrangement of β -phase after the host phase transformation.	52
3-5. Crystallographic evolution of $\text{SrAl}_2\text{O}_4:\text{Ce}^{3+}, \text{Dy}^{3+}, \text{Eu}^{2+}$ with post-annealing temperature.	53
3-6. Raman spectra of $\text{SrAl}_2\text{O}_4:\text{Ce}^{3+}, \text{Dy}^{3+}, \text{Eu}^{2+}$ before and upon post-annealing at 1473 K.	53
3-7. SEM and TEM images of luminescent $\text{SrAl}_2\text{O}_4:\text{Ce}^{3+}, \text{Dy}^{3+}, \text{Eu}^{2+}$ nanotubes obtained by solid-state synthesis and post-annealing at a) 1273 K, and b-c) 1473 K; b) EDX spectrum of the γ -nanotube; c) SAED pattern of the nanotube recorded along the $[1\bar{1}0]$ zone axis [75].	54

3-8. a) TEM image of luminescent SrAl ₂ O ₄ :Ce ³⁺ , Dy ³⁺ , Eu ²⁺ product post-annealed at 1273 K; HRTEM images reveal in b) and c) the anti-phase boundaries; and in d) the crystalline lattice spacing of about 0.3 x 0.5 nm.	55
3-9. AFM analysis of SrAl ₂ O ₄ :Ce ³⁺ , Dy ³⁺ , Eu ²⁺ in a 5 μm × 5 μm scanning area: a) morphology of an orientated thin structure; b) A-B cross-section; c) host lattice vectors 80 x 500 nm; d) inter-crystalline distances in a A-B cross-section profile [75].	56
3-10. a) AFM scans of SrAl ₂ O ₄ :Ce ³⁺ , Dy ³⁺ , Eu ²⁺ samples; and b) their intercrystalline distances [75]: (1) monoclinic particles; d ₁ = 50 nm; post-annealed at: (2) 573 K, d ₂ = 72 nm; (3) 973 K, d ₃ = 90 nm; (4) 1273 K, d ₄ = 118 nm; (5) 1473 K, d ₅ = 137 nm.	57
3-11. a) Emission and b) excitation spectra from steady-state PL spectroscopy of SrAl ₂ O ₄ :Ce ³⁺ , Dy ³⁺ , Eu ²⁺ : pressed and non-supported samples - curves (a) = α-monoclinic particles; curves (b) and (c) = β-hexagonal and γ-nanotube crystals obtained by post-annealing at 1273 and 1473 K, respectively; pressed samples onto a ceramic substrate - curves (d) and (e) = β-hexagonal and γ-nanotube crystals obtained by post-annealing at 1273 and 1473 K, respectively.	59
3-12. Afterglow phenomenon on SrAl ₂ O ₄ :Ce ³⁺ , Dy ³⁺ , Eu ²⁺ nanotubes by post-annealing at 1473 K: a) photoluminescence emission after excitation at 253, 300, 360 392.5 and 463 nm showing a series of <i>f-f</i> and <i>f-d</i> transitions [75].	60
3-13. Afterglow decay curve of polymorphic SrAl ₂ O ₄ :Ce ³⁺ , Dy ³⁺ , Eu ²⁺ β-hexagonal and γ-nanotubes by post-annealing. In detail: emission spectra after post-annealing at 1273, 1373 and 1473 K onto the ceramic substrate; the large bands correspond to the Ce ³⁺ electronic transitions in the host lattice.	61
3-14. Time-resolved emission spectra of the SrAl ₂ O ₄ :Ce ³⁺ , Dy ³⁺ , Eu ²⁺ samples acquired with starting delays of (1) 0.05 ms, (2) 50.00 ms and (3) 200.00 ms, using an integration window of 20.00 ms and excited at 360 nm: α-monoclinic particles (a); non-supported pellets of β-hexagonal and γ-nanotubes crystals (b) and (c); pressed pellets deposited onto a ceramic substrate (d) and (e). The arrowhead thin structure with preferential 1D-growth indicates the formation of SrAl ₂ O ₄ :Ce ³⁺ , Dy ³⁺ , Eu ²⁺ nanotubes at 1473 K; scale bar = 300 nm.	62
3-15. Representation of the conduction band of SrAl ₂ O ₄ :Ce ³⁺ , Dy ³⁺ , Eu ²⁺ polymorphs.	64
3-16. Intercrystalline distal-effect on the afterglow phenomenon performed to SrAl ₂ O ₄ :Ce ³⁺ , Dy ³⁺ , Eu ²⁺ in α-monoclinic particles, β-hexagonal and γ-nanotubes crystals [75].	67

Chapter 4

4-1. Evolution of particle size distributions of precursor of SrAl ₂ O ₄ :Ce ³⁺ , Dy ³⁺ , Eu ²⁺ with milling time (1, 3 and 7 h).	72
4-2. X-ray diffraction patterns of SrAl ₂ O ₄ :Ce ³⁺ , Dy ³⁺ , Eu ²⁺ nanowires/nanorods obtained by milling for 1 and 7 h, followed by ultrasonification for 1 h to 3 MHz, and post-annealing at 373 K.	73
4-3. TEM micrographs of SrAl ₂ O ₄ :Ce ³⁺ , Dy ³⁺ , Eu ²⁺ nanowires and nanorods.	74
4-4. TEM micrograph of a SrAl ₂ O ₄ :Ce ³⁺ , Dy ³⁺ , Eu ²⁺ nanorod characterized by a diameter of about 40-50 nm and a longitudinal length of about 350 nm with an aspect ratio of about 7-8.	75
4-5. Selected area electron diffraction with a qualitative chemical analysis performed during transmission electron microscopy of SrAl ₂ O ₄ :Ce ³⁺ , Dy ³⁺ , Eu ²⁺ nanowires and nanorods, showing the presence of Sr, Al and O crystal field components of the host.	75
4-6. Emission spectrum of photoluminescence of SrAl ₂ O ₄ :Ce ³⁺ , Dy ³⁺ , Eu ²⁺ nanowires and nanorods characterized by ultraviolet (UV) emission peaking at λ = 52 nm and ultraviolet visible (UV-VIS) emission peaking at λ = 525 ± 5 nm under atomic excitation at 320 nm.	76
4-7. TEM micrograph showing a detail of a self-assembly growth of SrAl ₂ O ₄ :Ce ³⁺ , Dy ³⁺ , Eu ²⁺ nanowires and nanorods in parallel; the black rectangle indicates the selected area electron diffraction (SAED) of the Figure 5-5.	77
4-8. SEM visualizations of SrAl ₂ O ₄ :Ce ³⁺ , Dy ³⁺ , Eu ²⁺ nanowires and nanorods. Note that the nanowire morphology varies between the nanoparticles (length of 1.32 μm and a diameter of 60.9 nm indicated in the image), comprising an aspect ratio of about 22, much higher than the average aspect ratio of about 5 measured for nanorods.	78

Chapter 5

5-1. Schematic representation of: a) SrAl ₂ O ₄ :Ce ³⁺ , Dy ³⁺ , Eu ²⁺ phosphor applied onto a ceramic substrate (65% SiO ₂ —21% Al ₂ O ₃ —14% alkali) [108]; b) surface interactions upon hydrolysis of uncoated monoclinic nanoparticles in contact with water, leading to a high pH value (~12.7).	81
5-2. Non-encapsulated SrAl ₂ O ₄ :Ce ³⁺ , Dy ³⁺ , Eu ²⁺ micro and nanoparticles: a) zeta potential and electronic conductivity measurements in ethanol (IEP at pH~8.56); b) kinetics of the hydrolysis process in water time-resolved measurements after 0, 10, 60, 240, 1440 and 3120 minutes, by Coulter DELSA 440 SX.	82
5-3. Structural SEM analysis of SrAl ₂ O ₄ :Ce ³⁺ , Dy ³⁺ , Eu ²⁺ hydrolyzed after 3000 min at pH >10 with the formation of Al(OH) ₃ polymorphs: a-c) nordstrandite nanocrystals; e-f) the arrow indicates the selected area revealing elongated crystals.	82
5-4. XRD patterns of nordstrandite derived from hydrolysis of SrAl ₂ O ₄ :Ce ³⁺ , Dy ³⁺ , Eu ²⁺ for 3000 min at pH >10, resulting in the formation of Al(OH) ₃ polymorphs.	83
5-5. Hybrid layer of strontium aluminate co-doped with lanthanide ions.	85
5-6. Schematics of the encapsulation process by TiO ₂ coating layer: a) hybrid organic-inorganic core-shells; and b) inorganic core-shells.	86
5-7. XRD profiles of SrAl ₂ O ₄ :Ce ³⁺ , Dy ³⁺ , Eu ²⁺ @TiO ₂ core—shell particles encapsulated in the presence (a, b) and absence of PEG-300 (c) and heat treated at 353 K (a) or 673 K (b, c). Legend: m= monoclinic core structure; a = anatase and r = rutile shell structures (Ti _{0.784} O ₂ or TiO ₂).	87
5-8. TEM analysis of SrAl ₂ O ₄ :Ce ³⁺ , Dy ³⁺ , Eu ²⁺ encapsulated with semi-crystalline TiO ₂ nanotubes/nanowires coating layer deposited in the presence of PEG-300, heat treated at 353 K.	88

5-9. TEM analysis of SrAl ₂ O ₄ :Ce ³⁺ , Dy ³⁺ , Eu ²⁺ encapsulated with semi-crystalline TiO ₂ coating layer deposited in the presence of PEG-300 and heat treated at 353 K, presenting anatase nanowires (a-c) and nanotubes (d).	89
5-10. SEM micrographs of SrAl ₂ O ₄ :Ce ³⁺ , Dy ³⁺ , Eu ²⁺ encapsulated by TiO ₂ coating layer deposited in the presence of PEG-300 and heat treated at 353 K for: a) 30 min; b) 1 hour; and c) 2 hours.	89
5-11. SEM micrographs of core-shell particles obtained in the presence (a), and absence (b) of PEG-300 and heat treated at 673 K.	90
5-12. TEM micrographs of core-shell particles obtained in the presence (a), and absence (b) of PEG-300 and heat treated at 673 K.	90
5-13. TEM micrographs of core-shell particles obtained in the absence of PEG-300 and heat treated at 673 K.	91
5-14. NMR MAS spectra of SrAl ₂ O ₄ :Ce ³⁺ , Dy ³⁺ , Eu ²⁺ @TiO ₂ core-shells obtained in the presence (ENC1 and ENC3) and in the absence (ENC2) of PEG-300 and heat treated (ENC1 and ENC2) and at 353 K (ENC3): a) ¹³ C MAS of hybrid organic-inorganic phosphors; b) ²⁷ Al MAS of non-encapsulated phosphor and core-shell particles.	92
5-15. Formation of photocatalytic TiO ₂ shell on phosphor surface.	93
5-16. Hole trapping model of photocatalytic TiO ₂ shell on phosphor surface.	94
5-17. Evolution with time of zeta potential and electronic conductivity for SrAl ₂ O ₄ :Ce ³⁺ , Dy ³⁺ , Eu ²⁺ @TiO ₂ core—shells dispersed in water.	95
5-18. SEM analysis of the SrAl ₂ O ₄ :Ce ³⁺ , Dy ³⁺ , Eu ²⁺ @TiO ₂ core—shell samples, after 240 min exposed in aqueous fluids: a) ENC1; b) ENC2; and c) ENC3.	95

Chapter 6

6-1. Comparative diagnoses from pre-clinical standard and computational colour vision test FM 100-HUE, Leite & Leite Ocular Microsurgery, Coimbra, Portugal (2006).	98
6-2. Designing the solutions for the medical equipment (e.g. lightning system, focal plan, dimensioning) by CAD 2D/3D virtual modelling; lightning system of the medical equipment with D65 and UV-dark (360 nm) illuminance.	99
6-3. Medical equipment testing retinal cells "in space", medical equipment prototype with dimensions 930 x 830 x 620 mm constructed at Ceramic and Glass Engineering Department of University of Aveiro, Portugal.	100
6-4. Medical equipment with biofunctional outline of the method according to the light generated [147]; (1) the human eye receives stimuli in several wavelengths, with constant focal distance between the observer and monitor (~ 0.40 m) in standard monocular (right/left eye) and binocular vision during the test; scheme of the biofunctionality responses in ocular neural network (multimedia), which may be represented in colour coordinates (e.g. RGB, CIEL*a*b*); (2) the photoreceptors cells are exposed to the stimulus upon the retina light rays entering the pupil from fluorescent lamps with illuminance higher than 500 lux, according to the standard illuminant D65; (3) the FM100-HUE test made on the computer generates colour signals emitted by the cathode luminescence of matches based on rare earths, with luminance typical of a commercial monitor (~250 cd/m ²), valid for the sensitivity of photoreceptors in the long (L), medium (M) and short (S) wavelengths of the visible spectrum of light (350-750 nm); (4) the spatial configuration is ergonomically adapted for all users (e.g. persons in wheelchairs), and with castors on the metallic base to facilitate the portability of the equipment; diagram of a binocular testing biofunctionality of photoreceptors cells "in space", showing: (5) medical equipment with ergonomic adapted shape; (6) local for the conventional FM100-HUE test (caps); and (7) geometric configuration of the focal length between the user and monitor.	102
6-5. Conglomerated places where the samples were recruited and the medical equipment was experimented, in Aveiro, Portugal (2009): a) Ophthalmologic Medical Sector of the Infante Dom Pedro Hospital (treatment); and b) Humanitarian Society of Voluntary Firemen (references).	109
6-6. Medical equipment experimented in 38 patients with diabetic retinopathy (treatment) located in the Ophthalmologic Medical Sector of the Infante Dom Pedro Hospital, Portugal (2009).	109
6-7. Medical equipment experimented in 38 patients with diabetic retinopathy (treatment) located in the Ophthalmologic Medical Sector of the Infante Dom Pedro Hospital, Portugal (2009).	110
6-8. Description of the error scores from retinal responses of references and treatments by FM100HUE diagnoses in white and black backgrounds.	113
6-9. Distributions for reference and treatment groups, of: a) colour vision in white and black backgrounds (log error scores), in function of the age (years); b) age vs. glucose levels (log-transformed data); and c) colour vision (log error scores) vs. glucose levels (log-transformed data).	114
6-10. Colour vision from the retinal responses of 2 patients with diabetic retinopathy.	116
6-11. SEM of cataract intra-ocular lens (IOL) with an UV absorbing compound by optic design equiconvex. Note that after cataract surgery, the difference between the colour vision scores of diabetic and non-diabetic patients is reduced [152].	116
6-12. ANOVA plots from the analysis with covariates for residual values (variability not explained), for: a) log White; b) log Black; and c) log White – log Black.	120
6-13. Photopic colour vision of a photoluminescent material (light emitting after excitation): a) diagram of comparative diagnoses of a binocular test of the retinal biofunctionality <i>in space</i> between white (light) and black (dark) backgrounds to be used as an estimative of visibility in darkness, valid on the first 10 minutes of PL visibility, while the photoreceptors cells are still hyperpolarized in response to illumination, and processing the colour signal; b) biofunctionality of retinal cells in function of the excitation source (λ_{ex}) _{PL} , energy transfer (E.T.) and emission by a sensitizer (S) or activator (A) that produces the PL light emission (λ_{em}) _{PL} . The photon energy emitted by luminescent centres in the UV-VIS region must be detected by the human eye cells with biofunctionality for long-, middle- and short- wavelengths (λ_{abs} L, M, S).	122
6-14. Biostatistics of retinal responses of treatments with diabetic retinopathy from (C31) to (C53) in the yellow-green-blue region (485-555 nm), in black background, for personalization of SrAl ₂ O ₄ :Ce ³⁺ , Dy ³⁺ , Eu ²⁺ in emergency, specifically at 525 nm (C35).	126

Chapter 7

7-1. Warning detectable tiles applied in: a) Japan; b) and c) Germany; and d) China.	129
7-2. Stages of the exploratory application of SrAl ₂ O ₄ :Ce ³⁺ , Dy ³⁺ , Eu ²⁺ nanomaterials on the development of the photoluminescent-warning ceramic tiles (PL-WCT).	131
7-3. Typologies of multisensory photoluminescent-warning ceramic tiles comprising visual, sonorous and tactile contrast features, which may be functionalized with antibacterial, antimicrobial and self-cleaning surfaces, under D65-illuminant and upon afterglow-in-dark emission (0 lux) [113].	133
7-4. PL-WCT crossing tile under a solar exposition absorbing the sunlight energy on the photoluminescence relief surfaces (1) adjacent to non-luminescent (inert) surfaces (2); and under afterglow-in-dark (0 lux) by persistent luminescence upconversion and emission from relief surfaces (4) in contrast with dark surfaces (2).	136
7-5. PL-WCT stopped tile under a solar exposition absorbing the sunlight energy on the photoluminescence relief surfaces (7) adjacent to non-luminescent (inert) surfaces (8) and (9); and under afterglow-in-dark (0 lux) by persistent luminescence upconversion and emission from relief surface (10) in contrast with dark surface (11).	137
7-6. PL-WCT directional guiding tile (connected) under a solar exposition absorbing the sunlight energy on the photoluminescence relief surfaces (12) adjacent to non-luminescent (inert) surfaces (13); and under afterglow-in-dark (0 lux) by persistent luminescence upconversion and emission from relief surfaces (14) in contrast with dark surfaces (15).	138
7-7. PL-WCT directional guiding tile (non-connected) under a solar exposition absorbing the sunlight energy on the photoluminescence relief surfaces (16) adjacent to non-luminescent (inert) surfaces (17); and under afterglow-in-dark (0 lux) by persistent luminescence upconversion and emission from relief surfaces (18) in contrast with dark surfaces (19).	139
7-8. Example of a functional Emergency Plan using directional (connected), stopped and crossing tiles typologies combined in an escape route.	140
7-9. a-b) Top view and building plan of Empire State Building, New York City, US (2006). Schematic example of a functional dark adapted Emergency Plan: c) tower and d) standard floor plans for evacuation using the photoluminescent-warning ceramic tiles. This solution was planned based on the elemental circulation pathways. Not scaled (n/s). http://www.safe-t-first.com/reference-standard-rs6-1.pdf	141
7-10. Example of a functional dark adapted Emergency Plan of the University of Aveiro Library for evacuation using the photoluminescent-warning ceramic tiles. The solution was planned based on the elemental circulation pathways [113]. Not scaled.	142
7-11. Example of a functional dark adapted Emergency Plan of the University of Aveiro Library for evacuation, using the photoluminescent-warning ceramic tiles [113]. The solution was planned based on the elemental circulation pathways. Not scale.	143
7-12. Processing routes attempted for preparing PL-WCT products.	144
7-13. Examples of semi-industrial moulding: a) polymeric moulding of substrates [10]; b) design of a second moulding of PL layer and transparent glass frit.	145
7-14. SEM images of porcelain stoneware substrate annealed at 1473 K. Opened porosity and roughness on the surface samples are showed and facilitate the interfacial adhesion of luminescent micro- and nano-particles layer in post-annealing conditions.	146
7-15. AFM morphology analysis of a porcelain stoneware substrate, annealed at 1473 K: a) and b) cross sections, with an average roughness of 2.7 μm (b); c) RMS= 4.7 μm, and surface area= 37.8 μm ² ; d) self-correlation, with respective grain size = 15 nm.	146
7-16. Surface transmission light-emitting reliefs: a) transparent glass frit (e.g. PbO-based); b) photoluminescent material (e.g. SrAl ₂ O ₄ :Ce ³⁺ , Dy ³⁺ , Eu ²⁺ nanotubes, nanowires, nanorods or core-shells); c) support; and d) ceramic substrate (e.g. porcelain stoneware).	147
7-17. Dilatometric curves of different materials for a multilayered system of PL-WCT via sintered route.	150

List of Tables

2-1. Lanthanides Series of the Periodical Table of Elements.	14
2-2 Comparison of luminance between of SrAl ₂ O ₄ and ZnS co-doped products [28].	17
2-3. Luminance of SrAl ₂ O ₄ co-doped product in function of the source of excitation [28].	17
2-4. DIN 67510 luminance classifications of photoluminescent materials [14].	20
2-5. PSPA indications of the colour appearance for safety signs [16].	21
2-6. Farnsworth-Munsell 100-HUE colour vision diagnoses [52].	25
2-7. Optical features of SrAl ₂ O ₄ :Ce ³⁺ , Dy ³⁺ , Eu ²⁺ starting material (N1 sample) upon a light source with Xenon lamps at 500 lux for 10 min of excitation.	43
2-8. Elemental analysis of as-received commercial phosphor, as determined by ICP-MS and EDX Bruker AXS Microanalysis.	43
2-9. Oxide composition of the stoneware ceramic substrate as determined by XRF.	44
3-1. Intercrystalline distal-effect on the afterglow phenomenon in SrAl ₂ O ₄ :Ce ³⁺ , Dy ³⁺ , Eu ²⁺ .	66
4-1. Formation of SrAl ₂ O ₄ :Ce ³⁺ , Dy ³⁺ , Eu ²⁺ nanowires and nanorods.	72
5-1. Encapsulation process of MAl ₂ O ₄ :Eu ²⁺ , RE ³⁺ (M = Sr or Ca) phosphors.	84
6-1. Comparative aspects in the FM100-HUE test using the medical equipment.	103
6-2. Ergonomic parameters for interactive testing eyes.	104
6-3. Matrix model of ophthalmic data processing.	105
6-4. Descriptive biostatistics of the reference group (fireman); the concatenate data were obtained from their responses in white-black backgrounds.	111
6-5. Descriptive biostatistics of the treatment group (diabetic retinopathy); the concatenate data were obtained from their responses in white-black backgrounds.	111
6-6. Descriptive biostatistics of concatenated error-scores from reference (fireman) and treatment (diabetic retinopathy) groups, for white and black backgrounds, respectively listed.	112
6-7. Descriptive biostatistics of concatenated glucose levels (mg/dL) and age (years) from reference (fireman) and treatment (diabetic retinopathy) groups.	112
6-8. Pearson correlation coefficients between age, glucose and error scores ($p < 0.05$).	115
6-9. ANOVA with covariates for log error scores from white background (=log White), using Adjusted SS for Tests.	117
6-10. ANOVA with covariates for log error scores from black background (=log Black), using Adjusted SS for Tests.	118
6-11. ANOVA means for covariates: age and glucose levels.	118
6-12. ANOVA least square means: log White and log Black.	118
6-13. ANOVA with covariates for difference between log error scores in white and black backgrounds (= [log White – log Black]), using Adjusted SS for Tests.	118
6-14. ANOVA least square means for log error scores in white and black backgrounds (= [log White – log Black]).	119
6-15. REFERENCE GROUP: Paired T-test and CI for log White - log Black.	121
6-16. TREATMENT GROUP: Paired T-test and CI for log White - log Black.	121
6-17. Descriptive statistics of the treatment group for colour vision from (C31) to (C53), in black background: a) error scores; b) log-transformed error scores.	124
6-18. Pearson correlation coefficients from (C31) to (C53) in black background for treatment (log-transformed error scores).	124
7-1. Photoluminescent-warning ceramic tiles for risk areas and emergency [113].	132
7-2. Transversal characterization of the photoluminescent-warning ceramic tiles, predicted after exposition to illuminance >25 lux, for 10 min.	134
7-3. Evaluation of the photoluminescent-warning ceramic tiles based on the Principles of Universal Design for an emergency system [113].	135
7-4. Prediction of technical characteristics of the PL-WCT in multilayered system.	148
7-5. Colour appearance of photoluminescent reliefs and inert substrate surfaces.	148

Chapter 1

General Introduction:

— How to save lives of people with disabilities in emergency?

Accessibility for all is a fundamental right in an inclusive society, considering the special conditions for mobility, participation and integration in the activities of life. A "disability" is not an absolute term in the European Union and some Member States do not have accurate statistics on the number of people living with functional disabilities. In economic terms (e.g. eligibility for benefits), social (e.g. inclusion in activities), and medical (e.g. diagnosis of diseases), there are wide discrepancies between European countries adopting the concept of people with disabilities [1]. Internationally, endorsing the rights of these people is a priority of the United Nations Educational, Scientific and Cultural Organization (UNESCO) devoted to an estimate of over 330 million disabled people living in the world [2]. In synergy to *European Year of Creativity and Innovation* (2009), in continuity to activities in the *European Year of Equal Opportunities for All* (2007), architects, engineers and other professionals involved in the design and construction of physical space should promote the construction of appropriate measures and innovative methods to ensure access for people with disabilities, as a process of achieving equal opportunities in all spheres of society.

In this work, "*people with disabilities*" or "*disabled*" are framed as a convergent term that defines a non-homogeneous group of individuals in a community in a plurality of functional human conditions from a physical disability, temporary or permanent, including motor, sensory, cognitive and respiratory disabilities — also including users with low mobility, low visibility or dependence of assistive technologies and devices, most usually the wheelchairs, walk sticks and warning tiles [3-12]. The accessibility of these disabled people requires to be met with effective technologies that help in their movement, thus avoiding social exclusion. In case of emergency, «*the right to come and go*» must prevail as an essential vital factor that assures the possibility of evacuation in skilful time, with physical integrity and security. However, there is a serious problem of public security until be developed sufficient resources to offset the restrictions on mobility of persons with disabilities in emergency evacuation process. In general, these people feature low mobility (low velocity of 0-0.5 m/s, low physical resistance and agility) and, therefore, the movement occurs with less autonomy.

The development of the new solutions of persistent luminescent nanomaterials, products and architectural adequacy of the physical space accessible for all persons (e.g. hazardous areas, including buildings, hospitals, rehabilitation centres and residential and institutional use) during the evacuation process from risk areas, in darkness, constitutes the main scientific and technologic priority of this research, intending the social inclusion in public security with a priority to save lives of people with disabilities in emergencies.

For applications in signage, advanced materials with persistent photoluminescence (PL) have been recently developed [13] and implemented in several European countries regulated by strict German standard DIN 67510 [14]. In the United States, an effective PL system has been used on evacuation routes and emergency exits of the International Space Station (ISS), using the «strontium aluminate» photoluminescent material in the manufacture of signs [15], a global benchmark of good light emission — but whose system is not suitable for people with disabilities. An international standardization of such PL materials in emergency escape is particularly described by a British Institution, the Photoluminescent Safety Products Association – PSPA [16], establishing some criteria and recommendations for installation of PL materials and products.

However, both DIN 67510 or the code of practices of PSPA leaves a serious hole in the case of PL systems including users with disabilities. The PSPA proposes that PL system solutions in horizontal evacuation for people with special needs should be addressed by specialists (Section 3.2 - Special Needs [16]), attesting to the lack of specific solutions for accessibility of these persons in emergencies. This thesis brings to light a multidisciplinary scientific study that demonstrates new solutions to change this reality through the use of the property of persistent luminescence (light emission by more than 10 hours) of new nanomaterials (one size smaller than 100 nm) [17-20]. The content of this Doctorate in Materials Science and Engineering Thesis, embraces transversal areas of Architecture, Design, Physics and Medicine, especially dedicated to people with disabilities.

The methodology used in developing the thesis was based on the theoretical and practical experience of activities undertaken since 1998 under the patronage of «German Commission for UNESCO, Bonn e.V.», from the development of new products for the rehabilitation of people with disabilities, organized by the «Fördern durch Spielmittel», Berlin [21-22]. The close contact and interactive learning made with the international disabled has been useful in revealing multicultural needs that such users require in the rehabilitation process, and the policies that support the rights and quality of life of these citizens. In this context, theoretical and practical issues are determined with a critical importance of save lives of people with disabilities in emergencies. Simultaneously, the solutions proposed by this thesis and their use may contribute to a continuous process of rehabilitation, concomitant to utilization of such assistive technologies.

In the field of nanoscience, new light-emitting nanostructures of strontium aluminate co-doped with cerium (III), dysprosium (III) and europium (II), $\text{SrAl}_2\text{O}_4:\text{Ce}^{3+}$, Dy^{3+} , Eu^{2+} , were developed in the frame of this work. Solid-state synthesis is the main route investigated for large scale production of strontium aluminate materials, in nanotubes (chapter 3), nanowires/nanorods (chapter 4), and multifunctional core-shells (chapter 5), bring the contingency of persistent luminescence in an inclusive approach. From the generality of the various types of disabilities, higher detail was assigned to the persons in risk of acquire visual impairment. This topic is focused in the visibility of photoluminescent materials through the development of new medical equipment (chapter 6), in a personalized approach, which equipment should be further investigated for the eye examination with the end users. Finally, the luminescent nanostructures, created in the previous chapters, were deposited onto ceramic substrates, in order to engineer an exploratory application in photoluminescent-warning ceramic tiles for risk areas and emergency (chapter 7).

The integrated solution facility was designed for to be accessible for all persons with disabilities in emergency, according to the principles of Universal Design, and to contribute for a social inclusion in public security. ■

1.1. Luminescence Field for People with Disabilities

Advanced materials used in solutions for accessibility have been developed and implemented in many European countries regulated by DIN 67510 [14]. A referential standard for emergency way finding guidance systems that are used for safety and security in photoluminescent systems is particularly described by the «PHOTOLUMINESCENT SAFETY PRODUCTS ASSOCIATION - PSPA» [16]. The PSPA Code of Practice provides recommendations for the installation of emergency way finding guidance systems produced from photoluminescent signing and markers along escape routes. Furthermore, this Code provides installation recommendations that constitute a major improvement in escape path marking in premises required by Health and Safety legislation to be protected with adequate emergency lighting for use in public, industrial and commercial buildings, and in advanced premises not at this time required by legislation to provide electrical emergency lighting. Intending the luminescence lighting application for people with disabilities, the following PSPA definitions are also applied.

Photoluminescent (PL) material [16]

PL material is a compound that, when activated by illumination with visible light from natural, fluorescent or tungsten sources, emits, for some considerable time, a readily perceived green-yellow light on removal of the activating source.

Photoluminescent (PL) product [16]

PL product is a commercially available artefact having photoluminescent material incorporated in their construction.

Emergency way finding guidance system (EWGS) [16]

EWGS is a complete but discrete installation of photoluminescent material and products that provide direction, way finding and safety information, visual and orientation cues along escape and intervention paths in a building.

Luminescent nanomaterials [17-20]

Luminescent nanomaterials is a newly emerging field at the frontier of science, provide challenges to both fundamental research and breakthrough development of technologies in various areas such as electronics, photonics, nanotechnology, display, lasing, detection, optical amplification, fluorescent sensing to biomedical engineering, and environmental control. Luminescent nanomaterials come in many forms such as nanoclusters, quantum dots, tubes, wires, cages, balls, and nanostructured units. They can be made up of rare earth elements, semiconductors, metals, oxides, and inorganic and organic polymers. However, the investigation on the nanoscience is still in infant stages. Luminescent nanomaterials have unique properties which greatly differ from those of micro scale and bulk materials, being very promising field for interesting luminous applications, including those related to people with disabilities.

Afterglow phenomenon [23]:

The afterglow phenomenon has been studied in physics and astronomy since 40's assigned from forbidden to allowed transitions. Gaseous-liquid substances as nitrogen, argon or neon mixtures also present this phenomenon at atmospheric pressure. In astrophysics, for example, this phenomenon emitted from gamma ray bursts (GRBs) has been intensively investigated and used for detection of stars and galaxies by optical afterglow. GRBs are short and intense flashes of cosmic high energy ($\sim 100 \text{ keV} - 1 \text{ MeV}$) photons. Despiting the scale of magnitude, this radiative phenomenon occurs as a luminescence of materials that persists after the removal of the excitation, also called **afterglow** [23f].

1.2. Background Research: People with Disabilities

This topic describes the main experiences acquired in previous studies and in international rehabilitation centres, about accessibility, design and rehabilitation of persons with disabilities.

1.2.1. Pilot Project for Urban Accessibility

The «*Pilot Project of Technical Solutions for Urban Accessibility of People with Disabilities and Elaboration of Municipal Law Facilities N.º 2.153.784*» executed in the Álvaro de Carvalho and Esteves Júnior Streets of the Historical Centre, in Florianópolis, Brazil constituted the starting background [6-8] of this thesis. The project was focused in Architecture and Urbanism of public spaces, developing technical solutions in curb ramps, crosswalk and paving for urban adequacy of accessibility for people with disabilities, executed by the Institute of Urban Planning of Florianópolis and Federal University of Santa Catarina in 1998 (Figure 1-1a).

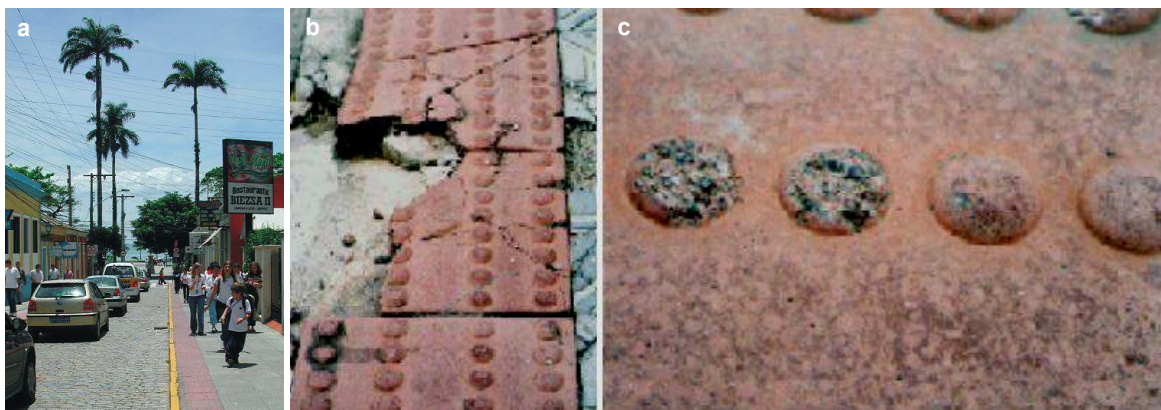


Figure 1-1. a) Urban landscape of warning tiles applied at Álvaro de Carvalho and Esteves Júnior Streets, in the Historical Centre of Florianópolis, Brazil; b-c) alert typology in concrete material with relative low mechanical resistance and durability for high pedestrian traffic in open spaces [6, 7].

However, some limitations were identified after the application of warning tiles in alert typology that was implemented in the pathways, particularly produced in concrete material. After two years of utilization of these tiles, the pieces revealed the presence of fractures and stressful on the ledges (Figure 1-1b-c). The relative low mechanical resistance ($\sim 5 \text{ N/mm}^2$) and low durability for high pedestrian traffic in open urban spaces, in which tribological conditions are aggravated by the solar exposition and maritime environment, represented an important technical problem that has been promptly solved by removing and substituting the broken pieces.

1.2.2. Ceramic Tiles for Accessibility

Justified by the reported technical problem of low resistance of these tiles in concrete material, new typologies of **ceramic tiles for accessibility** (CTA) were developed in porcelain stoneware [9-11], presenting mechanical resistance ($> 25 \text{ N/mm}^2$) much superior than the concrete. Moreover, the ceramic tiles for accessibility are suitable for the high pedestrian traffic and signalling of pedestrian pathways, presenting multisensory properties of visual, tactile and sonorous contrasts, according to the international legislations ANSI ICC/A117.2 [3], ADAAG 4.29 [4], and ISO/TC 173 [5].

The scientific investigation was realized during the Master in Materials Science and Engineering, called «*Methodology of the Design Process and Classification of Tiles for Accessibility Applied to Porcelain Stoneware Material*» [10]. Figure 1-2 shows the ceramic tiles for accessibility (from Portuguese, “*Pisos Cerâmicos para Acessibilidade*”) created with the typologies of alert (Figure 1-2a), stopped (Figure 1-2b), guide (Figure 1-2c) and crossing (Figure 1-2d), compounding a line on the covering floors segment.

This technology was awarded by the Brazilian Ceramic Society in 2004, and was finalist on the category New Ideas/Concepts of the “Museu da Casa Brasileira Design Award”, in event organized by the Governemnt of the State of São Paulo. Actually, the ceramic tiles for accessibility are being manufactured in Brazil since March 2007, and similar products have also been produced in Portugal. However, only multisensory tiles had already been created in this multidisciplinary field [9, 11 and 12], without the persistent luminescence property for signalling in emergency.

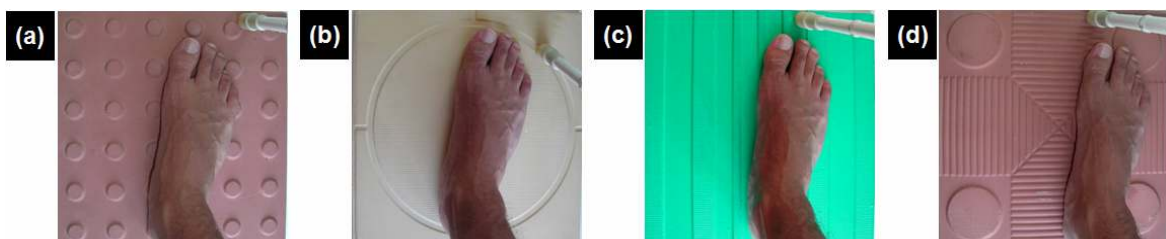


Figure 1-2. Multisensory assistive devices on surfaces of the Ceramic Tiles for Accessibility [9] with: a) alert, b) stopped, c) guide, and d) crossing typologies. A sensorial test was realized by a blind using a walking stick.

1.2.3. Rehabilitation Background

The background in the field of rehabilitation of persons with disabilities was acquired in rehabilitation centres of Mexico, China and Germany, during activities organized by the institution *Fördern durch Spielmittel e.V.*, Berlin, in partnership of the German Commission for UNESCO e.V., Bonn. Interactive sessions with elderly having age between 80-100 years old, and living at Bethel Altenhilfe Institution, Germany (Figure 1-3), offered a specific feedback on the related topics of this thesis: human disabilities, elderly degeneration and rehabilitation [21, 22], and development of assistive products with the functionality for «rehabilitation».



Figure 1-3. Elderly using assistive devices in the rehabilitation centre, at Bethel Altenhilfe Institution, Germany.

1.3. Scope of Work, Motivation and Contribution

The scope of this research is ranged on the theoretical and experimental aspects related to the preparation of persistent photoluminescent nanomaterials with afterglow-in-the-dark phenomenon. In a global and multicultural context of about 330 million people with disabilities [2], the main motivation is regarded to swell the life quality and security including these individuals. Note that in Portugal, the study includes a specific population of about 905,488 individuals with disabilities [24a], namely about 64.5 % of the Portuguese disabled people with visual (25.7 %), hearing (13.2 %), and locomotion (24.6 %) disabilities. A community of 32,085 people with disabilities (0.32% of the national ratio) in Aveiro City is locally considered in this investigation.

This transversal thesis is focused on the investigation of luminescent nanomaterials, namely the strontium aluminate co-doped with cerium (III), dysprosium (III) and europium (II), $\text{SrAl}_2\text{O}_4:\text{Ce}^{3+}$, Dy^{3+} , Eu^{2+} , aiming applications in emergency signalling for save lives of people with disabilities in darkness conditions (0-25 lux). **Persistent photoluminescence** is defined here as the appropriate property of a lighting material with phosphorescence, also called phosphor, dependent of the nanostructure that will satisfy certain performance requirements for the darkness architecture during the long afterglow time for emergency evacuation. Lanthanide (Ln) elements from Eu, Dy and Ce co-doping strontium monoaluminate oxide (SrAl_2O_4), in order to fully support strong and long-lasting phosphor afterglow, face a number of new challenges with regards to the preparation and application of $\text{SrAl}_2\text{O}_4:\text{Ce}^{3+}$, Dy^{3+} , Eu^{2+} nanomaterials.

1.4. Legal Postulations

1. § - United Nations - Convention on the Rights of Persons with Disabilities and Additional Protocol, adopted in December 13, 2006 at the United Nations Headquarters in New York, enable from May 3, 2008, signed by Portugal in March 30, 2007:

The purpose of the present Convention is to promote, protect and ensure the full and equal enjoyment of all human rights and fundamental freedoms by all persons with disabilities, and to promote respect for their inherent dignity.

Persons with disabilities include those who have long-term physical, mental, intellectual or sensory impairments which in interaction with various barriers may hinder their full and effective participation in society on an equal basis with others [24b].

2. § - United Nations - Standard Rules on the Equalization of Opportunities for Persons with Disabilities:

States should recognize the overall importance of accessibility in the process of the equalization of opportunities in all spheres of society. For persons with disabilities of any kind, States should (a) introduce programmes of action to make the physical environment accessible; and (b) undertake measures to provide access to information and communication [24c].

3. § - Data from UNESCO - United Nations for Educational, Scientific and Cultural Organization, in accordance with the estimate of the WHO - World Health Organization (2006):

World population of 330 million people with some type of disability due to mental, physical or sensory [2].

'Disability' is any loss or alteration of a structure or function of a psychological, physiological or anatomical, temporary or permanent.

Visual impairment: 110,000,000 people.

Blindness: 40,000,000 people with an inability to count fingers at a distance of 3 meters.

'Blindness' as more severe visual impairment, is common in countries in development due to lack of attention to eye and 50% of cases are caused by cataract, and the WHO estimates more than 700 thousand people with visual impairment due to non-surgery cataract, which would entail an annual average of 90 thousand cataract surgeries.

4. § - Decision N° 771/2006/EC of the European Parliament and Council of 17 May 2006 establishing the European Year of Equal Opportunities for All (2007) - Towards a Just Society:

The European Year of Equal Opportunities for All 2007 intended as a general objective, to raise awareness of the benefits of a more just and inclusive, through the promotion of equality and non discrimination. It is necessary to provide to all persons regardless of sex, age, racial or ethnic origin, religion or belief, disability or sexual orientation, the same opportunities [24d].

5. § - INE - National Institute of Statistics (2001):

*Portugal: 905,488 people with some type of disability;
Visual impairment: 25, 7% of the population with some type of disability;
Total: 150.037 people;
Blindness: 14,609 people;
Physical disabilities: 24.6% of the population with some type of disability;
Hearing loss: 13.2% of the population with some type of disability.*

'Rehabilitation' means any assistance to recover a greater or lesser extent, the disability that affects a person. It includes: orthopaedic, including surgery, weights corrective exercises and walking movements of the extremities, the exercise alone, the rehabilitation of language, the recognition of space and mobility for the blind, as well as programs in education special, vocational training, employment and social cohesion [24a].

6. § - IBGE - Brazilian Institute of Geography and Statistics (2000):

*Brazil: 24,600,256 people with a disability [24e];
Visual impairment: 16,000,000 people;
Blindness: 140,000 people.*

7. § - Law for Prevention and Rehabilitation and Integration of People with Disabilities - Law N°. 9/1989 of May 2, Portugal:

It is disabled because the one loss or congenital or acquired abnormality of structure or function of psychological, intellectual, physical or anatomical could restrict capacity, may be considered at a disadvantage to the exercise of activities regarded as normal in account age, sex and socio-cultural dominant [24f].

8. § - People with disabilities and access to public buildings, public roads and public amenities - Decree-Law N°. 123/1997 of 22 May, Portugal:

The inaccessibility of the physical environment is a serious factor of discrimination for people with limited mobility whether temporary or permanent. Architectural barriers not only affect people with disabilities but also the elderly or people with temporary mobility limitations (...) There is the part of designers and builders a great lack of awareness of accessibility issues [24g].

9. § - PNPA - National Plan for the Promotion of Accessibility - Resolution of the Council of Ministers N°. 9/2007 of 17 January, and Decree-Law 163/2006 of 8 August, Portugal:

Systematization of a series of measures to give people with disabilities or sensory impairment, autonomy, equal opportunities and social participation that they are entitled as citizens. Rules governing access to buildings (...) ensuring mobility without conditions, in public and private spaces [24h].

10. § - DGS - Directorate General of Health of the Ministry of Health, Portugal (2001):

'Urgencies' are all clinical situations of sudden onset, since from the not serious to the serious, with the risk of a failure establishment of vital functions.

'Emergencies' are all clinical situations of sudden establishment, where there is established or imminent, a commitment to one or more vital functions [24i].

1.5. Objectives

Herein, the hypothesis that the persistent luminescence of $\text{SrAl}_2\text{O}_4:\text{Ce}^{3+}$, Dy^{3+} , Eu^{2+} as a functional property to save lives of people with disabilities in emergency is objectively explored by developing solutions (assistive products) and experimentals with nanomaterials (selection, processing, characterization, visualization and application), accessible for persons with disabilities. The study was focused to reach 5 specific objectives:

- Post-annealing influence:** defined hypothesis for a correlation between the alterations on the nanostructure (morphology) and optical features of $\text{SrAl}_2\text{O}_4:\text{Ce}^{3+}$, Dy^{3+} , Eu^{2+} under a thermal treatment over and above temperature of host lattice transformation (~ 923 K), aiming at improve post-annealed phosphor applications.
- Grinding influence:** defined hypothesis for a correlation between the alterations on the particle size and the nanostructure of $\text{SrAl}_2\text{O}_4:\text{Ce}^{3+}$, Dy^{3+} , Eu^{2+} under a mechanical treatment of ball-milling and ultrasonification, aiming at improve grinded and sonificated phosphor applications.
- Surface modification:** defined hypothesis for the creation of photocatalytic properties (antibacterial, antimicrobial, and water resistance) of $\text{SrAl}_2\text{O}_4:\text{Ce}^{3+}$, Dy^{3+} , Eu^{2+} by a coating layer, through an encapsulation process for the synthesis of a core-shell structure with combined features from the core (PL material) and the shell (photocatalytic agent) for architectural, pharmacological and medicinal applications.
- Personalization of PL materials:** defined hypothesis for the personalization of $\text{SrAl}_2\text{O}_4:\text{Ce}^{3+}$, Dy^{3+} , Eu^{2+} luminescence emission, through to the development and experimentation of a medical equipment and a method of personalization by retinal diagnostic test of colour vision, in black background, aiming at improving the PL visibility as a vital factor in emergencies.
- Application of PL materials:** opened exploratory hypothesis for the application of $\text{SrAl}_2\text{O}_4:\text{Ce}^{3+}$, Dy^{3+} , Eu^{2+} nanomaterials in photoluminescent-warning ceramic tiles, aiming at improving the persistent luminescence property in signalling systems for save lives of people with disabilities in emergency.

1.6. Overview and Document Structure

General overview of the afterglow phenomenon with persistent photoluminescence approach to solve the conditions of accessibility from the illuminance (> 25 lux) to total darkness (0 lux), using assistive technologies in escape routes for emergency evacuation, is presented in Figure 1-4.

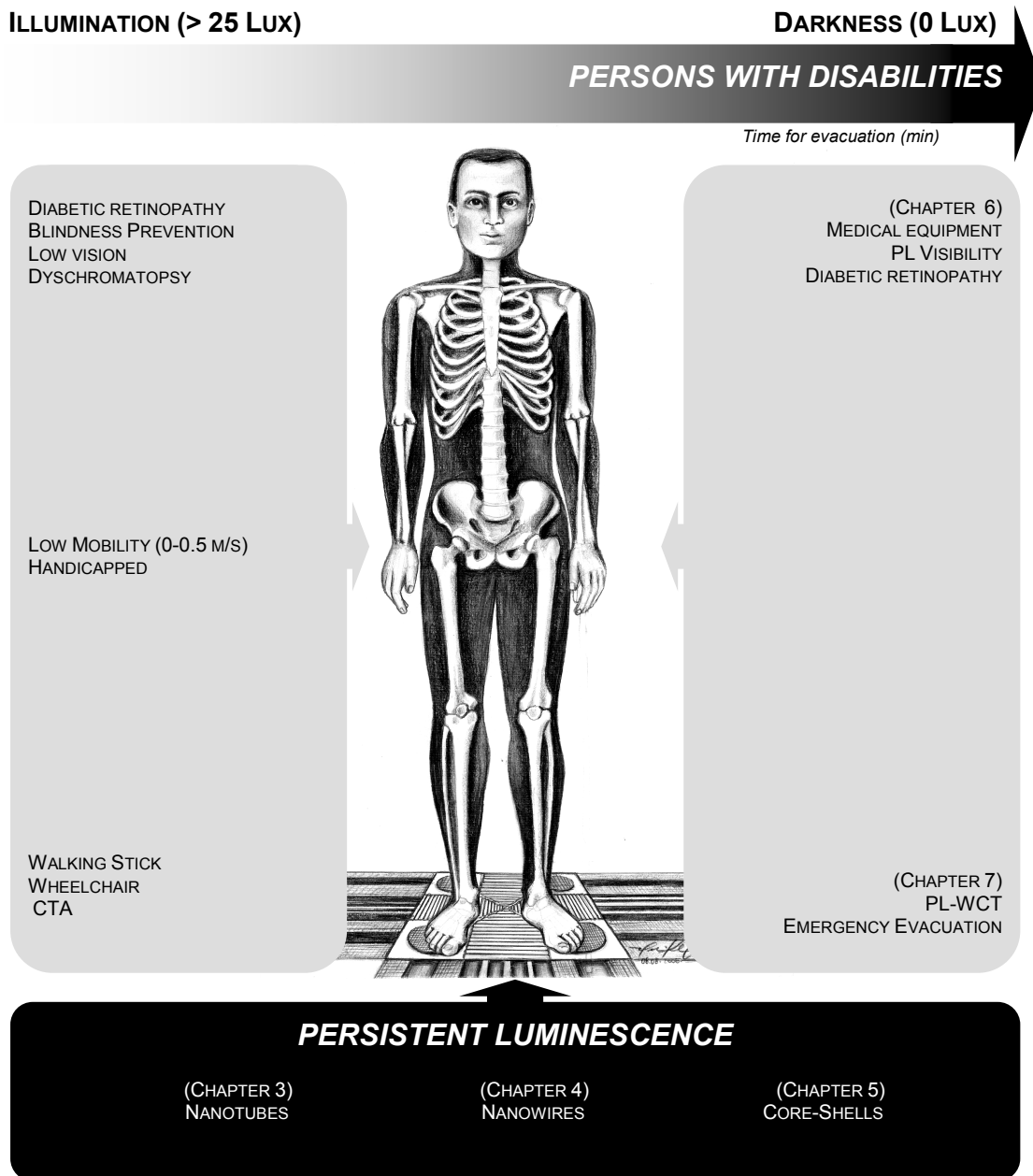


Figure 1-4. Persistent luminescence approach for emergency signalling accessible for persons with disabilities, upon illuminance < 25 lux: activation of the afterglow phenomenon.

This document presents the theoretical and experimental aspects correlated to this research, and the respective results obtained from it.

Chapter 2 presents the main conceptual background, characterization techniques, starting materials, and processing performed in the thesis. The persistent luminescent strontium aluminate doped with cerium (III) and co-doped with dysprosium (III) and europium (II), $\text{SrAl}_2\text{O}_4:\text{Ce}^{3+}, \text{Dy}^{3+}, \text{Eu}^{2+}$, as-received and synthesized by solid-state reaction, is defined as the baseline material for further investigation in emergency signalling.

Chapter 3 discloses the post-annealing effects on the nanostructure of luminescent $\text{SrAl}_2\text{O}_4:\text{Ce}^{3+}, \text{Dy}^{3+}, \text{Eu}^{2+}$ micro- and nano-particles. Luminescent nanotubes were obtained, and investigated by PL-spectroscopy, TRE, RAMAN, XRD, AFM, SEM and TEM techniques.

Chapter 4 discloses the grinding and ultrasonification effects on the nanostructure of luminescent $\text{SrAl}_2\text{O}_4:\text{Ce}^{3+}, \text{Dy}^{3+}, \text{Eu}^{2+}$ micro- and nano-particles. Luminescent nanowires and nanorods were obtained, and investigated by PL-spectroscopy, XRD, SEM and TEM techniques.

Chapter 5 is concerned with the surface modification effects of $\text{SrAl}_2\text{O}_4:\text{Ce}^{3+}, \text{Dy}^{3+}, \text{Eu}^{2+}$ micro- and nano-particles coated with TiO_2 nanotubes. Water resistant, antibacterial, antimicrobial and photocatalytic core-shell nanopropes were obtained, and investigated by zeta potential, pH, RMN, SEM, and TEM.

Chapter 6 presents the development and experimentation of ophthalmic medical equipment for computational colour vision test in white/black background. The retinal cells response for photoluminescent materials was statistically diagnosed among the photopic biofunctionality “*in space*” from trial groups in a personalized approach.

Chapter 7 presents the creation of photoluminescent-warning ceramic tiles with multisensory mechanisms: afterglow luminescence, tactile and sonorous contrasts, in addition of antibacterial, antimicrobial and self-cleaning properties as well. The application of these tiles in floor plans was exemplified for people with disabilities in escape routes.

Chapter 8 presents a summary of results and conclusions obtained in the frame of this thesis in a multidisciplinary outlook. Considers future works that might be investigated following a research line focused on exploiting the persistent luminescence property. ■

Chapter 2

Tools

Conceptual Background, Characterization Techniques, Materials and Processing

The theoretical and experimental tools involved on the development of the thesis are divided in two parts. In the first part, the conceptual background about luminescent materials, current standards, as well as human and spatial factors for emergency signalling are reviewed. In the experimental tools section, the characterization techniques, starting materials and processing are described. The persistent luminescent $\text{SrAl}_2\text{O}_4:\text{Ce}^{3+}, \text{Dy}^{3+}, \text{Eu}^{2+}$ commercial phosphor, as-received, consisting of micro- and nano-particles synthesized via solid state route, was established as the baseline material for this study of persistent luminescence, satisfying the current standards and legislations for emergency applications.

Key-words: luminescence, DIN 67510, colour vision, emergency signalling, strontium aluminate.

PART I — THEORETICAL TOOLS

2.1. Conceptual Background

The main concepts that support this thesis research, including the study of luminescent materials, specifically the strontium aluminate doped with lanthanide ions, the current standards, as well as human and spatial factors for emergency signalling, are reviewed in the following items.

2.1.1. Luminescent materials

Luminescence is a term introduced in literature in 1888 by Wiedemann. In a complete definition, luminescence is a non-equilibrium radiation that is an excess over and above the thermal radiation background and arises in the presence of an intermediate process of energy transformation between absorption and emission. The duration of luminescence and the possibility of quenching it are direct consequences of the intermediate process [25]. The luminescence characterization might be effected with luminescence spectra of two types:

- **Excitation spectrum:** the wavelength of the exciting light is varied and the intensity of the emitted light at the fixed emission wavelength is measured as a function of the excitation wavelength, giving the information on the **positions of excited states that result in the emission of light**;
- **Emission spectrum:** provides information on the **spectral distribution of the light emitted by a sample** produced from an excitation source. The data acquisition means: an excitation source, the sample, an excitation monochromator, a sample compartment, an emission monochromator, and a detector.

Luminescence is also characterized by the afterglow emission, namely by the luminance that is the light reflected by the surface in a given direction measured in candelas per square metre (cd/m^2), and by the radiance ($\mu\text{W/cm}^2$). These characteristics from lighting-materials depend on the amount of the incident light, which emission in the UV-VIS region might be perceived by the human eyes. In this work, luminance defines the spatial visualization of emergency signalling in escape routes, when the spatial illuminance is ranging lower than 25 lux (to 0 lux).

In 1931, the *Commission Internationale de l'Éclairage* (CIE) created a standardized system of quantitative colour measurement in which all tristimulus values would be positive [23f]. This colour space was defined in terms of chromaticity coordinates; the tristimulus values scaled by their sum, which reflect a colour's hue and saturation. Luminescence is also characterized by the appearance in colour coordinates. Chromaticity coordinates are defined by help of tristimulus values X, Y and Z; and colour sensitivity curves are described with help of chromaticity coordinates x, y and z. Because of the relation $x + y + z = 1$, it is sufficient to quote x and y only, then it is possible to identify any colour using only two coordinates (x and y) and to map the visible colours onto a two-dimensional surface, which is commonly known as the CIE chromaticity diagram.

Lifetime

Lifetime is defined as the average time spent by an ion from the excited state to return to the ground state [26]. Time-resolved emission (TRE) spectroscopy provides important information from the lifetime of an excited state on the nature of the state and the local ionic environment. In a simple lifetime experiment measures the population in excited states by applying a short, intense excitation pulse at $t=0$, which creates a population $N(0)$ in the excited state, and the intensity of the emission from the excited state is measured as function of time, according to Equation (2-1):

$$I(t) = I(0) \exp(-t/\tau_R) \quad (2-1)$$

where τ_R is the radiative decay time, which is the inverse of the transition probability [26]. A luminescence classification is determined in function of the lifetime:

- $\tau < 10^{-8}$ s, short decay time or **fluorescence**;
- $\tau > 10^{-8}$ s, long decay time, or **phosphorescence**;
- $\tau > 10$ hours, is usually called **persistent luminescence**, in a phenomenon involving **energy traps** (electron and hole traps).

The difference in lifetime of luminescence can be used to separate overlapping luminescence spectra from different lanthanide co-dopants by measuring them for different delay times after end an excitation pulse.

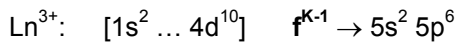
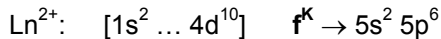
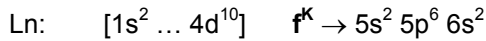
Lanthanide (co)doping

In the **ground state**, the lanthanide (Ln) elements present similar configuration to $[\text{Xe}] 4f^{n-1} 5d^1 6s^2$ for the Ce, Gd and Lu atoms, and $[\text{Xe}] 4f^n 6s^2$ for the others lanthanide elements (n is the number of electrons in the f orbitals). The specification of lanthanides with atomic numbers from 57 to 71 corresponds to the $4f$ orbitals with electronic configuration. For **trivalent Ln^{3+} ions**, the electronic configuration is regular $[\text{Xe}] 4f^{n-1} 5s^2 5p^6$ with $4f$ level increasing progressively from lanthanum $[\text{Xe}] 4f^0$ (La, $n=0$), cerium $[\text{Xe}] 4f^1$ (Ce, $n=1$) to lutetium (Lu, $n=14$). The $4f$ electrons are not the outermost ones and they are shielded from external fields by two electronic shells with larger radial extension (for instance $5s^2 5p^6$), which explains the atomic nature of their spectra. The $4f$ electrons are weakly perturbed by surrounding ligand charges. The energy levels of a free Ln^{3+} ion are usually interpreted by considering only interactions between the $4f$ electrons. Secondary effects are usually neglected in this treatment [27]. The lanthanides ions have derivative configurations f^k and f^{k-1} to their incomplete levels of Ln, Ln^{2+} and Ln^{3+} ions, where K is a factor of order for their electronic levels, as systematized in Table 2-1.

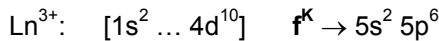
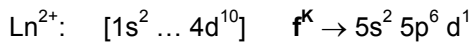
Table 2-1. Lanthanides Series of the Periodical Table of Elements.

Z	57	58	59	60	61	62	63	64	65	66	67	68	69	70	71
Ln	La	Ce	Pr	Nd	Pm	Sm	Eu	Gd	Tb	Dy	Ho	Er	Tm	Yb	Lu
n	0	1	2	3	4	5	6	7	8	9	10	11	12	13	14
K	0	2	3	4	5	6	7	7	9	10	11	12	13	14	14

The lanthanide ions have these electronic configurations [27]:

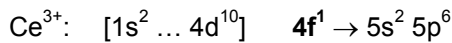
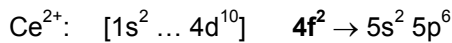
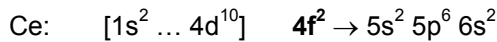


Specifically for the La (K=0), the Gd (K=7) and Lu (K=14), the configurations are [27]:

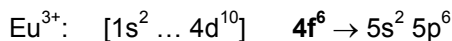
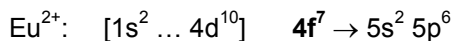
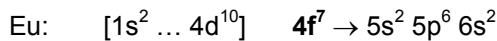


For this thesis, the electronic configuration of Ce, Dy and Eu ions are presented:

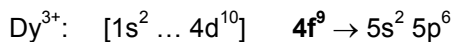
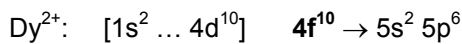
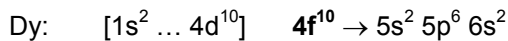
Cerium, K=2 (n=1)



Europium, K=7 (n=6)



Dysprosium, K=10 (n=9)



The ionization process for the lanthanide consists in a transition $(\text{Ln}^{2+}) \rightarrow (\text{Ln}^{3+}) + e^-$. In general, the +3 oxidation state is the most stable for all lanthanide elements. The most accessible +2 are Eu^{2+} ions, and the most accessible +4 are Ce^{4+} ions [25].

The electronic transitions between lanthanide elements are characterized by the following types:

- **Forbidden transitions:** intra-configurational $\mathbf{4f}^n \rightarrow \mathbf{4f}^n$ transitions, spectrum in **thin band**;
- **Allowed transitions:** inter-configurational $\mathbf{4f}^n \rightarrow \mathbf{4f}^{n-1} \mathbf{5d}$ transitions, spectrum in **large band**.

Given these electronic transitions from most internal levels, the lanthanides are characterized by presenting light emission in typical thin spectra. In general, the Ln^{3+} trivalent cations present predominant **intra-configurational** transitions in thin bands. The Ln^{2+} divalent cations present predominant **inter-configurational** transitions in large bands. A special example is Ce^{3+} , that presents intra 4f-f transitions in thin bands in the visible region, and 4f-5d transitions in large band in UV region.

A complete $4f^n$ energy level diagram for all lanthanide ions is indicated in the **Dieke Diagram** in Figure 2-1, showing the energy levels in crystals [27a]. These parameter values are also valid from the lowest $4f^n \rightarrow 4f^{n-1} 5d$ transitions. The ground states levels of the co-dopants of the main material of this work are: $^2F_{5/2}$ (Ce^{3+}); 7F_0 (Eu^{3+}); and $^6H_{15/2}$ (Dy^{3+}).

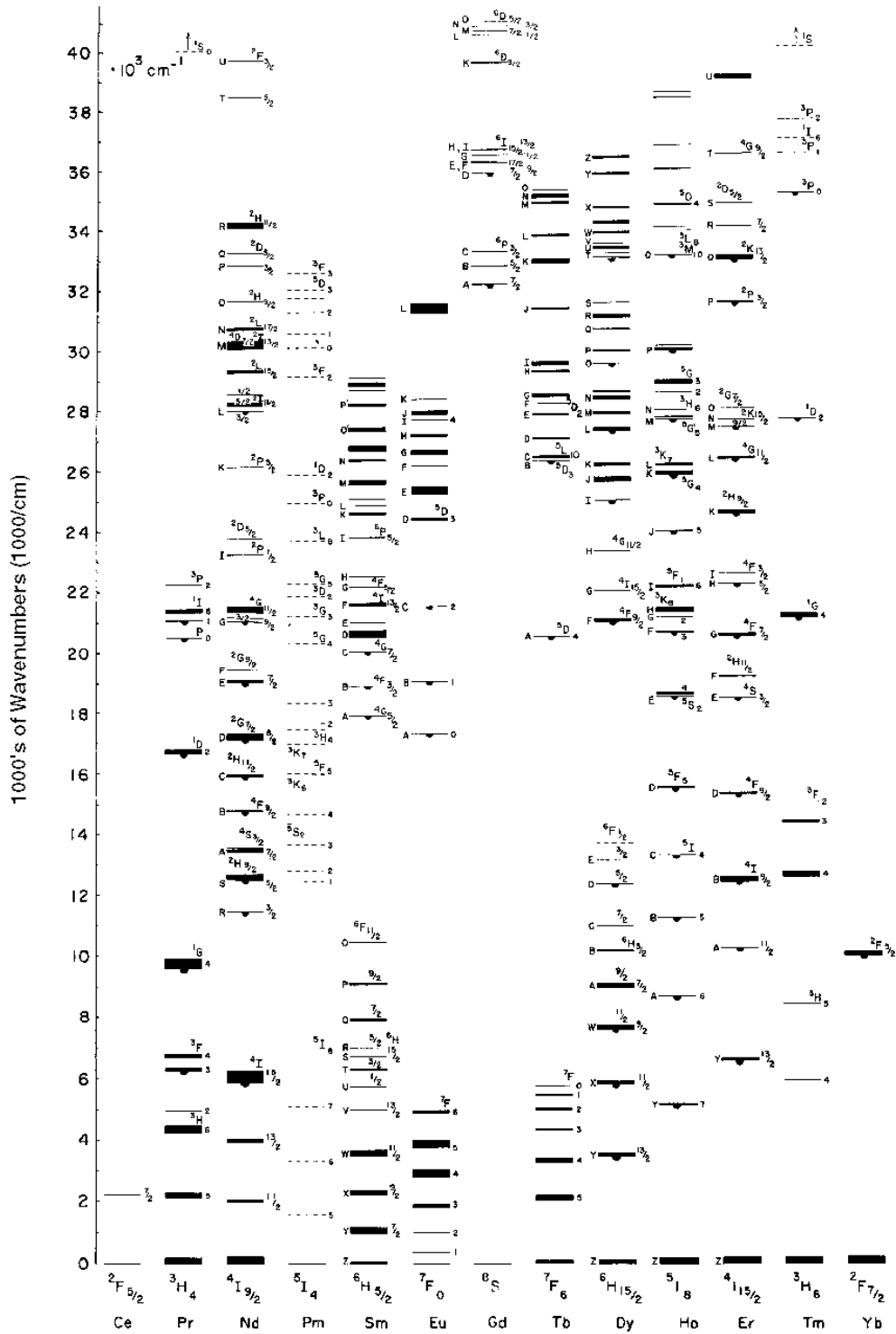


Figure 2-1. Dieke diagram with Ln³⁺ energy levels observed in LaCl₃³⁺ [27a].

Strontium aluminate luminescent phosphor material

Strontium aluminate lanthanide co-doped ($\text{SrAl}_2\text{O}_4:\text{Ln}$) is a type of luminescent material about 10 times brighter, 10 times longer glowing, and 10 times more expensive than its predecessor copper-activated zinc sulphide ($\text{ZnS}:\text{Cu}$), Figure 2-2 [23f]. Strontium aluminate phosphors produce yellow-green, blue-green and blue hues, for the excitation wavelengths from 200 to 450 nm, with wavelength emission at ≈ 520 nm, blue-green at ≈ 505 nm, and blue at ≈ 490 nm, depending of the lanthanide co-doping. Note that “*phosphor*” is a term herein used to designate a lighting material, and does not refer to the chemical element P. This word *phosphor* was invented in the 17th century from a sintered stone that emitted red light in the dark after exposure to sunlight, called “*Bolognian stone*” (actually known as being BaS) in the pigment industry [23f].

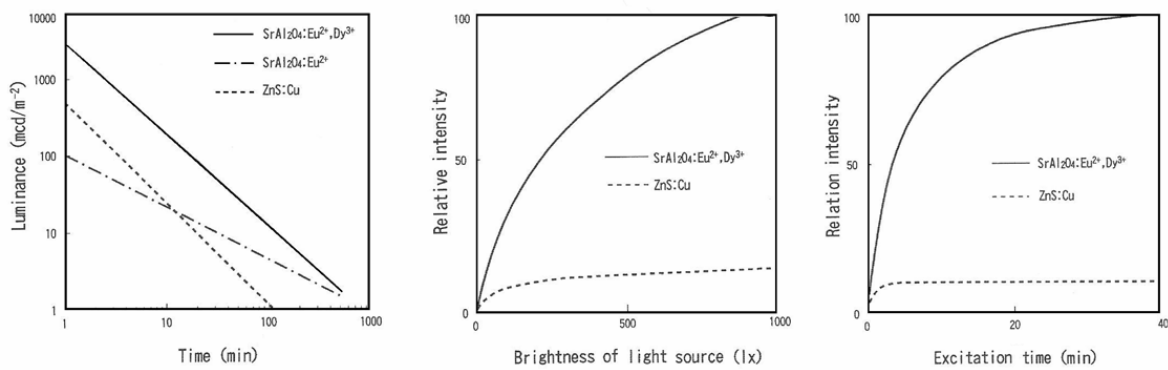


Figure 2-2. Optical features of SrAl_2O_4 and ZnS co-doped phosphors [23f].

Complementary technical data from commercial products of SrAl_2O_4 co-doped (Tables 2-2 and 2-3 [28]) indicated the suitable optical properties for long afterglow-in-the-dark applications. Note that these data represent the features of similar products identified in commercial materials.

Table 2-2 Comparison of luminance between of SrAl_2O_4 and ZnS co-doped products [28].

Excitation for 5 minutes under illuminance of Xenon lamps 150 watt – 1000 lux	ZnS co-doped products	SrAl_2O_4 co-doped products
1 minute	290 mcd/m ²	700 mcd/m ² to 2650 mcd/m ²
10 minutes	25 mcd/m ²	80 mcd/m ² to 312 mcd/m ²
60 minutes	3,4 mcd/m ²	11 mcd/m ² to 44 mcd/m ²
Limit of 0,3 mcd/m ²	7 h 30 m	20 h to 58 h

Table 2-3. Luminance of SrAl_2O_4 co-doped product in function of the source of excitation [28].

Excitation	10 minutes	60 minutes
Xenon lamp 150 W, illuminance of 1000 lux Excitation for 5 minutes	408 mcd / m ²	53 mcd / m ²
Osram white lamp, L35/21-840, illuminance of 30 lux Excitation for 60 minutes	115 mcd / m ²	26 mcd / m ²
Osram white lamp, L35/21-840, illuminance of 15 lux Excitation for 60 minutes	65 mcd / m ²	16 mcd / m ²

Strontium aluminate host lattice

Crystalline strontium aluminate compounds of the system S_aA_b (where a is the molar ratio of SrO, and b is the molar ratio of Al_2O_3), such as $SrAl_2O_4$ (SA), $SrAl_4O_7$ (SA_2), $SrAl_{12}O_{19}$ (SA_6), $Sr_2Al_6O_{11}$ (S_2A_3), $Sr_3Al_2O_6$ (S_3A), $Sr_4Al_{14}O_{25}$ (S_4A_7), are functional materials for persistent luminescence when doped with rare-earth metals. In this family, the $SrAl_2O_4$ is extensively mentioned in the literature as the most efficient host lattice phosphor [29-30]. In the monoclinic α - $SrAl_2O_4$ phase, there are two interstitial sites for cations to occupy, i.e. Sr^{1+} and Sr^{2+} . These sites provide different spatial symmetry and orientation direction that result in emission shifts of Eu-doped phosphors [31]. The $SrAl_2O_4$ has a α -monoclinic structure constructed by corner-sharing $[AlO_4]$. The charge deficiency introduced by the occupancy of Al^{3+} ions in these tetrahedral is compensated by the incorporation of Sr^{2+} ions within the interstitial sites [32-33]. Lanthanides with compatible ionic ratio might be added as co-dopant luminescent centres. The metastable phase is obtained via an endothermic process at temperatures of about 923 K ($\Delta H=3.2$ kJ/mol) [34-35] presenting β -hexagonal tridymite-type structure [36]. The crystalline structure of luminescent materials that accepts a substitutional lanthanide element in ionic vacancies is called host lattice. The chemical formula for luminescence is expressed as **H:A, S**, where H is the host lattice material (or matrix, M), A is an activator of luminescence, and S is a sensitizer of the energy transfer mechanism (Figure 2-3).

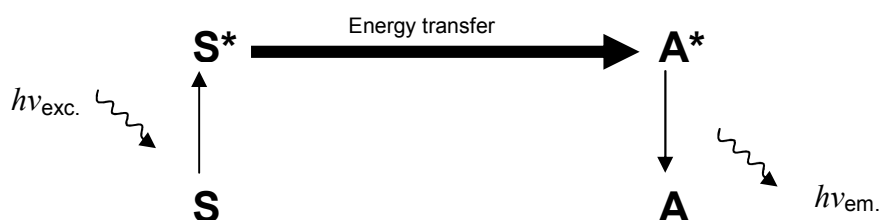


Figure 2-3. Energy transfer mechanism between sensitizer and activator.

A special criterion of order between sensitizers and activators (Figure 2-3) was arbitrated for $SrAl_2O_4:Ce^{3+}$, Dy^{3+} , Eu^{2+} owing the relative quantity of **cerium (III) as the main activator** doping the strontium aluminate host lattice co-doped with Dy (III) and Eu (II). From the cationic point of view, the strontium ions in the positions of aluminium are unfavourable to occur. The energy transfer might be originated from the follow mechanisms:

- Transference in emission – reabsorption (radiative);
- Transference in multipolar resonance (non-radiative);
- Transference non resonant (non-radiative).

Host lattice defects are produced with element vacancies during the synthesis process, such as:

- Vacancies of strontium: $V_{Sr^{2+}}$ or $V_{Sr^{1+}}$
- Vacancies of aluminium: $V_{Al^{3+}}$, $V_{Al^{2+}}$ or $V_{Al^{1+}}$
- Ions of strontium in aluminium position: $Sr_{Al^{1+}}$
- Decrease of the concentration of oxygen vacancies: VO^{00} (2 $^-$) or VO^0 (1 $^-$).

Solid-state reaction is a satisfactory route for the synthesis of co-doped strontium aluminates for large scale applications in luminescence [37], requiring temperatures usually above 1373 K. Recently, the solid-state reaction between SrCO_3 and Al_2O_3 has been studied comprising the temperature dependent formation of SrAl_2O_4 [36b]. The strontium aluminates are established compounds in the $\text{SrO}-\text{Al}_2\text{O}_3$ system, which crystalline phases formation depend of the starting components, such as the concentration of a catalytic reagent B_2O_3 [38]. The B-doping in tridymite-like structure of SrAl_2O_4 drastically reduces the synthesis temperature [39]. A micrometer particle size and coexistence of crystalline phases were generally obtained [39-44].

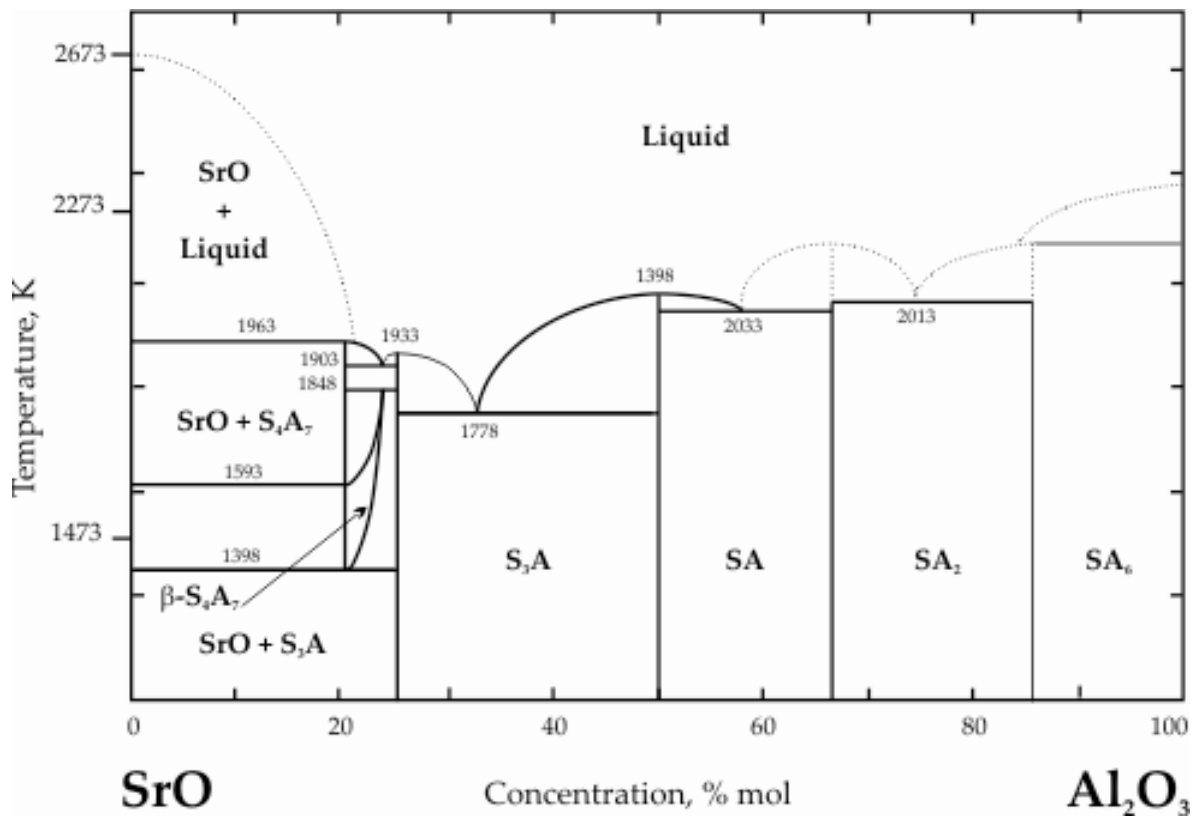


Figure 2-4. Kelvin temperature conversion of the $\text{SrO}-\text{Al}_2\text{O}_3$ phase diagram [40].

However, many uncertainties still remain, especially concerning the melting points of many compounds, or more basically the existence of some compounds [31],[37] and [39]. Note that the $\text{SrO}-\text{Al}_2\text{O}_3$ phase diagram [40] does not contain all crystalline compounds (Figure 2-4).

For the synthesis of strontium aluminates host lattices via solid state reaction using the boron catalyst [41-45], see the experimental study presented in the ANNEX I.

2.1.2. Standards & Legislations of photoluminescent materials and products

This section presents a brief summary of the current standards and legislations of photoluminescent (PL) materials and products, describing its main features and definitions, namely focused for emergency application.

► **DIN 67510 — Deutsch Industrial Standard, Germany [14]**

The photoluminescent pigments and products tested according to DIN 67510 standard (Part 1 - 1992) should give luminance values (in milicandelas per square metre, mcd/m^2) versus decay times (minutes, min) in the range as shown in Table 2-4. These limit values from afterglow performance are the parameters for its classification in CLASS I, CLASS II or CLASS III [14]. The DIN 67510 standard is referenced for several documents worldwide.

Table 2-4. DIN 67510 luminance classifications of photoluminescent materials [14].

CLASS I				
Time period	10 min	30 min	60 min	>240 min
Luminance (mcd/m^2)	>17.0	4.0	1.7	0.3
CLASS II				
Time period	10 min	30 min	60 min	170-240 min
Luminance (mcd/m^2)	$17.0 > L > 12.5$	$4.0 > L > 2.9$	$1.7 > L > 1.2$	0.3
CLASS III				
Time period	10 min	30 min	60 min	80-160 min
Luminance (mcd/m^2)	$12.0 > L > 8.5$	$2.8 > L > 1.5$	$1.1 > L > 0.5$	0.3

► **PSPA — Photoluminescent Safety Products Association, United Kingdom [16]**

The current legislation and standards determine that all people should be evacuated from a building if there is an emergency such as a fire. This may represent a special challenge for people with disabilities. Many building managers, as part of a solution to the problem of safety evacuation, have introduced 'refuge areas'. However, refuge areas are only relatively safe waiting areas for short periods of time. They are not areas where people with disabilities should be left indefinitely until rescued by the fire service, or until the fire is extinguished. Some concepts defined by PSPA in this standard are described below.

- **Low location lighting (LLL):** is a key element of emergency way-finding guidance systems. It consists of using continuous, unbroken lines located at floor and/or at a low level on walls, that emit a light source that clearly delineates the escape path. LLL provides a source of reflected light and contrast that is sufficient to assist orientation and identification of change in direction and level of escape paths.
- **Fire exit:** is an exit which is intended to be used only during an emergency.

- **Escape route:** is a route that establishes means of escape from a point in a building to a final exit.
- **Exit:** refers a way out which is intended to be used at any time whilst the premises are occupied, in emergency and non-emergency situations.
- **Final exit:** is the terminal point of an escape route, beyond which persons are no longer in danger of fire.
- **Normal lighting:** refers to all permanently installed electric lighting for regular operation which is intended for use in the absence of adequate daylight.

A correlation between the DIN 67510 [14] and PSPA [16] values is presented in Figure 2-5. The PSPA indication of the colour appearance for safety signs is showed in Table 2-5.

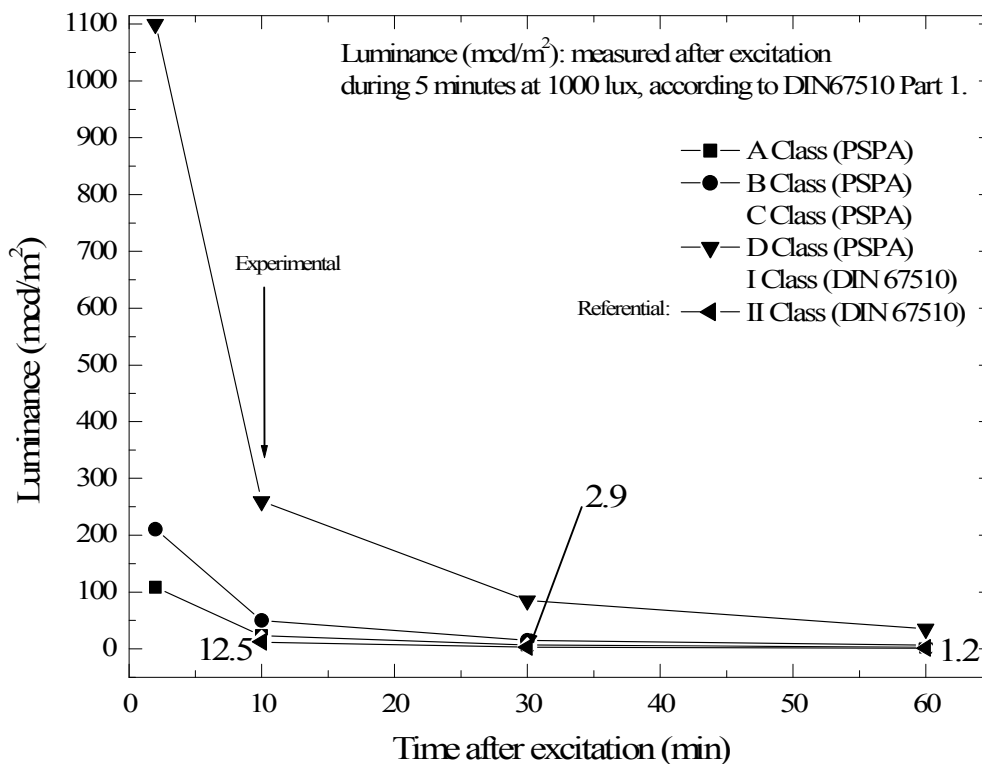


Figure 2-5. Luminance parameters of DIN 67510 [14] and PSPA [16] for emergency applications.

Table 2-5. PSPA indications of the colour appearance for safety signs [16].

Colour	Meaning or purpose	Instructions and information
Red	Prohibition sign	Dangerous behaviour
	Danger alarm	Stop, shutdown, emergency cut out devices Evacuate
	Fire-fighting equipment	Identification and location
Yellow	Warning sign	Be careful, take precautions Examine
Blue	Mandatory sign	Specific behaviour or action Wear personal protective equipment
Green	Emergency escape	Doors, exits, routes, equipment, facilities
	First aid sign	
	No danger	Return to normal

Current legislative documents establish that the responsibility is clearly with the building management to ensure that there are suitable procedures in place to evacuate everyone, without relying on the fire service. However, the presumption of independent capability to use steps and stairs for egress is clearly inadequate when considering the safety of some people with disabilities.

► ASTM — American Society for Testing Materials, United States of America [46]

The related normatives of the ASTM for this study are listed below:

- ASTM 2030-02 (2004) “*Uses of Photoluminescent (Phosphorescent) Safety Markings*” defines recommendations of use of photoluminescent products of security;
- ASTM 2072-00 (2004) “*Specification for Photoluminescent (Phosphorescent) Safety Markings*” defines specifications of photoluminescent products of security;
- ASTM 2073-02 (2004) “*Test Method for Photopic Luminance of Photoluminescent (Phosphorescent) Markings*” defines a method to test photoluminescent products upon the photopic luminance. ASTM 2073-02 is performed with a laboratory-type activating light source of Xenon lighting. However, in real-life applications, the Xenon lighting is never the actual activating light source in applications where photoluminescent safety markings are used. By performing the material activation with the realistic light source fluorescent lighting which is typically used along buildings, escape path (means of egress), the luminance results measured will become more pertinent to building owner, architects, specifiers;
- ASTM E12.13 (2004) “*Standard Photoluminescent Safety Markings*”: assumes an illumination of 21.6 lux for 2 hours with a 4100 K white fluorescent lamp;

Luminance (after illumination):	10 minutes >25 mcd/m ² ;
	60 minutes >5 mcd/m ² ;
	90 minutes >3 mcd/m ² .

► ISO — International Standards Organization, United States of America [47]

The related normatives of the ISO for this study are following described:

- ISO 15370 (2001, Annex A) accepts the photoluminescence measurements with a light-source at 25 lux illumination for 24 hours. Complete darkness and reading after 10 and 60 minutes. Note a reduction of the charging light, and not 1000 lux (DIN 67510);
- ISO 16069 for standardization of Safety Way Guidance System (SWGS), according to ISO TC 145/SC2/WG3 – Technical Committee “*Way Guidance Systems*”.

► Building Code of New York City, United States of America [48]

The Building Code of New York City provides minimum requirements for low-level photoluminescent exit path markings that will aid in the evacuation from buildings, in the event of failure of both the power and backup power to the lighting and illuminated exit signs. The markings covered by this standard are not designed to provide enough light to illuminate a dark egress path,

but rather will provide luminescent signs and outlines of the egress path, handrails and stairs, so that occupants can discern these egress path elements in dark conditions. The markings are generally required to be located at a low level in case of smoke and to be readily seen. All photoluminescent products covered by this standard shall be independently tested to certify compliance with the following characteristics: brightness rating, washability, toxicity, radioactivity, and flame spread. If products are represented as UV-resistant, they must be tested to certify compliance for UV degradation.

► **NF X08-050 Standard, France [49]**

In France, the professional union for the safety signalling is based on the standard PR NF X08-050, which establishes the following aspects:

- PR NF X08-050-1 (2003): photoluminescent systems for security;
- PR NF X08-050-2 (2004): colours for security in safety signalling;
- PR NF X08-050-3 (2004): colours for security in safety signalling.

► **NBR-9050 Standard, Brazil [50a]**

The NBR-9050 defines that escape routes and emergency exits should be marked with visual information and sound. The mechanisms and emergency devices must contain tactile and visual information, represented by symbols. The door of access to areas of rescue should be identified with signage in photoluminescent material or be retro reflective.

► **National Legislation, Portugal [50]**

Some definitions and solutions for safety, in different buildings and uses, are established in Portugal by the following national documents [50b-g]:

- Decree-Law N^o. DL 141/91: defines the Portuguese legislation containing prescriptions for the signalization, safety, hygiene and health in work, according to the European Directive 92/58/CEE [50b];
- Decree-Law N^o. DL 441/91: defines general principles for all activities, according to the European Directive 92/58/CEE [50c];
- Document 1456-A/95: defines criteria of signalling for safety, using luminescent materials and graphical symbols, according to the European Directive 92/58/CEE [50d];
- Other related national documents [50e]: Decree-Law N^o. DL 64/1990 (habitation buildings), DL 414/1998 (scholar buildings), DL 368/1999 (commercial buildings), DL 409/1998 (hospital buildings), and DL 410/1998 (administrative buildings);
- NP 4386 (2001) defines the Emergency Plan as a complementary information of signalling in escape routes, equipment for fire protection and fire fighting, graphical symbols for fire Emergency Plans, and specifications [50f];
- NP 3992 (1994) defines some criteria for fire protection and safety signs [50g].

2.1.3. Human factors for emergency photoluminescent signalling

In the following topics, the human factors considered during the evacuation process are presented for emergency signalling, namely the visual system, illuminance, mobility time for evacuation, and preferential pedestrian pathways. The main requirements from these factors in the use of photoluminescent materials are defined for this study.

2.1.3.1. Visual system

Retinal colour vision of cone cells and the photopic biofunctionality diagnosis through Farnsworth-Munsell 100-HUE test are studied. The dark-adapted response from cone to rod cells is reviewed for colour detection from photoluminescent materials.

Photopic colour vision of L-, M-, S-cone cells

In presence of light, photopic biofunctionality of retinal cone cells with sensitivity to large (L), medium (M) and short (S) wavelengths (nm), i.e. L-, M-, S-cone cells, is a dominant function of colour vision. People with congenital dyschromatopsia are frequently not aware that their colour perception differs from those with normal, trichromatic colour vision. Others have learned to adapt to their limited perception of certain colours. Some of these people know that they cannot properly identify colours accurately in certain ranges of hue and luminance.

Patients with acquired dyschromatopsias are often unaware of the changes in their colour perception, due to the subtle onset and gradual progression of the damage. Not infrequently, this allows major colour vision disturbances to go unnoticed. Unilateral dyschromatopsias – if not associated with cataract – should be examined with tests of colour saturation in the affected eye, since this is frequently the clinical presentation for an optic neuropathy. Other neuro-ophthalmic disorders should initiate a targeted search for an acquired dyschromatopsia.

The origin of defects in colour vision may be associated with mechanisms of projections of the eye lens and the photoreceptor cells, the brain, and the signal processing. In the evaluation of retinal biofunctionality, the neuroscientists concluded that the ganglion cells, which act decoding photoreceptors in the transmission of electrical impulses to nerve cells, present distinct light polarization "*in vivo*" than which occurs "*in vitro*" [51]. Measurements of the biofunctionality of the retinal cells "*in space*" were never mentioned in literature. Additionally, the visual sensitivity peak to wavelengths is different even in persons with normal trichromatic vision [52].

Farnsworth-Munsell 100-HUE Test

In ophthalmology, the clinical method of colour vision discrimination of Farnsworth-Munsell 100-HUE test (FM100-HUE) [52a] is often used to examine professionals who work in the inspection of colours, test the type and degree of deficiency in colour vision (Figure 2-6) and contribute to measure the effects of medical treatments (Table 2-6). However, the indicated administration of

illumination conditions > 25 cd/m² (or 250 lux) [53] during the tests is not completely controllable, even in portable devices, directly affecting the results when there are lighting variations.

Table 2-6. Farnsworth-Munsell 100-HUE colour vision diagnoses [52].

FM100-HUE diagnoses	
Qualitative evaluation	Quantitative score
Excellent	Total error 0-10
Superior	Total error 11-25
Medium	Total error 25-100
Inferior	> 100

Colour vision testing using computer was first reported in the 1990s and caused scientific interest when *Toufeeq* published a clinical study in *Nature* in 2004 [54]. The test used a standard personal computer in CRT display, realized binocularly only with healthy individuals (normal=20, red/green colour defect=10) at CIE chromaticity phosphors gamut. The stimulus of red or green phosphor of display is measured for sRGB output standard.

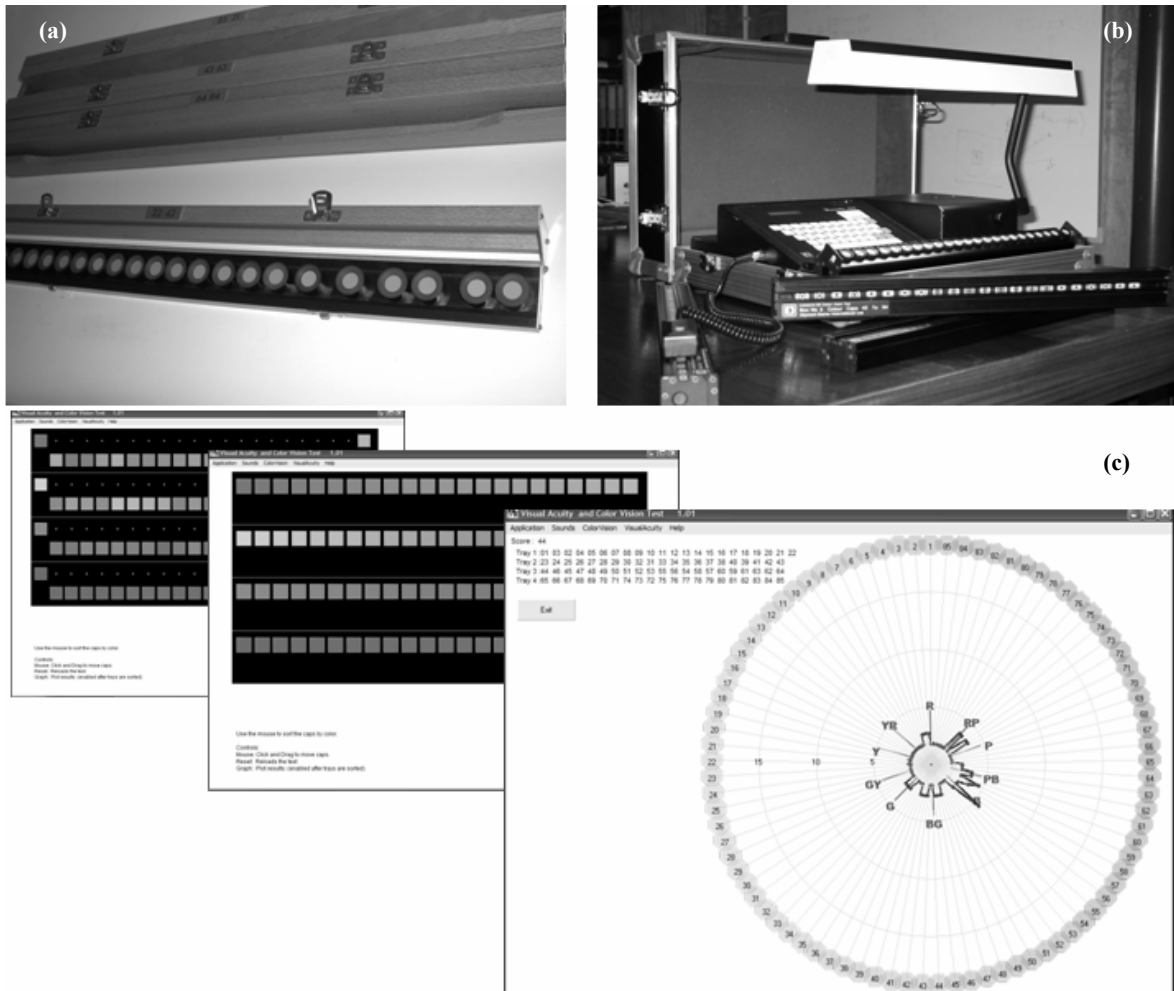


Figure 2-6. Ophthalmic colour vision test Farnsworth Munsell 100-HUE: a) first generation with coloured caps; b) second generation with electronic score results; and c) third generation with computational test.

Dark-adapted response from (L-, M-, S-) cone to rod cells

Dark adapted response of retinal photoreceptor cells (cones and rods) is a key function for visibility in emergency. All photo pigments have a chemical composition consisting of a protein (opsin) and a chromophor (retinene) which is structurally related to vitamin A. The light energy (photons) acts upon the chromophor and splits it from the opsin moiety. This reaction activates a phosphodiesterase enzyme thus, hydrolyzing the intracellular levels of cyclic guanosine monophosphate (cGMP) which leads to the transient blocking of Na^+ channels in the cell membrane, reducing the inward Na^+ current which normally occurs in the dark (the dark current). This results in a change in membrane potential (a receptor potential).

The receptor potential induces neural impulses in the optic nerve which projects to the brain via a class of interneurons called bipolar cells. Two other retinal cell types (horizontal and amacrine cells) also contribute to the processing of the visual signal before it leaves the retina via the axons of the retinal ganglion cells which constitute the optic nerve. This sequence of events involves the photo-transduction from light stimulus [55]. A lot of pigment is continuously being broken down and a time is required for accumulation of the amounts necessary for optimal rod function.

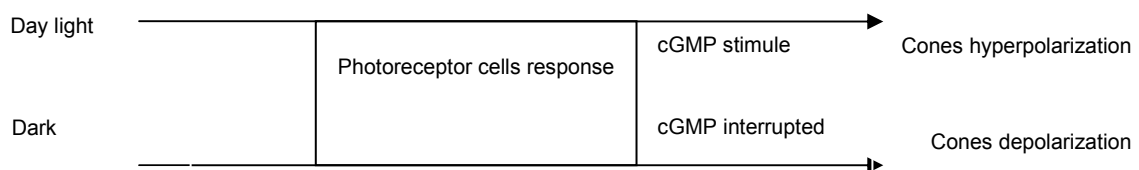


Figure 2-7. Retinal response in dark adaptation from hyperpolarization to depolarization of photoreceptor cone-cells via cGMP electron transmission [56].

In daylight, the photoreceptor cells are hyperpolarized in response to illumination. This response is generated by the coupling of G-protein that signals the way of stimulating of the cGMP-phosphodiesterase, when occurs the hydrolysis of cGMP, leading to transmission of electrical power. The dark-adaptation mechanism is produced from the cone- to rod-cells biofunctionality in the first 10 minutes of decreasing the light, when began the rod hyperpolarization. This time is related to the time required of the rhodopsin pathway.

In the dark, the cytoplasmatic process of cGMP is interrupted by the membrane cell in a non-selective cationic process, which destabilizes the electric flow and keeps the cell depolarized, and therefore ceases to send electrical impulses to formation of image, when occurs a cellular polarization → depolarization of cones [56], Figure 2-7. In vertebrates, the depolarizing light response of photoreceptors arises from an increase in cGMP concentration and the consequent activation of cGMP-gated cation channels on the outer segment of the cell [55-56]. This differential visibility that occurs during the dark adaptation from the photopic measurements in vertebrates is evidenced in Figure 2-8 [55].

A number of features of the dark-adaptation mechanism are already validated [55]:

- (1) The initial retinal sensitivity (at time = 0) is arbitrarily designated as 8. After approximately 30 minutes in the dark, the sensitivity to light has increased by a factor of 106 (represented by a decrease in \log_{10} threshold from 8 to 2);
- (2) There is an initial rapid decrease in the threshold intensity about 100 times lower than starting value. After this initial 7-8 minute period, there is an abrupt break in the flattened curve, starting a second episode of more gradual decrease, which eventually (after 30-40 minutes) approaches its final maximum value.

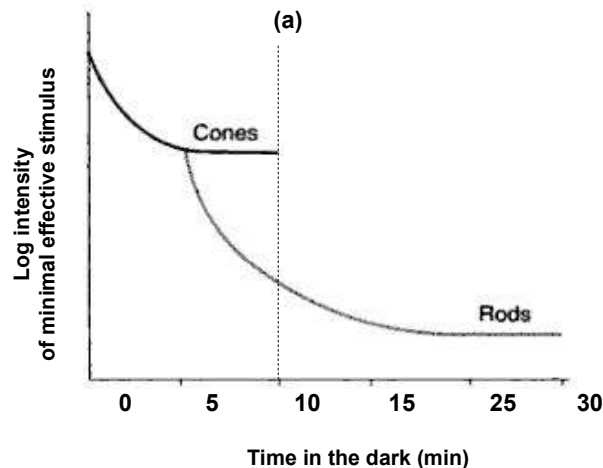


Figure 2-8. Dark-adapted retinal response vs. time in the dark, which dark adaptation is determined in part by the time required to build up the rhodopsin stores and for optimal adaptation of rod function [55]: (a) The time-limit (10 min) valid for our experimental of FM100-HUE colour vision test from photopic (cone cells) biofunctionality response for luminescent materials.

First 10 minutes of photopic colour vision response for photoluminescent materials

The photopic colour vision to blue-green light emission from photoluminescent (PL) materials is a fascinating theme to be investigated in a multidisciplinary approach. The photopic biofunctionality has been accepted for visual response of PL materials, as described in the ASTM E2073-02 specification “*photopic luminance of PL phosphorescent markings*”. The photopic vision parameter (reply retinal biofunctionality of L-, M- and S-cone cells, under the light stimulus) is a base for the limit of visibility of the human eye (0.032 mcd/m^2) of PL materials [46c]. The classification performance of a PL material in the dark from visual attributes of the light emitted is characterized by the colour appearance (values of luminance and colour coordinates, PSPA: Class I, II or III [16]). However, the colour science supports the preparation and characterization of materials only based on the colour specification from “*Commission Internationale de l'Eclairage*” – CIE [57], establishing standard observers and a set of illuminating patterns. Despite being widely distributed to colorimeters and spectroscopy of materials, the standard illuminant D65 (daylight illuminance correlated to a colour temperature of 6500 Kelvin) or other similar standards are restrict to the use

of materials by healthy individuals - without considering users with disabilities that have their visual skills extremely heterogeneous.

The main regulatory standards on the materials personalization are ASTM D1729 (visual analysis of opaque materials), ISO 3664 (analysis of reproduction of colours), GM 9220P, SAE J361 and other international standards. Only one study related with photometric evaluation of PL materials for multi-egress guidance has been published in literature [58]. According to the best of our knowledge, no studies pertaining to the integrated method of ophthalmology for PL materials dealing with personalization by the biofunctionality of the retinal cells for users with disabilities have been published in literature, and no a specific medical equipment (cabinet) has been developed to produce acceptable results for this application.

Colour vision under Purkinje Effect [59]

The visibility of persistent photoluminescent materials in escape routes is considered a vital factor in emergency, when the regular light intensity decreases still reaching a total darkness (0 lux). However, the visual system produces an adaptation in darkness, in which condition the PL materials must supply this adaptable sensitivity, in absence of illumination.

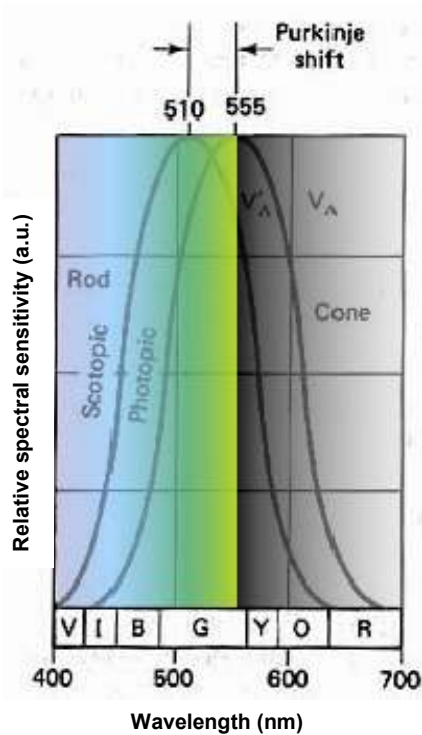
In ophthalmology, the dark adaptation is the change in the eyes biofunctional region of maximal visual acuity and sensitivity in function of availability of light. Two effects explain the dark adaptation that occurs when the visual system is exposed to the different illuminance levels:

- Adaptation for the **luminance absorption** from the pupil area (mm^2); the pupil diameter diminishes when the light intensity is increased, regulating a low luminance absorption; while the pupil diameter increases in darkness, enlarging the light absorption area;
- Adaptation for the **colour vision sensitivity** from retinal photoreceptor cells; the colour region sensitivity is highest at yellow range in the light-adapted eye; while the colour sensitivity is highest at blue-green range of the colour spectrum in the dark-adapted eye.

Note that colour vision is possible only with light levels of sufficient magnitude to activate the cone system (photopic biofunctionality). The cone system is composed by retinal photoreceptor cells with sensitivity to large (L), medium (M) and short (S) wavelengths (nm), i.e. L-, M-, S-cone cells. At intermediate levels of luminance, in lighting conditions, mesopic vision occurs, where rods (largely in the periphery) and cones (concentrated primarily in the central region of the fovea) systems work simultaneously. In total dark condition, only the rod system is functional (scotopic biofunctionality).

The Purkinje effect is a shift in the maximum sensitivity of the eye from photopic (cone cells biofunctionality) to scotopic vision (rods cells biofunctionality), according to *H. B. Balow* [59a]. The relative spectral sensitivity curve for cones (photopic curve) peaks at 555 nm. During rod or

scotopic vision, the relative spectral sensitivity¹ curve shifts 45 nm toward the 400-nm (blue) end of the spectrum so that the peak occurs at 510 nm. This shift results in an increase in sensitivity to shorter wavelengths (400 nm) and a decrease in sensitivity to longer wavelengths (700 nm) for the rod system (Figure 2-9).



- I. Rods and cones cells are not uniformly sensitive across the visible spectrum;
- II. The region of maximal sensitivity is 555 nm for cone vision (photopic curve) and 510 nm for rod vision (scotopic curve);
- III. The rod function denigrates above the cone function, indicating that throughout most of the spectrum the rods require less energy for vision (have a greater sensitivity) than the cones;
- IV. The rods and cones are equally sensitive to radiant energy in the long-wavelength (red) end of the spectrum.

Figure 2-9. Spectral sensitivity of the colour vision under the Purkinje effect [59], supporting the selection of photoluminescent materials for emergency.

The Purkinje effect produces 45 nanometre spectral shifts between maximum cone and rod sensitivity. This overall spectral sensitivity shift is from yellow green (photopic) to blue green (scotopic) is caused by the poor response of the rod cells to red light. Visual stimulation at scotopic levels does not produce colour vision anywhere along the spectrum. Four major facts can be derived from the sensitivity curves (Figure 2-9).

Herein, the Purkinje effect is described as the major parameter from the photopic user abilities to select a persistent luminescent nanomaterial for emergency application. Due to the Purkinje effect, only long afterglow-in-the-dark photoluminescent materials with yellow-green-blue emissions in wavelength lesser 555 nm are selected for emergency, suiting the better visibility of retinal rods-cells in darkness.

¹ The spectral sensitivity of the human eye to the entire visible spectrum can be established experimentally. The interval between the absolute threshold of visibility (scotopic curve) and the initial appearance of hue for a given homogeneous wavelength (photopic curve) is called photochromatic interval [59].

A contingency of visual disabilities and diseases

Official data of the World Health Organization (WHO), a UN agency for Health, estimates that there are around 110 million people with visual disabilities, among which 40 million have blindness or inability to count fingers at a distance of 3 meters [60-61]. The blindness as the most severe visual impairment is common in developing countries due to lack of eye care [62]. Of this global burden of blindness 90% is borne by developing countries and 80% of which is avoidable (preventable or treatable) with the application of existing knowledge and technology. Blindness is also more prevalent in the older age groups, largely as a result of non-communicable diseases. The number of blind people increases every year by 2 million and is expected to double by the year 2020 [61b; 62f-h].

The objective of 'prevention of blindness team' constituted by WHO has is dedicated towards assisting the Member States to effectively prevent blindness and restore sight, aiming to eliminate avoidable blindness by the year 2020. The global target is to ultimately reduce blindness prevalence to less than 0.5 % in all countries, or less than 1 % in any country.

In the WHO Programme for «*Prevention of blindness from diabetes mellitus*» [61a], the following specific data derived from the *diabetes mellitus* has been reported:

- diabetes is a chronic disease that occurs either when the pancreas does not produce enough insulin or when the body cannot effectively use the insulin (hormone that regulates blood sugar) it produces; in the long-term may lead to complications such as blindness, kidney failure and limb amputation, as well as to heart disease and stroke;
- loss of vision in persons with diabetes is the leading cause of blindness and visual disability in adults in economically developed societies; after 15 years of diabetes, approximately 2% of people become blind while about 10% develop severe visual handicap; India has the highest number of diabetics in the world; in Europe about 22.5 million adult people, 5% of the population, are diabetic and worldwide an estimated 150 million people;
- the WHO predicts a rise to 300 million by 2025 due to ageing, unhealthy diets, the fact that unhealthy food is frequently cheaper, obesity and a sedentary lifestyle; most of the direct costs of diabetes result from its complications; and, if the increase of diabetes and its complications occurs as predicted, the financial implications for the health services will be disastrous [61e]; 'diabetic eye' diseases refer to a group of eye problems that people with diabetes may face as a complication of diabetes that can cause severe vision loss or even blindness; diabetic eye may progressively develop diseases such as **cataract**, **glaucoma**, **maculopathy** and **retinopathy** [61-64].

Furthermore, the sight loss in diabetic patients is primarily as a consequence of diabetic retinopathy, and the loss of vision due to diabetic retinopathy can often be prevented by regular eye examinations and timely intervention with laser treatment or surgery [61d] and [63g-h]. The

increase of diabetes among many population groups has caused diabetic retinopathy to be added to the priority list, while glaucoma, an eye disease known for centuries, remains on the public health agenda due to difficulties in its early diagnosis and frequent necessity of life long treatment [61-62].

Cataract

Cataract is a clouding of the eyes lens. Cataract develops at an earlier age in people with diabetes and is a common cause of visual disturbances in the adult population. The slow, progressive opacification of the crystalline lens of the eye in phakic subjects distorts the optical passage of light to the retina resulting in diminished visual acuity. Cataract formation can be accelerated by a number of conditions, including injury, exposure to radiation, gout, certain medications (steroids), and the presence of diabetes mellitus [63]. Treatment for cataracts is surgical removal and placement of an intra-ocular lens (IOL) for replacing the natural crystalline of the human eye, through surgical intervention (pseudophakic).

Glaucoma

Glaucoma is an increase in fluid pressure inside the eye that leads to optic nerve damage and loss of vision [62] and [63a]. A person with diabetes is nearly twice as likely to get glaucoma as other adults [63c]. Glaucoma can cause deficits in peripheral vision. The abnormal regulation of intraocular pressure can result in gradual progressive atrophy of optic nerve cells. The development of chronic elevated intraocular pressure is generally painless, and the gradual loss of peripheral visual field can progress significantly before symptoms are noticed. Glaucoma may also affect a number of subtler visual functions, such as redirection of visual attention, night vision and colour vision. With glaucomatous damage, Snellen acuity test results may not be affected, but peripheral field test results may show deficits. Specialist examination may result in early detection and treatment before the occurrence of possibly disqualifying vision loss. Vision loss caused by glaucoma cannot be restored.

Maculopathy

Macular degeneration describes many ophthalmic diseases that impact the macula function and interfere with detailed, central vision. For the majority of treatment, macular degeneration is a slow process resulting in subtle visual defects; however, approximately 10% of treatment are a "malignant" form of the disease and cause rapid loss of central vision. Peripheral vision is generally spared in macular degeneration, and therapeutic options are still limited. Macular degeneration causes noticeable signs and symptoms: visual acuity drops, recovery from bright lights is lengthened, and eventually a scotoma develops in the direction of attempted gaze [62-63]. Snellen-type acuity testing will detect diminishing central acuity. Telescopic lenses redirect an affected peripheral vision to compensate for lost central acuity, resulting in a reduced peripheral field of vision [62-63].

Diabetic Retinopathy

Diabetic retinopathy is damage to the blood vessels in the retina caused by diabetes mellitus [63]. According to the *U.S. National Eye Institute* [63c], the diabetic retinopathy has four stages: i) mild non-proliferative retinopathy; ii) moderate non-proliferative retinopathy; iii) severe non-proliferative retinopathy; and iv) proliferative retinopathy.

According to *Hean-Choon Chen* [63e], the classification of diabetic retinopathy varies widely and it can be described in 3 stages:

- a. Background retinopathy;**
- b. Preproliferative retinopathy;**
- c. Proliferative retinopathy.**

Background retinopathy with micro aneurysms and intraretinal haemorrhages is common after 5-7 years with diabetes mellitus. In many treatments, the retinopathy does not progress beyond this stage; however, fluid leakage near the macula (diabetic macular oedema) can create partial scotomas in central vision or cause gross haemorrhage in the eye which can obscure vision and eventually lead to retinal detachment and blindness. Subtler visual modalities such as contrast sensitivity, flicker fusion frequency, and colour discrimination may also be affected. Blood vessels damaged from diabetic retinopathy can cause vision loss from fragile, abnormal blood vessels that can develop and leak blood into the centre of the eye, blurring vision in the most advanced stage of the disease (proliferative retinopathy). Furthermore, fluid can leak into the centre of the macula causing a macular oedema. The blurring vision from macular oedema can occur at any stage of diabetic retinopathy, although it is more likely to occur as the disease progresses [63c-d]. Strict reference of blood glucose, as well as medical reference of comorbid diseases (e.g., hypertension, renal disease, cardiac disease), may prevent or delay development of retinopathy.

All people with diabetes-both type 1 and type 2 are at risk to get diabetic retinopathy [61-63].

The Diabetes Reference and Complications Trial (DCCT) showed that better reference of blood sugar levels slows the onset and progression of retinopathy. The people with diabetes who kept their blood sugar levels as close to normal as possible also had much less kidney and nerve diseases. Better reference also reduces the need for sight-saving laser surgery. The gravity of the diabetes disease in vision is high; between 40-45% of Americans diagnosed with diabetes have some stage of diabetic retinopathy [63c].

Generally, no treatment is required for mild, moderate, and severe non-proliferative retinopathy [63c], other than thorough reference of levels of blood sugar, blood pressure, and serum cholesterol to retard early disease progression. A high number of laser burns are usually required to complete treatment and may slightly reduce the colour vision and night vision [63]. Treatment options for retinopathy include forms of **laser surgery**, called:

- **Focal photocoagulation:** tiny burns are placed on the retina with a special laser to seal the blood vessels and stop them from growing and leaking. Specific leaking blood vessels in a small area of the retina, usually near the macula, are addressed for maculopathy disease.
- **Scatter photocoagulation:** abnormal blood vessels are shrunk from 2,000 laser burns in a polka dot pattern in areas of the retina away from the macula. While some loss of side vision may occur, the scatter photocoagulation may keep the rest of the sight, but it is only effective before bleeding or detachment has progressed very far. Scatter treatment is effective even if bleeding has occurred. Proliferative retinopathy is treated with scatter.

However it was seen that annual eye examinations for persons diagnosed with diabetes are important for detecting potentially treatable vision loss [61-64]. Medical guidelines for individuals with diabetes mellitus include annual medical examination and ophthalmologist eye evaluation [63]. Several studies have been performed to assess the colour vision alterations in diabetic individuals [63-64], which alterations might be detected before beginning the retinopathy. In this topic, the investigation addressed to the development of new technologies and methods for the retinal diagnostic are strategically viable.

Abnormalities in colour vision from diabetes were first described in 1953 [64c]. Note that the colour vision alterations may be detected before the occurrence of retinopathy in diabetic individuals [64]. In common with other aspects of dysfunction in the visual pathway, the underlying mechanism is uncertain and may relate to metabolic derangement in the retina rather than to microvascular disease. Various tests are available to assess colour vision, and the results can be affected by the presence of lens opacities or colour blindness; one of the most widely used is the Farnsworth-Munsell 100-Hue Test [52], [54] and [64d].

After initial reports of altered colour vision in patients with diabetes [64c], a number of experimental studies have been conducted to assess this association formally [64e-q]. With the exception of one report [64q], the results from all other studies confirm a significant deterioration in colour vision (mainly assessed by the FM100-HUE test) in diabetic subjects without retinopathy compared with non-diabetic references. Alternatively, diabetic patients should be encouraged to use glucose meters wherever possible to avoid the effect of altered colour vision on matching colour changes [64].

2.1.3.2. Illuminance

Illuminance is measured in lux (lux) or foot-candles (ft-candles), and it is a spatial parameter for the activation of a photoluminescent material. The illuminance decreases according to the inverse square of the distance from a light source (e.g. fluorescent lamp, Xenon lamp, tungsten lamp, or solar radiation). **A light source emitting more than 25 lux, during a sufficient time, produces a total charge of a photoluminescent material, which will be useful in the total absence of illumination at 0 lux, emitting with highest luminance after ending the illumination.**

2.1.3.3. Mobility time for evacuation

The walking characteristics differ across the age spectrum and between genders [65]. In healthy adults, gait characteristics such as velocity and stride length remain relatively constant until the seventh decade of life. After 60 years of age, reductions in velocity have been documented and occur, in large part, due to decreases in stride length of approximately 7-20%. The trigonometric forces produced during walking are represented in Figure 2-10a [65]. For persons in wheelchairs, the locomotion occurs in a minimum free space of 1.20 meters (Figure 2-10b-c) [50a]. Their visual cone in a wheelchair is estimated from a height of about 1.15 meters [50a], reaching a horizontal projection (Hp) on the floor of 1.47 meters (Figure 2-10b). Furthermore, the time required to facilitate the occupant evacuation should be sufficient for a low mobility condition, considering a pedestrian walking speed of 0-0.5 m/s, and wheelchair speed from 0.01 to 9 m/s [65d].

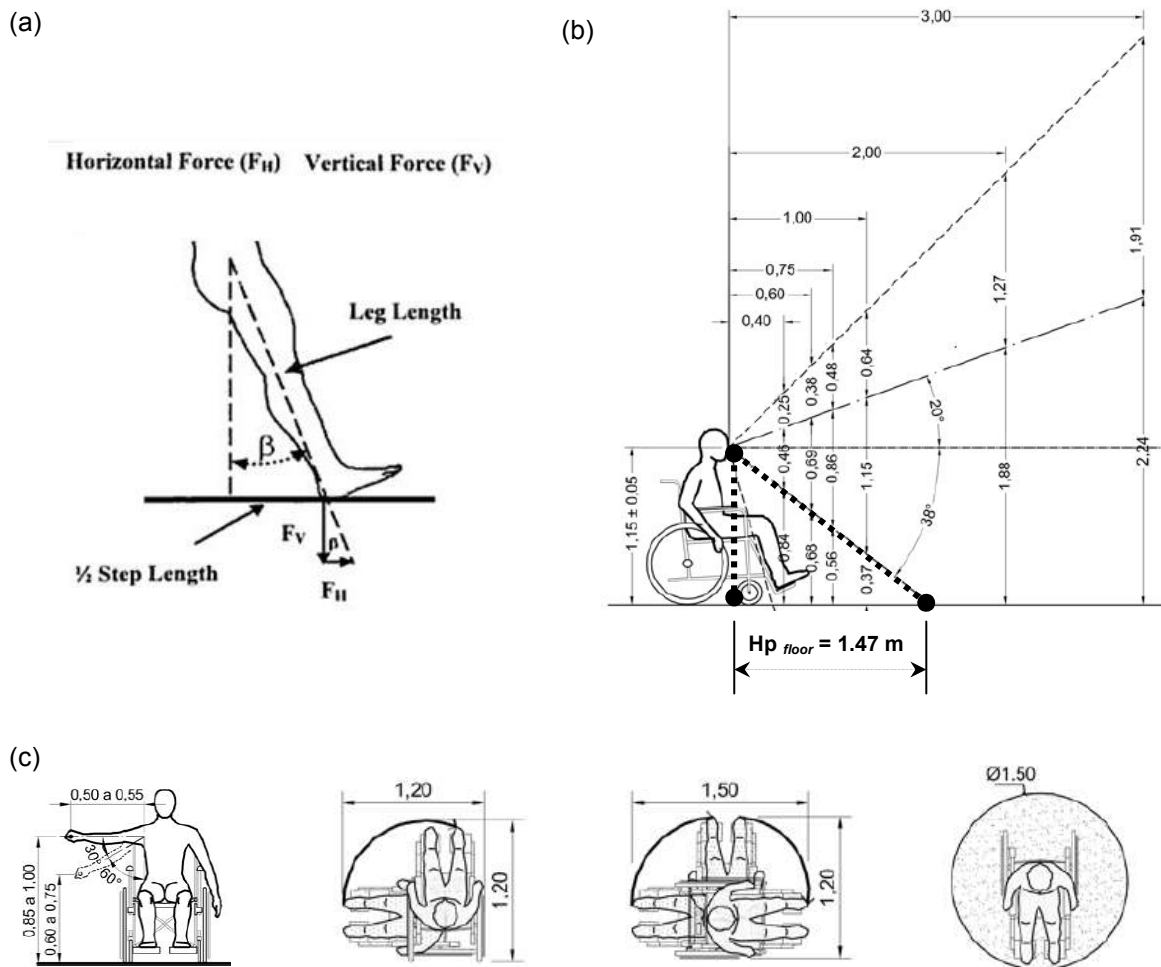


Figure 2-10. a) Trigonometric forces generated during the walking [65]; b) and c) dimensional space of a person in wheelchair [50a].

It can be seen therefore that the conditions for mobility are different between healthy individuals and wheelchair users, both in physical space as required by the locomotion speed. Thus, depending of the distances to evacuate, the photoluminescent materials should present a long afterglow time to illuminate the escape routes during the total evacuation process of all users.

2.1.3.4. Preferential pedestrian pathway

The accessibility of high pedestrian traffic occurs in preferential pathways (Figure 2-11 [48]). These routes (e.g. hallways, stairwells and emergency exits) are ideal places for localization of photoluminescent signals, such as an Emergency Plan. The correct location of the photoluminescent materials and products in escape routes enables the accessible information of emergency signalling during the fast evacuation process. Note that in darkness, the preferential pedestrian pathway keeps with a black background in a visual contrast against afterglow-in-the-dark photoluminescent materials applied in emergency signalling.

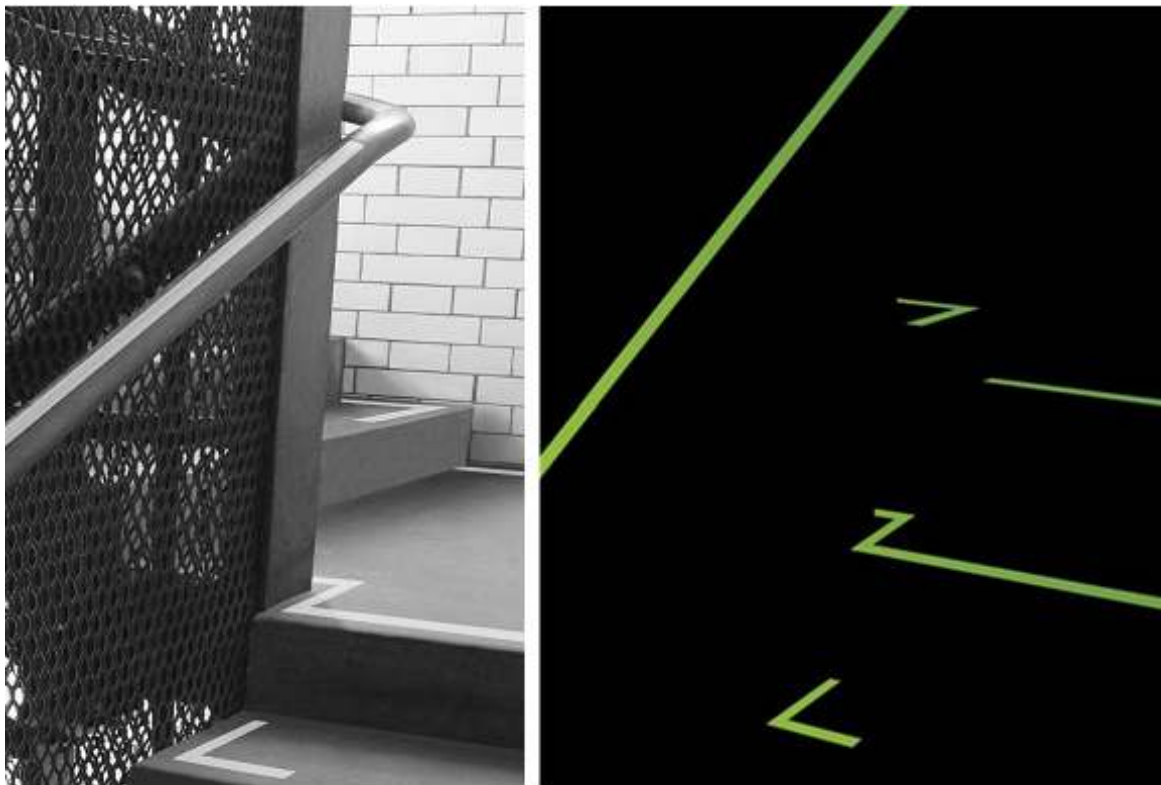


Figure 2-11. Preferential pedestrian pathway with a photoluminescent signalling, according to the New York City's Building Code [48] upon day light illumination (left side), and in darkness (right side).

PART II — EXPERIMENTAL TOOLS

2.2. Characterization Techniques

A description of the characterization techniques used throughout this work is presented in the following topics, highlighting its application in relation to the experiments performed.

2.2.1. Atomic force microscopy [66]

Atomic force microscopy (AFM) was originally designed to image solid substrates developed by *Binnig et al* in 1986, using the surface forces as the contrast mechanism [66]. Analysis of a commercially available AFM cantilever deflection-distance profiles, as well as knowledge of the spring constant of the cantilever, allows for the determination of a force versus separation curve. In contrast to electron microscopes, the characterization of samples using AFM does not generally require any special preparation. In this work, AFM was used to investigate the intercrystalline distances of $\text{SrAl}_2\text{O}_4:\text{Ce}^{3+}$, Dy^{3+} , Eu^{2+} polymorphs from post-annealing treatment (chapter 3). AFM measurements were performed in contact and Tapping Mode at room temperature using a commercial setup Multimode, Nanoscope® IIIA, DI from Digital Instruments [66e] (Figure 2-12). AFM was made by the size of the tip, considering force sensor dependent of cantilever properties (k , Q , f_0 , deflection sensor) and tip properties (sharpness, stiffness, conductivity, magnetism). A commercial cantilever (PPP-NCHR Nanosensors) with thickness 4.0 ± 1 mm, length 125 ± 10 mm, width 30 ± 7.5 mm, spring constant of $k=42$ N/m and typical tip radius less 10 nm of the tip was used. Others two cantilevers were used in the current work: Cantilever Super Sharp Silicon (2 nm) SSS-NCL-10 Tapping Mode; Cantilever Point Probe-Plus (10 nm), Metal support, Scoot double-face. Imaging visualization was performed in air (tapping mode with resonance frequency at 330 kHz) at the scanning speed by tip velocity about 3-15 $\mu\text{m/s}$.

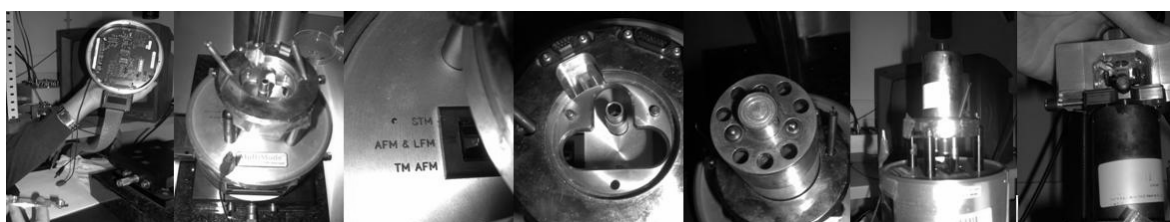


Figure 2-12. Assembly of AFM Multimode, Nanoscope IIIA, DI.

2.2.2. Scanning electron microscopy [67]

Powder microstructure and elemental composition of all samples were observed via scanning electron microscopy (SEM) coupled to energy dispersive X-ray (EDX) spectrometer in a SU-70 microscope at University of Aveiro, based on an electron beam that strikes the surface of a conducting sample, to study chemical composition and modifications after heat treatment. This is a technique widely used to study the surface topography. A high energy (typically 10 keV)

electron beam is scanned across the surface. The incident electrons cause low energy secondary electrons to be generated, and some escape from the surface. The secondary electrons emitted from the sample are detected by attracting them onto a phosphor screen. This screen will glow and the intensity of the light is measured with a photomultiplier. The incident electrons will also cause X-rays to be generated which are the basis of the EDX technique. Some of the incident electrons may strike an atomic nucleus and bounce back into the vacuum. These electrons are known as backscattered primaries and can be detected with a backscattered electron detector, given information on the surface topography and on the average atomic number of the area under the electron beam. The EDX measurements were obtained in a Bruker AXS Microanalysis GmbH, Germany. The energy of the beam is in the range 10-20 keV Puls, 2.92 kcps, caused X-rays emitted from the point the material. SEM SU-70 conditions: accelerating voltage from 4 to 15 kV, magnification of 35000 in working distance from 2 to 7 mm using an emission current of 32000 nA. Elements with high atomic number are easier to detect by EDX, as a convenient technique to analysis of lanthanide elements ($Z > 58$).

2.2.3. Transmission electron microscopy [67]

Transmission electron microscopy (TEM) is a technique using an electron beam that forms an image in transmission projection of the sample in the direction of the beam, used to characterize nanostructures [67b]. Accelerating electrons with sufficient energy through high voltages (kV) is suitable to imaging atomic features with high spatial resolution of samples in their morphology, structure and orientation. Analogous to the SEM, the incident electrons will also cause X-rays to be generated which are the basis of the EDX technique and diffraction patterns used to refine the crystal lattice structure. High-resolution (HR) TEM of samples was performed in a HITACHI-9000 microscope at Ceramic and Glass Engineering Department. TEM was a fundamental technique to identify the formation of luminescent nanotubes (chapter 3), nanowires (chapter 4) and core-shells (chapter 5). Some post-annealed samples (chapter 3) were analysed in a Philips CM-200 with field-emission source (FEG) microscope (Germany). For TEM and electron diffraction, powders were ultrasonically dispersed in an ethanol suspension and immersed into copper grids.

2.2.4. X-ray diffraction

X-rays were discovered accidentally in 1895 by the German scientist Wilhelm Conrad Roentgen conducting experiments involving high voltage currents in evacuated tubes. X-rays are a form electromagnetic radiation with a wavelength ranging from 10 to 0.01 nm. Herein, X-ray diffraction (XRD) was used to identify the crystalline structure of starting materials, synthesized host lattice, phases formed by the host phase transformations in post-annealed samples, nanowires and core-shells obtained at different temperatures and treatments. For this purpose, a high-resolution Rigaku Geigerflex D/Mac, C Series diffractometer was used with Cu $K\alpha$ radiation ($\lambda = 1.5406 \text{ \AA}$) produced at 30 kV and 25 mA scanned the diffraction angles (2θ) between 20° and 50° with a step size of

0.02° 2 θ per second. The positions of the characteristic peaks were characterized supported from the indexed cards JCPDS Powder Diffraction Files (PDF) of the International Centre for Diffraction Data (ICDD).

2.2.5. X-ray fluorescence spectroscopy

When a primary X-ray excitation source from an X-ray tube or a radioactive source strikes a sample, the X-ray can either be absorbed by the atom or scattered through the material. The process in which an X-ray is absorbed by the atom by transferring all of its energy to an innermost electron is called the photoelectric effect. During this process, if the primary X-ray had sufficient energy, electrons are ejected from the inner shells, creating vacancies as an unstable condition for the atom. As the atom returns to its stable condition, electrons from the outer shells are transferred to the inner shells and in the process giving off a characteristic X-ray whose energy is the difference between the two binding energies of the corresponding shells. The process of detecting and analyzing the emitted X-rays from a sample is called X-ray fluorescence spectroscopy (XRF), and it was used to characterize the chemical composition of oxides from the porcelain ceramic substrate (in this chapter, section 2.3.2). The secondary (fluorescent) X-rays from the oxides have been excited by bombarding of high-energy X-rays emitted from a Rh ampoule, using a Panalytical Axios equipment of the Geosciences Department of University of Aveiro.

2.2.6. Inductively coupled mass spectroscopy

Inductively coupled mass spectroscopy (ICP-MS) is an analytical technique used for elemental determinations. The technique is based in the ICP source that converts the atoms of the elements in the sample to ions, which are then separated and detected by the mass spectrometer. ICP-MS was made to quantify the chemical composition of commercial phosphors (in this chapter, section 2.3.1, and in ANNEX II), after a preliminary determination of their host lattice structures by XRD. The chemical quantification (ppm) of lanthanides and impurities was made to SrAl₂O₄:Ce³⁺, Dy³⁺, Eu²⁺ commercial phosphor from elemental analysis (Mg, Si, P, Ca, Sr, Y, La, Ce, Pr, Nd, Sm, Eu, Gd, Tb, Dy, Ho, Tm, Lu) at “*Laboratório Central de Análises (LCA)*” of the University of Aveiro.

2.2.7. Raman spectroscopy [68]

Raman spectroscopy is a light scattering technique used to diagnose the internal structure of molecules and crystals. In a light scattering experiment, light of a known frequency and polarization is scattered from a sample. The scattered light is then analyzed for frequency and polarization. Raman scattered light is frequency-shifted with respect to the excitation frequency, but the magnitude of the shift is independent of the excitation frequency. This Raman shift is therefore an intrinsic property of the sample. Raman spectroscopy was used in this thesis to determine the bonding changes [68f] evidenced by the spectra of SrAl₂O₄:Ce³⁺, Dy³⁺, Eu²⁺ before and post-annealing on the formation of hexagonal crystals and nanotubes (chapter 3). The

spectral curves were obtained in frequency range of about 4,000-50,000 by RFS100 Instrument at Chemistry Department of University of Aveiro.

2.2.8. Nuclear magnetic resonance spectroscopy

Solid-state nuclear magnetic resonance (NMR) provides information about short-range structure in amorphous and crystalline materials. NMR was qualitatively used in this thesis to compare the formation of a coating layer and the preservation of the host structure of particles encapsulated with TiO₂ (chapter 5). NMR was performed on a Bruker-400 equipment in ²⁷Al (5/2), and ¹³C (1/2) magic angles spinning (MAS) to detect NMR MAS spectra at 15 and 9 kHz, respectively, at Chemistry Department of University of Aveiro.

2.2.9. Zeta potential and electronic conductivity [68]

Many particles dispersed in an aqueous system will acquire a surface charge, principally either by ionization of surface groups or adsorption of charged species. These surface charges modify the distribution of ions around the dispersed particles or surfaces immersed into a liquid, creating a double layer (DL, also called an electrical double layer, EDL). The first layer, the surface charge (either positive or negative), comprises ions adsorbed directly onto the surface due to chemical interactions with the substrate. The second layer is composed of ions attracted to the surface charge via the Coulomb force, electrically screening the first layer. This second layer is loosely associated with the object, because is made of free ions which move in the fluid under the influence of electric attraction and thermal motion rather than being firmly anchored. It is thus called the diffuse layer. When a particle moves under the action of an electrical field, the first layer more strongly bound to the surface moves as part of the particle. The zeta potential is the electrical potential at the slipping plane where the particle with the strongly bound ions moves past the bulk solution [68e]. Zeta potential is very sensitive to the concentration and type of ions in solution, being one of the main parameters that mediate interparticle interactions. Particles with zeta potential values higher ± 30 mV of the same charge sign (positive or negative), will repel each other, conferring stability, i.e., the dispersed particles will resist to aggregation.

Zeta potential is not directly measurable but it can be calculated using theoretical models and experimental measurements of the dynamic electrophoretic mobility by applying an electric field across the dispersion. The electrically charged particles will migrate towards the electrode of opposite charge sign with a velocity proportional to the magnitude of the zeta potential. In order to investigate the colloidal/chemical stability as an estimate of water resistance of SrAl₂O₄:Ce³⁺, Dy³⁺, Eu²⁺ encapsulated with TiO₂ (chapter 5), zeta potential and electronic conductivity measurements using the starting material were made in aqueous suspensions using a Coulter DELSA 440 SX. The core-shell encapsulated samples were also analyzed by zeta potential and electronic conductivity in time-resolved measurements using a ZetaSizer NanoSeries ZS, Malvern Instrument [68e].

2.2.10. Particle size distribution

A Dynamic Light Scattering (DLS) was used to measure the particles size distributions of as-received and grinded samples of $\text{SrAl}_2\text{O}_4:\text{Ce}^{3+}$, Dy^{3+} , Eu^{2+} commercial phosphor (Chapter 4) in an organic solvent (ethanol) using a ZetaSizer NanoSeries ZS, Malvern instrument. This technique is established for measuring the size of particles typically in the submicron region from 0.3 nm to 10 μm . A laser illuminates the sample in the cell, and most of the laser beam passes through the sample. A detector measures the scattered light and the scattering intensity signal at successive time intervals is compared, the rate at which the intensity is varying is derived. Based on this information, the particle size and particle size distribution is computed. The ceramic substrate formulation, and the SrCO_3 and Al_2O_3 starting powder materials (ANNEX I) were characterized by using a Coulter Fraunhofer PIDS equipment.

2.2.11. Thermal analysis

Curves of thermal expansion of multilayered photoluminescent ceramics were performed from 300 to 1473 K (chapter 7) using a dilatometer DELSA, Model DIL801L in *Argon* atmosphere. The thermo gravimetric (TG) and differential thermal (DTA) analyses of starting compositions and host lattices samples were measured using a TG-DTA Setaram Labsys analyzer in *Argon* atmosphere (ANNEX I). The thermodynamic activities were determined using the FactSage 5.5 software in Integrated Thermodynamic Databank System (ITDS) that provides tools for the administration of thermochemical data of inorganic substances and tools for thermodynamic calculations (ANNEX I).

2.2.12. Photoluminescence spectroscopy

All photoluminescence characterizations (chapters 3, 4 and ANNEX II) were performed at Physics Department of University of Aveiro with experimental support of the Prof. Dr. Luís Dias Carlos group. The photoluminescence spectra were recorded at room temperature on a Fluorolog-3 Model FL3 – 2T with double excitation spectrometer and a single emission spectrometer using a monochromator (TRIAX 320) coupled to a Hamamatsu R928 photomultiplier, in a front face acquisition mode. The excitation source was a 450 W Xenon lamp.

Steady-state emission measurements (stationary mode) were corrected for the spectral response of the monochromators and the detector using typical correction spectrum provided by the manufacturer. The excitation spectra were corrected for the spectral distribution of the lamp intensity using a photodiode reference detector. A schematic functionalization of a spectrophotometer to obtain steady-state luminescence spectra in UV region is showed in Figure 2-13, in the left. The IS-SPECWIN software was used to adjust some measurement parameters (Figure 2-13, in the right).

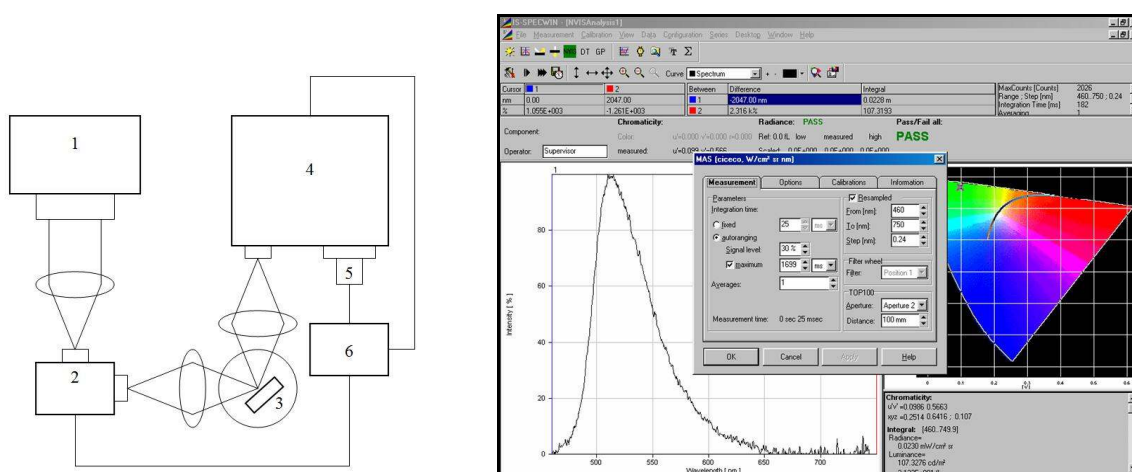


Figure 2-13. In left, a schematic functionalization of the spectrophotometer: (1) Xenon lamp; (2) excitation monochromator; (3) support and the sample; (4) the emission monochromator, photomultiplier, computer and data control. In right, IS-SPECWIN software.

In time-resolved emission (TRE), the measurements were acquired in non-stationary mode at room temperature with the setup described for the luminescence spectra using a pulsed Xe-Hg lamp (6 μ s pulse at half width and 20-30 μ s tail). TRE spectra of the samples were performed from excitation at 360 nm for precursor $\text{SrAl}_2\text{O}_4:\text{Ce}^{3+}$, Dy^{3+} , Eu^{2+} micro- and nano-particles (standard), and post-annealed samples. TRE was used to characterize the luminescence emissions and modifications produced by the post-annealing treatment. The spectra were acquired with starting delays of (1) 0.05 ms, (2) 50.00 ms and (3) 200.00 ms, using an integration window of 20.00 ms. TRE data are acquired in the phosphorimeter emission according to the Equation 2-2:

$$\text{TBF} = 20 + \text{SD} + W \quad (2-2)$$

used to adjust the equipment parameters, where TBF is the time between flashes [ms], number 20 is a constant value of the equipment, SD is the starting delay after flash [ms], and W is the sample window [ms], for an experimental number of flashes [#].

2.3. Materials

In this topic, the criteria used in this thesis for selecting the main baseline luminescent material is briefly described based on the functional requirements in terms of emission colour, luminance and time of afterglow. The other starting materials and reagents used in the experiments and their characterizations are also described.

2.3.1. Baseline material: $\text{SrAl}_2\text{O}_4:\text{Ce}^{3+}, \text{Dy}^{3+}, \text{Eu}^{2+}$ micro- and nano-particles

The selection of the luminescent baseline material for use in all experiments was made from 13 commercial phosphors supplied by *Lanxi Minhui Photoluminescent Co., Ltd., Minhui Zhejiang, China*. These commercial samples were preliminarily investigated by PL-spectroscopy (ANNEX II, Tables A1 and A2) to evaluate their suitability for emergency applications, namely, their ability to fulfil the 3 following criteria:

- (1) Presenting an emission peak in wavelength < 555 nm, considering the retinal sensitivity on the blue-green-yellow region in darkness, according to the Purkinje effect [59];
- (2) For the samples satisfying the criterion (1), selecting those presenting the highest values of luminance and radiance;
- (3) For the samples satisfying the criteria (1) and (2), selecting the sample presenting the longest afterglow time of emission, based on the information given by the fabricant.

For the criterion (1), a preliminary characterization of the PL emission was made for the commercial samples at the Physics Department of University of Aveiro. The selected $\text{SrAl}_2\text{O}_4:\text{Ce}^{3+}, \text{Dy}^{3+}, \text{Eu}^{2+}$ starting material sample presented similar emission in a yellow-green region with predominant emission peak at 525 nm upon different wavelengths of excitation (Figure 2-14).

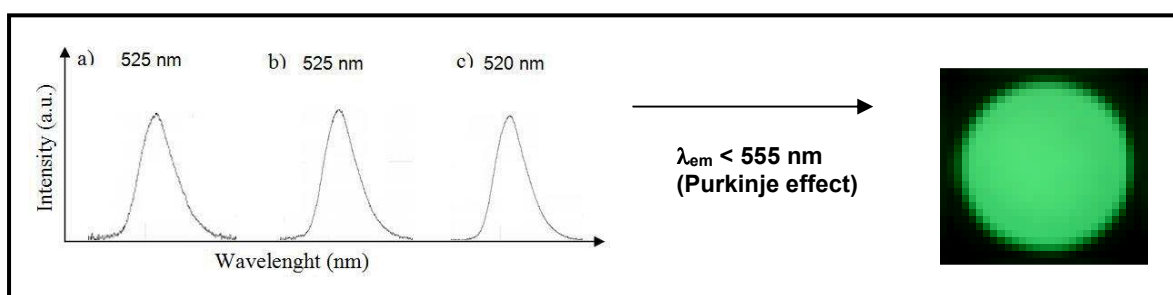


Figure 2-14. Yellow-green emission spectra of $\text{SrAl}_2\text{O}_4:\text{Ce}^{3+}, \text{Dy}^{3+}, \text{Eu}^{2+}$ starting material upon different wavelength of excitation: a) $\lambda_{ex} = 300$ nm, b) $\lambda_{ex} = 320$ nm, and c) $\lambda_{ex} = 360$ nm (UV-lamp).

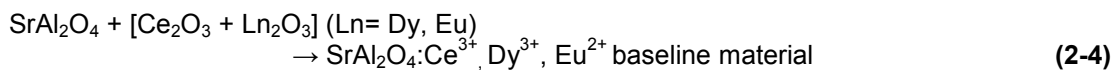
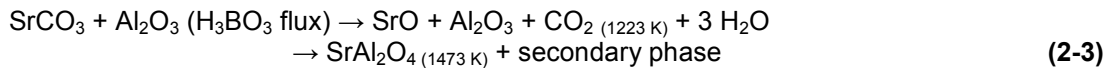
For the criterion (2), colour emission coordinates, radiance and luminance values were compared between the samples with emission < 555 nm. These optical features of $\text{SrAl}_2\text{O}_4:\text{Ce}^{3+}, \text{Dy}^{3+}, \text{Eu}^{2+}$ starting material upon a light source with Xenon lamps at 500 lux for 10 min of excitation are described in Table 2-7. Note that these characteristics present some experimental restrictions because the measurements were adjusted to the available TRIAX equipment, using a Xenon lamp, with lowest illuminance radiation (~ 500 lux) than the recommended by DIN 67510 of 1000 lux [14].

For the criterion (3), the afterglow measurements could not be performed in the available TRIAX equipment of University of Aveiro. Thus, this third criterion was attended according to the technical information received from the fabricant, revealing that the afterglow-in-the-dark time of $\text{SrAl}_2\text{O}_4:\text{Ce}^{3+}, \text{Dy}^{3+}, \text{Eu}^{2+}$ commercial phosphor is of about 12 hours, for the respective luminance test conditions: D65 standard light source at 1000 lux for 10 minutes of excitation.

Table 2-7. Optical features of SrAl₂O₄:Ce³⁺, Dy³⁺, Eu²⁺ starting material (N1 sample) upon a light source with Xenon lamps at 500 lux for 10 min of excitation.

Colour Appearance	Atomic excitation [nm]	Colour emission		Integral			Radiance [μ W/cm ²]	Luminance [mcd/m ²]
		u	v	x	y	z		
Yellow-green SrAl ₂ O ₄ :Ce ³⁺ , Dy ³⁺ , Eu ²⁺ baseline material	$\lambda_{\text{control}} = 300\text{nm}$	0.1960	0.5454	0.2696	0.5465	0.1830	18,7	79,9848
		0.1197	0.5453	0.2699	0.5463	0.1830	18,3	78,3760
		0.1198	0.5457	0.2704	0.5476	0.1820	18,0	77,1078
	$\lambda_{\text{UV-dark}} = 360\text{nm}$	0.1199	0.5472	0.2722	0.5523	0.1750	36,0	155,4660
		0.1200	0.5472	0.2724	0.5521	0.1750	35,6	153,9363
		0.1202	0.5472	0.2728	0.5520	0.1750	35,2	152,1167
	$\lambda_{\text{max } 1} = 320\text{nm}$	0.1201	0.5472	0.2726	0.5519	0.1750	28,1	121,6369
		0.1201	0.5473	0.2727	0.5521	0.1750	27,7	119,6633
		0.1203	0.5474	0.2732	0.5524	0.1740	27,4	118,6898

Based in the three criteria mentioned, one commercial sample (designated hereafter as N1) was selected from the 13 commercial phosphors for emergency application. XRD and ICP-MS techniques were used to identify the crystalline phases, and the elemental composition, respectively, presented in N1 (Table 2-8). The as-received N1 sample consists of strontium aluminate phosphor co-doped with cerium (III), dysprosium (III) and europium (II), i.e. SrAl₂O₄:Ce³⁺, Dy³⁺, Eu²⁺. This will be the starting material used along the present work. Further general characteristics of this material are described below. According to the technical information from the fabricant, this starting material was obtained from solid-state reactions between the reagents SrCO₃, Al₂O₃, Ce₂O₃, Ln₂O₃ (Ln = Dy and Eu) with added H₃BO₃ as flux. Synthesis was performed within the temperature range from about 1223 K until 1473 K, in N₂-H₂ reductive atmosphere as described by Equations (2-3) and (2-4).



The SrAl₂O₄:Ce³⁺, Dy³⁺, Eu²⁺ baseline material consists of α -monoclinic structure. Elemental analysis of the phosphor tested in this thesis is presented in Table 2-8.

Table 2-8. Elemental analysis of as-received commercial phosphor, as determined by ICP-MS and EDX Bruker AXS Microanalysis.

SrAl ₂ O ₄ :Ce ³⁺ , Dy ³⁺ , Eu ²⁺ baseline material							
Ionic function	Host lattice (SrAl ₂ O ₄)			Lanthanide (co)activators (Ln)			
	Sr	Al	O	Eu	Dy	Ce	
K [a]	2	3	1, 2	2	3	3	3
V [b]	Si ²⁺	Al ³⁺	O ²⁻	-	-	-	-
f \leftrightarrow f	-	-	-	-	Eu ³⁺ (F6)	Dy ³⁺ (F9)	-
f \leftrightarrow d	-	-	-	Eu ²⁺ (F7)	-	-	Ce ³⁺ (F1)
ICP-MS [ppm]	370300	303940	-	7223	-	13186	9980
EDX [wt.%]	46.43	14.49	32.45	1.57	-	0.82	2.78

[a] K is the number of e- transferred per mole from/to an oxidant or reductant in the balanced half-reaction, i.e. the valence state under spin changing. [b] V is the elemental vacancy for electronic transitions.

2.3.2. Porcelain stoneware ceramic substrate

A combination of 65%SiO₂—21%Al₂O₃—14% alkali oxides, corresponding to an industrial stoneware tile composition (*Source: Eliane S.A., Cocal do Sul, Brazil*) was used as ceramic substrate for the SrAl₂O₄:Ce³⁺, Dy³⁺, Eu²⁺ phosphor layer deposition. Elemental XRF analysis of this substrate composition is presented in Table 2-9.

Table 2-9. Oxide composition of the stoneware ceramic substrate as determined by XRF.

Oxides	SiO ₂	Al ₂ O ₃	F ₂ O ₃	Na ₂ O	K ₂ O	TiO ₂	Other
XRF [wt.%]	65.80	21.21	0.61	3.82	1.81	1.71	10.03

2.3.3. Materials and reagents for encapsulating the luminescent particles

Poly-(ethylene glycol) (PEG, Aldrich, $M_w \approx 300 \text{ g.mol}^{-1}$) and sodium titanate (Na₂TiO₃, *source: Cinkarna Met. Ind., d.d., Slovenija*) were used for encapsulating the SrAl₂O₄:Ce³⁺, Dy³⁺, Eu²⁺ luminescent baseline material with TiO₂. High-purity deionised water and ethanol (CH₃CH₂OH, Merck) were used as dispersion media. These starting materials were used in the chapter 5.

2.3.4. Transparent frit for covering the multilayered luminescent samples

Raw material composition of 80% PbO—20% SiO₂ (*source: Esmalticer Esmaltes Cerâmicos Lda., Portugal*) was used as transparent glass frit to cover the strontium aluminate luminescent baseline material. This starting material was used for a study of multilayered system in the chapter 7.

2.3.5. Characterizations of starting materials

As mentioned before, other more detailed characterizations of the SrAl₂O₄:Ce³⁺, Dy³⁺, Eu²⁺ luminescent material, as well as of other materials derived from it after undergoing several treatments, were made in the next chapters of this thesis. The as-received SrAl₂O₄:Ce³⁺, Dy³⁺, Eu²⁺ commercial phosphor was always used as the **baseline material** (standard sample) for comparison purposes under different contexts.

The characterization techniques that will be described in more detailed in the next chapters include:

- X-ray diffraction of the SrAl₂O₄:Ce³⁺, Dy³⁺, Eu²⁺ baseline material with α -monoclinic structure compared to the post-annealed samples (chapters 3 and 4);
- Steady-state PL spectroscopy of the SrAl₂O₄:Ce³⁺, Dy³⁺, Eu²⁺ baseline material with α -monoclinic structure compared to the post-annealed samples (chapters 3 and 4);
- Time-resolved emission of the SrAl₂O₄:Ce³⁺, Dy³⁺, Eu²⁺ baseline material with α -monoclinic structure compared to the post-annealed samples (chapter 3);

- Particle size distribution of the $\text{SrAl}_2\text{O}_4:\text{Ce}^{3+}, \text{Dy}^{3+}, \text{Eu}^{2+}$ baseline material as standard for the grinded samples (chapter 4);
- Zeta potential and electronic conductivity of the non-encapsulated $\text{SrAl}_2\text{O}_4:\text{Ce}^{3+}, \text{Dy}^{3+}, \text{Eu}^{2+}$ baseline material as standard for the encapsulated samples with TiO_2 (chapter 5);
- RMN spectroscopy of the non-encapsulated $\text{SrAl}_2\text{O}_4:\text{Ce}^{3+}, \text{Dy}^{3+}, \text{Eu}^{2+}$ baseline material as standard for the encapsulated samples with TiO_2 (chapter 5);
- FM100-HUE test of the $\text{SrAl}_2\text{O}_4:\text{Ce}^{3+}, \text{Dy}^{3+}, \text{Eu}^{2+}$ baseline material as standard emission for the visibility of photoluminescent materials for emergency application (chapter 6);
- Dilatometric behaviour of the $\text{SrAl}_2\text{O}_4:\text{Ce}^{3+}, \text{Dy}^{3+}, \text{Eu}^{2+}$ baseline material as standard for the photoluminescent multilayered system (chapter 7).

In particular, the $\text{SrAl}_2\text{O}_4:\text{Ce}^{3+}, \text{Dy}^{3+}, \text{Eu}^{2+}$ particles and powders of the ceramic substrate were characterized herein with their particle size distributions. As-received $\text{SrAl}_2\text{O}_4:\text{Ce}^{3+}, \text{Dy}^{3+}, \text{Eu}^{2+}$ baseline material presents a particle size distribution within the range of $\sim 60\text{-}150\ \mu\text{m}$ as measured by Coulter, LS Fraunhofer PIDS. Figure 2-15 shows that the powders consist mostly of particle agglomerates, as expected from solid state reaction synthesis. However, some the rare-earth spherical nanoparticles with sizes from 15 to 40 nm could also be observed in the SEM micrographs as illustrated in the insert. Figure 2-15 also shows the particle size distribution curve of the aluminosilicate substrate, which is composed of particles with an average diameter of $7\ \mu\text{m}$.

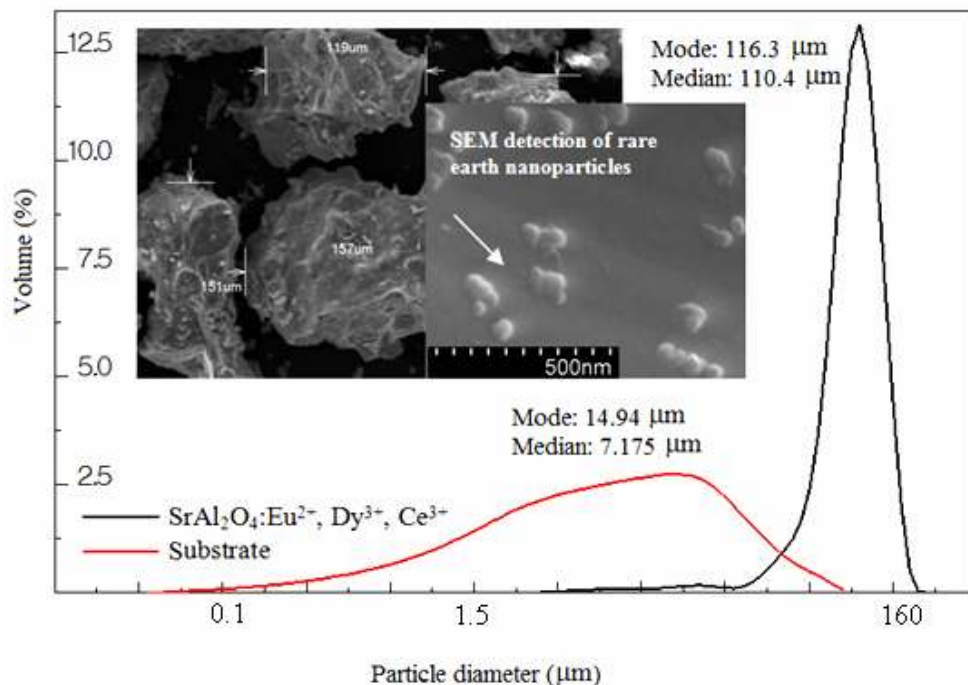


Figure 2-15. SEM and Coulter analyses of the particles size distribution of $\text{SrAl}_2\text{O}_4:\text{Ce}^{3+}, \text{Dy}^{3+}, \text{Eu}^{2+}$ precursor micro- and nano- particles and $65\%\text{SiO}_2\text{—}21\%\text{Al}_2\text{O}_3\text{—}14\%$ alkali oxides.

2.4. Processing

The basic processing performed in the thesis involved mechanical deposition of the starting powder materials, pressing, grinding, ultrasonification and/or heat treatment of post-annealing as described in the following items.

2.4.1. Mechanical deposition, dry-pressing and/or post-annealing

Mechanical deposition and dry-pressing of starting materials into pellets ($\varnothing = 10$ mm) were done using a U.S. Craver Laboratorial Press (~ 490 MPa), Figure 2-16. Samples were investigated in double-layered systems of as-synthesized micro- and nano-particles (commercial powders) onto the substrate (0.10 g and 0.25 g, respectively).

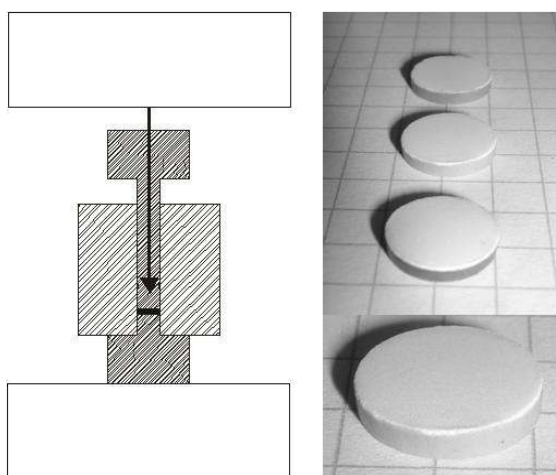


Figure 2-16. Pressed samples: a) laboratorial moulding; and b) typical pallet samples of the $\text{SrAl}_2\text{O}_4:\text{Ce}^{3+}, \text{Dy}^{3+}, \text{Eu}^{2+}$ precursor micro- and nano-particles phosphor (starting material) applied onto (65% SiO_2 —21% Al_2O_3 —14% alkalis) ceramic substrates.

Post-annealing was monitored over and above the temperature range of host phase transformation (> 923 K) in temperature range from 573 to 1473 Kelvin, for 1 hour in air atmosphere. All thermal treatments of samples realized in this work were carried out in the same TERMOLAB® laboratorial furnace at a heating rate of $10 \text{ K}\cdot\text{min}^{-1}$ in air atmosphere.

2.4.2. Grinding and/or ultrasonification

The precursor baseline material $\text{SrAl}_2\text{O}_4:\text{Ce}^{3+}, \text{Dy}^{3+}, \text{Eu}^{2+}$ in shape of micro- and nano-particles was deagglomerated by ball milling under the following conditions:

- Weight of balls (P_{balls}) was three times the weight of the precursor particles to be ground ($P_{\text{particles}}$), i.e. in the ratio of 3:1;
- Milling time: 1, 3 and 7 hours;
- Speed: 150 cycles per minute (cpm).

All ultrasonificated samples were treated in a laboratorial ultrasound at 3 MHz at different processing times, using ethanol as the dispersion medium. ■

Chapter 3

Afterglow phenomenon of luminescent $\text{SrAl}_2\text{O}_4:\text{Ce}^{3+}$, Dy^{3+} , Eu^{2+} nanotubes

Luminescent $\text{SrAl}_2\text{O}_4:\text{Ce}^{3+}$, Dy^{3+} , Eu^{2+} nanotubes were grown using solid-state reaction and post-annealing approach. This optical nanotubular structure was characterized by XRD, RAMAN, HR-TEM, SEM, AFM, EDX, steady-state and time-resolved PL spectroscopy. A series of *f-f* and *f-d*-transitions with light emission in structured bands peaked at 488 nm arising from the polymorphism of host lattice were correlated to an intercrystalline distal-effect on the afterglow phenomenon.

Key-words: solid-state reaction, nanotube, strontium aluminate, lanthanide, afterglow phenomenon.

PART I — NANOTUBES GROWTH

In this first part, the synthesis process of luminescent nanotubes growth from the baseline material produced by solid state route upon post-annealing heat treatment is discussed. This process of nanotubes growth contrasts with that described in literature, according to which the nanotubes are formed through hydrothermal or co-precipitation methods.

3.1. SrAl₂O₄ nanotube growth

Since the first detection of carbon nanotubes (CNTs) [69], one-dimensional inorganic nanotubes have extensively been investigated to meet the demands of science and nanotechnology. The formation of nanotubes was suggested to occur by a curving and seaming process of lamellar structures formed after heat treatment [70-71]. In this way, metal oxide strontium aluminate (SrAl₂O₄) nanotubes have been obtained via hydrothermal synthesis by rolling-up and post-annealing approach (Figure 3-1) [70].

This SrAl₂O₄ host material for persistent luminescence has a ~6.5 eV band-gap in the α -monoclinic structure. The high-temperature phase with β -hexagonal structure is obtained via phase transition at ~923 K. Rare-earths in the form of divalent/trivalent cations, such as Eu²⁺ (1.20 Å), Dy³⁺ (1.17 Å) and Ce³⁺ (1.03 Å), can replace the Sr²⁺ ions (1.21 Å) in the crystal lattice with possible charge compensations during luminescence.

In the luminescence field, many Ln₂O₃ lanthanide nanotubes have been prepared by varied routes, including hexagonal NaYF₄ nanotubes with outer diameters of about 250 nm and lengths of about 500 nm [72]. Luminescent nanorod- and nanotube-shaped phosphors, including those co-doped with Eu²⁺ and Dy³⁺ have already been prepared [70], [72], and [73], but thereof changes on the persistent afterglow luminescence were not elucidated concerning the polymorphism. Also, Ce³⁺ doped SrAl₂O₄ nanotubes have not been already reported.

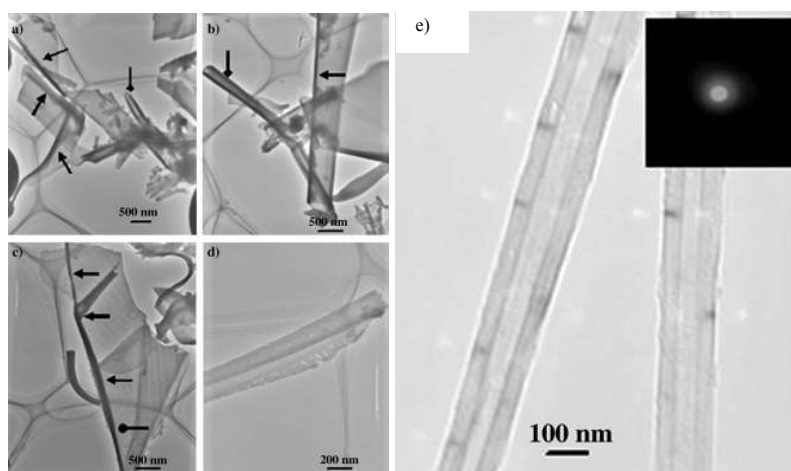


Figure 3-1. TEM images of SrAl₂O₄: (a)-(d) the roll-up layers to form nanoscrolls during hydrothermal synthesis at 393 K; (e) nanotubes [70].

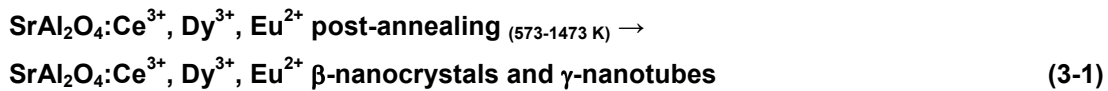
3.2. Synthesis process of luminescent nanotube growth [74]

The synthesis process of luminescence nanotube growth is hereafter described starting from the precursor particles (baseline material) presenting planar defects in the crystalline host lattice structure, and nanotubes are formed by a roll up mechanism during the heat treatment of post-annealing.

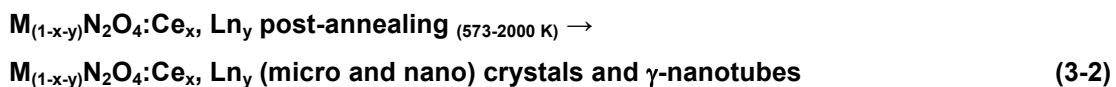
3.2.1. Utilization of $\text{SrAl}_2\text{O}_4:\text{Ce}^{3+}$, Dy^{3+} , Eu^{2+} micro- and nano-particles

A preparation method of luminescent nanotubes via heat treating precursor micro- and nano-particles as-synthesized through a solid-state reaction from SrCO_3 , Al_2O_3 , Eu_2O_3 , Dy_2O_3 , and Ce_2O_3 is here reported. The phosphor baseline material used in this work was a commercial powder supplied by *Lanxi Minhui Photoluminescent Co., Ltd., Minhui Zhejiang, China*. A combination of SiO_2 , Al_2O_3 and alkali oxides was used as substrate (please, see chapter 2). In contrast to the formation of SrAl_2O_4 nanotubes derived from precursor particles synthesized by hydrothermal [70] or co-precipitation [73] methods, the emphasis here is put on solid-state chemistry of $\text{SrAl}_2\text{O}_4:\text{Ce}^{3+}$, Dy^{3+} , Eu^{2+} nanotubes in absence of a catalyst under heat treatment temperatures below 1473 K [74-75].

Luminescent strontium aluminate nanotubes develop according to the schematics described by Equation 3-1:



Equation 3-2 could be used to describe the general development of luminescent metal-earth nanotubes:



where M is Be, Mg, Ca, Sr, Ba or a mixture thereof, N is Al, and Ln is a cation from the Lanthanide Series of Elements.

3.2.2. Lattice defects and rolling up mechanism [75]

Initially, α -monoclinic $\text{SrAl}_2\text{O}_4:\text{Ce}^{3+}$, Dy^{3+} , Eu^{2+} micro- and nano-particles presenting multifunctional piezo-, thermo-, sono-, electro- and long afterglow photo-luminescence were characterized by transmission electron microscopy (TEM). The nanotube morphology was not observed at this stage (Figure 3-2). Figure 3-2a reveals isotropically-distributed crystallographic linear defects. A lamellar anisotropic distribution is also observed in Figure 3-2b. This asymmetry is coherent with the formation of nanotubes by a rolling mechanism [70].

Continuous post-annealing of α -monoclinic nanoparticles was carried out within a temperature range of host phase transformation, i.e. from 573 to 1473 K. A structural polymorphism of $\text{SrAl}_2\text{O}_4:\text{Ce}^{3+}$, Dy^{3+} , Eu^{2+} occurs during the crystallographic arrangement from $\alpha \rightarrow (\beta \rightarrow \gamma)$ phases produced by post-annealing. Reticular displacement vectors were originated during the β -hexagonal crystals growth from linear displacement defects present in the α -phase (Figure 3-2c-e), and in which a hexagonal structure exhibits the light emission polarized through the c -axis.

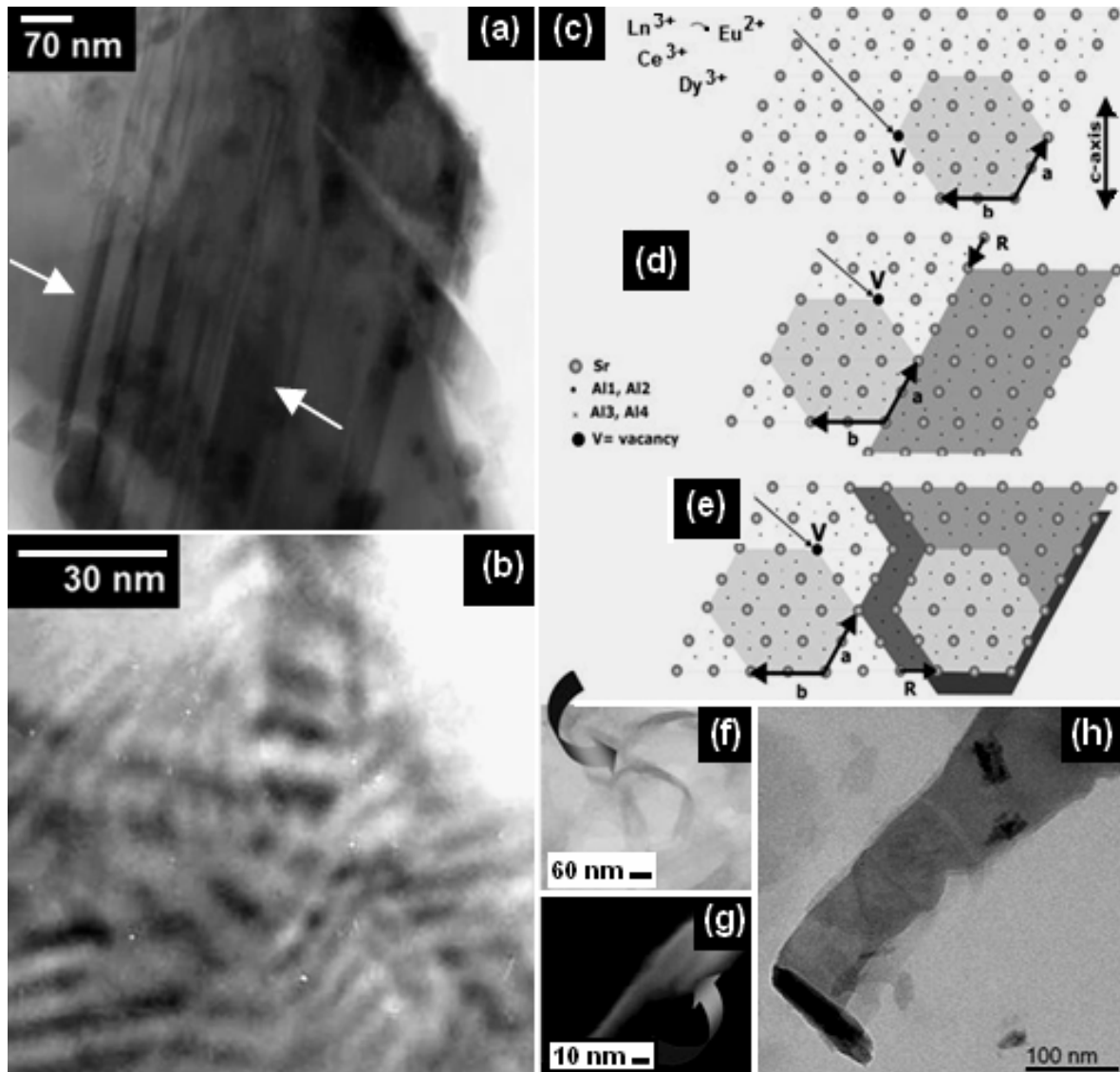


Figure 3-2. TEM image of a precursor α -monoclinic $\text{SrAl}_2\text{O}_4:\text{Ce}^{3+}$, Dy^{3+} , Eu^{2+} isolated nanoparticle with linear lattice defects (arrowed) having a) isotropic distribution, and b) anisotropic lamellar distribution; c-h) crystallographic arrangement and rolling-up mechanism of (α, β) phases $\rightarrow \gamma$ -nanotubes transition under a solid-state synthesis and post-annealing at 1473 K [75].

Continuing to increase the thermal energy, a planar roll-up is evidenced (Figure 3-2f-h), comprising the rolling mechanism of a nanotube due to unstable dangling bonds [70-71]. A structural model based on the crystallographic arrangement of precursor α -monoclinic $\text{SrAl}_2\text{O}_4:\text{Ce}^{3+}, \text{Dy}^{3+}, \text{Eu}^{2+}$ particles with linear lattice defects suggests 1D growing of β -hexagonal phase. These co-doped lanthanide crystals present a linear displacement defect, which formation produces a reticular displacement vector. The Sr^{2+} vacancies produce holes for afterglow photoluminescence when occupied by a lanthanide rare-earth metal, such as $\text{Eu}^{2+}, \text{Dy}^{3+}$ and Ce^{3+} .

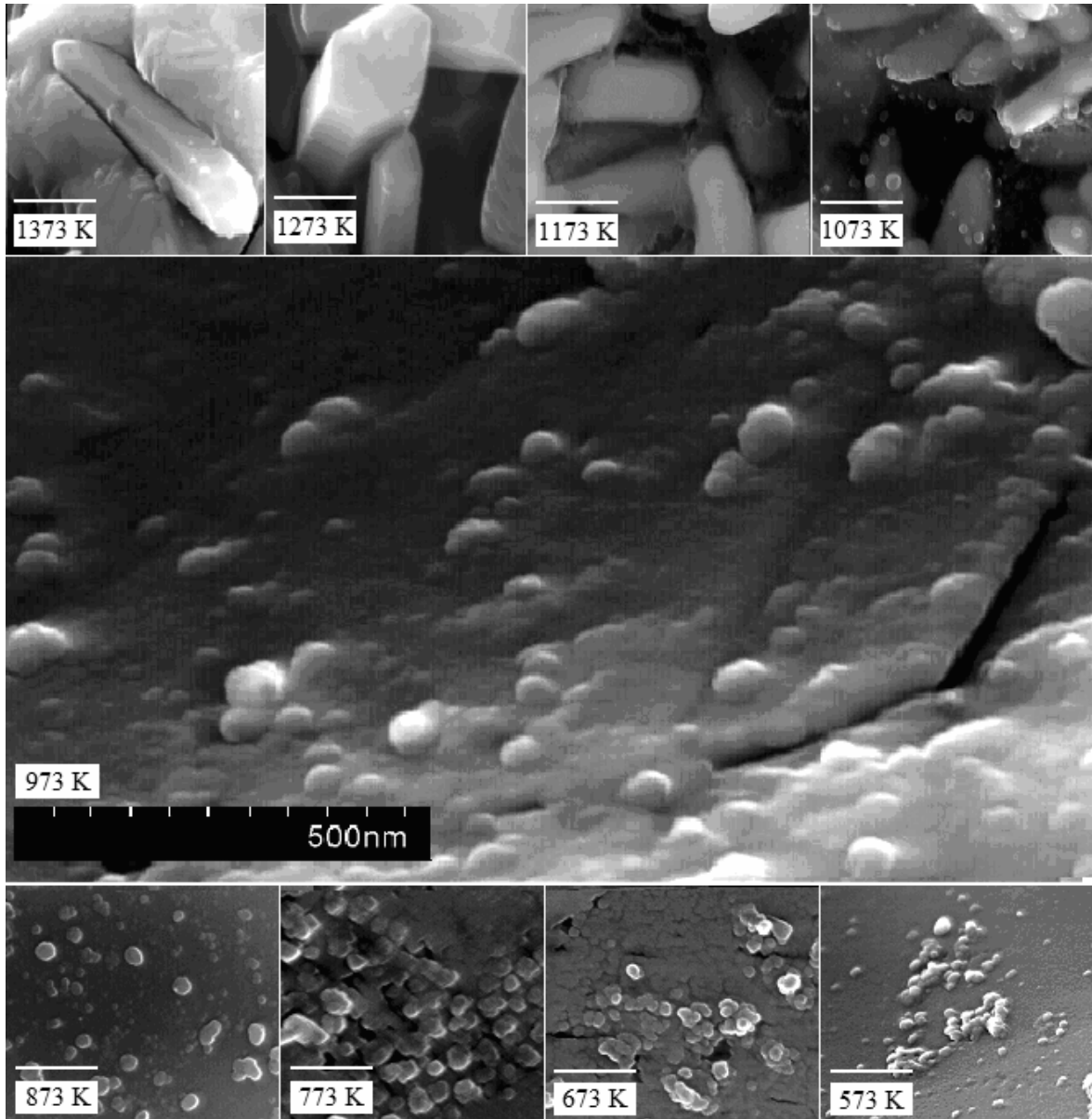


Figure 3-3. SEM analysis of post-annealed $\text{SrAl}_2\text{O}_4:\text{Ce}^{3+}, \text{Dy}^{3+}, \text{Eu}^{2+}$ samples. From 573 to 873 K the α -type present nanoparticles grouped and dispersed (1-D < 70 nm). At 973 K, the limit of phase transformation temperature, the α - β transition was characterized by planar defects and the starting of polymorphic hexagonal phase. From 1073 to 1373 K, the material presents micro and nano crystals with β -type structures. Scale bar= 500 nm.

Figure 3-3 shows morphologies of post-annealed $\text{SrAl}_2\text{O}_4:\text{Ce}^{3+}, \text{Dy}^{3+}, \text{Eu}^{2+}$ from 573 to 1473 Kelvin observed by scanning electron microscopy (SEM). Most representative nanostructure of chemically treated samples showed α -monoclinic spherical nanoparticles predominantly formed above a temperature of about 973 K. On the limit of phase transformation, the α - β transition is characterized by the formation of planar defects and the starting of the polymorphic hexagonal phase growth (Figure 3-4). Over 923 K, the β -hexagonal nanocrystals were observed growing with small lanthanide nanoparticles adhered on the SrAl_2O_4 host surfaces. At the temperature of 1373 K, nanocrystals with preferential hexagonal shape were easily found. The nanotube growth mechanism is favoured by a systematic crystallographic arrangement and rolling-up mechanism involving the host (α, β) phases transformation \rightarrow γ -nanotubes under the post-annealing process.

The effect of post-annealing temperature ($T \geq 923$ K) on crystal structure of $\text{SrAl}_2\text{O}_4:\text{Ce}^{3+}, \text{Dy}^{3+}, \text{Eu}^{2+}$ was examined by X-ray diffraction (XRD) and vibrational spectroscopy (Raman). XRD patterns further indicated that the nanocrystals obtained from 573 to 973 K are α -monoclinic (Figure 3-5). For temperatures higher than 1073 K the nanocrystals consist predominantly of β -hexagonal phase of SrAl_2O_4 , with $\text{Sr}_4\text{Al}_{14}\text{O}_{25}$ being also identified as a secondary phase. Raman spectra of $\text{SrAl}_2\text{O}_4:\text{Ce}^{3+}, \text{Dy}^{3+}, \text{Eu}^{2+}$ presented in Figure 3-6 show significant shifts when passing from α -monoclinic crystal structure before annealing to the high temperature β -hexagonal phase. The structural transformation to γ -nanotubes was evidenced by strong reorganization of covalent bonds during the post-annealing at 1473 Kelvin. In the β -hexagonal phase and γ -nanotubes, the Raman shift at about 464.5 cm^{-1} assigned to the O—Al—O bond-stretching vibrations exhibits higher peak prominence due to the open structure of post-annealed (1473 K) sample, in contrast to the more closed structure of monoclinic particles. Recently, *Cordoncillo-Escribano* [68f] also detected an ubiquitous 465 cm^{-1} band attributed to the bending of O—Al—O bonds in corner-sharing tetrahedral of $\text{Eu}:\text{SrAl}_2\text{O}_4$, indicating that the polymorphs present very closely packed structures. Within the range of about $500\text{--}970 \text{ cm}^{-1}$, the Raman shifts were assigned to the Al—O angle vibrations from the $[\text{AlO}_4]$ rearrangements [43], evidenced in the phase transformation to β -hexagonal and γ -nanotube structures. These neighbouring regions were also assigned by *Kim-Lee* [68g] to the O—Al—O bending mode ($650\text{--}700 \text{ cm}^{-1}$), and Al—O stretching mode ($750\text{--}850 \text{ cm}^{-1}$).

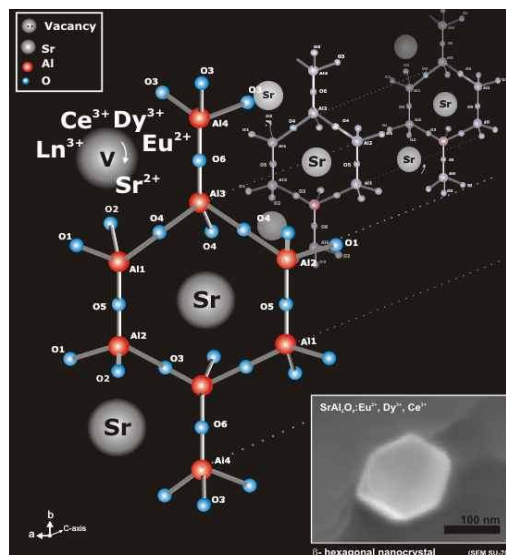


Figure 3-4. Crystallographic arrangement of β -phase after the host phase transformation.

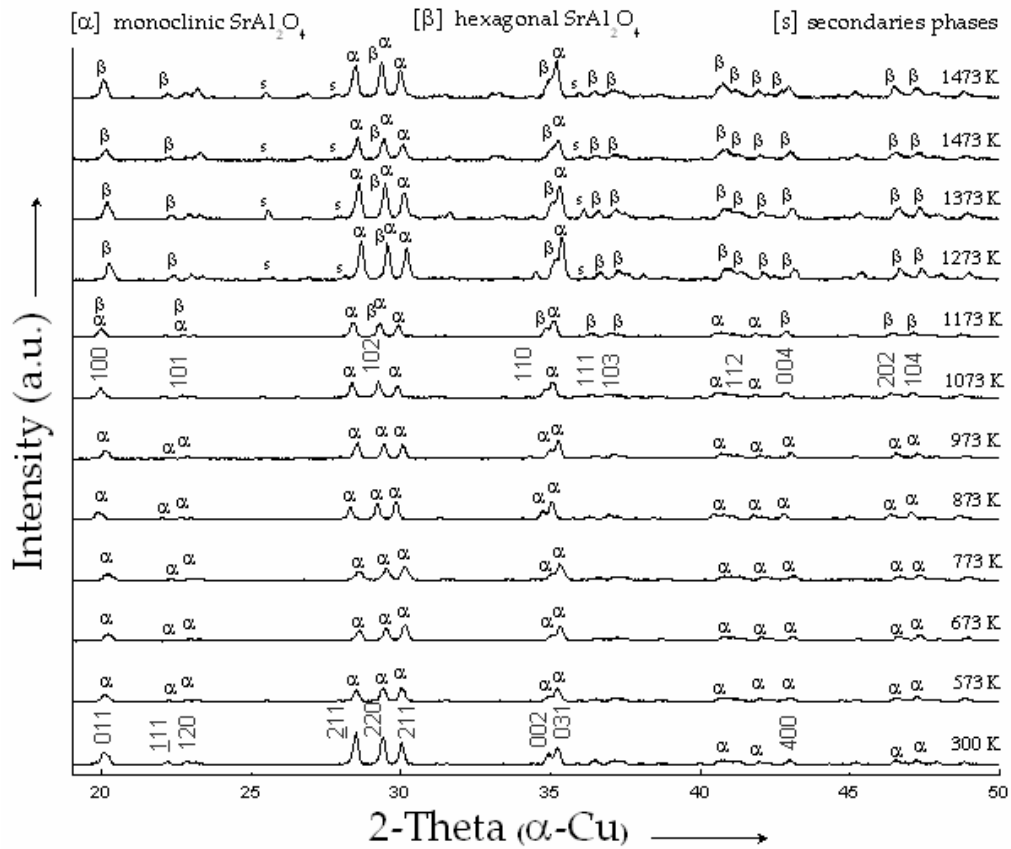


Figure 3-5. Crystallographic evolution of SrAl₂O₄:Ce³⁺, Dy³⁺, Eu²⁺ with post-annealing temperature.

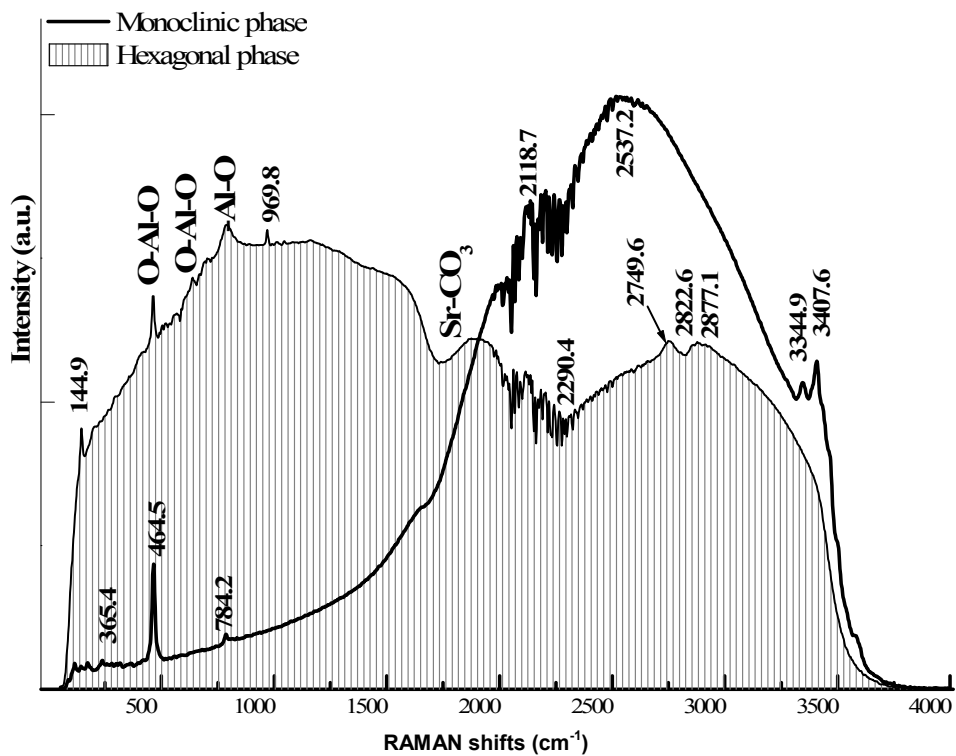


Figure 3-6. Raman spectra of SrAl₂O₄:Ce³⁺, Dy³⁺, Eu²⁺ before and upon post-annealing at 1473 K.

3.3. Luminescent $\text{SrAl}_2\text{O}_4:\text{Ce}^{3+}, \text{Dy}^{3+}, \text{Eu}^{2+}$ nanotube growth

In the following topics, the structural characterization of nanotubes is presented by SEM and TEM techniques. The intercrystalline distances in $\text{SrAl}_2\text{O}_4:\text{Ce}^{3+}, \text{Dy}^{3+}, \text{Eu}^{2+}$ polymorphs were measured by AFM for different temperature rates of post-annealing.

3.3.1. Luminescent nanotubes

Unusually, such post-annealing treatment of $\text{SrAl}_2\text{O}_4:\text{Ce}^{3+}, \text{Dy}^{3+}, \text{Eu}^{2+}$ precursor micro- and nano-particles promotes rolling-up and the formation of γ -nanotubes at $\sim 1273\text{-}1473\text{ K}$ [75]. Nanotubes of 90 nm in diameter and 650 nm in length are shown in SEM (Figure 3-7a-b) and TEM (Figure 3-7c) micrographs. Substantial meso porosity is noticed, resulting from O^{2-} vacancies, typical defects at the 2d sites [25a] and [77]. Energy dispersive X-ray (EDX) spectroscopy indicates the presence of rare-earth elements in heat-treated samples (Figure 3-7b). The values found are coherent with the literature with respect to an Al/O atom ratio in the tetrahedral $[\text{AlO}_4]$, accepting substitutional Sr^{2+} ions in open channels of the reticular crystals.

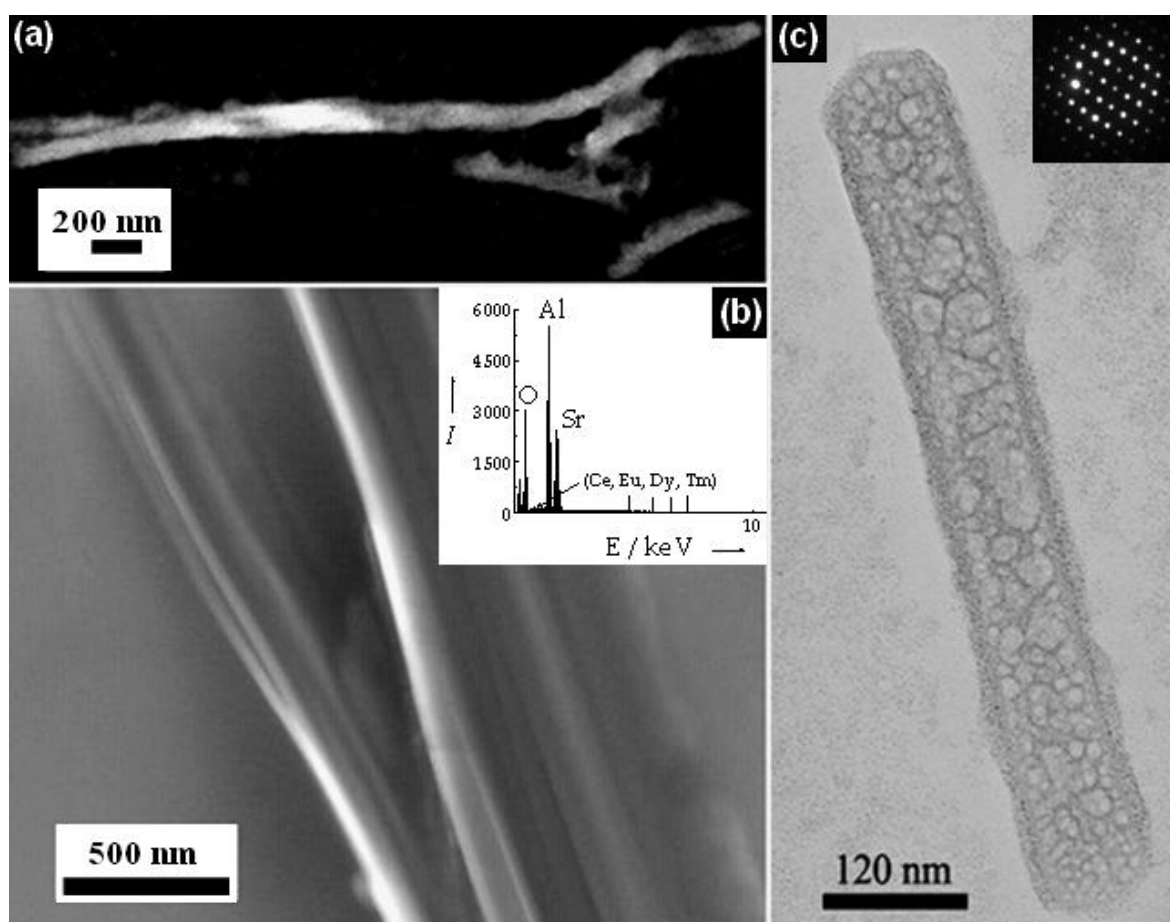


Figure 3-7. SEM and TEM images of luminescent $\text{SrAl}_2\text{O}_4:\text{Ce}^{3+}, \text{Dy}^{3+}, \text{Eu}^{2+}$ nanotubes obtained by solid-state synthesis and post-annealing at a) 1273 K, and b-c) 1473 K; b) EDX spectrum of the γ -nanotube; c) SAED pattern of the nanotube recorded along the $[1\bar{1}0]$ zone axis [75].

The selected area electron diffraction (SAED) pattern in conjunction with the high-resolution TEM (HRTEM) image along the $[1\bar{1}0]$ zone axis (Figure 3-7c) reveals that nanotube is crystalline. The nanotubes characterized by TEM technique showed edge lengths from about 10 nm to less than 1 micron. The nanotubes tended to present most frequent diameters within the range of 50-100 nm and contained very few, if any amorphous impurities, being substantially nanoporous, as shown in Figure 3-7c. Note that host phase transformation of α -monoclinic precursor particles to polymorphic β -hexagonal nanocrystals and γ -nanotubes structures occurs during post-annealing. Figure 3-8a-c are HRTEM images revealing the anti-phase boundaries and lattice spacing of about 0.3 x 0.5 nm of high-temperature phases (Figure 3-8d).

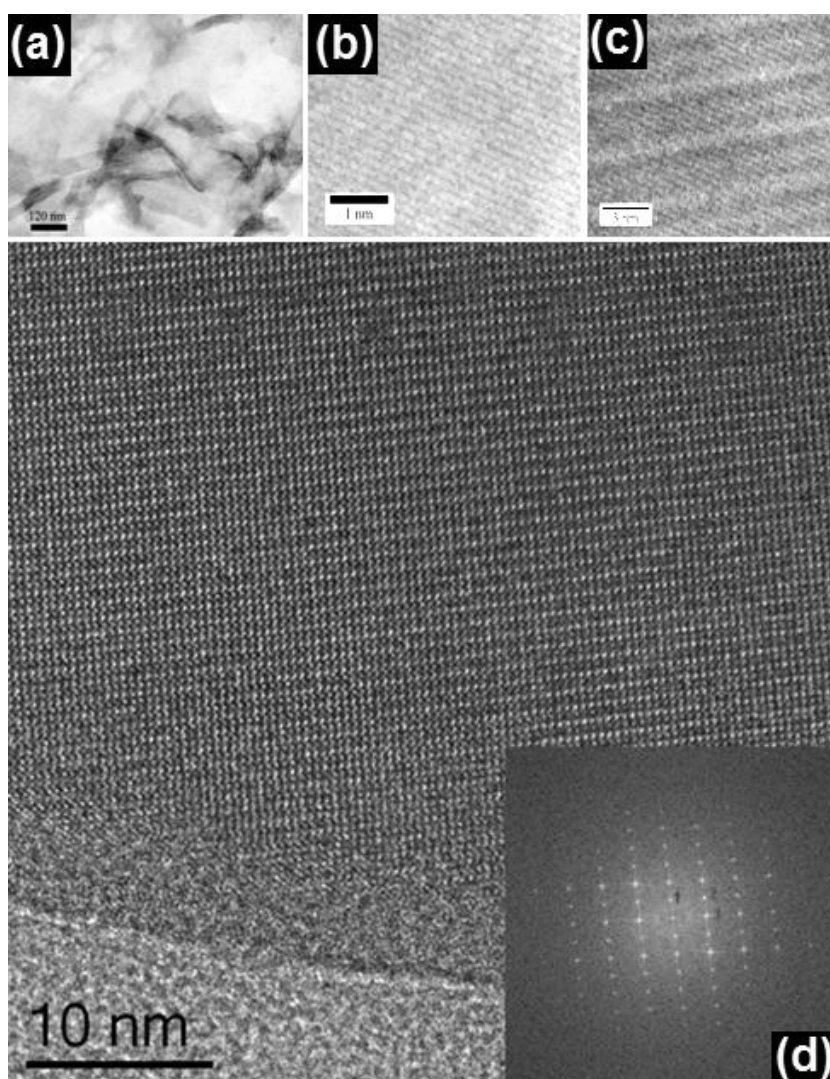


Figure 3-8. a) TEM image of luminescent $\text{SrAl}_2\text{O}_4:\text{Ce}^{3+}, \text{Dy}^{3+}, \text{Eu}^{2+}$ product post-annealed at 1273 K; HRTEM images reveal in b) and c) the anti-phase boundaries; and in d) the crystalline lattice spacing of about 0.3 x 0.5 nm.

3.3.2. Intercrystalline distances of $\text{SrAl}_2\text{O}_4:\text{Ce}^{3+}, \text{Dy}^{3+}, \text{Eu}^{2+}$ polymorphs

Photoluminescent strontium aluminate co-doped with lanthanide ions with preferential one-dimensional was detected by tapping-mode atomic force microscopy (AFM), as depicted in Figure 3-9a. A grain size of $\sim 1\text{-}3\ \mu\text{m}$ and roughness RMS = 180 nm are seen (Figure 3-9b). Correlation between the layer periods with height for different grains is shown in Figure 9b. The average intercrystalline distances were measured by the lattice vectors method with 160 and 80 nm (Figure 3-9c), and were verified by the cross-section profiles (e.g., the A-B cross-section, Figure 3-9d).

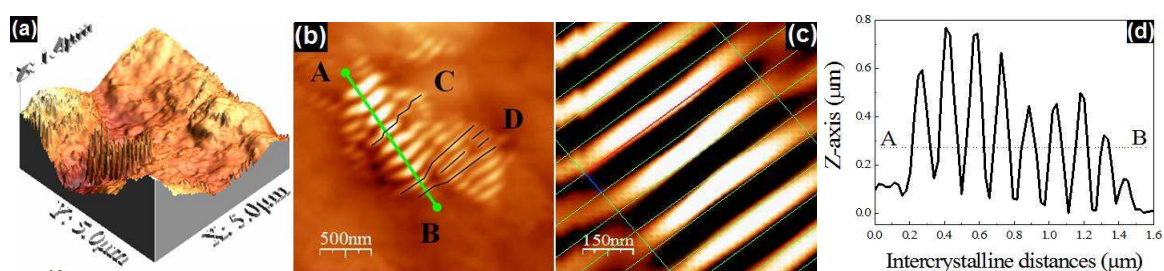
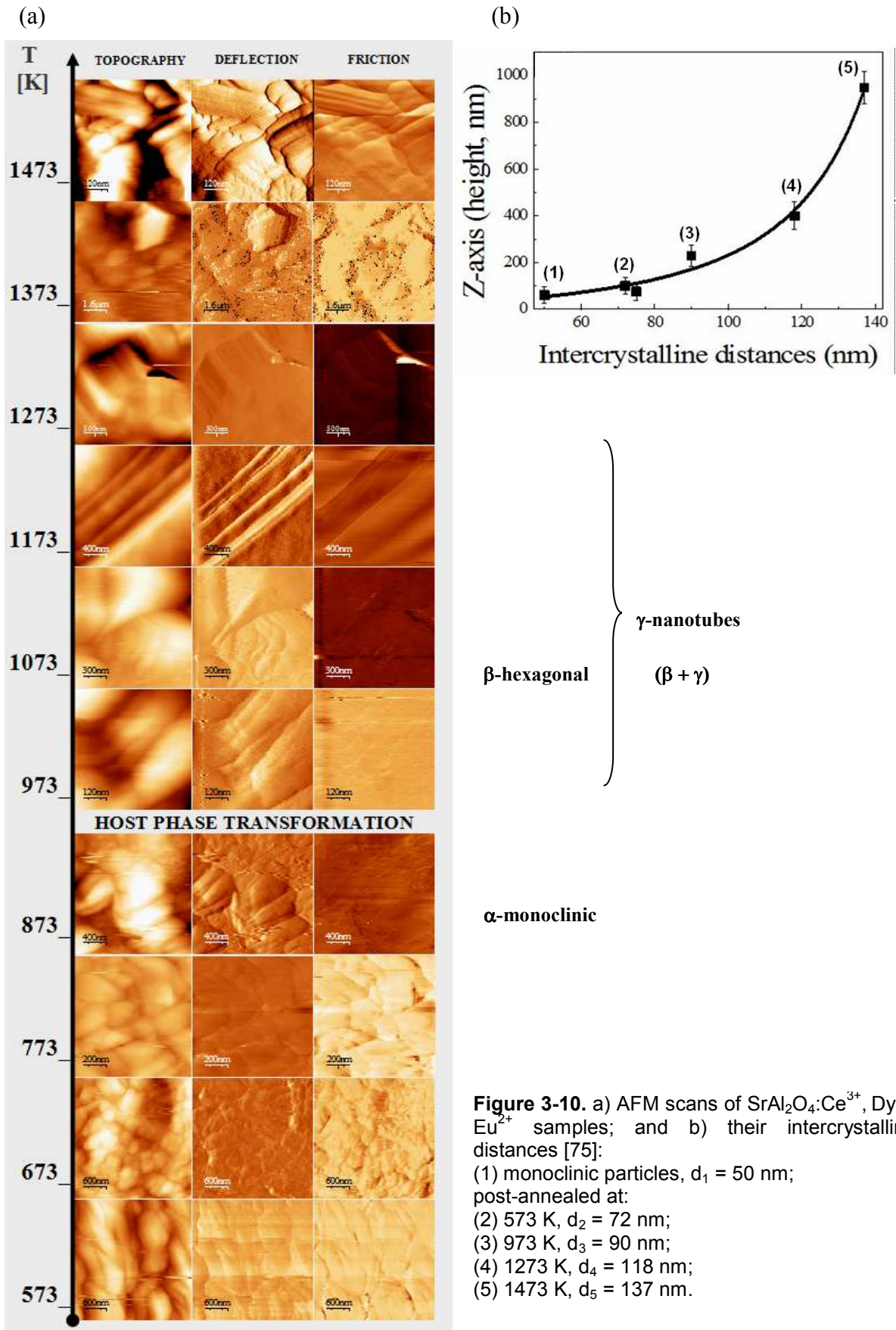


Figure 3-9. AFM analysis of $\text{SrAl}_2\text{O}_4:\text{Ce}^{3+}, \text{Dy}^{3+}, \text{Eu}^{2+}$ in a $5\ \mu\text{m} \times 5\ \mu\text{m}$ scanning area: a) morphology of an orientated thin structure; b) A-B cross-section; c) host lattice vectors $80 \times 500\ \text{nm}$; d) inter-crystalline distances in a A-B cross-section profile [75].

The evolution with temperature (573 to 1473 K) of AFM contact mode morphological analysis along the post-annealing $\text{SrAl}_2\text{O}_4:\text{Ce}^{3+}, \text{Dy}^{3+}, \text{Eu}^{2+}$ and phase transformation is shown in Figure 3-10. Correlating the cross section of the nanocrystals with the evolution of host phase transformation by post-annealing approach, AFM analysis showed an increase of the intercrystalline distances between the nanocrystals, where the luminescent centres (lanthanides) are located. Figure 3-10a shows the AFM scans of as-synthesized $\text{SrAl}_2\text{O}_4:\text{Ce}^{3+}, \text{Dy}^{3+}, \text{Eu}^{2+}$ nanoparticles post-annealed at 573-1473 K. When the polymorphs intercrystalline distances become visible, microscopic techniques can be employed (e.g. AFM/cross section imaging) to measure these distances in different points of a sample. The AFM cross sections of samples were measured to define the average distal series of the host phases. The intercrystalline distances increase substantially from 50, 72, 75, 90, 118 to 137 nm, after the host phase transformation in the row $\alpha \rightarrow \beta \rightarrow \gamma$ (Figure 3-10b). The average intercrystalline distances of the samples presented layer thickness, and height ranging from 50 to 250 nm, and from 80 to 900 nm, respectively, in cross-sectional profiles. These findings support some nanoscale changes of the $\text{SrAl}_2\text{O}_4:\text{Ce}^{3+}, \text{Dy}^{3+}, \text{Eu}^{2+}$ material produced by the post-annealing [75].



PART II — INTERCRYSTALLINE DISTAL-EFFECT

In this part of the chapter, the photoluminescence characterization of grown nanotubes was made by comparing the baseline material with post-annealed samples. The afterglow modifications produced from polymorphism are discussed, and the intercrystalline distal-effect is defined.

3.4. Photoluminescence of α , β and γ -nanotube phases [75]

The optical characteristics of emission, excitation and afterglow lifetime of α , β and γ -nanotube phases are presented in the following topics.

3.4.1. Photoluminescence excitation and emission

The steady-state photoluminescence spectra of the as-synthesized precursor $\text{SrAl}_2\text{O}_4:\text{Ce}^{3+}$, Dy^{3+} , Eu^{2+} micro- and nano-particles exhibited yellow-green light emission (Figure 3-11a, curve a).

Further, the following observations are made:

- The spectrum of α -monoclinic particles is formed by a large Gaussian band between 450 and 650 nm, peaking at 525 nm, which characteristic might be assigned principally to the SrAl_2O_4 host lattice and cerium (III) doping;
- After the post-annealing treatment [74-75], the formation of β -hexagonal phase and γ -nanotubes produces a blue-shift emission peaking at 495 nm, and originates a reduction in the «full width at half maximum», *fwhm*, from as-synthesized nanoparticles, curve a, to post-annealed samples at 1273 and 1473 K, curves b and c, respectively;
- The post-annealing treatment induced the appearance of a low-intensity and structured band in the range 380 to 450 nm, from the Ce^{3+} inter- $[4f^1 \rightarrow 5d^1]$ transitions, peaking at 425 nm;
- The post-annealing treatment induced the appearance a series of straight lines from 570-680 nm ascribed to the co-doping:
 - Eu^{3+} intra- $4f^6$ transitions, $[^5D_0 \rightarrow ^7F_2]$, peaking at 615 nm;
 - Dy^{3+} intra- $4f^9$ transitions, $[^2F_{15/2} \rightarrow ^6F_{11/2}]$ and $[^6H_{15/2} \rightarrow ^4M_{15/2} + ^6P_{7/2}]$, peaking at 578 nm.

The inclusion of the compound onto a ceramic substrate does not produce considerable modifications in the emission features, as shown in Figure 3-11a for the 1273 K- and 1473 K-substrate materials (curves d and e, respectively). Excitation spectra in Figure 3-11b were monitored at the emission peak position at 525 nm for the precursor α -monoclinic particles, β -hexagonal and γ -nanotubes obtained by post-annealing at 1273 and 1473 K (curves a-c), and at 495 nm for the 1273 K- and 1473 K-substrate materials (curves d and e, respectively). The excitation spectrum of the standard α -monoclinic particles displays a large broad band between 270 and 500 nm with, at least, two components at 400 nm and a shoulder at 300 nm. Similarly to what was found for emission analysis (Figure 3-11a), there was a blue-shift in the spectra upon heat treating at 1273 and 1473 K.

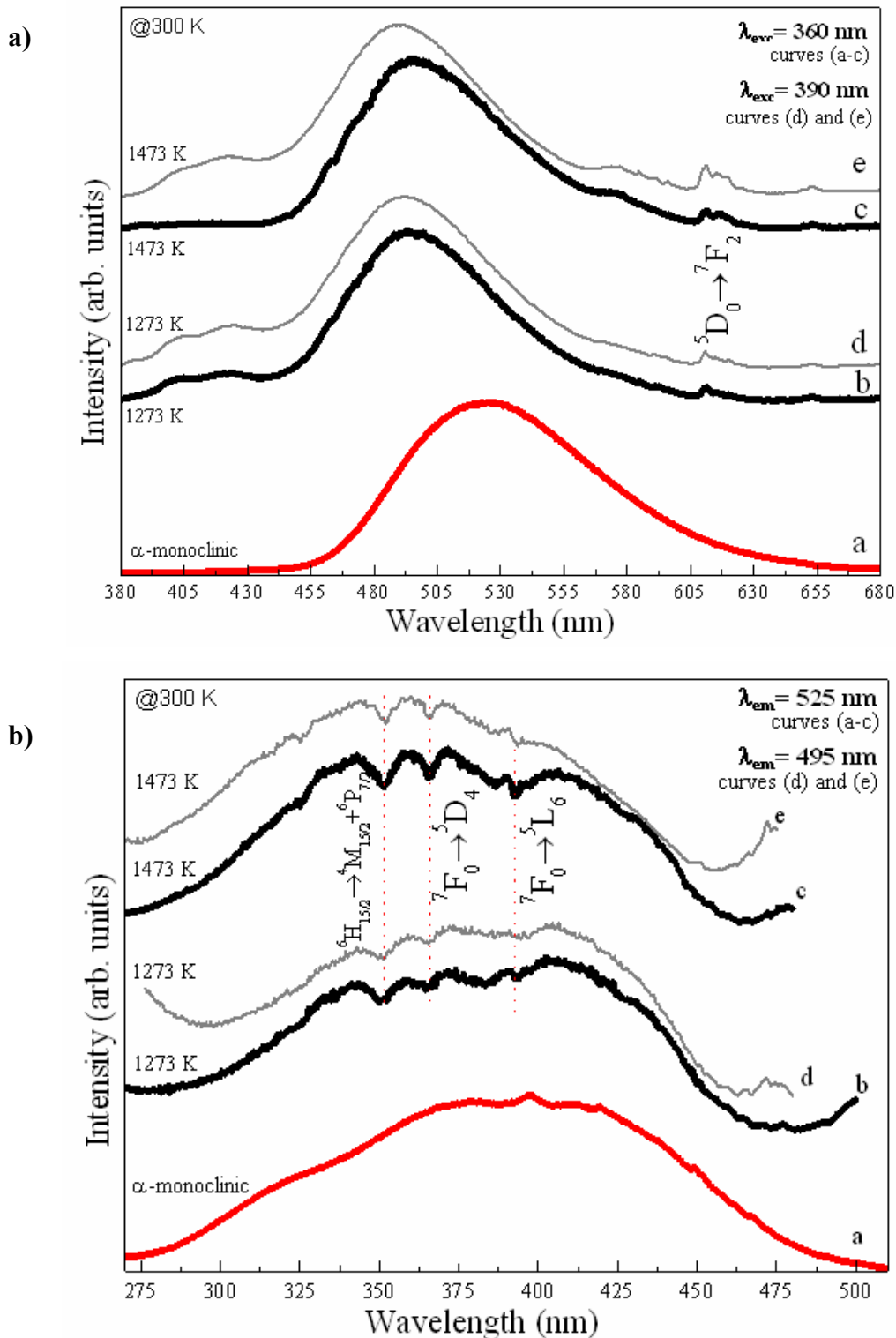


Figure 3-11. a) Emission and b) excitation spectra from steady-state PL spectroscopy of $\text{SrAl}_2\text{O}_4:\text{Ce}^{3+}$, Dy^{3+} , Eu^{2+} : pressed and non-supported samples - curves (a) = α -monoclinic particles; curves (b) and (c) = β -hexagonal and γ -nanotube crystals obtained by post-annealing at 1273 and 1473 K, respectively; pressed samples onto a ceramic substrate - curves (d) and (e) = β -hexagonal and γ -nanotube crystals obtained by post-annealing at 1273 and 1473 K, respectively.

The β -hexagonal and γ -nanotube product obtained by the post-annealing at 1473 K was analysed for emissions as a function of wavelength excitation at 253, 300, 360, 392.5 and 463 nm [75], with a series of f - f and f - d transitions [25], [76] and [77], as shown in Figure 3-12:

- **485-488 nm:** 5d excited states of Ce^{3+} ions, assigned to intra- $4f^1$ transitions, [$^2F_{5/2} \rightarrow ^2F_{7/2}$], and Ce $4f \rightarrow \text{O } 2p$ transitions, in overlap with Dy^{3+} ions, transitions [$^4F_{9/2} \rightarrow ^6H_{15/2}$], and possible emission shifts from $4f^6 5d^1$ to the $4f^7$ configuration of Eu^{2+} ions;
- **578 nm:** Dy intra- $4f^9$ transitions, [$^2F_{15/2} \rightarrow ^6F_{11/2}$] and [$^6H_{15/2} \rightarrow ^4M_{15/2} + ^6P_{7/2}$];
- **600-700 nm:** Eu intra- $4f^6$ transitions [$^5D_0 \rightarrow ^7F_{0-4}$], peaking in different points in thin bands.

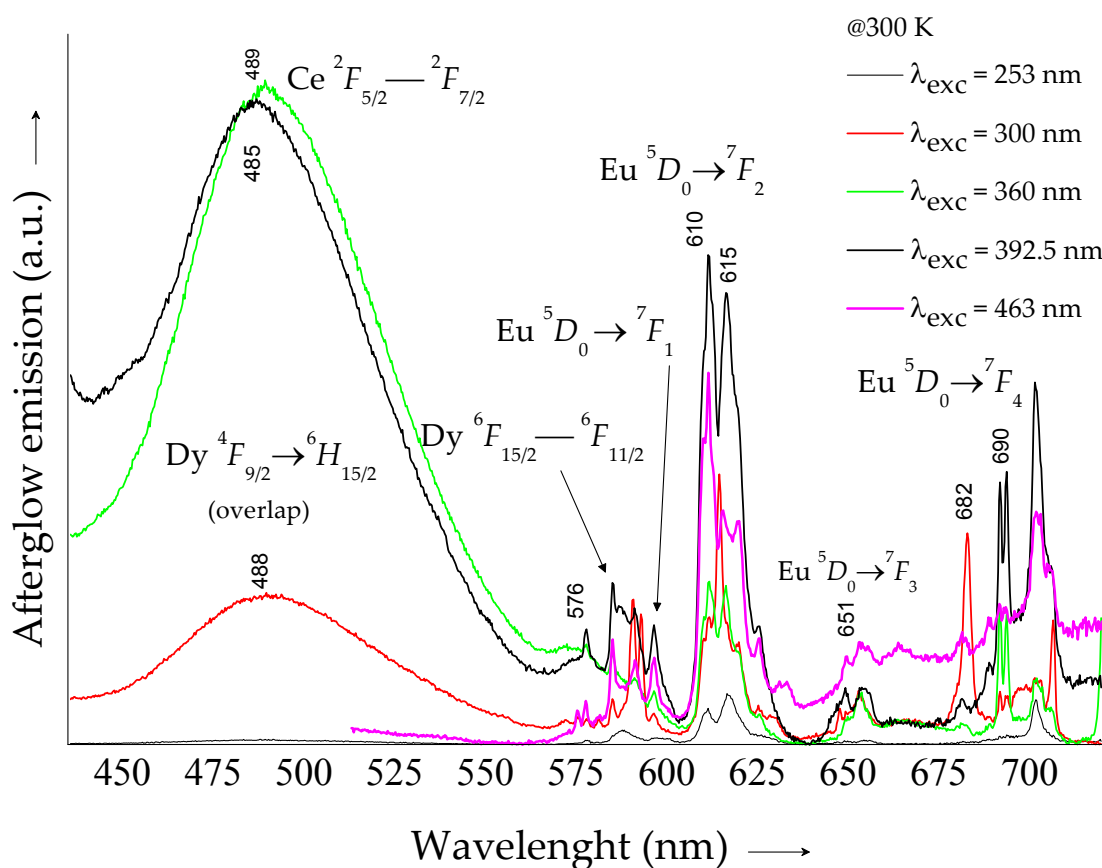


Figure 3-12. Afterglow phenomenon on $\text{SrAl}_2\text{O}_4:\text{Ce}^{3+}, \text{Dy}^{3+}, \text{Eu}^{2+}$ nanotubes by post-annealing at 1473 K: a) photoluminescence emission after excitation at 253, 300, 360, 392.5 and 463 nm showing a series of f - f and f - d transitions [75].

Note that the co-dopants Dy and Eu ions of the $\text{SrAl}_2\text{O}_4:\text{Ce}^{3+}, \text{Dy}^{3+}, \text{Eu}^{2+}$ are co-activators of luminescence, but this material emits with colour appearance peaking at 488 nm. In this case, the function of the co-activators is to produce an overlap of the charge distribution of the neighbouring ions and $4f$ electrons, and additionally with host lattice, contributing for the energy transfer mechanism of persistent luminescence [27c].

3.4.2. Afterglow lifetime

Figure 3-13 shows the afterglow decay patterns of $\text{SrAl}_2\text{O}_4:\text{Ce}^{3+}, \text{Dy}^{3+}, \text{Eu}^{2+}$ β -nanocrystals and γ -nanotubes at room temperature (300 K), where I is the phosphorescence intensity at any time ' t ' after switching off the excitation illumination for the exponential (1-order) decay components with maximum initial intensity, I_0 , among the phases. The β -nanocrystal and γ -nanotube high temperature phases show an abnormal stabilization with short decay time above 0.5 ms to lower limit of visibility of dark-adapted eye detection. This characteristic can be associated with defects of the oxygen ion at the 2d site [76-77], where Ce^{3+} and Ln^{3+} ions substitute some Sr^{2+} sites, and which vacancies are necessarily introduced owing to charge compensation [77]. Compared to the long-lived luminescence of α -monoclinic structures [30], [32], [76], [77] and [79], the afterglow decay curves of $\text{SrAl}_2\text{O}_4:\text{Ce}^{3+}, \text{Dy}^{3+}, \text{Eu}^{2+}$ nanotubes and β -hexagonal phase structures reveal modifications in light emission for shorter persistent luminescence (Figure 3-13).

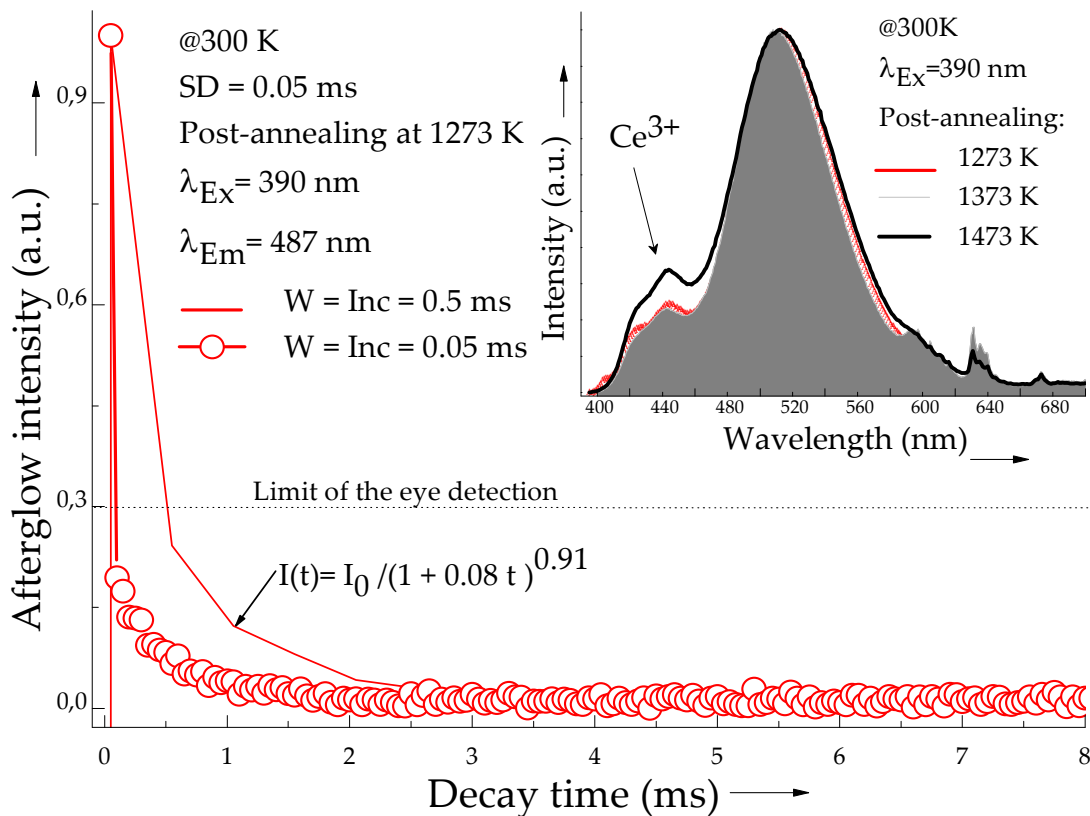


Figure 3-13. Afterglow decay curve of polymorphic $\text{SrAl}_2\text{O}_4:\text{Ce}^{3+}, \text{Dy}^{3+}, \text{Eu}^{2+}$ β -hexagonal and γ -nanotubes by post-annealing. In detail: emission spectra after post-annealing at 1273, 1373 and 1473 K onto the ceramic substrate; the large bands correspond to the Ce^{3+} electronic transitions in the host lattice.

Time-resolved emission (TRE) spectra of all the compounds were acquired at different starting delay times in non-stationary mode (Figure 3-14). The spectra of the as-synthesized nanoparticles shows a large broad band, whose maximum peak position is deviated to blue and display a narrower *fwhm* value, when compared to the steady-state emission spectrum (Figure 3-11a, curve a). Apart from an intensity decrease the emission features does not depend on the selected starting delay in the time range 0.05 to 200.00 ms.

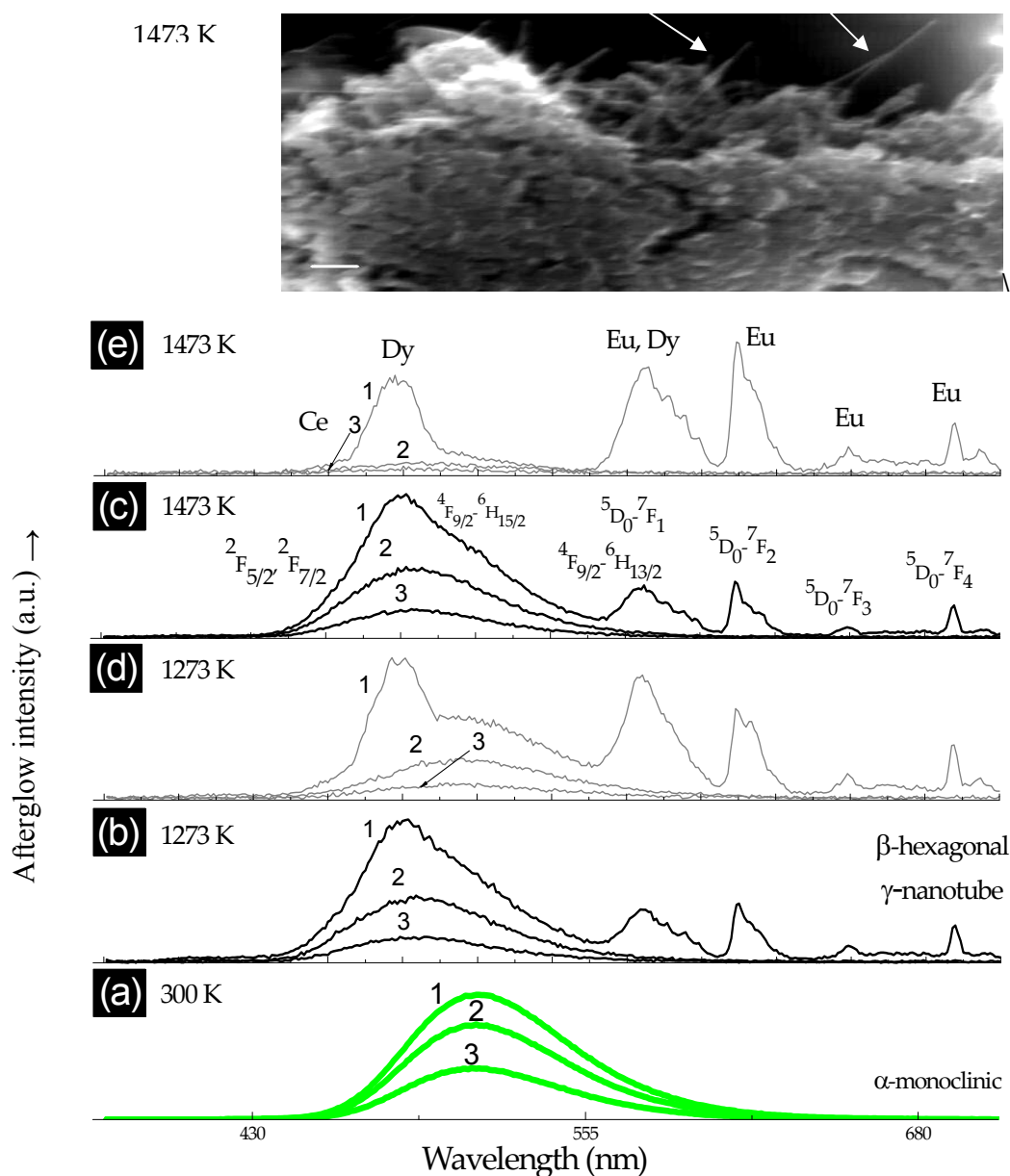


Figure 3-14. Time-resolved emission spectra of the $\text{SrAl}_2\text{O}_4:\text{Ce}^{3+}$, Dy^{3+} , Eu^{2+} samples acquired with starting delays of (1) 0.05 ms, (2) 50.00 ms and (3) 200.00 ms, using an integration window of 20.00 ms and excited at 360 nm: α -monoclinic particles (a); non-supported pellets of β -hexagonal and γ -nanotubes crystals (b) and (c); pressed pellets deposited onto a ceramic substrate (d) and (e). The arrowhead thin structure with preferential 1D-growth indicates the formation of $\text{SrAl}_2\text{O}_4:\text{Ce}^{3+}$, Dy^{3+} , Eu^{2+} nanotubes at 1473 K; scale bar = 300 nm.

The emission features of the post-annealed β -hexagonal phase and γ -nanotubes are composed of a large broad band superimposed on a series of shorter-lived straight lines ascribed to the Eu^{3+} intra- $4f^6$ [$^5D_0 \rightarrow ^7F_{0-4}$] transitions and to the Dy^{3+} intra- $4f^9$ [$^4F_{9/2} \rightarrow ^6H_{15/2, 13/2}$] transitions (most evident for the compound heated at 1473 K), Figure 3-14, curves b-e. The Ce^{3+} $f-d$ emission dominates between the allowed transitions from the lowest $5d$ -level to the [$^2F_{5/2}$] and [$^2F_{7/2}$] states of the $4f$ -configuration. For starting delays in the interval 50.00 to 200.00 ms, only the large broad band could be observed, whose energy and *fwhm* is independent of the starting delay.

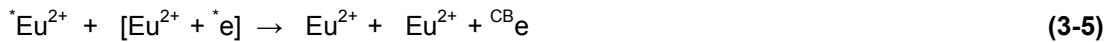
The calculated lifetime variation was estimated (Prof. Dr. Luís D. Carlos and Prof. Dr. Maria R. André from Physics Department, University of Aveiro) from the relation of the intensity of maximum peak position in TRE spectra (Figure 3-14), measured at starting delays of 0.05 ms ($I_{0.05}$) and at 200.00 ms (I_{200}). **For the α -monoclinic particles and post-annealed β -hexagonal and γ -nanotubes crystals, the results of $I_{0.05}/I_{200}$ are 0.4 (α -particles) and 0.15 (β -, γ - crystals) reveal a decrease in the lifetime scale by the post-annealing.**

3.5. Afterglow modifications from polymorphism

The results presented in the 3.4 section showed that presence of cerium (III), dysprosium (III) and europium (II) lanthanide elements elucidated all luminescence emission characteristics in $5d$ states of these ions, and that occur when trivalent ions Ln^{3+} captures the excited electron in the $4f$ shell between the ($4f^n$) and ($4f^{n-1}-5d$) configurations of the divalent lanthanide ion Ln^{2+} [23f]. However, the modification produced on the afterglow phenomenon from α -monoclinic phase transition to β -hexagonal and γ -nanotube of the SrAl_2O_4 host lattice (bandgap of 6.5 eV) is not yet elucidated. It was also observed that in addition to the Sr^{2+} vacancies (electrochemical potential $\text{Sr}/\text{Sr}^{2+} = -2.89$ eV) created by the post-annealing, a lot of O^{2-} vacancies were produced because all β -hexagonal and γ -nanotube samples were sintered in air atmosphere. Such high ionic reactivity vacancies modulate the electronic states that perturbed electronic bands, dislocating the luminescence peaks from 525 to 488 nm.

3.5.1. Trap model of energy transfer mechanism

From the conduction band ($^{\text{CB}}e$) mechanism [23f], [25a] and [78], the photoluminescence emission depends of the photon numbers in emission, absorption and traps. A hole trap model of $\text{SrAl}_2\text{O}_4:\text{Ce}^{3+}$, Dy^{3+} , Eu^{2+} nanomaterial with lanthanide ions (re)trapping, (re)combining for luminescence emission is showed in Figure 3-15. In this conduction band of excited states, vacancies and impurities serve as hole traps, and the excited electrons are left as quenching centres (e.g. Eu^{2+} , as [$\text{Eu}^{2+} + ^*e$]). The excited states of Ce^{3+} , Dy^{3+} and Eu^{2+} ions, ($^*\text{Ce}^{3+}$), ($^*\text{Dy}^{3+}$) and ($^*\text{Eu}^{2+}$), return to their ground state via a radiative and non-radiative energy transfer to the [$\text{Ce}^{3+} + ^*e$], [$\text{Dy}^{3+} + ^*e$] and [$\text{Eu}^{2+} + ^*e$], and centres resulting in the release of the trapped electrons to the conduction band ($^{\text{CB}}e$), as expressed from Equations (3-3) to (3-5).



The electrons in the conduction band (^{CB}e) can be re-trapped by other Ce^{3+} , Dy^{3+} and Eu^{2+} ions, and recombine with the holes trapped at Ln^{3+} sites. The quenching mechanism by energy transfer may occur via cross relaxation between $^*Ce^{3+}$ and $[Ce^{3+} + ^*e]$ centres, for example. Cross relaxation takes place via the energy of donors and acceptors pairs

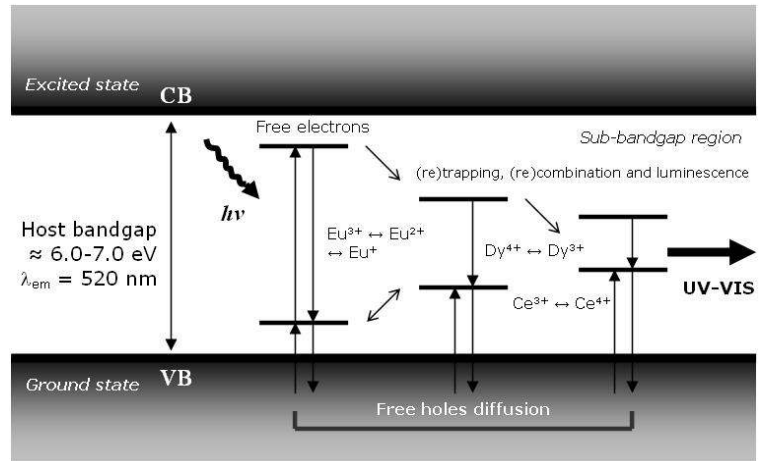


Figure 3-15. Representation of the conduction band of SrAl₂O₄:Ce³⁺, Dy³⁺, Eu²⁺ polymorphs.

(DAPs) existing in the crystal lattices or the energy migration among the donors and acceptors. After pulsed excitation, a number of electrons are promoted into the conduction band resulting in the population of the trap. The emission occurs from cerium, dysprosium and europium ions in an excited state (as Eu^{3+} , Dy^{4+} and Ce^{4+}) after losing one electron.

3.5.2. Spatial separation of DAPs

Let us now consider the energy transfer that occurs only locally due a spatial separation of DAPs. As suggested by *Blasse* [78], the average separation between the (co)activators respects to a critical distance of energy transfer at the interatomic scale. The critical distance of energy transfer from lanthanide ions is defined as the distance for which the probability of transfer equals the probability of radiative emission of these ions. The host α -SrAl₂O₄ phase transformation to β -hexagonal and γ -nanotube occurs with a decrease of radiative luminescence due to a decreasing number of traps occupied. Besides, the electrons in the conduction band can be re-trapped by other Eu^{2+} , Dy^{3+} and Ce^{3+} ions, or recombined with the holes trapped at lanthanide sites, this energy transfer is not done so easily due to the large separation of DAPs. Consequently, the luminescence emission of SrAl₂O₄:Eu²⁺, Dy³⁺, Ce³⁺ β -hexagonal and γ -nanotube must be considered from a conduction band mechanism under a significant increase of the intercrystalline distances between crystals after the host lattice had been strongly changed.

3.6. Intercrystalline distal-effect on the afterglow phenomenon

Herein, according to experimental results reported before, the «**intercrystalline distal-effect**», d , is defined as a geometrical influence of the crystalline nanoarchitecture (morphology, size, shape and distribution of crystals) on the afterglow luminescence phenomenon [75], detected by the crystalline phase transformation of the host lattice.

The intercrystalline distal-effect can be of two types:

- i) intercrystalline of one-phosphor;
- ii) intercrystalline mixture-phosphor.

The former refers to crystallization effects between particles of the same phosphor, while the latter refers to the crystallization effects between dissimilar phosphor particles. It follows from these definitions that a single component phosphor crystals can only display one-phosphor intercrystalline distal effect, while a multi component phosphor crystal can exhibit one or both of these phenomena. At nanoscale luminescence field, dependence of the crystal sites where the luminescent centres are located has been identified as a possible mechanism affecting the charging transfer between (co)activators. The arrangement of metal rare-earth nanoparticles adhered in crystals surface and host lattice produces a light emission inversely proportional to the crystalline distances between the donor-acceptor pairs (DAPs), complementary to the atomic scale. According to *Gribkovskii* [25a], a theoretical relation covering to the interatomic distance parameter on the dependence of the recombination time is given by the distance between the donor-acceptor pairs, Equation (3-6):

$$1/\tau(r_n) = [1/\tau(0)] \exp(-2r/a_B) \quad (3-6)$$

where τ is the lifetime, r_n is the interatomic distance between the donor and the acceptor of n^{th} pair, and a_B is the Bohr radius of the impurity. Empirically, the DAPs and intercrystalline host distances were never been exposed before as a nanoscale factor of the luminescence performance. This physical parameter can be responsible and prevails over the interatomic distance effects on the luminescence, because the spatial limitation for energy transfer is exceedingly larger. Owing to the dependence of transition probabilities on intercrystals, the DAP luminescence spectrum can be deformed and shifted toward short wavelengths and emission intensity with crystal phase transformation. The intercrystalline distance between luminescent centres can be measured by microscopic techniques (e.g. AFM, TEM or SEM), in different points of a sample. Substituting r_n by d at nanoscale in Equation (3-6), the intercrystalline distal-effect is defined as in Eq. (3-7):

$$1/\tau(d) = [1/\tau(0)] \exp(-2d/a_B) \quad (3-7)$$

where d is the intercrystalline distance between the donor and the acceptor of n^{th} pair, given a DAPs intercrystalline relation between the lifetime scale changes by the host phase transformation. This relation can be compared between the lifetime scales for diverse samples, for example upon

different post-annealing treatments. The total distal-effect on the afterglow phenomenon produced by the stable phase transformation for a luminescent material must be constant, and are defined as in Equation (3-8):

$$1/\tau (d) \rightarrow \text{constant} \quad (3-8)$$

where the crystallographic stabilization results in a constant value of the intercrystalline distances. Considering the crystal phase on the afterglow rise and decay, the rate for energy transfer depends more strongly on the intercrystalline distance between divalent/trivalent ions.

Intercrystalline distal-effect in polymorphism

The results from the crystallography of host phases (Figure 3-6), the decay time (Figure 3-13), and the distal distribution measured by AFM (Figure 3-10) give clear evidences of the intercrystalline distal-effect on the afterglow phenomenon in $\text{SrAl}_2\text{O}_4:\text{Ce}^{3+}, \text{Dy}^{3+}, \text{Eu}^{2+}$ polymorphs. During the post-annealing, an anisotropic formation of the SrAl_2O_4 host lattice over temperature of phase transformation (~ 923 K) produces the nucleation of β -hexagonal nanocrystals and γ -nanotubes. The average distance between the crystals with preferential hexagonal morphology systematically increased upon the host phase transformation. This progressive increase of the intercrystalline distances occurred concomitantly with a decrease of lifetime scale resulted in a transition from persistent phosphorescence to fluorescence (Figure 3-16). The main intercrystalline effects are systematized in the Table 3-1.

Table 3-1. Intercrystalline distal-effect on the afterglow phenomenon in $\text{SrAl}_2\text{O}_4:\text{Ce}^{3+}, \text{Dy}^{3+}, \text{Eu}^{2+}$.

Intercrystalline effects	Qualitative example	Luminescence performance	Applied technique	Values
Host lattice	SrAl_2O_4 phase transformation	Reduction of the host lattice energy absorption mechanism and bandgap (eV) upon host phase transformation	XRD AFM SEM TEM	From α to β - and γ - types
Distances	Intercrystalline distances of DAPs in the γ - β -types $\gg \gg \alpha$ -type	Reduction of the energy transfer mechanism between DAPs by the spatial separation larger than the critical distance of energy transfer at the atomic scale (nm)	AFM TEM SEM	Figure 3-10: increase of the intercrystalline distances from 50 nm (α -monoclinic) to 137 nm (β -hexagonal and γ -nanotube phases)
Afterglow lifetime	τ (α -type) $\gg \gg \tau$ (γ - β -type)	Reduction of the lifetime scale on the afterglow phenomenon	Steady-state TRE Lifetime	Reduction of the $I_{0.05}/I_{200.00}$ ratio from 0.4 (α -monoclinic) to 0.15 (β -hexagonal and γ -nanotube phases)

The thermal energy promotes ionic diffusion and arrangement of β - nanocrystals and γ -nanotubes in a disordered nanoarchitecture, increasing the intercrystalline distances and decreasing the energy transferred intercrystals between the DAPs. **The intercrystalline distances of the α - α phase are lower than β - β phase (hexagonal) co-existent with γ -nanotubes (β - γ).** The DAPs physical limitation for electrons (de)trapping with a simultaneous establishment of the reduced free energy of the system by formation of nanocrystals are two factors associated to the

luminescence decay reported in this thesis. Qualitative performance of $\text{SrAl}_2\text{O}_4:\text{Ce}^{3+}$, Dy^{3+} , Eu^{2+} polymorphs by the host phase transformation during the afterglow phenomenon reveals an increase of $d_{(\alpha-\alpha)} < d_{(\beta-\gamma)} < d_{(\beta-\beta)}$ distal series, elucidating a previous concept [25a] and [77] for the alterations from the phosphorescence to fluorescence. The energy transferred between DAPs has been strongly reduced by the weak interaction between these luminescent centres with a physical limitation for electrons (de)trapping and (re)combining during the spatial separation of DAPs after host phase transformation upon post-annealing.

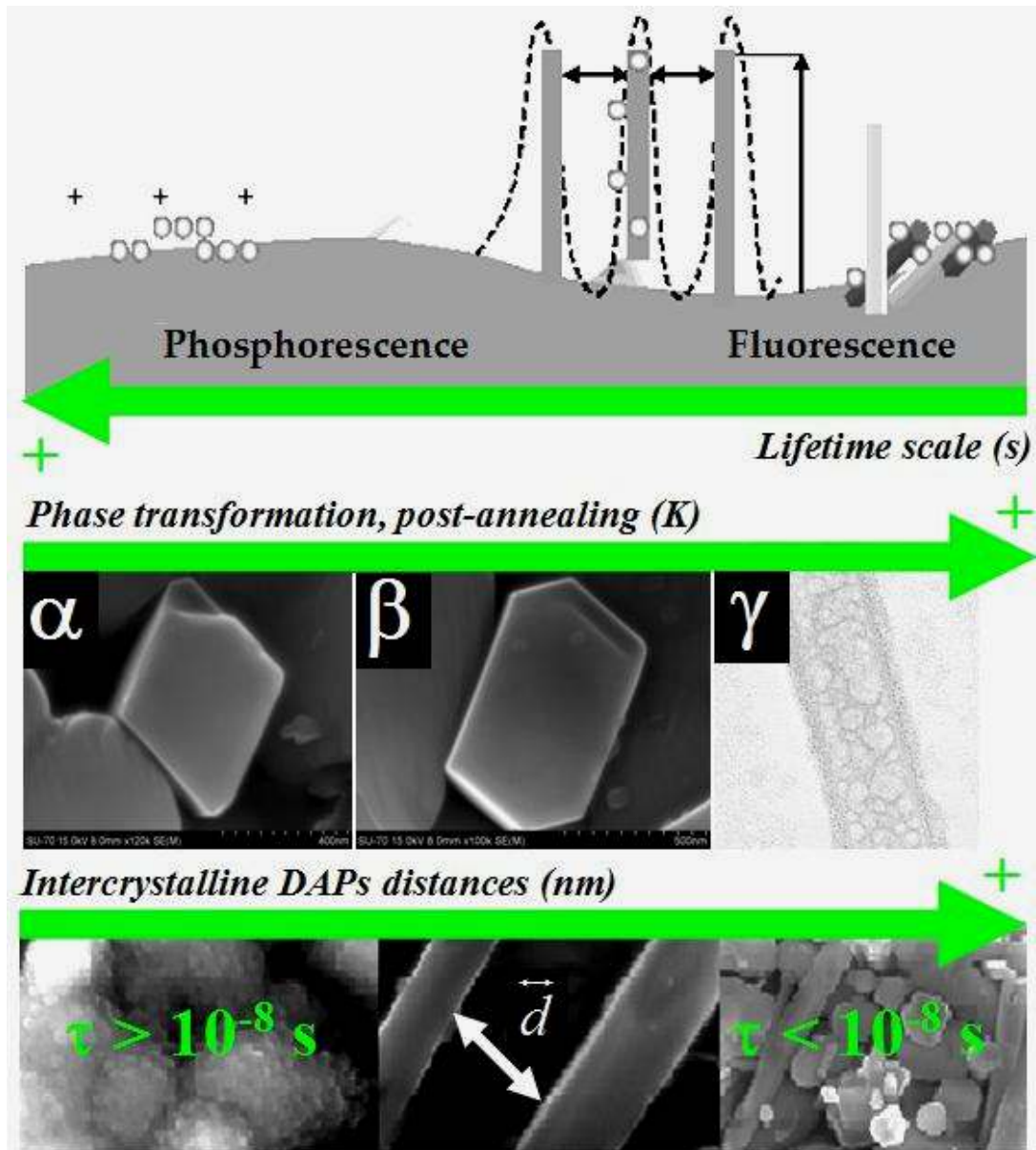


Figure 3-16. Intercrystalline distal-effect on the afterglow phenomenon performed to $\text{SrAl}_2\text{O}_4:\text{Ce}^{3+}$, Dy^{3+} , Eu^{2+} in α -monoclinic particles, β -hexagonal and γ -nanotubes crystals [75].

3.7. Conclusion

Luminescent $\text{SrAl}_2\text{O}_4:\text{Ce}^{3+}$, Dy^{3+} , Eu^{2+} nanotubes were obtained by solid-state reaction and post-annealing of precursor micro- and nano-particles (baseline material) presenting planar defects that facilitate the roll-up mechanism. The nanotubes formation occurred during the nanocrystals growth with hexagonal morphology as a secondary phase at temperatures in the range of 1273-1473 Kelvin. The combination of the steady-state and time-resolved emission measurements indicates alterations in the emission shifts and lifetime scale after the heat treatment. The intercrystalline distal-effect was defined and performed to $\text{SrAl}_2\text{O}_4:\text{Ce}^{3+}$, Dy^{3+} , Eu^{2+} polymorphs from the nanotubular structure growth. The investigation of this effect on the afterglow phenomenon can be extended to other persistent luminescent materials to further clarify their changes from phosphorescence to fluorescence. The control of luminescent nanotube growth can find many applications in nanotechnology, such as optical devices, biosensors and afterglow-in-the-dark technologies. ■

Chapter 4

Luminescent $\text{SrAl}_2\text{O}_4:\text{Ce}^{3+}, \text{Dy}^{3+}, \text{Eu}^{2+}$ nanowires and nanorods

The present work reports a method for the synthesis of single-crystalline luminescent strontium aluminate nanowires and nanorods doped with cerium (III) and lanthanide co-doped, $\text{SrAl}_2\text{O}_4:\text{Ce}^{3+}, \text{Dy}^{3+}, \text{Eu}^{2+}$, by using mechanical ultrasonic vibrations at a frequency > 16 kHz. These new optical multifunctional nanostructures were characterized by XRD, HR-TEM, SEM, EDX and PL spectroscopy. The nanowires and nanorods with diameters of 200–500 nm and aspect ratios from 3 to 300 show a broad emission band at 525 nm and an ultraviolet peak at around 52 nm for an excitation at 320 nm. These one-dimension nanostructures with persistent luminescence are useful for long afterglow applications. Furthermore, they may find many applications in luminescent devices, electrical, ferroelectrics, magnetic and biological systems, namely when nanofunctionalized.

Key-words: solid-state reactions, nanowire, nanorod, strontium aluminate, lanthanide.

4.1. Formation of SrAl₂O₄ nanowires and nanorods

Inorganic one-dimension (1D) nanostructures of nanotubes, nanowires and nanorods have been investigated since the first detection of carbon nanotubes in the 90s [69]. This is a timely topic for the development of new linear-shaped nanomaterials for advanced applications, such as in optoelectronics, biomedical devices, solar cells, biosensors, etc.

The nomenclature of nanowires and/or nanorods is derived from the aspect ratio between the diameter and length at a nanometre scale [80]. The term nanowires refers to any elongated material, conductor, semiconductor or superconductor, in which at least one transverse dimension is less than 500 nm, and preferably less than 100 nm, and aspect ratio is greater than 10, preferably greater than 50-100. The term nanorod refers to any elongated material, conductor, semiconductor or superconductor, similar to a nanowire, but presents smaller aspect ratios in comparison to nanowires. Unlike nanotubes, nanowires and/or nanorods do not present any hole along the longitudinal structure.

This chapter reports on the development of new luminescent nanomaterials in the form of nanowires and/or nanorods, more specifically, strontium aluminate lanthanide co-doped with persistent luminescence. The strontium aluminate doped with rare earth metals has been investigated with great interest worldwide, both in terms of synthesis (e.g. solid-state reaction, sol-gel, co-precipitation, pyrolysis, combustion or detonation methods [76, 77, 79]), both aiming at the improvement of their optical luminescence properties. However, it is clear that many of their potential correlated with the morphology has not been explored so far, since only in 1996 the first SrAl₂O₄:Eu²⁺, Dy³⁺ was reported by *Nemoto et al* [79].

The first nanotubes and nanorods of strontium aluminate, SrAl₂O₄, synthesized via hydrothermal and post-annealing approach were reported in 2006 by *Ye et al* [70], but these nanorods are not doped with lanthanides. In the area of luminescence, the formation of nanowires and/or nanorods doped with rare earths metals has been investigated for various oxides with the formula Ln₂O₃ (Ln is La, Ce, Pr, Nd, Pm, Sm, Eu, Gd, Tb, Dy, Ho, Er, Yb, Tm or Lu), among which are Ga₂O₃ and Eu₂O₃. In recent years, nanosized CeO₂-shaped nanowires, nanorods and nanoparticles also have to be prepared by various synthesis techniques [81]. More specifically, the first synthesis of luminescent SrAl₂O₄:Eu²⁺, Dy³⁺ nanowires was performed in 2008 by a combustion process [82].

Homologue oxides, as aluminium-magnesium spinel (MgAl₂O₄) in the form of nanotubes, nanowires and nanorods; the magnesium borate, or MgO, or Al₂O₃ nanowires were usually synthesized by chemical vapour deposition (CVD) [83-84]. Aiming at large-scale applications, magnesium oxide nanorods were used as starting material for the manufacture of new superconductor composite nanorods, and have been nanofunctionalized with controlled parallel and perpendicular orientations. Prior art also reports the production of micro and nano spherical CaAl₂O₄:Ce³⁺, and also doped with other rare earths (e.g. Eu²⁺, Dy³⁺) [85]. Luminescence of Eu²⁺ doped SrAl₂O₄ in the green region (450-520 nm), as well as their counterparts oxides of base

metals, such as CaAl_2O_4 , MgAl_2O_4 and BaAl_2O_4 , doped with Eu^{2+} and other lanthanide ions has been previously documented [86], but aluminates doped with Ce (III), specifically in the form of nanowires and nanorods, have not been reported so far.

The generality of the state-of-the-art includes the preparation of other nanostructures of different chemical composition intended for various uses, such as ZnO nanowires [87] (used as precursors to manufacture zinc aluminate nanotubes [88]), lithium aluminate nanorods [89], SiO_2 nanorods [90] and V_2O_5 nanorods/nanowires [91]. The state-of-the-art also includes several methods of manufacturing nanowires and nanorods [92-98].

4.2. Ultrasonic method of manufacturing nanostructures [99]

Herein, a new method for the synthesis of nanowires and nanorods of $\text{SrAl}_2\text{O}_4:\text{Ce}^{3+}$, Dy^{3+} , Eu^{2+} and homologue nanostructures Ce (III) co-doped (e.g. $\text{MAl}_2\text{O}_4:\text{Ce}$, Ln, where M is Be, Mg, Sr, Ca or Ba) with persistent luminescence that uses ultrasonic vibrations is described [99].

4.2.1. Processing of alkaline-earth aluminates doped with cerium (III)

In order to investigate the grinding and sonification effects on the nanostructure, and aiming at developing luminescent nanowires and nanorods of alkaline-earth aluminates doped with cerium (III) and co-doped with other lanthanide ions for large-scale applications, an «**Ultrasonic method of manufacturing nanostructures – UMMN**» [99] was developed. The UMMN comprises the steps described in Equation (4-1) from precursor particles (e.g. baseline material):



where M is Be, Mg, Ca, Sr, Ba or a combination thereof (for $0 < x \leq 1$ and $0 \leq y \leq 1$), and the symbol)))) denotes the step of ultrasonification.

4.2.2. Grinding of precursor particles

The precursor $\text{SrAl}_2\text{O}_4:\text{Ce}^{3+}$, Dy^{3+} , Eu^{2+} micro- and nano-particles (baseline material) were deagglomerated by ball milling for 1, 3 and 7 hours under 150 cycles per minute (cpm). Figure 4-1 shows the variations in the distribution of particle size as a function of grinding time. It is clear that the ball milling is an effective process to reduce the size of micro particles.

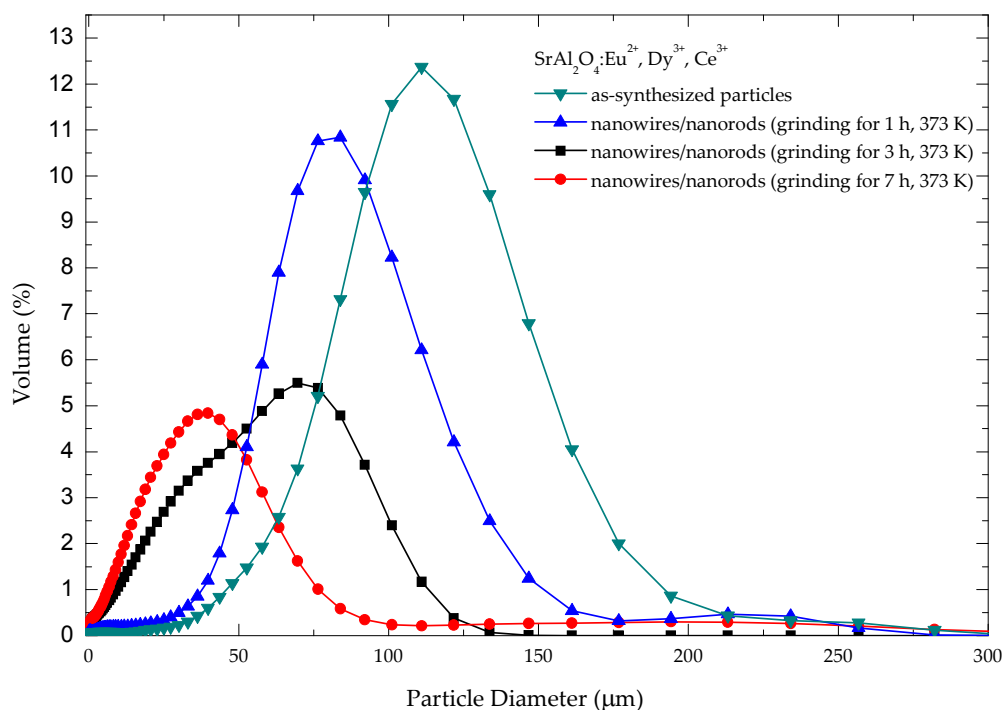


Figure 4-1. Evolution of particle size distributions of precursor of $\text{SrAl}_2\text{O}_4:\text{Ce}^{3+}$, Dy^{3+} , Eu^{2+} with milling time (1, 3 and 7 h).

4.2.3. Ultrasonification of particles

The milled particles were dispersed in ethanol under ultrasonic mechanical vibrations at a frequency of 3 MHz, which produce a propagating wave disturbance in a dispersion medium that breaks down the agglomerates. This action is due to the frictional forces caused by cavitations (energy shock wave), shear stress and thermo chemical effects. In addition, the use of ultrasound is useful in the separation of thin layers partially sheared during the milling, facilitating the formation of luminescent strontium aluminate nanowires and nanorods. The selection of ethanol as dispersing medium was intended to avoid hydrolysis reactions during the ultrasonification step that would occur if water was used instead.

4.2.4. Post-annealing of milled and sonificated particles

The experimental conditions used for the preparation of nanowires and nanorods according to the UMMN are described in Table 4-1. Batches of 15 g of $\text{SrAl}_2\text{O}_4:\text{Ce}^{3+}$, Dy^{3+} , Eu^{2+} were dispersed in 20 mL of ethanol at a speed of 150 cpm.

Table 4-1. Formation of $\text{SrAl}_2\text{O}_4:\text{Ce}^{3+}$, Dy^{3+} , Eu^{2+} nanowires and nanorods.

Grinding (h)	Sonification (MHZ)	Particle size (μm)	T_{p-a} (K)	t (h)	Nanostructure
-	-	109.7	-	-	Spherical particles
1	3	80.72	373	1	Nanorods
3	3	39.72	373	1	Nanorods
7	3	26.27	373	1	Nanowires and nanorods

4.3. Luminescent $M_{(1-x-y)}N_2O_4:Ce_x, Ln_y$ nanowires/nanorods [99]

The luminescent strontium aluminate nanowires and nanorods doped with cerium (III), dysprosium (III) and europium (II), $SrAl_2O_4:Ce^{3+}, Dy^{3+}, Eu^{2+}$, synthesized at the Department of Ceramic and Glass Engineering of University of Aveiro, were characterized by XRD, HR-TEM, SEM, EDX, and PL spectroscopy.

4.3.1. Structure of nanowires/nanorods

The $SrAl_2O_4:Ce^{3+}, Dy^{3+}, Eu^{2+}$ nanowires/nanorods obtained from starting powders, that were milled for 1, 3 and 7 hours, sonificated for 1 hour at 3 MHz, and subsequently annealed at 373 K, kept its crystalline α -monoclinic structure as verified by X-ray diffraction (Figure 4-2).

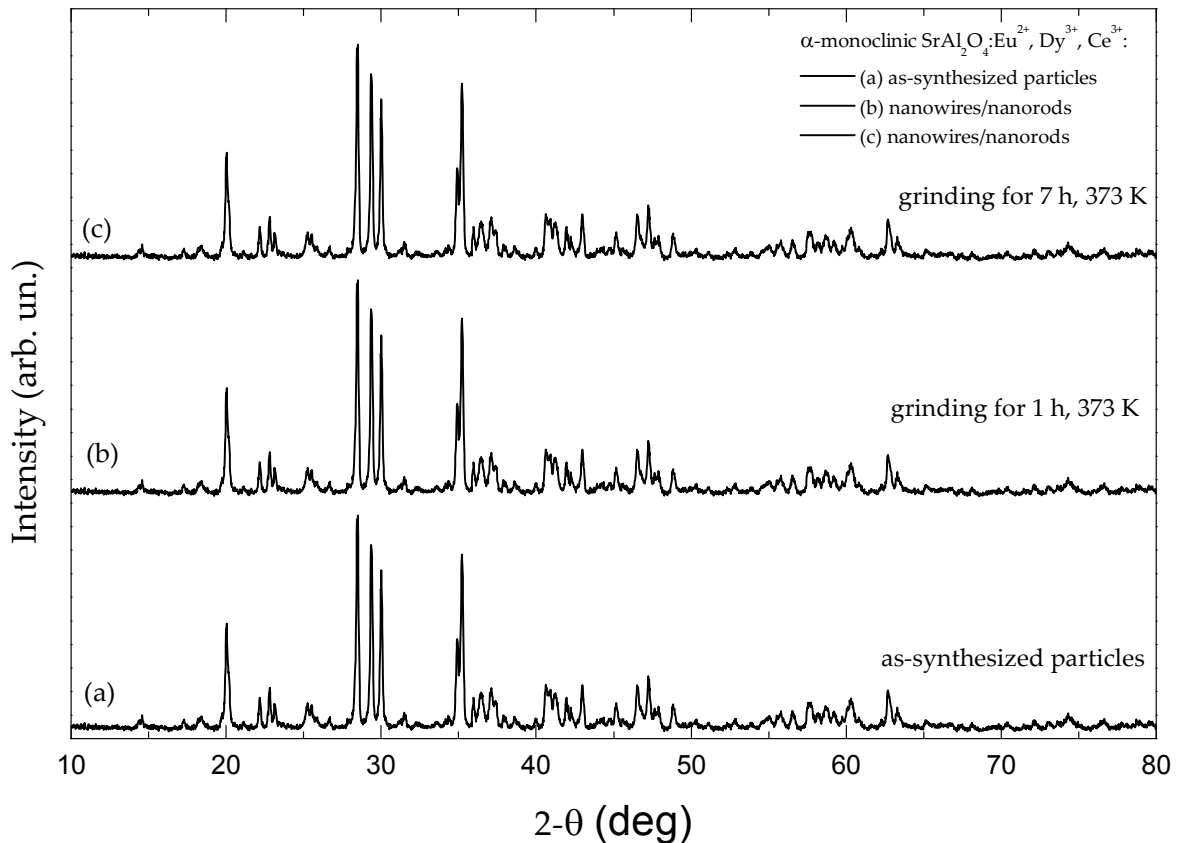


Figure 4-2. X-ray diffraction patterns of $SrAl_2O_4:Ce^{3+}, Dy^{3+}, Eu^{2+}$ nanowires/nanorods obtained by milling for 1 and 7 h, followed by ultrasonification for 1 h to 3 MHz, and post-annealing at 373 K.

4.3.2. Morphology of nanowires/nanorods

The luminescent $\text{SrAl}_2\text{O}_4:\text{Ce}^{3+}, \text{Dy}^{3+}, \text{Eu}^{2+}$ nanowires and/or nanorods obtained by this method of manufacture are characterized by diameters in the range of 40-60 nm and longitudinal lengths between 100 and 600 nm, as seen in Figures 4-3 and 4-4. These nanowires/nanorods can be arranged in an orderly manner (aligned), as shown in Figure 4-5, or irregularly. These new nanowires and nanorods present aspect ratios from 3 to 300.

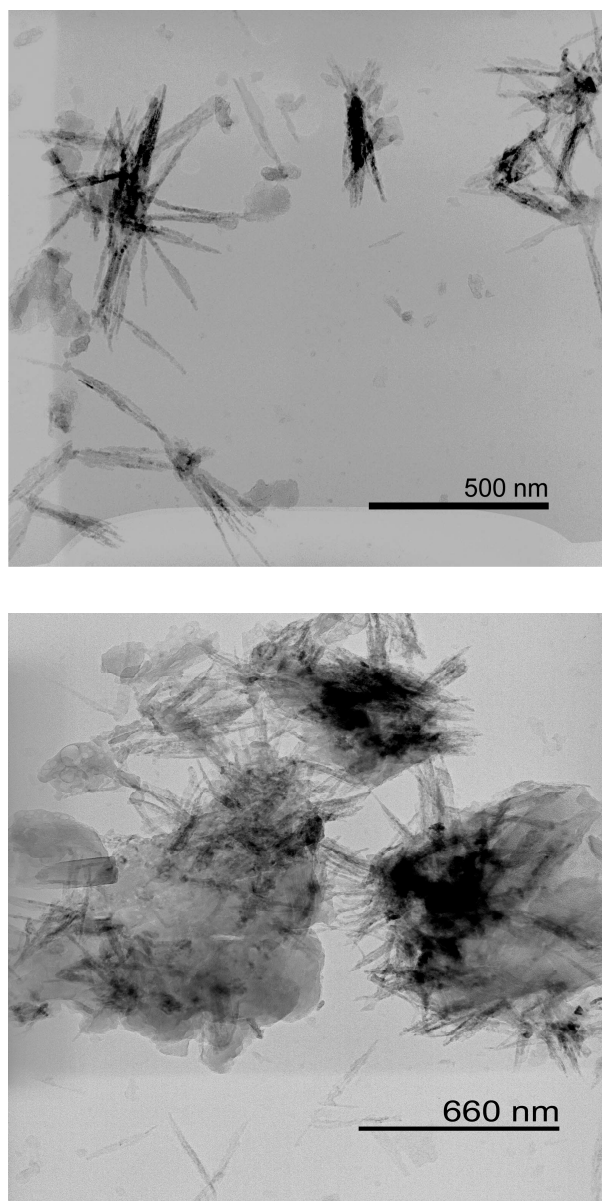


Figure 4-3. TEM micrographs of $\text{SrAl}_2\text{O}_4:\text{Ce}^{3+}, \text{Dy}^{3+}, \text{Eu}^{2+}$ nanowires and nanorods from UMMN.

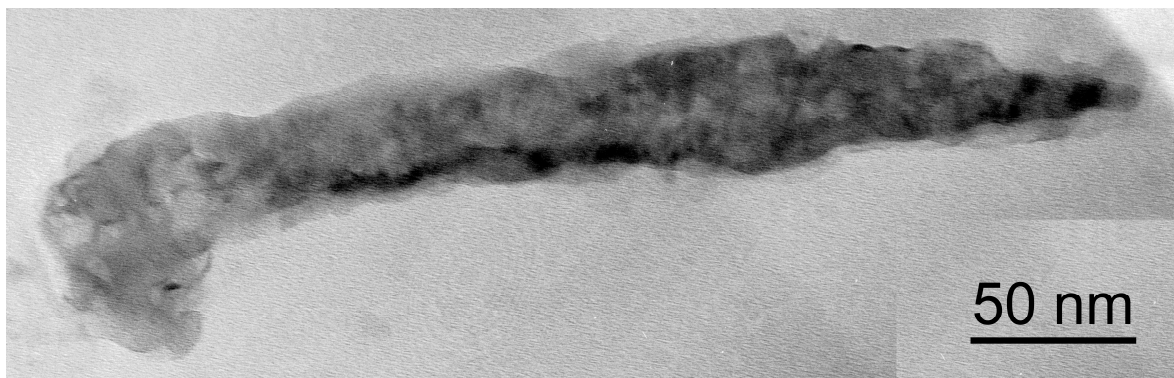


Figure 4-4. TEM micrograph of a $\text{SrAl}_2\text{O}_4:\text{Ce}^{3+}, \text{Dy}^{3+}, \text{Eu}^{2+}$ nanorod characterized by a diameter of about 40-50 nm and a longitudinal length of about 350 nm with an aspect ratio of about 7-8.

4.3.3. Chemical characterization of nanowires/nanorods

Photoluminescent $\text{SrAl}_2\text{O}_4:\text{Ce}^{3+}, \text{Dy}^{3+}, \text{Eu}^{2+}$ nanowires and nanorods samples were analyzed by SAED and show the stoichiometric Sr/Al/O ratios characteristic of the host precursor particles (Figure 4-5).

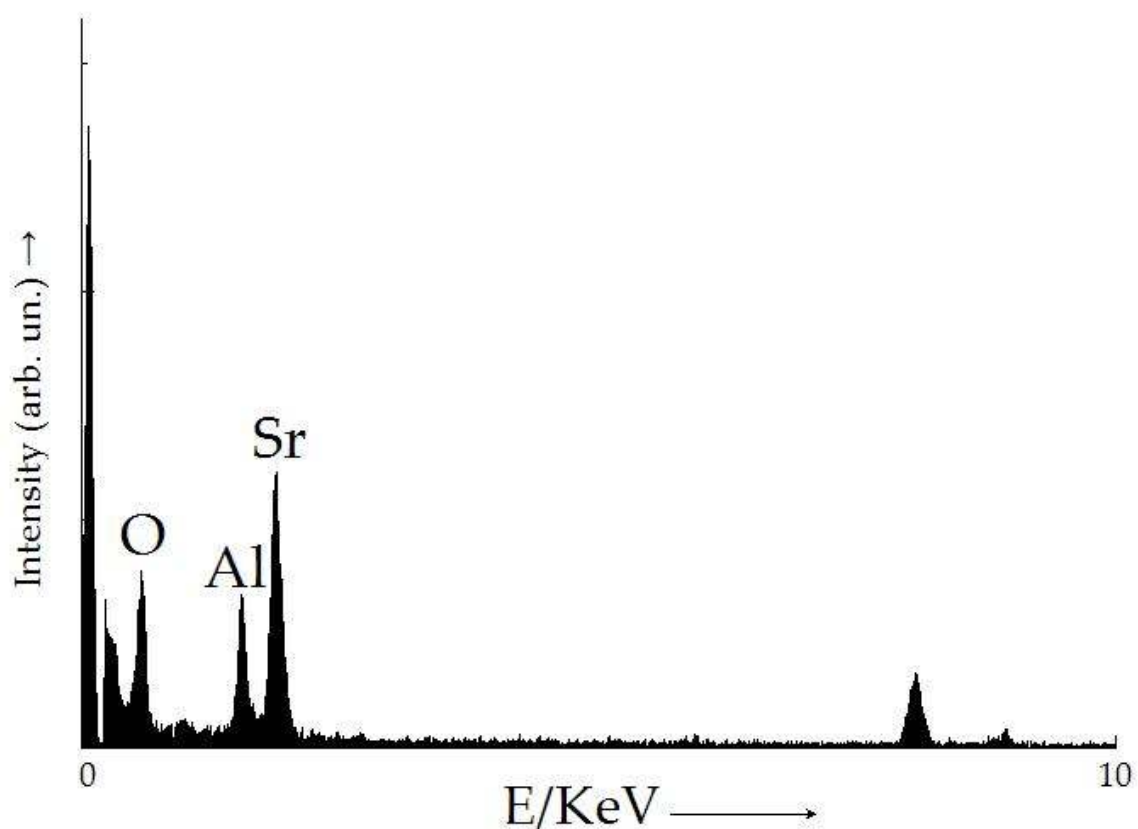


Figure 4-5. Selected area electron diffraction with a qualitative chemical analysis performed during transmission electron microscopy of $\text{SrAl}_2\text{O}_4:\text{Ce}^{3+}, \text{Dy}^{3+}, \text{Eu}^{2+}$ nanowires and nanorods, showing the presence of Sr, Al and O crystal field components of the host.

4.3.4. Photoluminescence of nanowires and nanorods

The $\text{SrAl}_2\text{O}_4:\text{Ce}^{3+}$, Dy^{3+} , Eu^{2+} nanowires/nanorods are characterized with the following property of photoluminescence in UV and UV-VIS (Figure 4-6):

- Photoluminescence emission in broadband: ultraviolet visible (UV-VIS) between 400 and 680 nm, characterized by a series of electronic transitions typical ion Ce^{3+} intensely with the peak $525 (\pm 5)$ nm, with the colour appearance in the yellow-green region, intra- $4f$ and inter- $4f^* \rightarrow 5d$;
- Photoluminescence emission in a narrow band: ultraviolet (UV), with intense peak at 52 nm;
- Distance between UV and UV-VIS spectral peaks of $473 (\pm 5)$ nm.

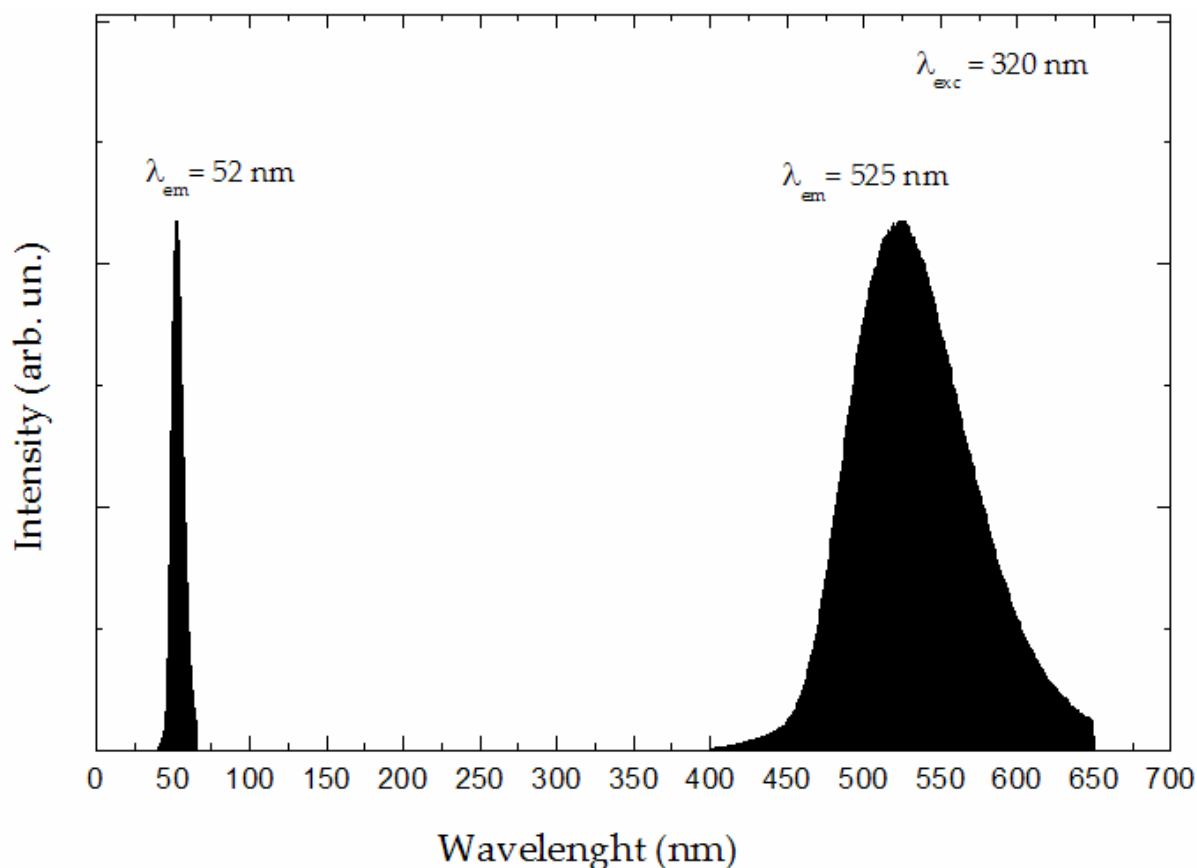


Figure 4-6. Emission spectrum of photoluminescence of $\text{SrAl}_2\text{O}_4:\text{Ce}^{3+}$, Dy^{3+} , Eu^{2+} nanowires and nanorods characterized by ultraviolet (UV) emission peaking at $\lambda = 52$ nm and ultraviolet visible (UV-VIS) emission peaking at $\lambda = 525 \pm 5$ nm under atomic excitation at 320 nm.

4.4. Potential utilizations of nanowires and nanorods

A potential utilization of nanowires/nanorods with persistent luminescence in a new long afterglow application is described in chapter 7. Alternative uses for these luminescent aluminate nanowires/nanorods doped with cerium (III) may involve their application onto the surface of various substrates, nanofunctionalized, and incorporated in combination with other materials to form nanostructured composites [99], such as:

- Nanorods of $\text{MAI}_2\text{O}_4:\text{Ce}^{3+}$ embedded in (amorphous) glass matrix of SiO_2 ;
- Nanowires of $\text{MAI}_2\text{O}_4:\text{Ce}^{3+}$ crystal embedded in matrix of TiO_2 ;
- Nanowires of $\text{MAI}_2\text{O}_4:\text{Ce}^{3+}$ embedded in glass matrix of SiO_2 ;
- Nanowires of $\text{MAI}_2\text{O}_4:\text{Ce}^{3+}$, Gd^{3+} embedded in matrix of carbon nanotubes.

These aluminates can be used in the manufacture of nanotubes of similar or distinct chemical composition when the nanowires are nanofunctionalized as a "matrix form", adding and subtracting material for the formation of the hole on the longitudinal tubular structure.

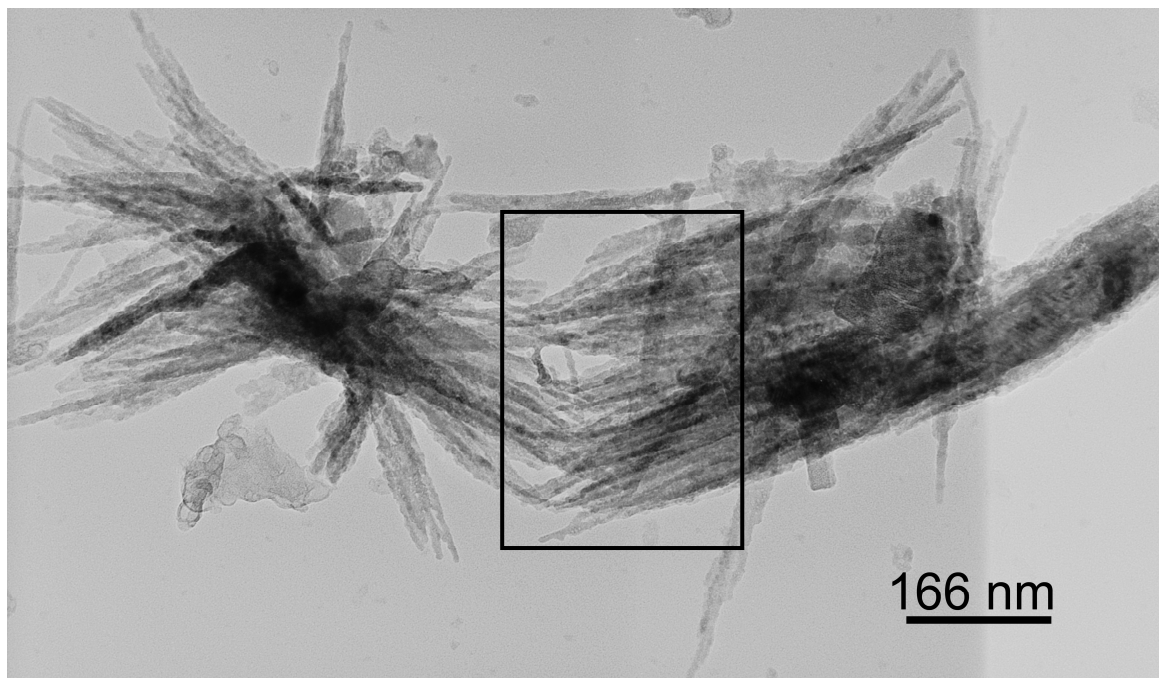


Figure 4-7. TEM micrograph showing a detail of a self-assembly growth of $\text{SrAl}_2\text{O}_4:\text{Ce}^{3+}$, Dy^{3+} , Eu^{2+} nanowires and nanorods in parallel; the black rectangle indicates the selected area electron diffraction (SAED) of the Figure 4-5.

When presented in a self-assembly organisation (Figure 4-7), these luminescent materials have the advantage of emitting light radiation in a preferred direction, they can be used with greater precision on the nanofunctionalization of biological systems [84], such as transportation of DNA structures, in drugs delivery systems, in cells detection, and imaging diagnostic. After the surface modification, these aluminates can be also used to detect biomolecular interactions in cellular and molecular level.

From the scientific point of view, these nanowires/nanorods (Figure 4-8) might be further investigated correlating the energy transfer mechanism of electrons from the persistent luminescence property to the superconductivity at low temperatures, T_c [85], not yet explored.

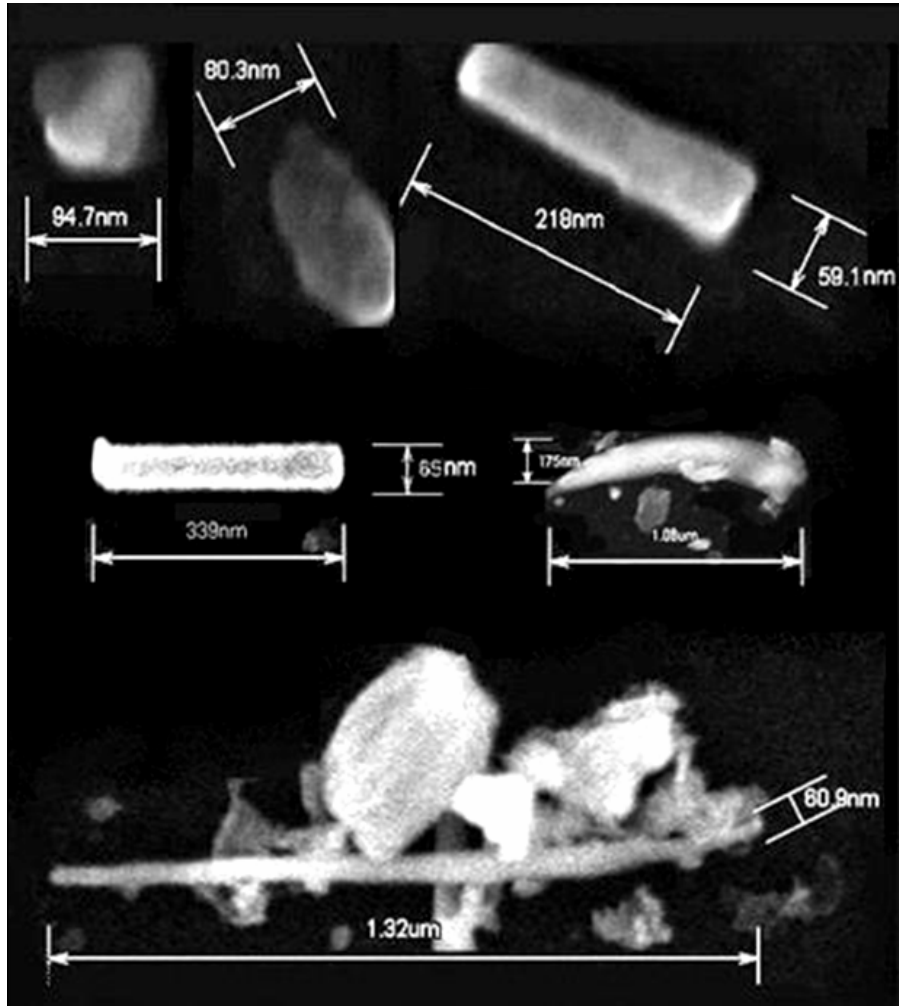


Figure 4-8. SEM visualizations of $\text{SrAl}_2\text{O}_4:\text{Ce}^{3+}$, Dy^{3+} , Eu^{2+} nanowires and nanorods. Note that the nanowire morphology varies between the nanoparticles (length of $1.32\ \mu\text{m}$ and a diameter of $60.9\ \text{nm}$ indicated in the image), comprising an aspect ratio of about 22, much higher than the average aspect ratio of about 5 measured for nanorods.

4.5. Conclusion

$\text{SrAl}_2\text{O}_4:\text{Ce}^{3+}$, Dy^{3+} , Eu^{2+} nanowires and nanorods were developed by grinding, sonification and post-annealing. A particular interest of these luminescent materials with analogous formulations might be correlated with energy transfer mechanisms of electrons in emission from the persistent luminescence property to the superconductivity at low temperatures. The new nanowires and nanorods, with diameters of 40-60 nm, aspect ratios from 3 to 300, and luminescence emission in bands peaking at 525 nm and at 52 nm, enlarge the gamut of new persistent luminescent nanomaterials for emergency applications. ■

Chapter 5

Photocatalytic core-shells of $\text{SrAl}_2\text{O}_4:\text{Ce}^{3+}$, Dy^{3+} , Eu^{2+} @ TiO_2 nanotubes

In this chapter, medicinal core-shell structures of $\text{SrAl}_2\text{O}_4:\text{Ce}^{3+}$, Dy^{3+} , Eu^{2+} luminescent particles coated with TiO_2 were obtained through an encapsulation process that involves aging in a Na_2TiO_3 solution in the absence (inorganic) and in the presence (hybrid) of polyethylene glycol (PEG), followed by a heat treatment at 353 or 673 K. Surface modifications were investigated by zeta potential and electronic conductivity measurements, SEM, HR-TEM analyses, and ^{13}C , ^{27}Al NRM MAS spectroscopy. The titania shell with a thickness of about 60-300 nm presents a short ordered anatase in form of nanowires and nanotubes with lengths between 5 and 40 nm. ^{27}Al MAS NMR data demonstrate that only small modifications are created on the host lattice core-structure peaking at 74.85 ppm from the Ti-bonds shell. ^{13}C MAS NMR data clearly demonstrate the OCH_2CH_2 functional group in hybrid systems. The as-synthesized core-shell structures presented elevated electronic stability in presence of water, making this coating process promising to protect luminescent particles against hydrolysis. Moreover, the coating with TiO_2 confers to the core-shell particles photocatalytic properties making multifunctional.

Key-words: core-shell, strontium aluminate, titania nanotube, photocatalysis, luminescence.

5.1. Hydrolysis of the crystalline host lattice

As stated before, inorganic Eu^{2+} , Ln^{3+} (Ln = lanthanide elements, e.g. Dy, Ce, Tm) co-doped alkaline earth aluminates $\text{MAl}_2\text{O}_4:\text{Eu}^{2+}, \text{Ln}^{3+}$ (M = Be, Mg, Sr, Ba, and Ca) are functional materials with persistent afterglow luminescence [100–104]. In general, these phosphorescent materials have high quantum efficiency, long-lifetime luminescence, chemical stability, replacing the traditional ZnS-based phosphors [101–104].

The afterglow-in-the-dark applications include luminous plastics, coatings and ceramic products [105–108]. However, when the $\text{SrAl}_2\text{O}_4:\text{Eu}^{2+}, \text{Ln}^{3+}$ phosphor is exposed to water contact, hydrolysis of the crystalline host occurs according to Equation (5-1):



The products of hydrolysis include aluminium hydroxide $\text{Al}(\text{OH})_3$ and soluble strontium hydroxide and result in an increase of pH of the medium. The crystal structure of the phosphors is destroyed during hydrolysis, and the persistent phosphorescence is degraded. *Yang-Chong* [109] reported the formation of $\text{SrAl}_2(\text{OH})_{12}$ and $\text{SrAl}_3\text{O}_5(\text{OH})$ as hydrolyzed sub-products. The nordstrandite phase formation was identified as a third crystalline form of $\text{Al}(\text{OH})_3$ in admixture with gibbsite and bayerite [110-112]. In 1958, this material was obtained in pure form by ageing gels at high pH. Actually, the nordstrandite is synthesized by reacting hydrolytic precipitation of aluminium with aqueous ethylene glycol at $\text{pH} > 8.0$ favouring the crystallization of pure phase.

The present study aims at improving the water resistance of $\text{MAl}_2\text{O}_4:\text{Ce}^{3+}, \text{Dy}^{3+}, \text{Eu}^{2+}$ phosphors to make viable its processing in aqueous environment and applications in long-lifetime afterglow photoluminescence, namely in photoluminescent ceramic tiles for emergency applications [113]. Figure 5-1 shows schematic representations of $\text{SrAl}_2\text{O}_4:\text{Ce}^{3+}, \text{Dy}^{3+}, \text{Eu}^{2+}$ phosphor under different reaction conditions. The condensed polarization of H_2O molecules on the surface of phosphor during the ceramic processing means a limitation for industrial production of photoluminescent ceramics. Furthermore, the humidity accumulated during the utilization of these tiles requires special treatment for long lived persistent luminescence.

The hydrolysis kinetics of $\text{SrAl}_2\text{O}_4:\text{Ce}^{3+}, \text{Dy}^{3+}, \text{Eu}^{2+}$ non-encapsulated particles was evaluated by dispersing 10 g of powder in 100 mL of KCl (10^{-3} mol) solution in deionised water ($\text{pH} \approx 6.8$), HCl (0.01 mol). Zeta potential measurements were performed in ethanol in an acid medium ($\text{pH} \approx 2.8$) to enable assessing the surface properties in absence of hydrolysis. Micro and nanoparticles were mixed by ultrasonic stirring for 5 min.

The uncoated $\text{SrAl}_2\text{O}_4:\text{Ce}^{3+}, \text{Dy}^{3+}, \text{Eu}^{2+}$ powders showed an isoelectric point (IEP) at $\text{pH} \sim 8.6$, as shown in Figure 5-2a. Considering that the coating TiO_2 species exhibit an IEP at about $\text{pH} 4-6$ [114a], it comes out that the ideal region of pH to encapsulate the phosphor particles is between $\text{pH} 6-8$. In general, electrostatically stable suspensions are obtained for absolute zeta potential values $> \pm 30$ mV, which are observed in the acid region.

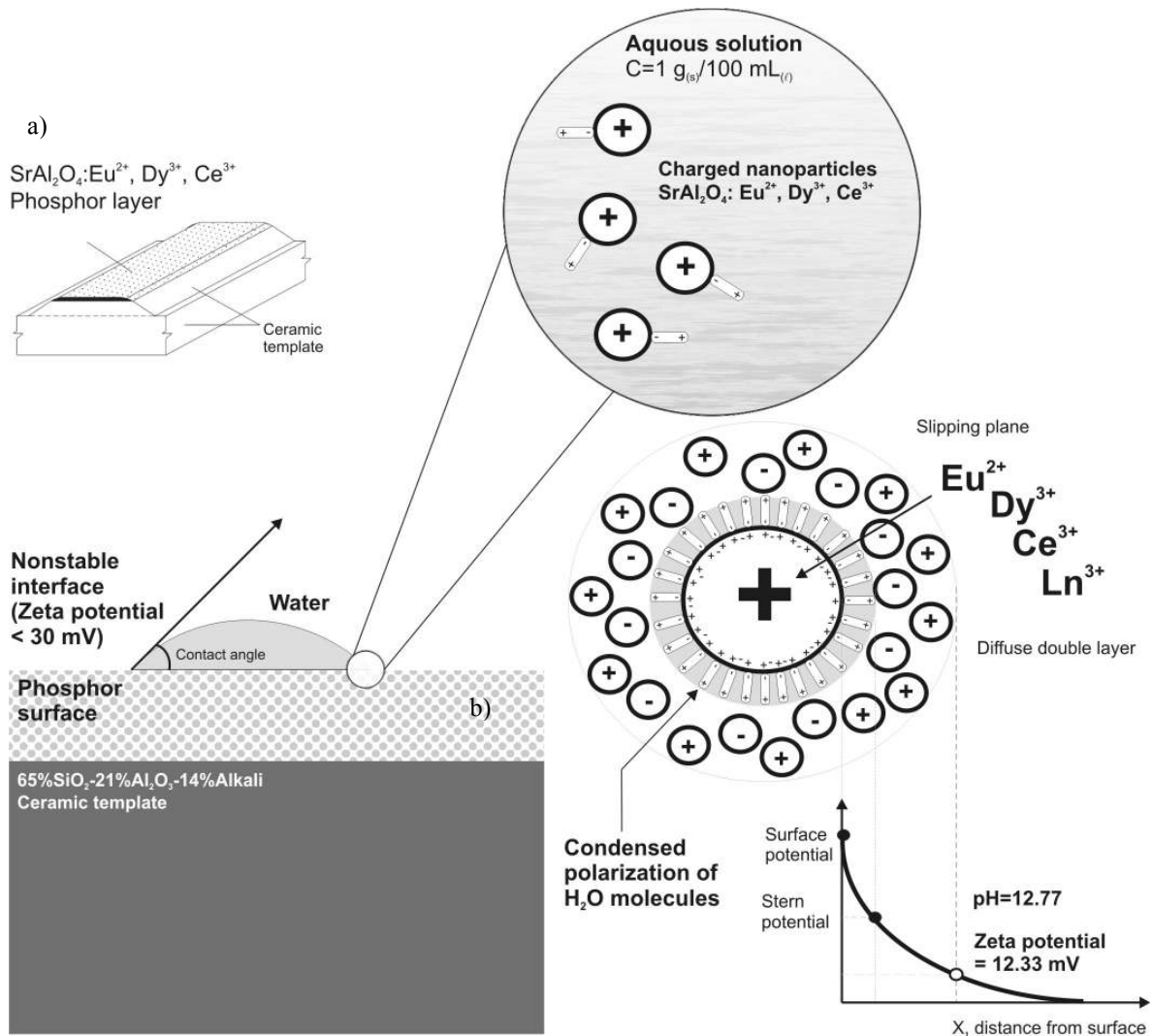


Figure 5-1. Schematic representation of: a) $\text{SrAl}_2\text{O}_4:\text{Ce}^{3+}, \text{Dy}^{3+}, \text{Eu}^{2+}$ phosphor applied onto a ceramic substrate [113]; b) surface interactions upon hydrolysis of uncoated monoclinic particles in contact with water, leading to a high pH value (~ 12.7).

Figure 5-2b shows time-resolved measurements from zero to about 3000 minutes after contact in water. Hydrolysis resulted in a progressive increase of alkalinity up to $\text{pH} \sim 11$, accompanied by concomitant increases of electronic conductivity and zeta potential derived from the destruction of the crystalline host lattice.

The SEM observations of non-encapsulated $\text{SrAl}_2\text{O}_4:\text{Ce}^{3+}, \text{Dy}^{3+}, \text{Eu}^{2+}$ single particles hydrolyzed after 3000 min at $\text{pH} > 10$ show the formation of $\text{Al}(\text{OH})_3$ polymorphs (Figure 5-3). Nordstrandite nanocrystals with sizes of about 40-100 nm were precipitated onto strontium hydroxide products enlarging the surface area, as shown in Figure 5-3a-c. A large nordstrandite with triclinic pedial structure (space group P_1) is also observed close to the selected area arrowed in Figure 5-3d, which reveals elongated crystals organized in shape of a “natural tree” distribution (Figure 5-3e-f).

$\text{Al}(\text{OH})_3$ polymorphs were obtained as hydrolysis products after the destruction of the crystalline host lattice of the $\text{SrAl}_2\text{O}_4:\text{Ce}^{3+}$, Dy^{3+} , Eu^{2+} , as shown in XRD patterns (Figure 5-4). A secondary $\text{Sr}_4\text{Al}_{14}\text{O}_{25}$ phase was also observed as residual crystalline host lattice coexistent with the $\text{SrAl}_2\text{O}_4:\text{Ce}^{3+}$, Dy^{3+} , Eu^{2+} phosphor.

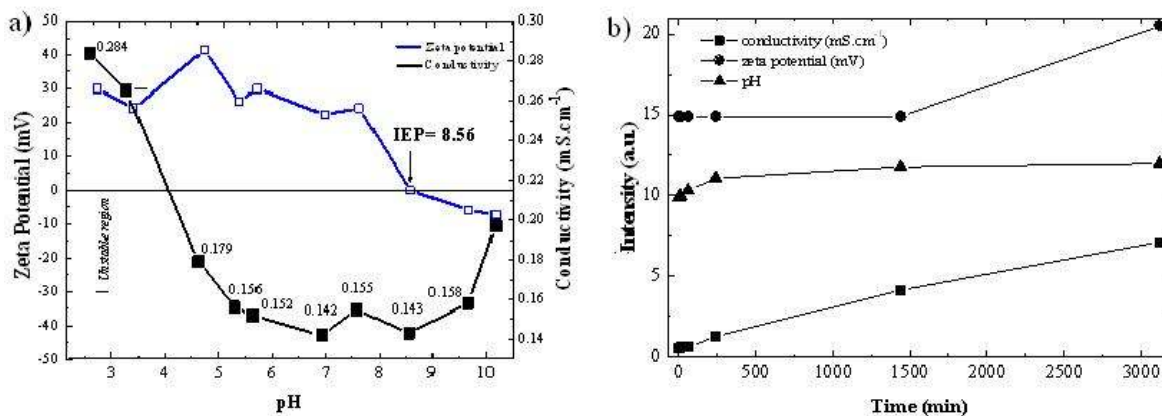


Figure 5-2. Non-encapsulated $\text{SrAl}_2\text{O}_4:\text{Ce}^{3+}$, Dy^{3+} , Eu^{2+} micro and nanoparticles: a) zeta potential and electronic conductivity measurements in ethanol (IEP at pH~8.56); b) kinetics of the hydrolysis process in water time-resolved measurements after 0, 10, 60, 240, 1440 and 3120 minutes, by Coulter DELSA 440 SX.

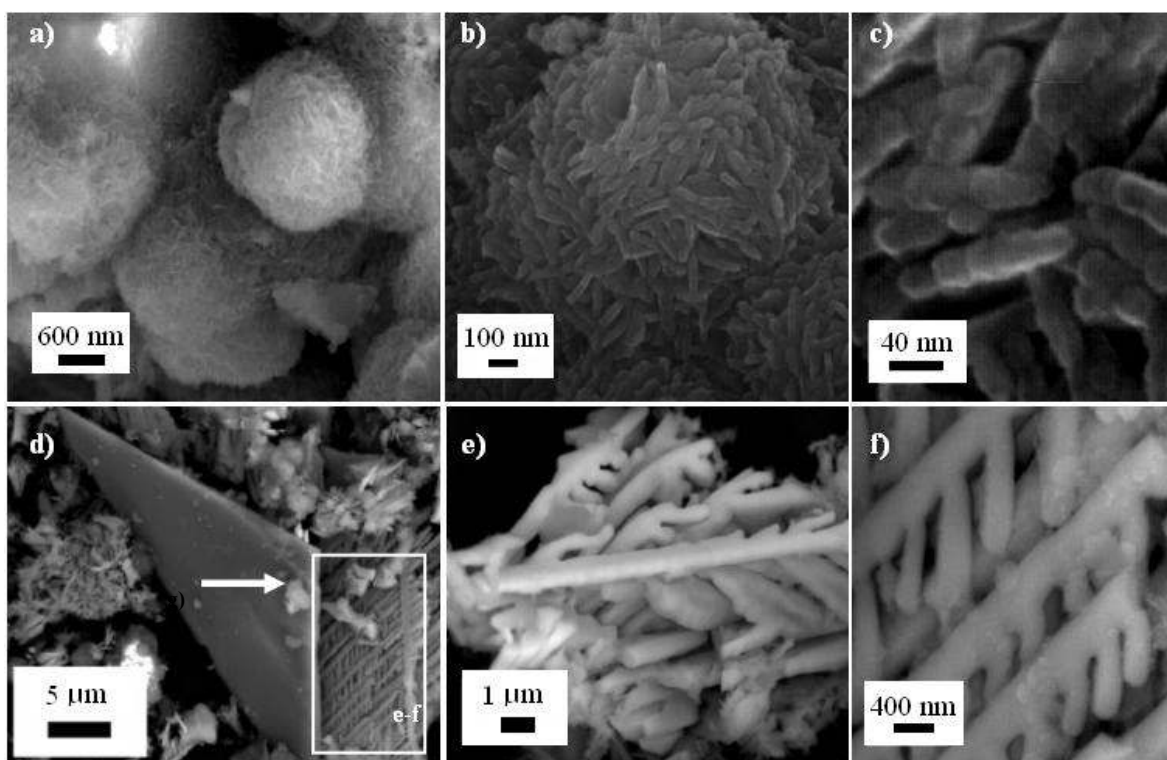


Figure 5-3. Structural SEM analysis of $\text{SrAl}_2\text{O}_4:\text{Ce}^{3+}$, Dy^{3+} , Eu^{2+} hydrolyzed after 3000 min at pH >10 with the formation of $\text{Al}(\text{OH})_3$ polymorphs: a-c) nordstrandite nanocrystals; e-f) the arrow indicates the selected area revealing elongated crystals.

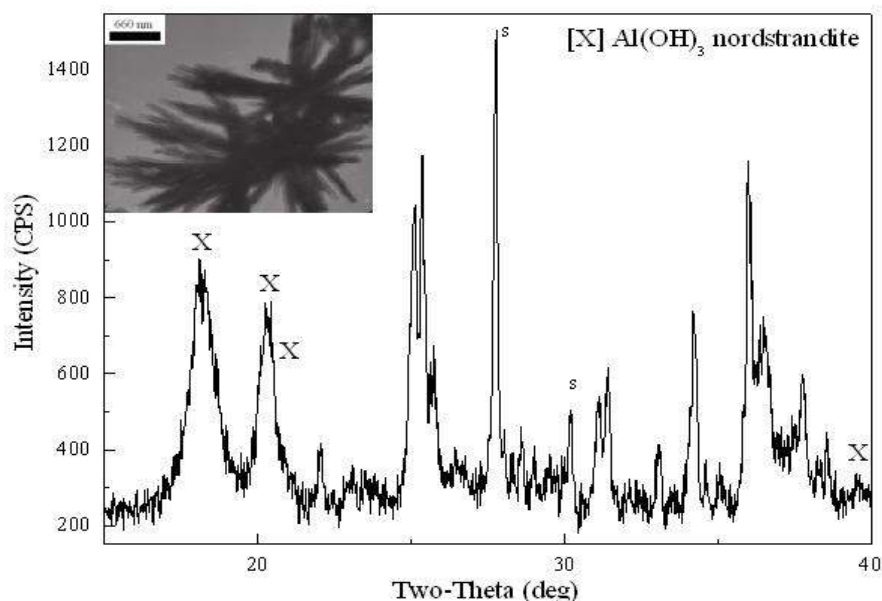


Figure 5-4. XRD patterns of nordstrandite derived from hydrolysis of $\text{SrAl}_2\text{O}_4:\text{Ce}^{3+}$, Dy^{3+} , Eu^{2+} for 3000 min at $\text{pH} > 10$, resulting in the formation of $\text{Al}(\text{OH})_3$ polymorphs.

TiO₂ photocatalytic agent

To circumvent the hydrolysis problem of $\text{MAl}_2\text{O}_4:\text{Eu}^{2+}$, Ln^{3+} ($\text{M} = \text{Sr}$ or Ca) phosphors materials [111-112], several processes of encapsulation have been proposed so far [114b-125] as shown in Table 5-1. Recently, a sol-gel process using tetrabutylorthotitanate as TiO_2 precursor has been proposed by *Zhong-Chen* [125] to encapsulate $\text{SrAl}_2\text{O}_4:\text{Eu}^{2+}$, Dy^{3+} with TiO_2 .

Since the discovery of the photocatalytic splitting of water on TiO_2 electrodes [126], TiO_2 has been further investigated in photocatalysis [127-142]. The illumination of photocatalyst with UV-visible light suitable for its bandgap energy generates electrons (e^-) and holes (h^+), initiating oxidation and reduction reactions [127]. The positive oxidation potentials of holes (h^+) in TiO_2 are induced by UV irradiation of a wavelength below 400 nm [128].

TiO_2 presents three possible crystalline phases, anatase, rutile and brookite, with different properties and structures, with anatase showing a highest photocatalytic activity [129], whereas rutile is a more suitable material for white pigments and coatings because of its great refractivity and notable chemical inertia. In some other cases, a mixture of anatase and rutile shows a better photocatalytic activity over the single TiO_2 phase [130].

The encapsulation processes already reported [131-142] are cumbersome, as depicted from Table 5-1. Therefore, a simple process for coating phosphors materials with TiO_2 and confer them photocatalytic and antibacterial properties was envisaged in the present work. The surface modification of multifunctional luminescent core-shell particles has the potential to combine the luminescent properties of core with photocatalytic attributes of TiO_2 shell, thus enlarging the range of potential applications (analytical chemistry, catalysis, medicine and sensors).

Table 5-1. Encapsulation process of $\text{MAl}_2\text{O}_4:\text{Eu}^{2+}$, RE^{3+} (M = Sr or Ca) phosphors.

Coating layer	Systematisation of recent encapsulation processes	Results	References
Silica	<ul style="list-style-type: none"> Glycol (0.1 mol⁻¹ H₂SO₄ solvent) using a Na₂SiO₃ solution; pH = 10.5, thermal treatment at 353 K for 3 h, and after exposed in a filter press; Reaction: $[\text{Na}_2\text{SiO}_3 + 2\text{H}^+ + (x-1)\text{H}_2\text{O}] \rightarrow [\text{SiO}_2 \cdot x\text{H}_2\text{O} + 2\text{Na}^+]$; Silica layer on the phosphor surface. 	↑ Water resistance ↓ ↑ PL	[114a] Lü (2005)
Poly(methyl methacrylate), PMMA	<ul style="list-style-type: none"> MMA (liquid monomer) to PMMA polymerization; Encapsulation layer ~20-30 nm in hybrid systems to enhance the photoluminescence. 	↑ Water resistance ↑ PL	[115] Dong-Gen (2005)
Alumina	<ul style="list-style-type: none"> Glycol (0.1 mol⁻¹ Al₂(SO₄) solvent) using a NaOH solution, pH = 5.0-6.0, thermal treatment at 343-353 K for 3 h, exposed in distilled water for 3 times, and thermal treatment at 423 K for 4 h; Reaction: $[\text{Al}_2(\text{SO}_4)_3 + 3\text{H}_2\text{O}] \rightarrow [2\text{Al}(\text{OH})_3 + 6\text{H}^+ + \text{SO}_4^-]$; Precipitation of aluminium hydrated on the phosphor surface. 	↑ Water resistance ↓ PL	[116] Lü-Wang (2007)
SrF₂	<ul style="list-style-type: none"> AR, NH₄HF₂ (S1) 2:1, thermal treatment at 873-973 K for 2 h; Formation of SrF₂ coating layer on the phosphor surface. 	↑ Water resistance ↓ ↑ PL	[117] Guo-Lv (2007)
Organic ligands	<ul style="list-style-type: none"> Ethanol, 1,10-phenanthroline, 8-hydroxyquinoline, acetyl acetone, citric acid, tartaric, pH = 8-9, span-80 (surfactant), thermal treatment at 313-318 K for 3 h, and washed (water/ethanol); O, N, F, Cl from ligands provide electrons with unsaturated metal ions (Sr²⁺, Al³⁺, Eu²⁺, Dy³⁺) on the phosphor surface. 	↑ Water resistance (hydrolysis 8h to 96 h) ↑ PL	[118] Wu-Yang (2007)
Coordination bonds	<ul style="list-style-type: none"> Polymer ligands containing O atoms provide electrons with unsaturated metal ions (Sr²⁺, Al³⁺, Eu²⁺, Dy³⁺) on the phosphor surface. 	↑ Water resistance ↑ PL	[119] US Patent, Zhang-Yang (2007)
Maleic anhydride	<ul style="list-style-type: none"> Chloroform (50 ml), maleic anhydride, pH = 9.5 by ammonia, thermal treatment at 323 K for 9 h, filter press/washed, thermal treatment at 353 K for 4 h; Maleic anhydride containing oxygen atoms provide electrons with unsaturated metal ions on the phosphor surface. 	↑ Water resistance ↑ PL	[120] Yu-Yang (2008)
Phosphate	<ul style="list-style-type: none"> Triethyl phosphate, stirred for 3 h, thermal treatment in autoclave at 473-513 K for 12-24 h, washed in anhydrous ethanol for 3 times, vacuum-dried; Aluminium organic-phosphate was a micro-porous inorganic-organic hybrid whose channel walls were modified by introduction of organic groups attached to P atoms; Al[OOP(OC₂H₅)₂]₃ was a product of encapsulation. 	↑ Water resistance ↑ PL	[121] Zhu-Liu (2009)
Glass	<ul style="list-style-type: none"> Improved Performance of Strontium Aluminate Luminous Coating on the Ceramics Surface (no details). 	↑ Water resistance ↑ PL	[122] Gao-Liu (2008)
Titanium dioxide, TiO₂	<ul style="list-style-type: none"> Photocatalytic CaAl₂O₄:Eu²⁺, Dy³⁺ Coated with TiO₂; 	↑ Water resistance ↑ PL	[123-124] Wang-Li (2009)
	<ul style="list-style-type: none"> Photocatalytic performance of TiO₂/SrAl₂O₄:Eu²⁺, Dy³⁺, tetrabutylorthotitanate (C₁₆H₃₆O₄Ti), diethanolamine (DEA), thermal treatment at 773 K for 2 h. 	Air purification	[125] Zhong-Chen (2009)

5.2. Encapsulation process [143]

The type of TiO_2 precursor used in the encapsulation process and the formation of the coating layer are described in this topic.

5.2.1. Na_2TiO_3 approach for the synthesis of core-shells

The encapsulation process to obtain strontium aluminate@ TiO_2 core-shells was carried out in the absence and in the presence of poly-(ethylene glycol) molecules with an average of about 6 oxyethylene units, i.e. PEG-(300). Sodium titanate (Na_2TiO_3) was used as source of titanium dioxide hydrolysed species.

5.2.2. Formation of a film of hybrid strontium aluminate co-doped

10.0 g of $\text{SrAl}_2\text{O}_4:\text{Ce}^{3+}$, Dy^{3+} , Eu^{2+} micro and nanoparticles were mixed with 10.0 mL of poly(ethylene glycol) (PEG) and ultrasonically dispersed for 30 minutes and then heated treated at 313 K. The effect of heat treatment time on the hybrid encapsulation performance was studied. The interaction between the surface hydroxyl groups of $\text{SrAl}_2\text{O}_4:\text{Ce}^{3+}$, Dy^{3+} , Eu^{2+} and poly-(ethylene glycol) molecules is schematized in Figure 5-5.

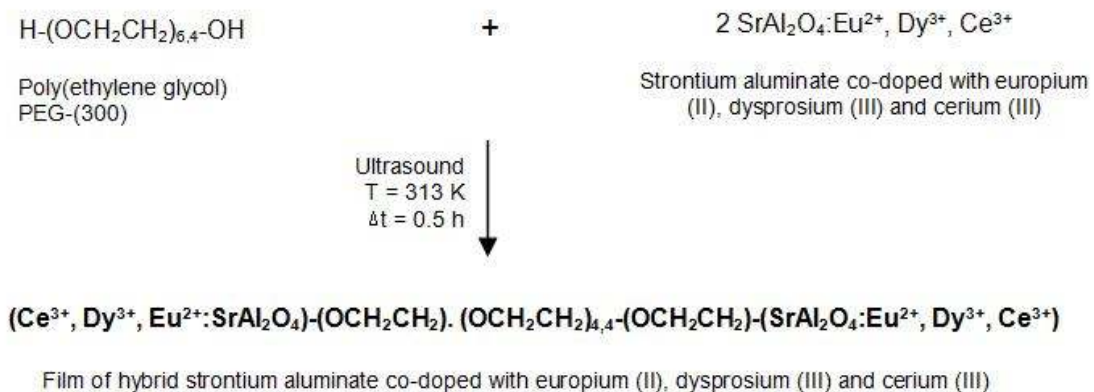


Figure 5-5. Hybrid layer of strontium aluminate co-doped with lanthanide ions.

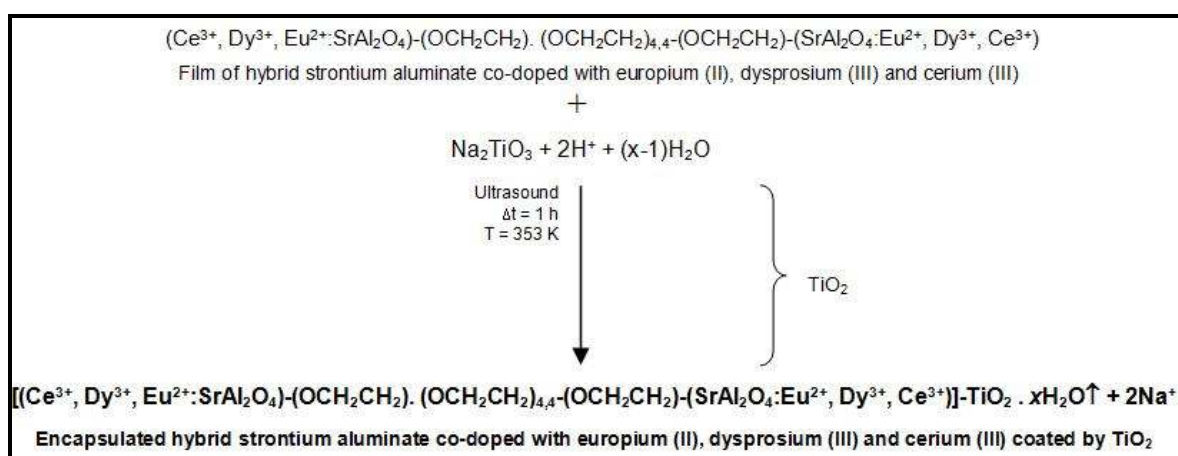
5.2.3. Encapsulation of $\text{SrAl}_2\text{O}_4:\text{Ce}^{3+}$, Dy^{3+} , Eu^{2+} @ TiO_2 core-shells

20 mL of as received liquid solution of Na_2TiO_3 was used as source of hydrolyzed TiO_2 species and mixed with 10.0 g of as received or PEG-coated particles (step 1) and ultrasonicated for 1 h at room temperature. The solid particles were separated from liquid by vacuum filtration, and then heat treated for 1 h, at 673 K, or at 353 K in the presence and the absence of PEG-300. The sample codes of $\text{SrAl}_2\text{O}_4:\text{Ce}^{3+}$, Dy^{3+} , Eu^{2+} @ TiO_2 core—shells are as follows:

- ENC1: core—shell encapsulated in the presence of PEG-300, post-annealed at 673 K;
- ENC2: core—shell encapsulated in the absence of PEG-300, post-annealed at 673 K;
- ENC3: core—shell encapsulated in the presence of PEG-300, post-annealed at 353 K.

The schematics of the encapsulation process are presented in Fig.5-6). In Figure 5-6 a and b, the x corresponds to the degree of hydration water content from 1 to 4, while n has to do with the degree polymerization of PEG. The encapsulation process was concluded when the O and Ti atoms from TiO_2 coating layer provide electrons to unsaturated metal ions (Sr^{2+} , Al^{3+} , Eu^{2+} , Dy^{3+} and Ce^{3+}) on the phosphor surface. This process is also applicable to TiO_2 encapsulation of $\text{MAl}_2\text{O}_4:\text{Ce}^{3+}$, Ln (M = Be, Mg, Ca, Sr or Ba, or a combination therefore) phosphors co-doped with ions from Lanthanide Series of the Periodic Table of Elements.

a) Hybrid core-shells:



b) Inorganic core-shells:

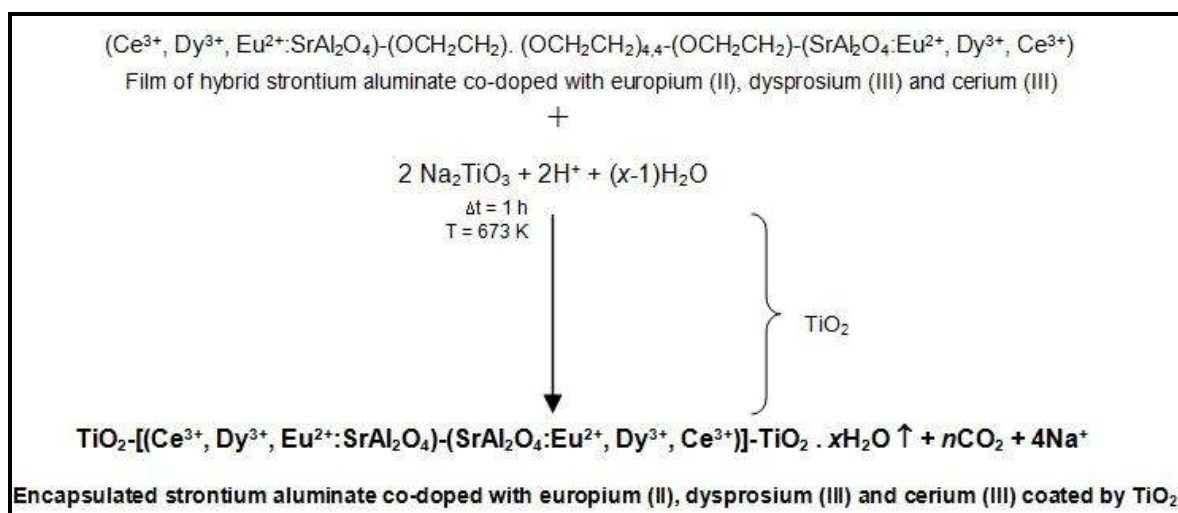


Figure 5-6. Schematics of the encapsulation process by TiO_2 coating layer: a) hybrid organic-inorganic core-shells; and b) inorganic core-shells.

5.3. Encapsulation process analysis

The XRD patterns of $\text{SrAl}_2\text{O}_4:\text{Ce}^{3+}, \text{Dy}^{3+}, \text{Eu}^{2+}@\text{TiO}_2$ core-shell particles are presented in Figure 5-7. Although the diffractions lines of anatase (TiO_2 and $\text{Ti}_{0.784}\text{O}_2$) and rutile (TiO_2) are of low intensity, as expected from a nanometer layer (see TEM results below), it seems clear that the coating approach used is effective for obtaining $\text{SrAl}_2\text{O}_4:\text{Ce}^{3+}, \text{Dy}^{3+}, \text{Eu}^{2+}@\text{TiO}_2$ core-shell particles. Low intensity signal of strontium aluminium hydroxide ($\text{Sr}_3\text{Al}_2(\text{OH})_{12}$) was also detected for the hybrid core-shell sample heat treated at the lower temperature (353 K). In the sample heat treated at 673 K, the formation of $\text{Ti}_{0.784}\text{O}_2$ anatase shell (Figure 5-7b) with a bandgap of about 3.2 eV offers good prospects for photocatalytic activity. Rutile was also formed in the core-shells prepared at 673 K (Figure 5-7c).

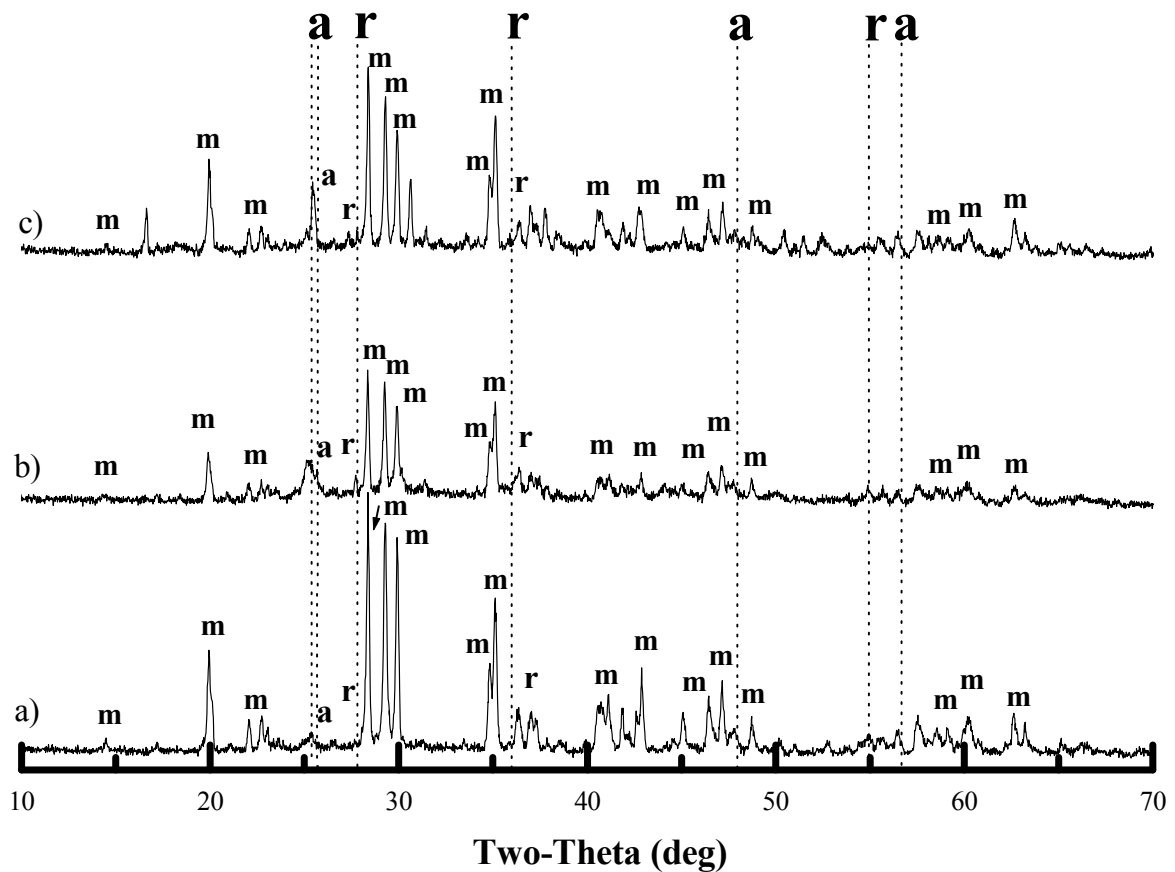


Figure 5-7. XRD profiles of $\text{SrAl}_2\text{O}_4:\text{Ce}^{3+}, \text{Dy}^{3+}, \text{Eu}^{2+}@\text{TiO}_2$ core-shell particles encapsulated in the presence (a, b) and absence of PEG-300 (c) and heat treated at 353 K (a) or 673 K (b, c). Legend: m= monoclinic core structure; a = anatase and r = rutile shell structures ($\text{Ti}_{0.784}\text{O}_2$ or TiO_2).

5.4. Core-shells: biocompatible nanoprobles

The core-shells were also characterized by HR-TEM, SEM, ^{13}C and ^{27}Al MAS NMR, photocatalytic activity, zeta potential and electronic conductivity analysis, as detailed below.

5.4.1. TiO_2 nanotubes shell

TEM characterization of $\text{SrAl}_2\text{O}_4:\text{Ce}^{3+}$, Dy^{3+} , Eu^{2+} @ TiO_2 core-shell particles heat treated at 353 K for 1 hour reveals the formation of TiO_2 coating layer (Figure 5-8). This shell layer with oxygen and titanium atoms bonded to unsaturated metals at phosphor surface is homogeneous, and the selected area electron diffraction (SAED) reveals its semi-crystalline nature.

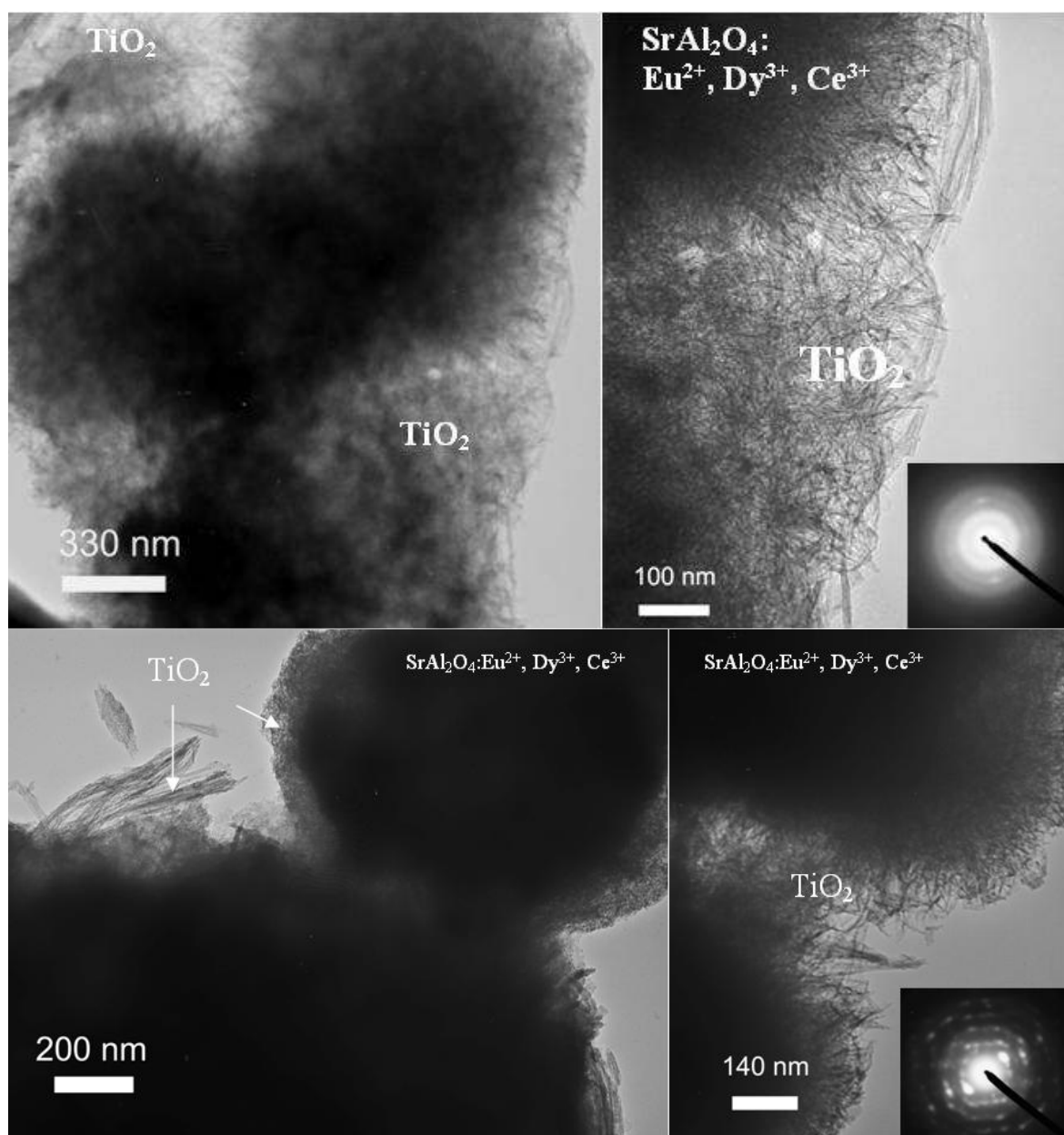


Figure 5-8. TEM analysis of $\text{SrAl}_2\text{O}_4:\text{Ce}^{3+}$, Dy^{3+} , Eu^{2+} encapsulated with semi-crystalline TiO_2 nanotubes/nanowires coating layer deposited in the presence of PEG-300, heat treated at 353 K.

This shell layer consists of anatase nanowires (Figure 5-9a-c) and nanotubes (Figure 5-9d), with thicknesses in the range of 60-300 nm.

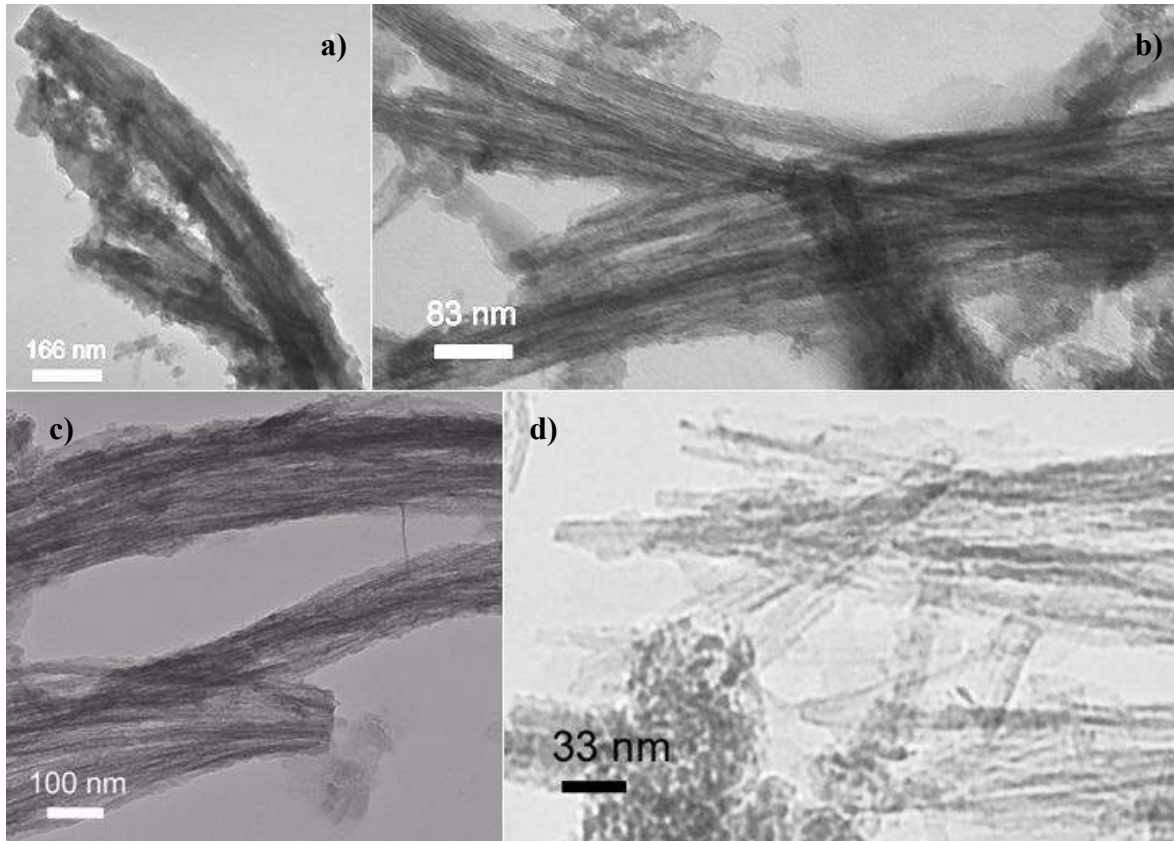


Figure 5-9. TEM analysis of $\text{SrAl}_2\text{O}_4:\text{Ce}^{3+}$, Dy^{3+} , Eu^{2+} encapsulated with semi-crystalline TiO_2 coating layer deposited in the presence of PEG-300 and heat treated at 353 K, presenting anatase nanowires (a-c) and nanotubes (d).

SEM micrographs of $\text{SrAl}_2\text{O}_4:\text{Ce}^{3+}$, Dy^{3+} , $\text{Eu}^{2+}@\text{TiO}_2$ core-shells obtained for different heat treatment time periods at 353 K, shown in Figure 5-10, exhibit agglomerated core particles covered by titania. It seems that the holding time does not significantly affect the morphology of encapsulated particles.

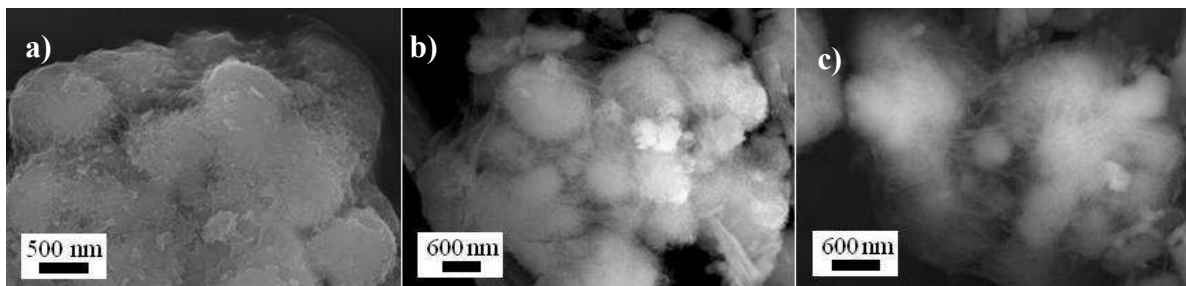


Figure 5-10. SEM micrographs of $\text{SrAl}_2\text{O}_4:\text{Ce}^{3+}$, Dy^{3+} , Eu^{2+} encapsulated by TiO_2 coating layer deposited in the presence of PEG-300 and heat treated at 353 K for: a) 30 min; b) 1 hour; and c) 2 hours.

SEM micrographs of $\text{SrAl}_2\text{O}_4:\text{Ce}^{3+}, \text{Dy}^{3+}, \text{Eu}^{2+}@\text{TiO}_2$ core-shells obtained in the presence and in the absence of PEG-300 and heat treated at 673 K (Figure 5-11) show a compacted agglomeration similar to the samples treatment at 353 K. TEM observations of the shells reveal the formation of semi-crystalline amorphous/anatase elongated TiO_2 nanoparticles (Figure 5-12a) when deposited in the presence of PEG-300, while semi-crystalline titania nanotubes with diameters in the range of 5 - 40 nm were formed in the absence of PEG-300 (Figures 5-12b and 5-13).

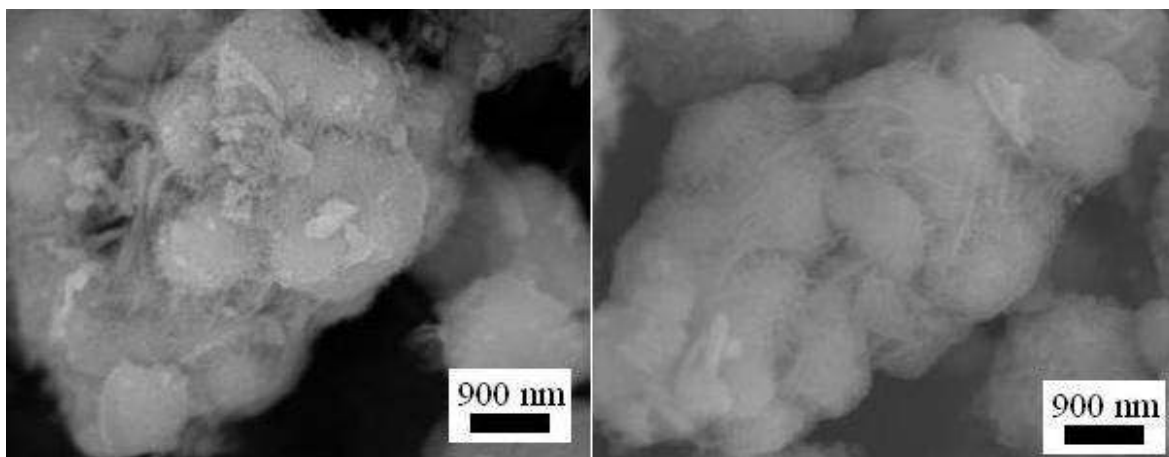


Figure 5-11. SEM micrographs of core-shell particles obtained in the presence (a), and absence (b) of PEG-300 and heat treated at 673 K.

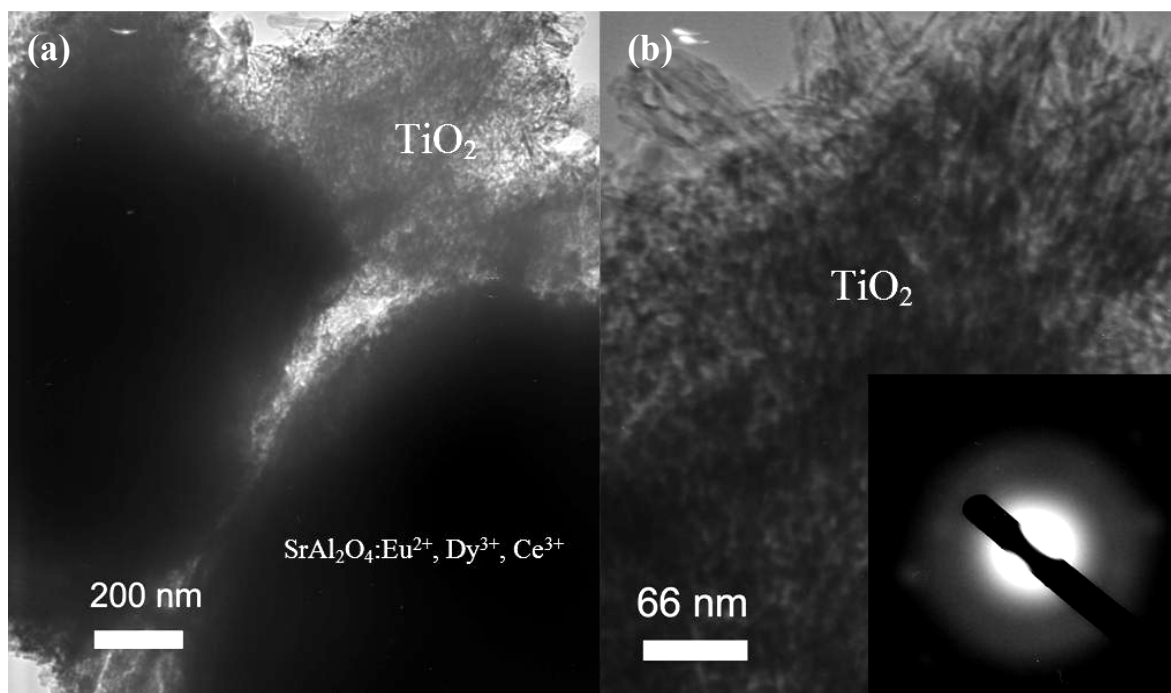


Figure 5-12. TEM micrographs of core-shell particles obtained in the presence (a), and absence (b) of PEG-300 and heat treated at 673 K.

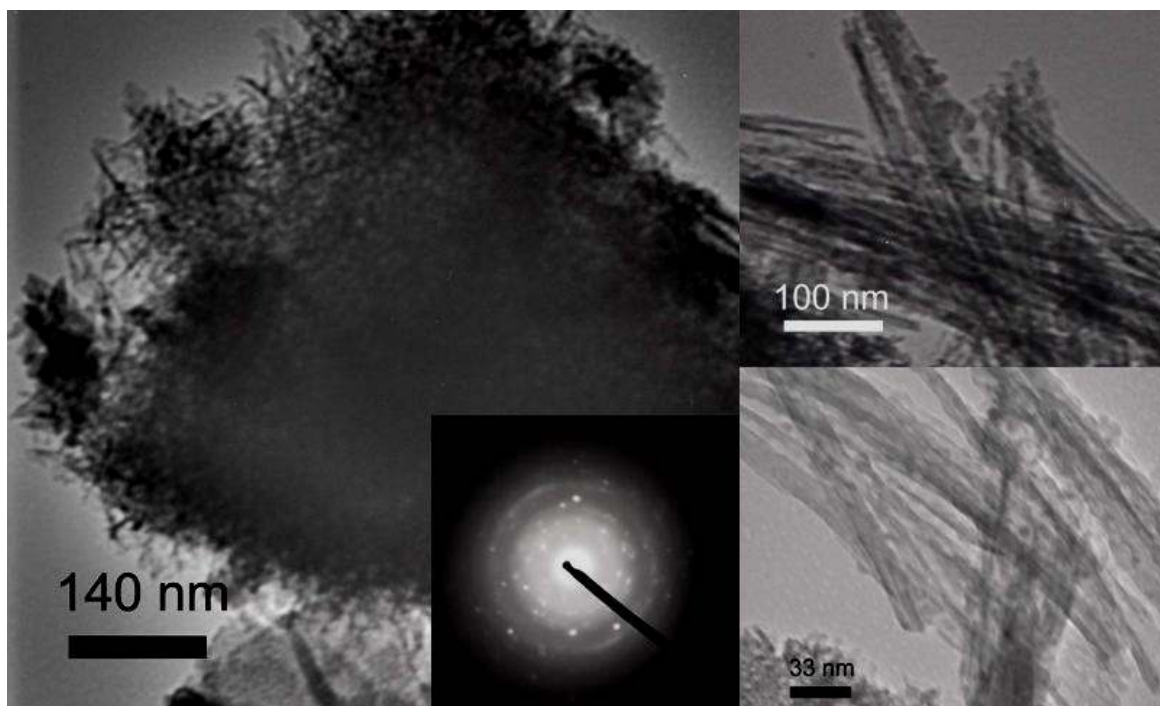


Figure 5-13. TEM micrographs of core-shell particles obtained in the absence of PEG-300 and heat treated at 673 K.

5.4.2. ^{13}C and ^{27}Al MAS NMR of core-shells

In order to get more insight on the structure of the encapsulated samples, solid state NMR studies were performed for the $\text{SrAl}_2\text{O}_4:\text{Ce}^{3+}$, Dy^{3+} , $\text{Eu}^{2+}@\text{TiO}_2$ core—shells (**Figure 5-14**). The NMR chemical shifts (δ) of ^{13}C and ^{27}Al were determined for the atomic structural environment at the nearest-neighbour coordination geometry of OCH_2CH_2 (PEG-300) and $\text{SrAl}_2\text{O}_4:\text{Ce}^{3+}$, Dy^{3+} , Eu^{2+} groups, respectively, after the formation of the TiO_2 coating layer (Figure 5-14). ^{13}C CPMAS NMR analysis shows two groups of resonances from the PEG-300: $\text{O}-\text{CH}_2-\text{CH}_2-\text{O}$ and $-\text{CH}_2-\text{CH}_2-\text{CH}_2-$. The δ yields of ^{13}C were attributed to the CH_2 groups of resonances of the PEG-300 (Figure 5-14a), in ENC1 peaking at 58 ppm and ENC3 sample peaking at about 73 ppm. In these hybrid layers, the ^{13}C δ yields are attributed to the C[3], C[2], and C[1] carbon atoms of the polyethylene glycol that chains, most evidently in ENC3 sample, in the range of 30 and 10 ppm. The δ yields of ^{27}Al in the region between about 18 and 0 ppm present two narrow peaks well evidenced in ENC2 and ENC3 samples peaking at 12.76 and 7.73 ppm, respectively (Figure 5-14b), corresponding to the symmetrical octahedral Al[1] and Al[4] sites of Al environments [144]. In Al—O environments of ^{27}Al MAS spectrum, the ^{27}Al chemical shifts in broad and intense bands between 100 and 50 ppm region were interpreted as resulting from Al[2] atoms of the 4-coordinated Al sites $[\text{AlO}_4]$ tetrahedra displaced from the central position of the SrAl_2O_4 host lattice with tridymite-like structure, peaking at 74.85 ppm. In agreement with previously reported in literature [144], the characteristic tail observed toward ^{27}Al chemical shifts indicates a distribution in Al quadrupolar coupling constants and chemical shifts.

Compared to the uncoated baseline material, ^{27}Al MAS NMR data of encapsulated aluminate nanostructures demonstrate that only small modifications on the $\text{SrAl}_2\text{O}_4:\text{Ce}^{3+}$, Dy^{3+} , Eu^{2+} core are created by the Ti-bonds to the shell layer, more evidenced in the ENC2 and ENC3 samples. On the other hand, ^{13}C MAS NMR data clearly demonstrate the presence of OCH_2CH_2 functional group in the hybrid layer through the covalent bond within the PEG molecules in ENC3. However, this peak disappeared in the sample ENC1 because of the thermal degradation of PEG-300 at 673 K.

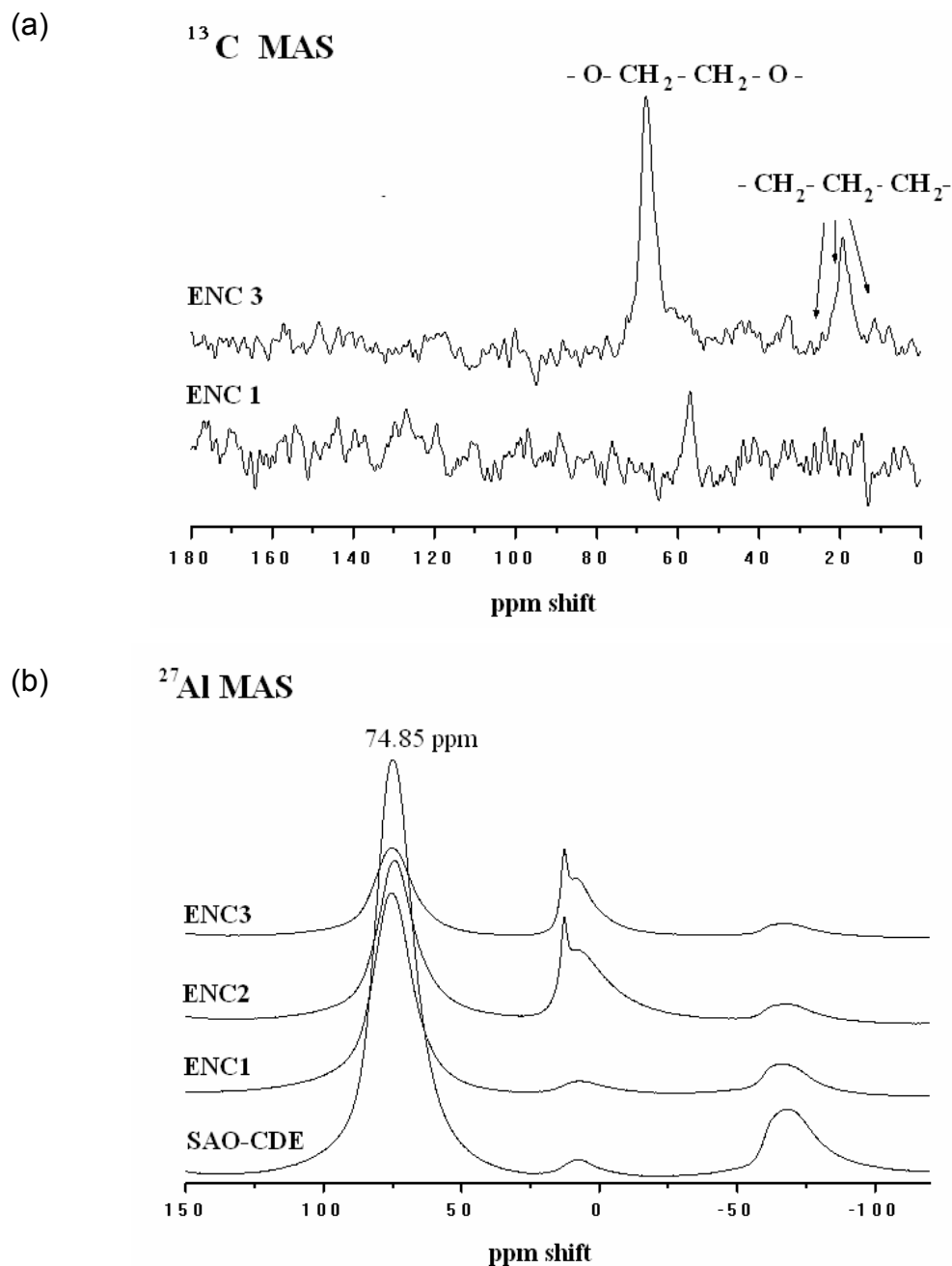


Figure 5-14. NMR MAS spectra of $\text{SrAl}_2\text{O}_4:\text{Ce}^{3+}$, Dy^{3+} , $\text{Eu}^{2+}@\text{TiO}_2$ core-shells obtained in the presence (ENC1 and ENC3) and in the absence (ENC2) of PEG-300 and heat treated (ENC1 and ENC2) and at 353 K (ENC3): a) ^{13}C MAS of hybrid organic-inorganic phosphors; b) ^{27}Al MAS of non-encapsulated phosphor and core-shell particles.

5.4.3. Photocatalytic core-shells

The hybrid and inorganic $\text{SrAl}_2\text{O}_4:\text{Ce}^{3+}$, Dy^{3+} , $\text{Eu}^{2+}@\text{TiO}_2$ core-shells are hereafter represented by the abbreviated formula, Equations (5-2) and (5-3), respectively:



It has been reported that TiO_2 surfaces exhibit superhydrophilicity when ultraviolet light has partially removed oxygen atoms, making water droplets to acquire a flat shape (lower contact angle) [126-130]. The areas from where oxygen atoms were removed are hydrophilic, while the areas where no oxygen atoms were taken away are hydrophobic. This enables to infer that $\text{SrAl}_2\text{O}_4:\text{Ce}^{3+}$, Dy^{3+} , $\text{Eu}^{2+}@\text{TiO}_2$ core-shell particles, Figure 5-15, will exhibit superhydrophilicity characteristics under similar conditions [126-130].

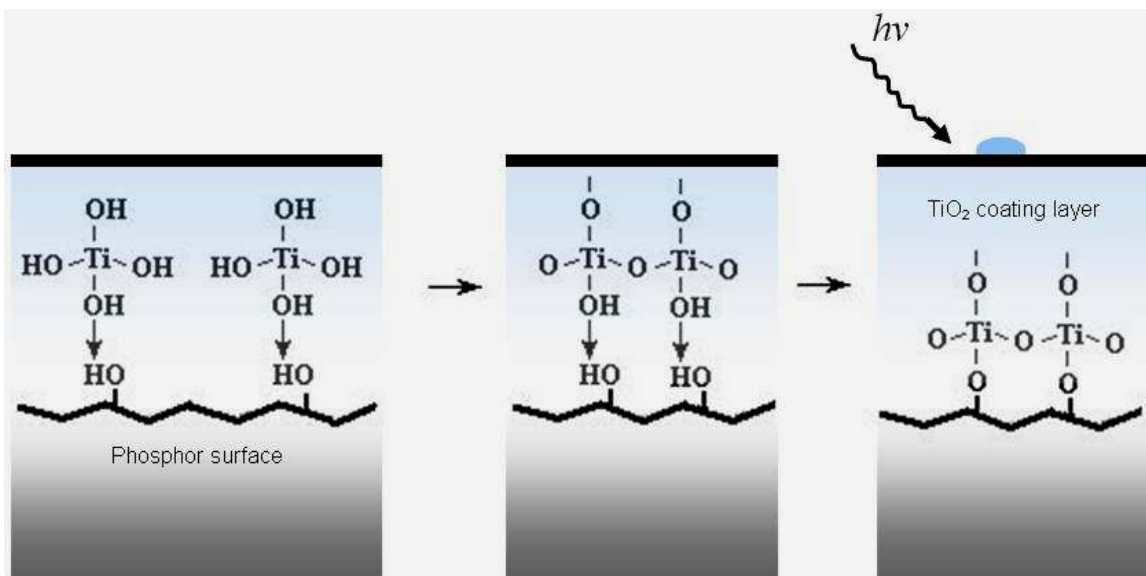


Figure 5-15. Formation of photocatalytic TiO_2 shell on phosphor surface.

Figure 5-16 is useful to express the resulted hole (h^+) and electron (e^-) trapping photocatalytic activity for the hydrophilic \blacksquare - or \blacktriangle - $@\text{TiO}_2$ core-shell particles. Equations from (5-4) to (5-7) describe the formation of $^*\text{OH}$ groups.



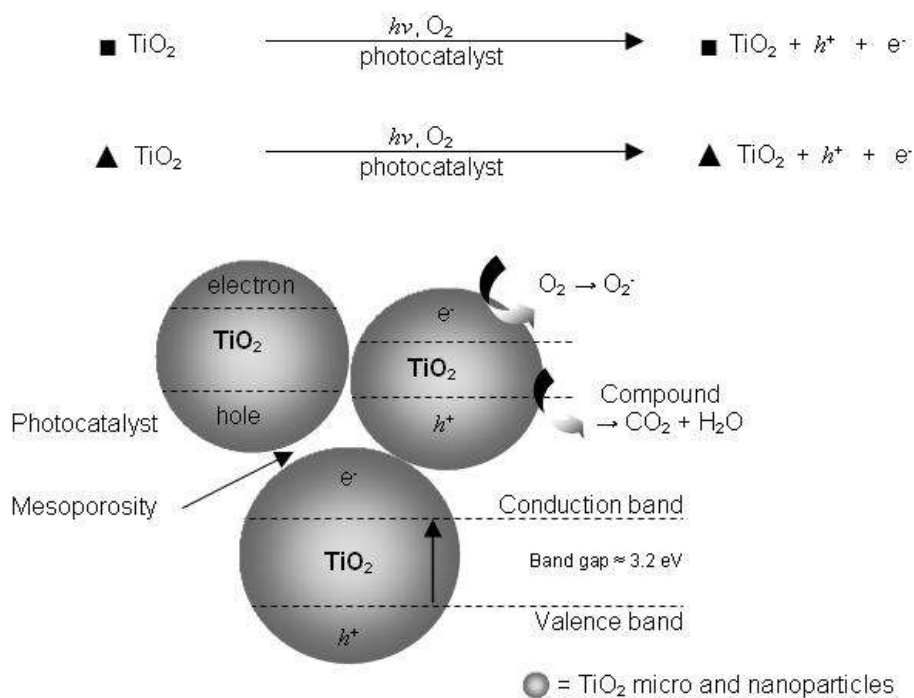


Figure 5-16. Hole trapping model of photocatalytic TiO_2 shell on phosphor surface.

5.4.4. Aqueous resistance of core-shells

The resistance of core-shell to aqueous fluids greatly depends on the thickness and compactness of the coating layer, which, in turn, affects the phosphor photoluminescence. Zeta potential and electronic conductivity measurements were used to estimate the resistance to hydrolysis conferred by the TiO_2 nanotubes shell structure (Figure 5-17). The data obtained from colloidal systems in time-resolved measurements until 3000 minutes showed evidences of chemical stability within the first 240 minutes for all encapsulated samples in presence of aqueous fluids. This indicates that the water resistance property of $\text{SrAl}_2\text{O}_4:\text{Ce}^{3+}$, Dy^{3+} , $\text{Eu}^{2+}@\text{TiO}_2$ core-shells prevails up to about 4 hours in liquid water.

Note that the uncoated particles also presented an increase of the zeta potential and electronic conductivity after contact in water (see Figure 5-2). The outcome difference is that the increase of the zeta potential and electronic conductivity occurred in the core-shells were mostly produced from the shell surface structure — as evidenced by SEM analysis of $\text{SrAl}_2\text{O}_4:\text{Ce}^{3+}$, Dy^{3+} , $\text{Eu}^{2+}@\text{TiO}_2$ core-shells up to 240 minutes (Figure 5-18), while in the uncoated sample underwent extensive hydrolysis of the crystalline host lattice (Figure 5-3).

Considering that PEG molecules are expected to undergo thermal degradation under 673 K, no difference should be expected between the samples ENC1 and ENC2, which were encapsulated in the presence and in the absence, respectively, of PEG. As a matter of fact, both samples ENC1 and ENC2 exhibit initial positive zeta potential values close to 3.4 mV. On the other hand, the

sample ENC3 that was encapsulated in the presence of PEG and heat treated at 353 K shows a starting zeta potential of about -11 mV. The difference between this last hybrid shell coating sample and the two former samples can be mostly attributed to the adsorption/presence of PEG at the surface of the ENC3 sample. After the first 240 minutes for all encapsulated samples undergo a similar gradual hydrolysis process as can be deduced from the parallelism of the zeta potential and electrical conductivity curves.

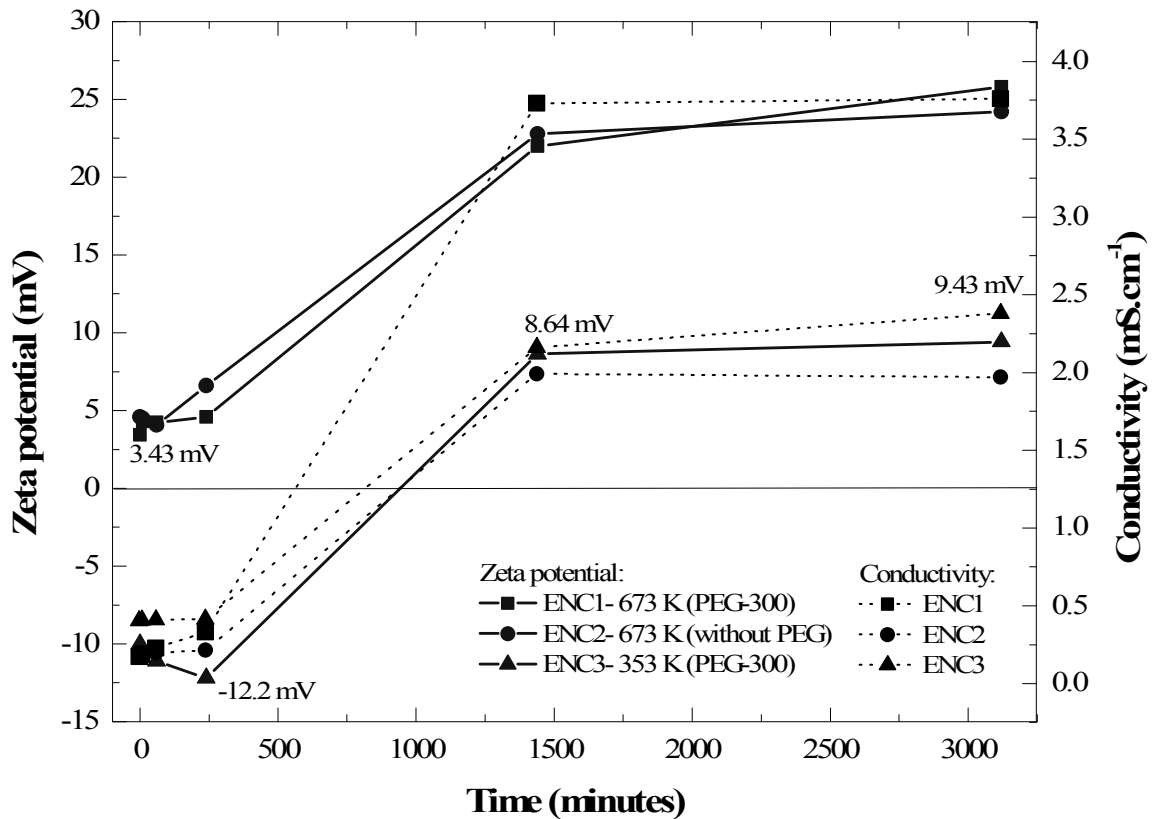


Figure 5-17. Evolution with time of zeta potential and electronic conductivity for $\text{SrAl}_2\text{O}_4:\text{Ce}^{3+}, \text{Dy}^{3+}, \text{Eu}^{2+}@\text{TiO}_2$ core—shells dispersed in water.

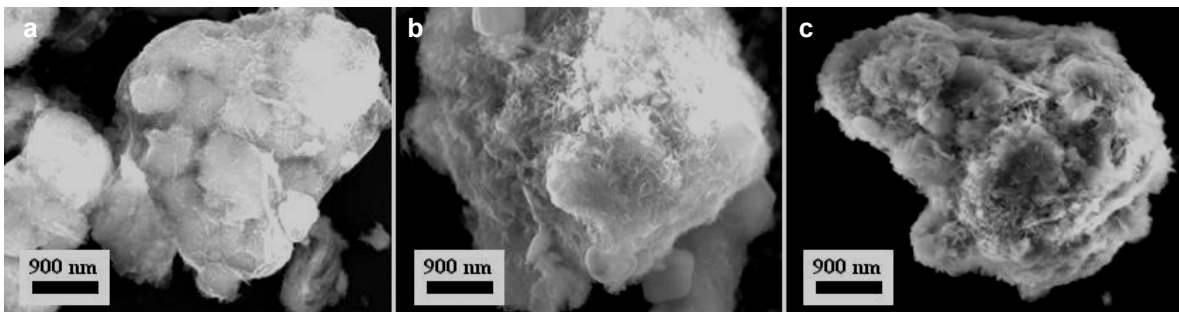


Figure 5-18. SEM analysis of the $\text{SrAl}_2\text{O}_4:\text{Ce}^{3+}, \text{Dy}^{3+}, \text{Eu}^{2+}@\text{TiO}_2$ core—shell samples, after 240 min exposed in aqueous fluids: a) ENC1; b) ENC2; and c) ENC3.

5.4.5. Antiseptic, antimicrobial and antibacterial core-shell nanoprobe

Antimicrobial and antibacterial properties have been attributed to $\text{SrAl}_2\text{O}_4:\text{Ce}^{3+}$, Dy^{3+} , $\text{Eu}^{2+}@\text{TiO}_2$ core-shell nanoprobes. These actions derive from the titanium coating layer as antiseptic agent [130, 142], because the hydroxyl radical $^{\bullet}\text{OH}$ groups produced during the photocatalytic activity under UV irradiation on the titania shell are highly toxic to the microorganisms. More specifically, the respective core-shell particles are potentially characterized by the defence property against the following microorganisms:

- *Staphylococcus aureus* (MRSA);
- *Escherichia-coli* (E-coli);
- *Salmonella*, *Candida albicans*;
- *Vancomycin-Resistant Enterococci* (VRE);
- *Colon Bacillus*;
- *Enterococcus faecalis* (E. faecalis);
- *Pseudomonas aeruginosa* (P. aeruginosa);
- *Bacillus cereus* (B. cereus)
- Etc.

All the above mentioned properties confer to the luminescent $\text{SrAl}_2\text{O}_4:\text{Ce}^{3+}$, Dy^{3+} , $\text{Eu}^{2+}@\text{TiO}_2$ core-shells a multifunctional nature. The $\text{MAl}_2\text{O}_4:\text{Ce}^{3+}$, $\text{Ln}@\text{TiO}_2$ core-shell particles (M = Be, Mg, Ca, Sr or Ba) may be employed in medicinal applications. For example, the coated products could be thought as a component for formulating luminescent dental pastes [145]. *In vitro* and *in vivo*, the core-shell nanoprobes would allow the control of functional, temporal and systemic use of drug delivery compounds. Furthermore, the core-shells might be a proficient material for the formulation of antibiotic, anti-infectious and antiviral medicaments, in the capture, destruction or decrease of the aerobic activity of microorganisms, and in the formulation of vaccines. *In vivo* imaging, these luminescent nanoprobes would be useful for cells detection by light emission in wavelength range of the infrared (IR) and ultraviolet visible (UV), such as in Nuclear Magnetic Resonance (NMR) contrast agent.

5.5. Conclusion

Water resistant, antimicrobial, antibacterial and luminescent $\text{SrAl}_2\text{O}_4:\text{Ce}^{3+}$, Dy^{3+} , $\text{Eu}^{2+}@\text{TiO}_2$ core-shell particles were assembled by the encapsulation process developed in the frame of this work. The Ti and O atoms from TiO_2 nanocoating layer became covalently bonded to core material providing electrons to the unsaturated metal ions (Sr^{2+} , Al^{3+} , Eu^{2+} , Dy^{3+} , Ce^{3+}) on the phosphor core surface. The photocatalytic activities of the shell conjugated with the persistent luminescence of the core are expected to potentiate applications in emergency (chapter 7). ■

Chapter 6

Biometric personalization of $\text{SrAl}_2\text{O}_4:\text{Ce}^{3+}$, Dy^{3+} , Eu^{2+} colour emission

Herein, the photoluminescence colour emission of $\text{SrAl}_2\text{O}_4:\text{Ce}^{3+}$, Dy^{3+} , Eu^{2+} material was personalized for trial groups, aiming it visual detection in emergency signalling. Focusing in this approach, an ophthalmic medical equipment was developed, involving the acquisition of biometric data from retinal diagnostic tests with the end users, upon the photopic colour vision biofunctionality in white/black backgrounds. In experimental studies, the retina cell responses were obtained from individuals with diabetic retinopathy (treatment group, $n=38$), in comparative diagnostics from voluntary fireman (reference group, $n=38$). All diagnostics were statistically treated through ANOVA (intergroup), T-test (intragroup) and Pearson correlation analysis. The results indicate that the treatment group presents lower log error score in black background, suggesting a better colour contrast sensitivity in the persons with diabetic retinopathy. On the blue-green UV-VIS region (~555-485 nm) tested in diabetics, the mean error scores in black background was above 5. The best colour vision quality of treatments was C44 as an ideal wavelength region for photoluminescence colour emission (~495 nm) and visual detection from these diabetic eyes. Moreover, the portability of the equipment (cabinet) enables to enlarge the number of individuals that can be seen in different geographical locations, and should be further investigated for the practice of ophthalmic telemedicine and personalized approaches.

Key-words: medical equipment, retinal cells, personalized approach, colour emission, diabetes.

PART I — EYE-BIO-VIS TELEMEDICAL WORKSTATION

In this section, conventional and computational Farnsworth-Munsell 100-HUE colour vision tests realized in pre-clinical studies are described. After this stage, the development of new ophthalmic medical equipment for retinal diagnostic tests of photoreceptor cells is discussed.

6.1. Pre-clinical colour vision FM100-HUE test

A pre-clinical colour vision FM100-HUE test was realized in 2006, in collaboration with the Professor Dr. Eugénio Óscar Baptista Leite, Ophthalmologist from Leite & Leite Ocular Microsurgery, Coimbra, Portugal. The feasibility of initiating this kind of experimentation was supported by a previous study realized about ophthalmologic biomaterials [146]. The method and respective equipments used during this pre-clinical stage are described as follows:

- Photometry of tests: illuminance measurements using digital luximeter LDR-208 with sensor –cell for different light sources (day light, fluorescent, tungsten, and mercury);
- Farnsworth-Munsell 100-HUE test in caps (conventional) or computational system (digital): computer Compaq 2100, using a software Visual Acuity and Colour Vision Test 1.01;
- Monitor Siemens 19" LCD 19-C with colour calibration in 6500 Kelvin temperature;
- Monocular occluder.

Figure 6-1 shows the examination of retinal cells via FM100-HUE test, in conventional colour caps (left), and in computational digital testing (right), monocular and binocularly.



Figure 6-1. Comparative diagnoses from pre-clinical standard and computational colour vision FM100-HUE test, Leite & Leite Ocular Microsurgery, Coimbra, Portugal (2006).

During this pre-clinical stage, it was concluded that it was difficult to repeat the standard test under alterations on the illuminance above 250 lux owing to the spatial lighting conditions. This result motivated the development of a medical equipment for testing the biofunctionality “*in space*”.

6.2 Designing the ophthalmic medical equipment [147]

The development of the ophthalmic medical equipment «*Integrated Cabinet for Visual Clinical Analysis*», or **EYE-BIO-VIS Telemedical Workstation**, is a contribution towards solving the problem of standardization of illuminance during eye examinations. In ophthalmology, this equipment might be used to assess the diagnostic of retinal cells by computational visual acuity (e.g. Snellen) and colour vision (e.g. Farnsworth Munsell 100-HUE) tests. The equipment also allows the development of personalized materials with custom functions associated to the retinal cells biofunctionality of the end users.

6.2.1. Construction and spatial configuration of the medical equipment

The solutions for medical equipment (e.g. lightning system, focal plan, dimensioning) were designed by CAD 2D/3D virtual modelling (Figure 6-2). The spatial configuration consists in an ophthalmic standard lighting, constant fluorescent illuminance (>500 lux), with additional emission of a UV lamp, which allows the activation of photoluminescent materials in wavelength shift of about 360 nm. The light emission in the cabinet is controlled by a digital photometer. The equipment with a daylight illuminance (D65) may be adjusted with other illuminant settings with intensities greater than 250 lux (minimum).

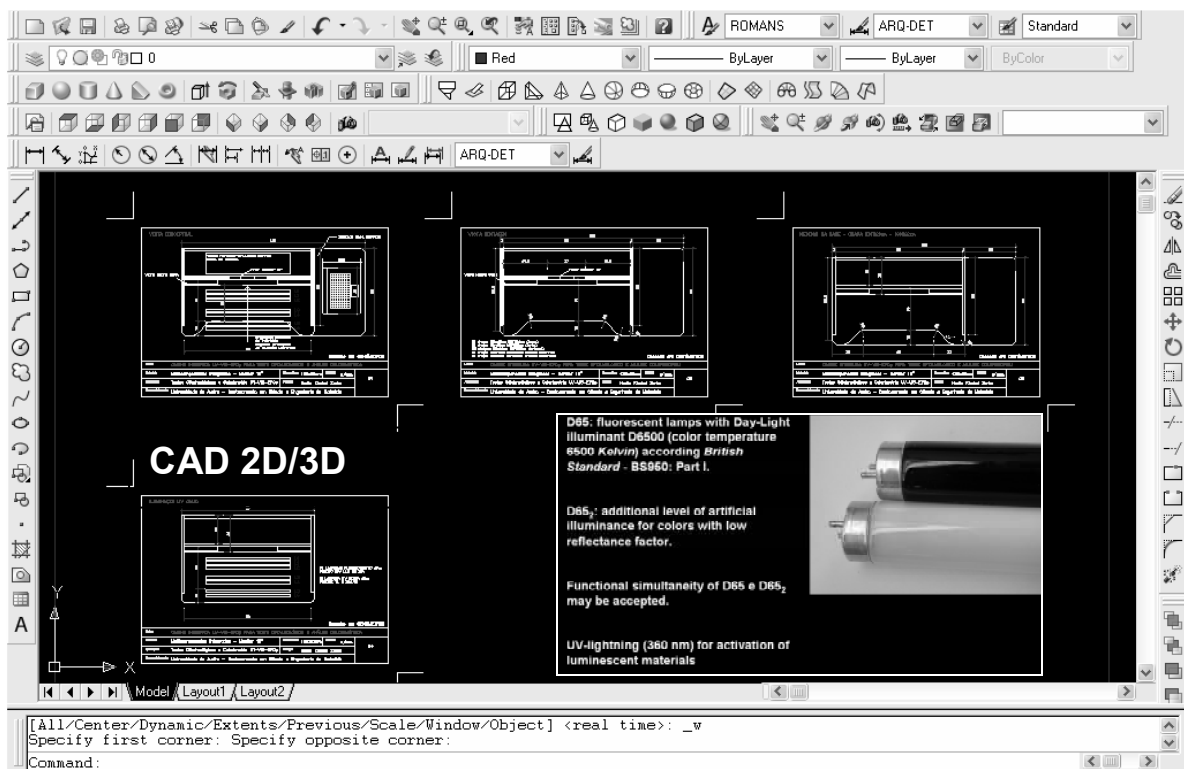


Figure 6-2. Designing the solutions for the medical equipment (e.g. lightning system, focal plan, dimensioning) by CAD 2D/3D virtual modelling; lightning system of the medical equipment with D65 and UV-dark (360 nm) illuminance.

6.2.2. Components of the medical equipment

The medical equipment presents the following components and characteristics:

- (i) Attached monitor (or coloured caps) for ophthalmic testing;
- (ii) Lighting system in ophthalmic standard;
- (iii) Adapted format to different ergonomic patterns and health conditions of patients, including elderly users, people with temporary or permanent disabilities, adults or children;
- (iv) Hardware: video monitor (optional touch interface) and a complete computer;
- (v) Software: ophthalmic test program, the treatment program of statistical data, program storage and transfer of files, in network communication systems (for use in telemedicine).

6.2.3. General instructions for use the medical equipment

For use the medical equipment (Figure 6-3), the electrical current is needed, and the following procedures are indicated:

- Connect the equipment to electricity current (120/220 V);
- Connect the switch to light bulbs;
- Connect the computer and monitor;
- Perform the measurement of illuminance (digital luximeter);
- Run the computer program of ophthalmologic testing.

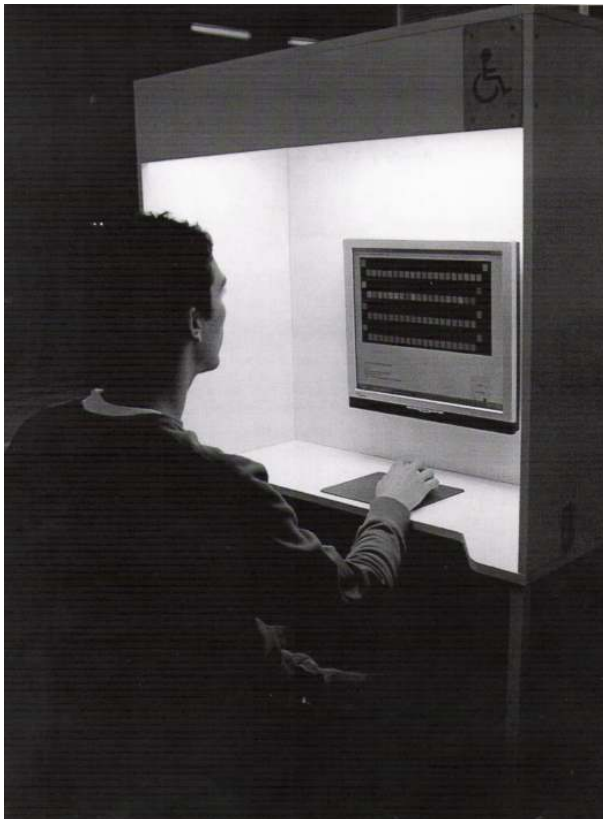


Figure 6-3. Medical equipment testing retinal cells “*in space*”, medical equipment prototype with dimensions 930 x 830 x 620 mm constructed at Ceramic and Glass Engineering Department of University of Aveiro, Portugal.

6.3. Biometric personalization of materials by retinal diagnostic

In this topic, a method for the acquisition of digital biometric data is explained from the retinal diagnoses and focused on the personalization of photoluminescent materials.

6.3.1. Interactive testing eyes

The personalization of materials is defined as the act to produce materials with a specific and appropriate function, and visual characteristics derived from biometric data of the end user(s). The method of personalization of materials developed is characterized by:

- **an interactive procedure (user, evaluator and equipment);**
- **the biometry (retinal biofunctionality),**
- **biostatistics (diagnostic of population);**
- **multimedia output (conversion of digital data and function).**

All procedures of the method are performed at the medical equipment in a constant spatial configuration. These procedures involve the following 2 steps:

- testing of eye colour vision (and/or visual acuity), which eye tests are used to obtain the diagnosis of biofunctionality of retinal cells photoreceptors (rods and L- M- and S- cones) and identify the colour perceived with different intensity and incidence of errors sensitivity;
- using the diagnostic output to customize materials from multimedia data; the selected diagnoses by the user or evaluator are used to implement an associated function to the retinal cell biofunctionality of the end user.

The method may be applied in standard conventional ophthalmic tests (coloured caps) and the standard digital ophthalmic tests (computer), depending of the ability to handle the technology of testing. The use of the equipment may produce personalized materials that are potentially visible from different abilities and limitations of the visual system of the end user.

The evaluator procedures aim at producing:

- Individual personalization: one user;
- Collective personalization: users in reference/treatment groups;
- Registration of diagnoses: digital file or printed output.

Initially, the tests are interactively performed to user(s) on the ophthalmic medical equipment (Figure 6-4). The diagnoses of the retinal biofunctionality are recorded on the computer. The storage, processing and data transfer is done so that the user or evaluator can select data to be converted into multimedia output, including a biostatistical analysis. The optical properties of personalized materials prevail even under different light conditions, because they were determined by the ocular biometry of colour vision of the end user in optimal lighting conditions, becoming the retinal biofunctionality of the photoreceptors cells "*in space*" as the predominant condition for personalization.

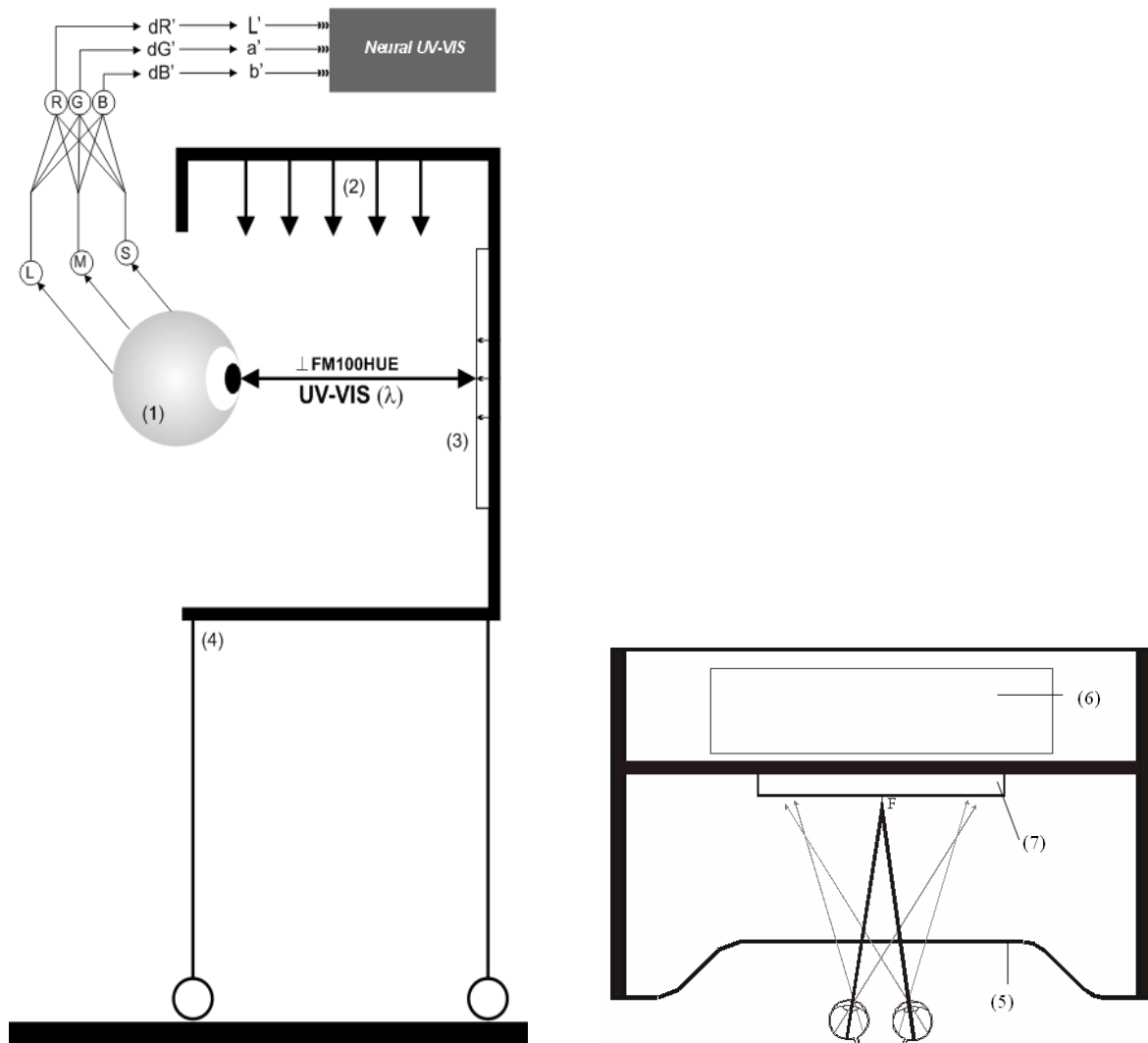


Figure 6-4. Medical equipment with biofunctional outline of the method according to the light generated [147]; (1) the human eye receives stimuli in several wavelengths, with constant focal distance between the observer and monitor (~ 0.40 m) in standard monocular (right/left eye) and binocular vision during the test; scheme of the biofunctionality responses in ocular neural network (multimedia), which may be represented in colour coordinates (e.g. RGB, CIEL*a*b*); (2) the photoreceptors cells are exposed to the stimulus upon the retina light rays entering the pupil from fluorescent lamps with illuminance higher than 500 lux, according to the standard illuminant D65; (3) the FM100-HUE test made on the computer generates colour signals emitted by the cathode luminescence of matches based on rare earths, with luminance typical of a commercial monitor (~ 250 cd/m²), valid for the sensitivity of photoreceptors in the long (L), medium (M) and short (S) wavelengths of the visible spectrum of light (350-750 nm); (4) the spatial configuration is ergonomically adapted for all users (e.g. persons in wheelchairs), and with castors on the metallic base to facilitate the portability of the equipment; diagram of a binocular testing biofunctionality of photoreceptors cells "in space", showing: (5) medical equipment with ergonomic adapted shape; (6) local for the conventional FM100-HUE test (caps); and (7) geometric configuration of the focal length between the user and monitor.

Table 6-1 shows the comparative aspects between conventional and digital colour vision test from the medical equipment.

Table 6-1. Comparative aspects in the FM100-HUE test using the medical equipment.

Devices	Conventional caps test (CCT)	New digital generation test (DGT)
Equipment and materials	Wood play and plastic caps with coloured surface ("caps") in black background	Computer and specific <i>software</i> for selection of "squares" in white and/or black background
Administration	D65 (Illum. "C") Illuminance > 250 lux (25 ftc) Observer $\angle 60^\circ$ Light source $\perp 90^\circ$ Long time sessions Time interval between the tasks	D65 (Illum. "C") Illuminance > 250 lux (25 ftc) Observer from $\angle 60^\circ$ to $\perp 90^\circ$ Light source $\perp 90^\circ$ Short time sessions Continued tasks
Data collection	Manual construction of score $S_i^n = X_i, \dots, X_n$ Manual construction of graph	Automatic determination of score Automatic construction of polar graph
Data obtained	Graphic containing errors in unitary curve lines from 2 to 14 Wavelength (λ) in nm	Automatic numeric linear score Graphic containing errors in discrete curve lines of errors in 5, 10 and 15 intervals Interface for colour graphic capture is CIEL*a*b* coordinates
Liability and optimization	Error introduced by paper print (less colour of the caps) Error introduced during the data collection and treatment	Error introduced by the monitor calibration
Compliance between the standard tests	Normalization of standard scores requires an application of a "filter" for simplification of values less than 5, and a discrimination to 5, 10 and 15 error peaks	Direct normalization of automatic standard scores No characterization of errors incidence in wavelength (nm)

To achieve the goal of the personalization of materials, the following procedures are required:

- (1) selecting a user (individual personalization) or a group of users (collective personalization) with the a priority criterion for personalization;
- (2) performing interactively the ophthalmologic test (e.g. Farnsworth-Munsell 100-Hue colour vision test) with the user at the medical equipment "*Integrated Cabinet for Visual Clinical Analysis*" in classic mode (coloured caps) or in digital mode (specific software);
- (3) diagnosing the biofunctionality of retinal photoreceptors rods and L-, M- and S-cone cells "*in space*" according to errors incidence registered on colour vision graphs/scores;
- (4) identifying the colour patterns obtained (e.g. luminance or brightness, saturation and tones) with best match profiles for the users;
- (5) converting the selected diagnoses represented in a colour space (e.g. Munsell, CIEL*a*b*) via ocular neural network with multimedia data, in order to define an **Optimized Preferential Spectrum (OPS)** for each user;
- (6) implementing a function associated to the retinal biofunctionality in a personalized material;
- (7) making use of a personalized material in spatial conditions similar to the illumination pattern of the medical equipment.

In view of the materials personalization in industry applications, the point (2) above refers to the colour vision test at the equipment, also serving to colour processing, visual inspection and colorimetric measurements of samples, similarly to those required in the automotive industry and pigment companies; the selection referred in paragraph (1) to diagnose the visual colour ability is performed by an ophthalmologist (3); to identify the colour patterns (4) and to convert the selected diagnoses (5), other professionals might be involved. In this method, the variable that prevails is the ability of the human eye to perceive and identify the colour, in photometric conditions, satisfying the points (1), (2) and (3) described in the goals.

The method of materials personalization comprises:

- **Light source** (optional configuration): fluorescent lamps (D65) and UV dark-lamp (activation at 360 nm) with light emission in a vertical angle of 90 degrees; illuminance >500 lux at visual focus (minimum 250 lux).
- **An ophthalmic test** to measure the biofunctionality of retinal cells in the cabinet, where the degree of colour vision is required by the ability of photoreceptors cells of the human eye (rods and L-, M- and S- cones); it is suggested the type Farnsworth-Munsell 100-HUE (FM100-HUE) test in large populations using a software (in calibrated monitor); if is not possible to perform the tests in the computational environment, coloured caps may be used for colour evaluation from the conventional ophthalmology.
- «**Integrated Cabinet for Visual Clinical Analysis**».

The ophthalmic tests are interactively performed by testing the user eyes *in space* at the medical equipment, as shown in Table 6-2.

Table 6-2. Ergonomic parameters for interactive testing eyes.

Ergonomic parameters	
Posture	sitting (including use of wheel chair)
Visual distance	~ 1.15 m
Focal length (F)	~ 0.40 m
Visual angle	90 ° to 60 °
Ocular vision (with/without occluder device)	monocular right-eye (RE)
	monocular left-eye (LE)
	binocular (BIN)

6.3.2. Retinal diagnoses of biofunctionality from the end user(s) *in space*

The type of diagnosis made in the cabinet configuration is called "*in space*" (in Latin "*in spatium*"), in addition to traditional biomedical procedures "*in vitro*" and "*in vivo*". This definition is assigned to the diagnoses of biofunctionality of the retinal photoreceptor cells obtained at a given spatial configuration, constant, which is always located at the medical equipment. The acquisition of

diagnoses can be made by any user who is not blind. The degree of accuracy of a type of colour vision is measured, for example, via FM100-HUE test, typically determined by numerical results (0-85) and in radial polar graphs. The use of digital graphic is needed, especially to convert the values of Munsell to *CIEL* *a*b* colour coordinates.

Table 6-3 presents a matrix model of data processing (partial structure) for biostatistics validation of the method of materials personalization for a collective group of individual diagnoses (n), and filled with the respective numerical result (score number) of the colour axis tested (e.g. red/yellow). For large scale applications, it is suggested a result treatment by using a stratified biostatistics sampling (e.g. children of preschool age).

Table 6-3. Matrix model of ophthalmic data processing.

Patient [n]	Monitor space	Ocular vision (RE/LE/BIN)	Colour numerical results (C) FM100-HUE test										
	Background		Red/Yellow axis										
			C1	C2	C3	C4	C5	C6	C7	C8	C9	C10	(Ci)
n ₁	White	LE											
		RE											
		BIN											
	Black	LE											
		RE											
		BIN											

6.3.3. Biometric data conversion via ocular neural network

The portability of the equipment enables the development of personalized materials and products with colour recognition biometric-based via an ocular neural network. Some examples of colour data conversion (and numerical result) obtained from the user's visual ability in digital media are described (to use in the equipment):

- FM100-HUE (OPS) → Munsell → (V, A, B) → (L*a*b*)

Conversion values: $V=V$ $A=C \cos\left(\frac{2\pi H}{100}\right)$ $B=C \sin\left(\frac{2\pi H}{100}\right)$
- FM100-HUE (OPS) → (L*a*b*) Munsell → (V, A, B)

Conversion values: Normalization $L^*a^*b^*$ [-1,1] → Normalization H, V, C [0,1]
- FM100-HUE (OPS) → (L*a*b*) = (H1, V1, C1) → Munsell (H2, V2, C2)

Conversion values: $\Delta E = \left\{ 2C_1C_2 \left[1 - \cos\left(\frac{2\pi}{100}(H_1 - H_2)\right) \right] + (C_1 - C_2)^2 + 16(V_1 - V_2)^2 \right\}^{\frac{1}{2}}$

6.3.4. Personalized materials

Personalized materials derived from this method, including ceramics, plastics, textiles, printing, "Light Emitting Diodes" - LED and others, might be suitable for applications in the biomedical area, assistive technology, accessibility, construction, architecture, physical medicine and rehabilitation. Some functions that may be associated to the personalization are described as follows:

Personalized coloured material:

Selection of colour coordinate data from the biofunctionality of retinal photoreceptors cells of the end user; adequacy of reflectance (R), absorbance (A) and transmittance (T) of materials.

Personalized photoluminescent material (coloured):

Selection of colour coordinates from the biofunctionality of retinal photoreceptors cells in dark contrast background, valid for the first minute of the photoluminescence light emission after end the light stimulus, by comparing the diagnoses from white to black background, matching the luminance (L), and lifetime (τ) adequacy of the individual limit of visibility of the human eye.

Personalized transparent material:

Adequacy of the refraction index (n), and adequacy of the dielectric constant (ϵ_r).

Personalized ophthalmic (bio)material:

Adequacy of the dioptr degree of artificial lenses (transparent material), adjustment of UV-filter, colour appearance of lenses (aesthetics), extra-ocular eyeglasses, or intra-ocular lens (e.g. IOL's opacification by bacteria adhesion, degradation or changes in the eye projection in cataract patients), binocular adequacy of implants (opaque material) or optical aids (e.g. orbital eye).

PART II — PERSONALIZATION OF LUMINESCENCE EMISSION

In this topic, the colour vision is investigated in the range of UV-VIS region at about 488-555 nm, using the medical equipment, for the biometric personalization of photoluminescence emission.

6.4. Retinal diagnostic test for personalization of PL materials

JUSTIFICATION OF THE CASE STUDY

Rodgers et. al [148] reported that the early stages of retinopathy are usually asymptomatic with respect to the quality of vision experienced by the patient. However, the changes observed in the early stages have been shown to be predictive of progression to sight-threatening proliferative retinopathy and maculopathy. Therefore, these authors recommend that early identification and monitoring of retinopathy is crucial for successful management, and regular screening examinations for sight threatening retinopathy are an essential part of effective diabetes care. According to *Ong-Casswell* [149], **colour vision assessment is an effective and clinically viable technique for detecting 'sight threatening diabetic retinopathy' (STDR)** before visual loss. *Wong-Chong* [150] reported that the debilitating nature of untreated diabetic retinopathy promotes the need for screening methods, which can reduce blind registration due to diabetes. From this reality, the trial examination of patients with diabetic retinopathy (treatment group) against reference group of rescue team of fireman, including only individuals that did not have a medical record of diabetes and, at the time of the investigation, did not have glucose level in the blood over 120 mg/dL, was investigated in a multidisciplinary outlook.

CRITICAL REVISION

Study selection, data extraction and quality assessment were undertaken by five specialist reviewers, independently, from 2006 to 2010, on the follow topics:

- **Medical equipment and trials:**
 - (1) Dr. Eugénio Óscar Baptista Leite, Ophthalmologist, Specialist in Cataract Surgery, from the Leite & Leite Microsurgery, Coimbra, Portugal;
 - (2) Dr. Paulo Torrão Fiadeiro, Physics, Associate Professor from the Department of Physics, University of the Beira Interior, Covilhã, Portugal;
- **Tests in patients with diabetic retinopathy:**
 - (3) Dr. Manuel dos Santos Mariano, Ophthalmologist, Medical Director of the Sector of Ophthalmology, from the Infante Dom Pedro Hospital, Aveiro, Portugal;
- **Biostatistical plan definition and analysis:**
 - (4) Dr. António Arsénio Nogueira, Statistician Biologist, Associate Professor, from the Department of Biology, University of Aveiro, Aveiro, Portugal;
- **Diabetic retinopathy:**
 - (5) Dr. Hean-Choon Chen, Ophthalmologist, Specialist in Diabetic Retinopathy [63e], from the Derby Hospitals, NHS Foundation Trust, London, United Kingdom.

OBJECTIVES

This study was focused on the following specific objectives:

- (1) To validate the functional aspects of the ophthalmic medical equipment (ergonomy, illuminance reference, transportation and data acquisition), for measurements of the colour vision, using the real prototype;
- (2) Satisfied the objective (1), to measure the colour vision (quality accuracy and sensitivity to the background contrast) of trial individuals, for personalization of PL materials light emitting at 485-555 nm, aiming at improve the PL visibility as a vital factor in emergency signalling.

METHOD

The method used was an exploratory analytical approach by **conglomerate** (C1= Hospital, and C2= Firemen Society). These places were selected by the geographic location, facility to transport the equipment and recruitment of the populations. Samples were recruited by cotes into the conglomerated: **treatment**-patients with known diagnosis of diabetic retinopathy, and **reference**-healthy voluntary fireman. Computational FM100-HUE colour vision test at the medical equipment and documented interview (ANEX III) were realized. The **non-probabilistic trial samples were valid for a specific personalization of PL materials** — non-valid as representative of the total population of patients with diabetic retinopathy and/or firemen. Section 6.3 described the method of personalization of materials.

SUBJECTS

A total of 85 individuals were examined. Trials of 38 patients with diabetic retinopathy at the hospital (treatment group) and 38 firemen were enabled for the study (reference group).

Inclusion criterion (treatment group): to be a patient with diabetic retinopathy previously diagnosed in the hospital.

Exclusion criteria (reference group): an individual who presents retinopathy; or records of diabetes type I or II; or glucose level over 120 mg/dL; or historic of an ocular trauma in one eye.

CONGLOMERATE SETTING

Ophthalmic Medical Sector, Infante Dom Pedro Hospital (Figures 6-9a, 6-10, and 6-11) and Bombeiros-Velhos Humanitarian Society of Voluntary Firemen (Figure 6-9b), Aveiro City, Portugal from November 17 to December 24, 2009. Clinical tests were conducted according to the standards of Ethics Committee Regulations - Clinical Trial Directive of the Infante Dom Pedro Hospital policies and procedures. All subjects were provided with an information sheet describing the elements of this study and sufficient information for subjects to make an informed decision about their participation in this study. See ANEX III for a copy of the Information Sheet. The subjects completed and signed a consent form to indicate that they given valid consent to participate.

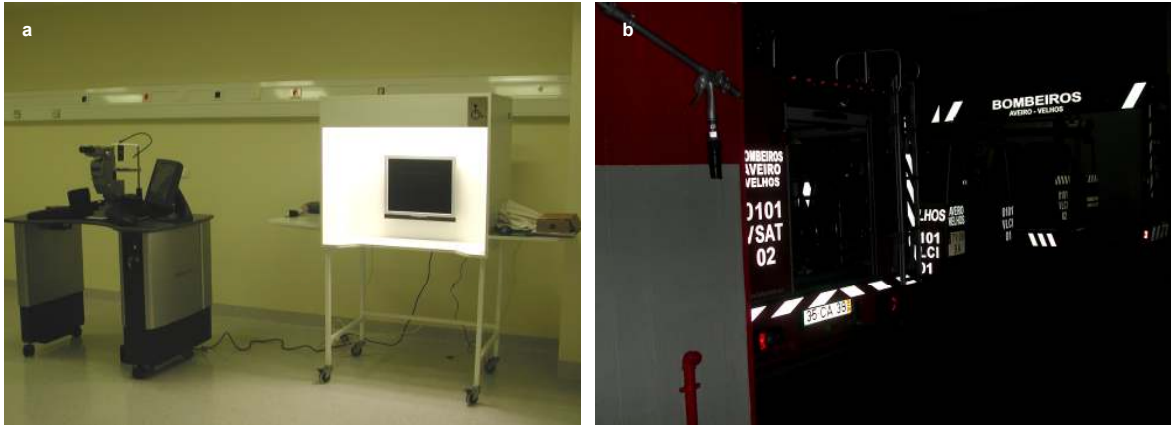


Figure 6-5. Conglomerated places where the samples were recruited and the medical equipment was experimented, in Aveiro, Portugal (2009): a) Ophthalmologic Medical Sector of the Infante Dom Pedro Hospital (treatment); and b) Humanitarian Society of Voluntary Firemen (references).



Figure 6-6. Medical equipment experimented in 38 patients with diabetic retinopathy (treatment) located in the Ophthalmologic Medical Sector of the Infante Dom Pedro Hospital, Portugal (2009).

STATISTICAL ANALYSIS

The main outcome measures were FM100-HUE error scores, age, glucose levels and their deviations. ANOVA analysis of log error scores was made with covariates (age and log glucose) to evaluate the group factor from comparative results obtained by the reference and treatment. Paired T-tests were realized to compare the log error scores in white and black background from trials. Parametric biostatistics by Pearson correlation coefficients (r , +1,00 to -1,00) and their significances ($p < 0,05$) were calculated to compare the correlations between the log error scores and variables. Correlation analysis of the treatment group from log error scores in black background, namely for (C31-C53) numerical results around 485-555 nm, was made for personalization. The colour vision (C35), corresponding to the $\text{SrAl}_2\text{O}_4:\text{Ce}^{3+}$, Dy^{3+} , Eu^{2+} luminescence emission at 525 nm, was specifically analysed.

INTERVENTION

Phase I: successive sessions on the medical sector were realized during the time period of attendances in the hospital. Dislocation of the equipment was supported with fireman transport when ended the phase I.

Phase II: successive sessions on the firemen corporation were realized.

From these two phases, the binocular retinal biofunctionality for photopic colour vision was valid for 76 individuals examined (152 eyes). Glucose levels (mg/dL, or mmol/L) were measured by a blood glucose test meter-sensor Glucocard® sets (*Source: A. Menarini Diagnostics Arkray Factory, Inc. Shiga, Japan*) using a glucoject with no-pain lancets [151]. Reference group of fireman was determined by glucose values above 120 mg/dL and interview, excluding some individuals from the study from this criterion, and by the historic of ocular interventions in one eye. The colour tested to see successive light stimuli of spectral luminescence grade and change in retinal sensitivity pattern was measured through computational Farnsworth Munsell 100-HUE tests, in white/black backgrounds, at the medical equipment (configuration: fluorescent lamps >500 lux, illuminant D65, monitor Siemens 19" LCD, 6500 K with typical luminance of 250 cd/m²) [147].



Figure 6-7. Medical equipment experimented in 38 patients with diabetic retinopathy (treatment) located in the Ophthalmologic Medical Sector of the Infante Dom Pedro Hospital, Portugal (2009).

SCIENTIFIC LIMITATIONS IN OPHTHALMOLOGY

Considering a critical review of the Dr. Hean-Choon Chen from the Derby Hospitals, UK, in agreement with the indications of Dr. Manuel Mariano, PT, this study presents the follow scientific limitations in Ophthalmology:

- a. The population group is small to define general characteristics of individuals with diabetic retinopathy;
- b. The diabetic group is considerably older than the reference group; the type of diabetes mellitus, i.e. type 1 or 2 or a mixture thereof, was not characterized;
- c. The approach did not analyse the type and severity of the retinopathy, type of laser treatment received, or Snellen visual acuities;
- d. It was identified that one third of the diabetic patients studied had cataracts (but was not analysed the type of cataract and severity); this factor is important and may be highly influential, i.e., the benefit that the work infers may be for patients with visual disabilities rather than specifically for patients with diabetic retinopathy.

These limitations were considered for the biostatistical analysis and interpretation of the results on this personalized approach.

6.5. Biostatistical analysis

The main outcome results obtained from the colour vision tests in treatment and reference groups are statistically discussed in the following topics.

6.5.1. Descriptive statistics

The descriptive statistics of the colour vision tests executed in treatment and references are presented from the Table 6-4 to 6-7.

Table 6-4. Descriptive biostatistics of the **reference group** (fireman); the concatenate data were obtained from their responses in white-black backgrounds.

	N total	Mean	Standard Deviation	Sum	Minimum	Median	Maximum
Age (years)	38	39.81579	12.97577	1513	16	38	69
Glucose level (mg/dL)	38	95.13158	17.04869	3615	69	95	120
White background (error score)	38	43.26316	26.46536	1644	8	36	96
Black background (error score)	38	51.15789	32.02915	1944	12	44	140
Concatenate (error score)	76	47.21053	29.45202	3588	8	42	140

Table 6-5. Descriptive biostatistics of the **treatment group** (diabetic retinopathy); the concatenate data were obtained from their responses in white-black backgrounds.

	N total	Mean	Standard Deviation	Sum	Minimum	Median	Maximum
Age (years)	38	65.71053	8.42746	2497	52	65.5	88
Glucose level (mg/dL)	38	191.97368	72.63514	7295	111	176.5	395
White background (error score)	38	197.26316	182.80956	7496	20	138	840
Black background (error score)	38	148.31579	125.13822	5636	20	108	576
Concatenate (error score)	76	172.78947	157.54113	13132	20	114	840

Table 6-6. Descriptive biostatistics of **concatenated error-scores from reference (fireman) and treatment (diabetic retinopathy) groups**, for white and black backgrounds, respectively listed.

	N total	Mean	Standard Deviation	Sum	Minimum	Median	Maximum
Concatenate White (error score)	76	120.26316	151.13062	9140	8	72	840
Concatenate Black (error score)	76	99.73684	103.06727	7580	12	66	576

Table 6-7. Descriptive biostatistics of **concatenated glucose levels (mg/dL) and age (years) from reference (fireman) and treatment (diabetic retinopathy) groups**.

	N total	Mean	Standard Deviation	Sum	Minimum	Median	Maximum
Glucose level (mg/dL)	76	143.55263	71.56822	10910	69	119	395
Age (years)	76	52.76316	16.96967	4010	16	54.5	88

Quality assessments of simultaneous ophthalmic incident diseases in **treatment**, obtained from the interviews at Hospital, are described:

Diabetic patients who had retinopathy: 100% (trial group);

Diabetic patients who had cataract: 36.84%;

Diabetic patients who had AMD: 1.05%;

Diabetic patients who had glaucoma: 2.63%.

Table 6-4 reveals that the mean error-score of **reference group** (fireman) in **white background** was **43.26** ($SD=26$), and **51.15** in **black background** ($SD=32$). However, the mean error-score of **treatment group** (diabetic retinopathy) in **white background** was **197.26** ($SD=182$), while in **black background** was **148.31** ($SD=148$), Table 6-5. These descriptive statistical analyses of error scores are graphically represented in Figure 6-8.

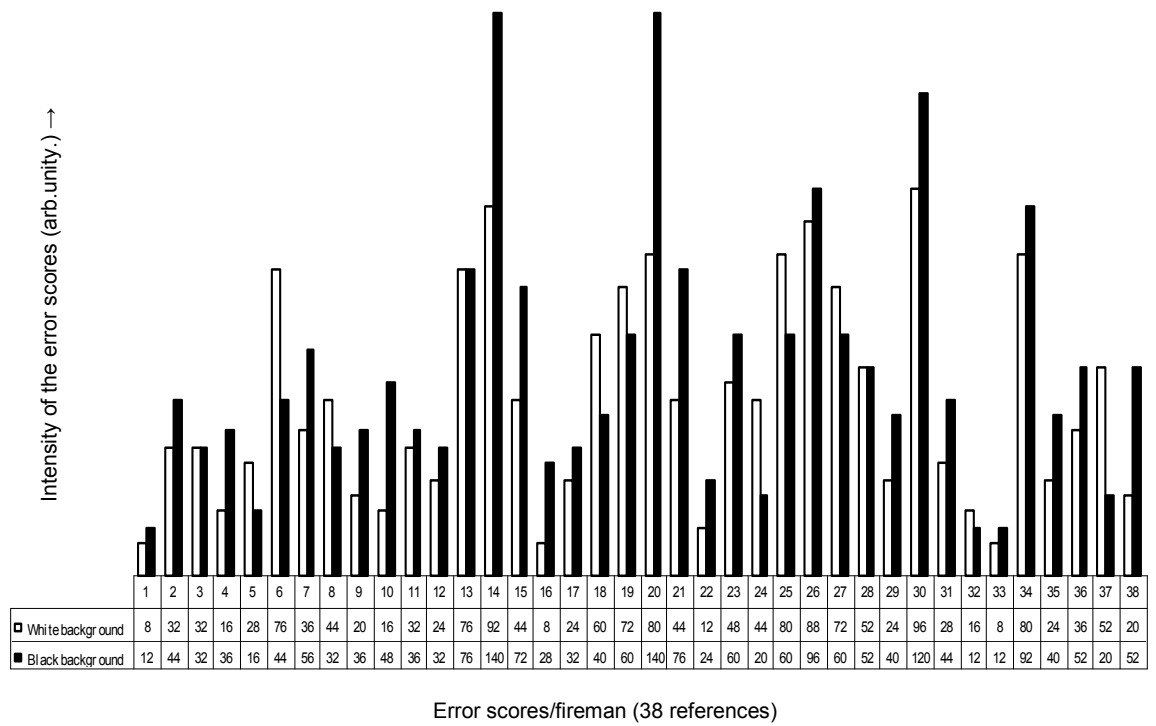
Concatenated results ($N=76$) indicated the **major error incidences in white background** when the colour vision of the two groups was analysed together (Table 6-6).

Concatenated results ($N=76$) of references was 47.2 ($SD=29$), and 172.7 for treatment ($SD=157$), when white and black backgrounds were analysed together, revealing a **heterogeneous quality on the colour vision in treatments examined** (Table 6-6). These results evidenced a **global healthier colour vision quality in references (medium quality), than in treatment (inferior quality)**, according to the FM100-HUE scale (chapter 2, Table 2-6, p.25).

The **mean glucose level was 95.13 mg/dL in references** ($SD=17.04$), and **191.97 mg/dL in treatments** ($SD=72.63$).

The **mean age of references was 39.8 years** (from 16 to 69, $SD=12.97$) and **65.7 years in treatments** (from 52 to 88, $SD=8.42$).

Considering both the treatment and reference groups as a single group, the **mean glucose level was 143.55 mg/dL** ($SD=71.56$), and the **mean age was 52.7 years** ($SD=16.96$), Table 6-7.



□ White background ■ Black background

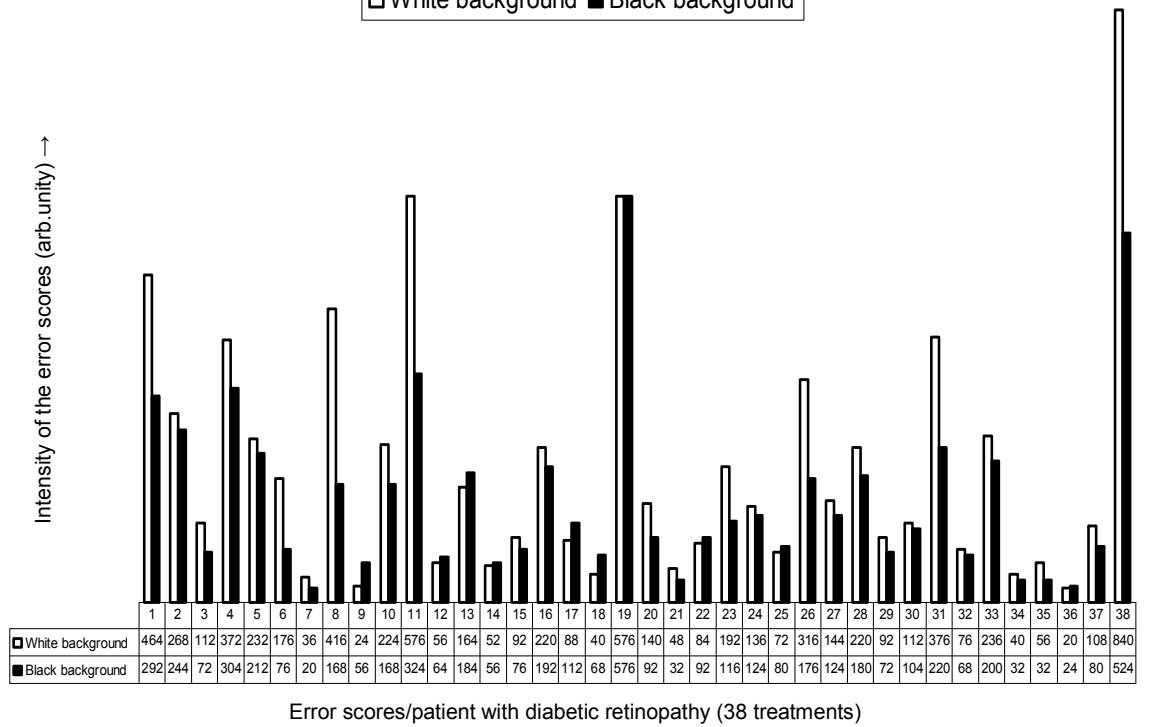


Figure 6-8. Description of the error scores from retinal responses of **references** and **treatments** by FM100-HUE diagnoses in white and black backgrounds.

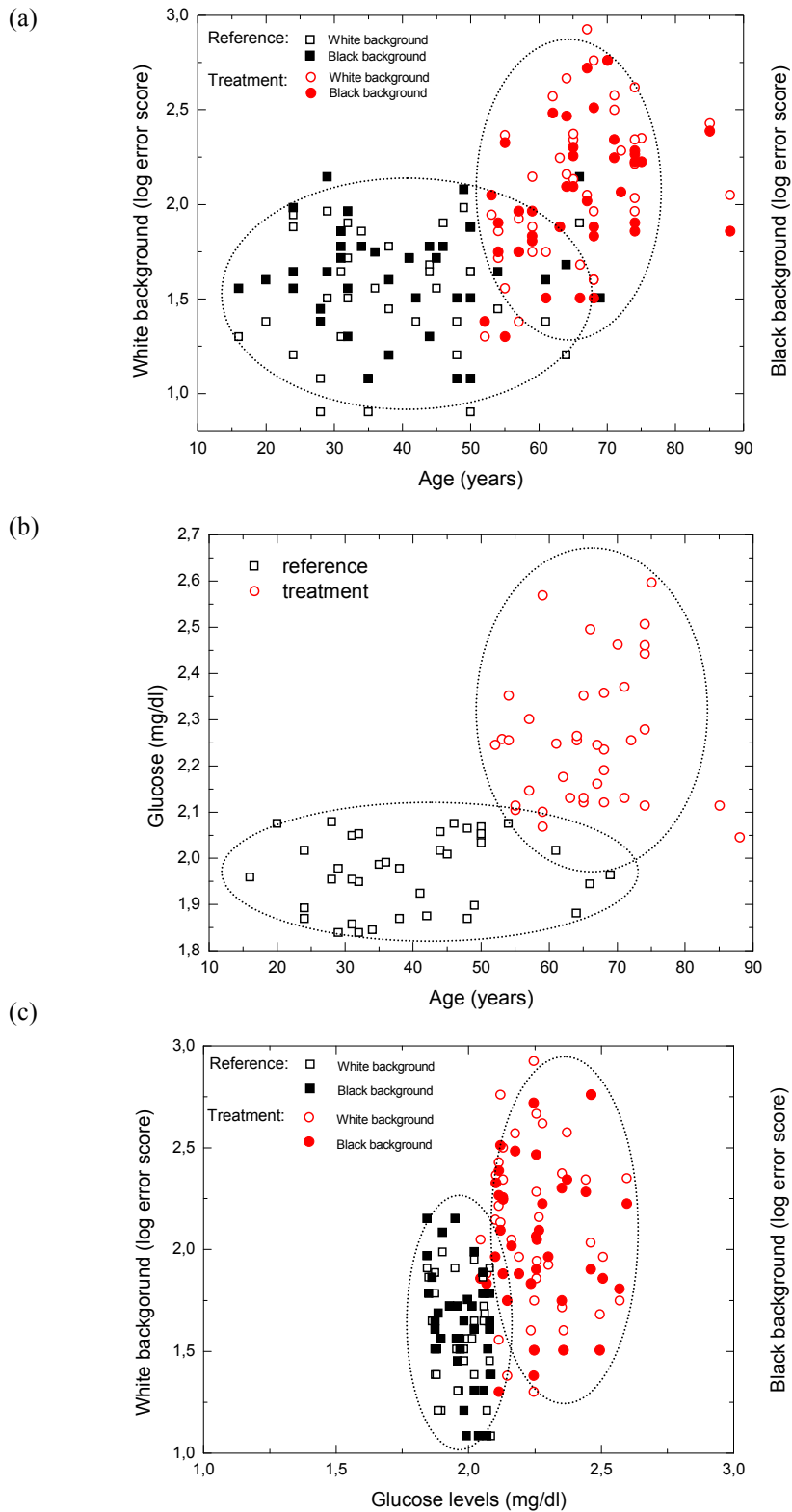


Figure 6-9. Distributions for reference and treatment groups, of: a) colour vision in white and black backgrounds (log error scores), in function of the age (years); b) age vs. glucose levels (log-transformed data); and c) colour vision (log error scores) vs. glucose levels (log-transformed data).

Table 6-8 describes the Pearson correlation coefficients of reference and treatment groups. In references, a **positive medium correlation was identified between the error scores in white and black backgrounds** ($r=0.7344$). In treatments, a **strong positive correlation of the mean error scores between white and black backgrounds was found** ($r=0.9271$).

Only slight Pearson correlations between the **age and log error scores**, in white ($r=0.4327$) or black ($r=0.3513$) backgrounds, were identified. This slight correlation between the colour vision and age is proofed in Figure 6-9a.

Figure 6-9 also evidenced the heterogeneous nature of these two groups, by analysing references and treatment in the graphic distribution of **age versus log glucose levels** (Figure 6-9b). Moreover, the variances in the glucose levels was of about 49.85% (*concatenated SD*=71.56, Table 6-4), and of 32.16% in the age (*concatenated SD*=16.96, Table 6-5).

Limiting the glucose levels <120 mg/dL in references, Figure 6-9c evidences in this group a concentration of lower (log) error-scores for white and black backgrounds. A vertical distribution concentrated with higher glucose levels and error scores on the colour vision was observed in treatments.

Table 6-8. Pearson correlation coefficients between age, glucose and error scores ($p<0.05$).

		Reference				Treatment			
		Age	Glucose (*)	Log White	Log Black	Age	Glucose (*)	Log White	Log Black
Age	<i>r</i> .	1.0000	0.1410	0.0301	0.0280	1.0000	0.0925	0.4327	0.3513
	<i>Sig.</i>	--	0.3983	0.8578	0.8673	--	0.5809	0.0067	0.0306
Glucose (*)	<i>r</i>	0.1410	1.0000	-0.1799	-0.3156	0.0925	1.0000	-0.0467	-0.0296
	<i>Sig.</i>	0.3983	--	0.2797	0.0536	0.5809	--	0.7807	0.8601
Log White	<i>r</i>	0.0301	-0.1799	1.0000	0.7344	0.4327	-0.0467	1.0000	0.9271
	<i>Sig.</i>	0.8578	0.2797	--	0.0000	0.0067	0.7807	--	0.0000
Log Black	<i>r</i>	0.0280	-0.3156	0.7344	1.0000	0.3513	-0.0296	0.9271	1.0000
	<i>Sig.</i>	0.8673	0.0536	0.0000	--	0.0306	0.8601	0.0000	--

(*) Log-transformed data for determination of Pearson correlation coefficients.

Several authors reported that more correlated aspects with colour vision biofunctionality are the diabetic complication state and the duration of diabetes [152], than the age of the diabetic person. In this study, it was identified a specific example that agrees with the widely reported in the literature. For example, a diabetic man, patient code HDI_p039, **67 years old** presenting glucose concentration of **176 mg/dL**, who had previous laser surgery and having cataract disease, had an **error-score of 840** at 753 lux (Figure 6-10a). Another diabetic patient code HDI_p003, **88 years old** presenting glucose concentration of **111 mg/dL**, having cataract disease, had an **error-score of 112** at 628 lux (Figure 6-10b).

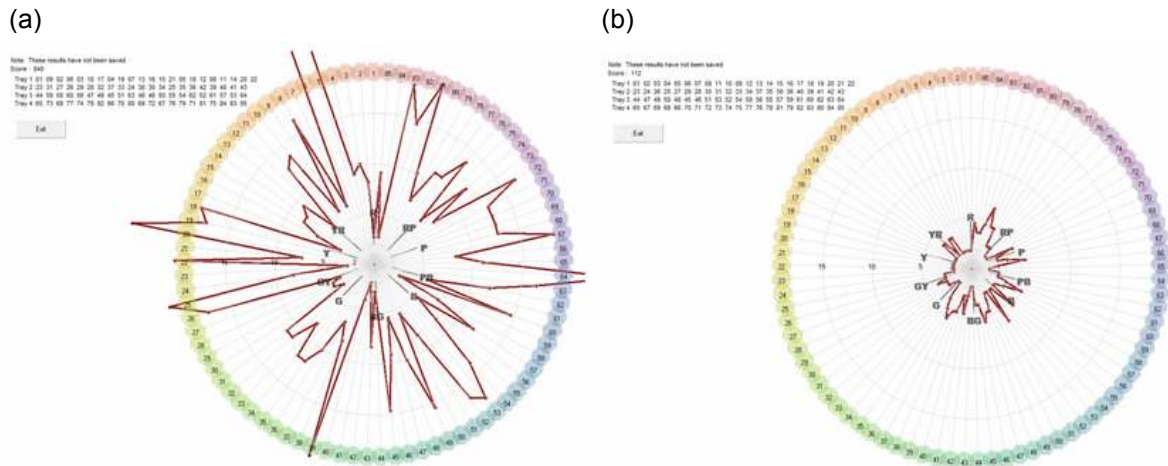


Figure 6-10. Colour vision from the retinal responses of 2 patients with diabetic retinopathy.

Qualitative assessment of ophthalmic biomaterials in treatments included the occurrence of cataracts and the type of IOL implanted (e.g. PMMA, acrylic, hydrogel). Data were obtained through an interview/questionnaire answered by the patients at the Infante Dom Pedro Hospital (ANEX III, Information Sheet). However, due the complexity and liability of the data obtained, these factors were only described on this study about the colour vision performance, and are:

- Diabetic patients who had laser surgery: 57.89%
- Diabetic patients who use glass: 71.05%
- Diabetic patients who use IOL: 18.42%
- Diabetic patients who use contact lens: 7.89%

Figure 6-11 is a SEM image of a cataract intra-ocular lens (IOL) (*Source: Visiontech® Medical Optics Ltda., Brazil*) with an UV absorbing compound by optic design equiconvex, which type is similar to the used in some patients with diabetic retinopathy at Infante Dom Pedro Hospital. The IOL's haste distance is of about 2.8 mm, with a detail of the diameter of 155 μm (Figure 6-15a). Figure 6-11b shows the surgical hole with 360 μm of diameter, displaced near to the curve of the lens surface (Figure 6-11c).

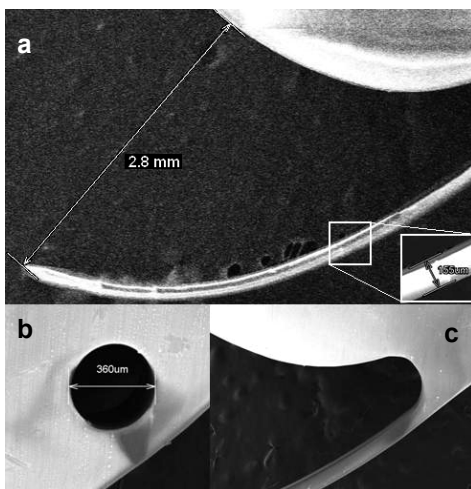


Figure 6-11. SEM of cataract intra-ocular lens (IOL) with an UV absorbing compound by optic design equiconvex. Note that after cataract surgery, the difference between the colour vision scores of diabetic and non-diabetic patients is reduced [152].

6.5.2. ANOVA with covariates (intergroup analysis)

The ANOVA analysis aimed to compare the background influence between the two groups.

- **Factor:** reference and treatment groups were compared;
- **Covariates:** age and glucose level (log-transformed data).

In the ANOVA tables and analysis, numerous abbreviators are used, where:

- (*) is a log-transformed data;
- (DF) is the number of degrees of freedom for testing;
- (Seq.) is a sequential analysis;
- (Adj.) is an adjusted analysis;
- (sq.) are squares;
- (SS) is the sum for squares;
- (MS) is the mean for squares;
- (F) is the ratio value of distributions with degrees of freedom;
- (SE) is the standard error;
- (R) is an observation with large standardized residual.

In the follow Tables from 6-9 to 6-14, the ANOVA results are described, with log-transformed data, if applicable.

Table 6-9. ANOVA with covariates for log error scores from **white background** (=log White), using Adjusted SS for Tests.

	Unity	DF	Seq SS	Adj SS	Adj MS	F	p
Age	(years)	1	5.5337	0.4258	0.4258	3.4	0.069
Glucose level*	(mg/dL)	1	0.1597	0.1065	0.1065	0.85	0.36
Exp (Groups)		1	1.2704	1.2704	1.2704	10.14	0.002
Error		72	9.0197	9.0197	0.1253		
Total		75	15.9834				
S= 0.353939		R-Sq=43.57%		R-Sq(adj)=41.22%			
	Unity	Coefficient		SE Coef	T	p	
Constant		2.1463		0.746	2.88	0.005	
Age	(years)	0.006969		0.00378	1.84	0.069	
Glucose level*	(mg/dL)	-0.3218		0.3491	-0.92	0.36	
Unusual Observations for log White							
Obs	log White	Fit	SE Fit	Residual	St.Residual		
45	1.38021	2.10035	0.07502	-0.72014	-2.08		
57	1.30103	2.033552	0.07718	-0.73249	-2.12		
76	2.92428	2.13805	0.0578	0.78623	2.25		

Table 6-10. ANOVA with covariates for log error scores from **black background** (=log Black), using Adjusted SS for Tests.

	Unity	DF	Seq SS	Adj SS	Adj MS	F	p
Age	(years)	1	2.7458	0.23	0.23	2.38	0.128
Glucose level*	(mg/dL)	1	0.031	0.1239	0.1239	1.28	0.262
Exp (Groups)		1	0.7335	0.7335	0.7335	7.58	0.007
Error		72	6.9686	6.9686	0.0968		
Total		75					
S= 0.311105 R-Sq=33.50% R-Sq(adj)=30.73%							
	Unity	Coefficient	SE Coef	T	p		
Constant		2.2981	0.6557	3.5	0.001		
Age	(years)	0.005122	0.003322	1.54	0.128		
Glucose level*	(mg/dL)	-0.3472	0.3068	-1.13	0.262		
Unusual Observations for log Black							
Obs	log Black	Fit	SE Fit	Residual	St. Residual		
45	1.30103	2.03403	0.0737	-0.733	-2.43		
57	2.76042	1.98988	0.08082	0.77054	2.56		
76	2.71933	2.04981	0.05081	0.66952	2.18		

Table 6-11. ANOVA means for covariates: age and glucose levels.

Covariate		Mean	SD
Age	(years)	52.763	16.9697
Glucose level*	(mg/dL)	2.114	0.1859

Table 6-12. ANOVA least square means: log White and log Black.

Exp	log White		log Black	
	Mean	SE Mean	Mean	SE Mean
Reference	1.586	0.0877	1.646	0.7709
Treatment	2.081	0.0877	2.022	0.7709

Table 6-13. ANOVA with covariates for difference between log error scores in **white and black backgrounds** (= [log White – log Black]), using Adjusted SS for Tests.

	Unity	DF	Seq SS	Adj SS	Adj MS	F	p
Age	(years)	1	0.48348	0.0299	0.0299	0.85	0.36
Glucose level*	(mg/dL)	1	0.04998	0.00066	0.00066	0.02	0.891
Exp (Groups)		1	0.07325	0.07325	0.07325	2.08	0.154
Error		72	2.53803	2.53803	0.03525		
Total		75	3.14474				
S= 0.187751 R-Sq=19.29% R-Sq(adj)=15.93%							
	Unity	Coefficient	SE Coef	T	p		
Constant		-0.1519	0.3957	-0.38	0.702		
Age	(years)	0.001847	0.002005	0.92	0.36		
Glucose level*	(mg/dL)	0.0254	0.1852	0.14	0.891		
Unusual Observations for log Black							
Obs	log Black	Fit	SE Fit	Residual	St. Residual		
10	-0.477121	-0.045429	0.06102	-0.43169	-2.43		
16	-0.544068	-0.110048	0.038521	-0.43402	-2.36		
24	0.342423	-0.078909	0.032488	0.421332	2.28		
37	0.414973	-0.100156	0.038083	0.515129	2.8		
47	-0.367977	0.067254	0.039796	-0.43523	-2.37		

Table 6-14. ANOVA least square means for log error scores in **white and black backgrounds** (= [log White – log Black]).

Exp	Mean	SE Mean
Reference	-0.06026	0.04652
Treatment	0.05862	0.04652

From the ANOVA analysis of data presented from Table 6-9 to 6-14, the results revealed that:

- Covariate analysis (log White):
REFERENCES (R) are significantly (S) different of TREATMENTS (T), or S (R ≠ T).
- Covariate analysis (log Black):
REFERENCES (R) are significantly (S) different of TREATMENTS (T), or S (R ≠ T).
- Covariate analysis (log White – log Black):
not significant (NS) that references (R) are identical to the treatments (T), or **NS (R = T).**

From the ANOVA analysis (see also Figure 6-12), it was possible to affirm that:

- **There are statistical differences between these two groups for colour vision (log error scores) in white or in black backgrounds;**
- **However, the age and glucose levels were not statistically associated as significant covariates on the colour vision (for $p < 0.05$).**

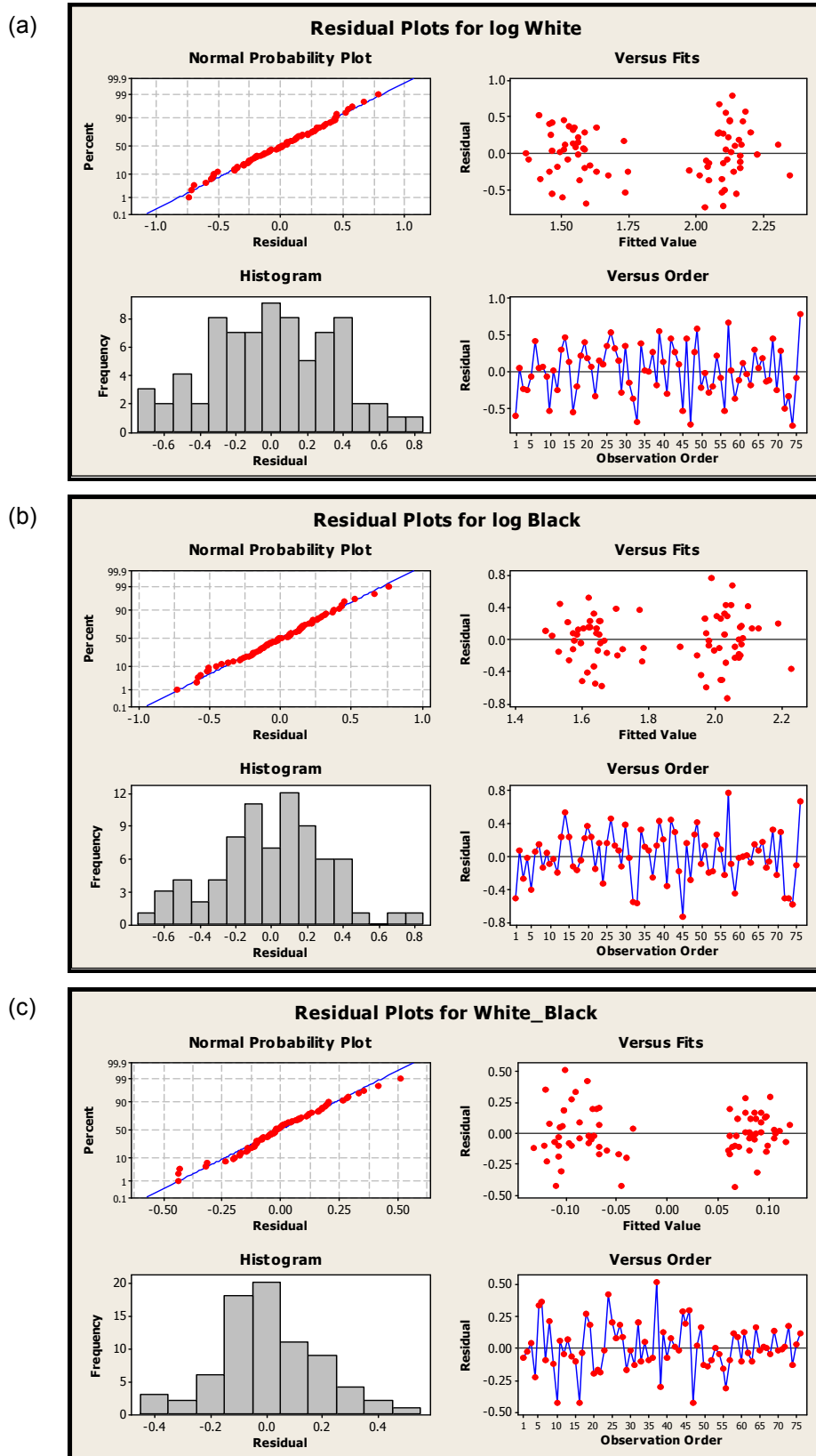


Figure 6-12. ANOVA plots from the analysis with covariates for residual values (variability not explained), for: a) log White; b) log Black; and c) log White – log Black.

6.5.3. Paired T-test (intragroup analysis)

The Paired T-test aimed to compare the background influence for each group. In the tables 6-15 and 6-16, the CI denotes the **confidence interval** for mean difference.

- **Factor:** error scores in white and black backgrounds are compared.

Table 6-15. REFERENCE GROUP: Paired T-test and CI for log White - log Black.

	N	Mean	SD	SE Mean
log White	38	1.5418	0.31	0.0503
log Black	38	1.6296	0.2731	0.0443
Difference	38	-0.0878	0.2152	0.0349

95% Confidence Interval for Mean Difference: (-0.1585, -0.0170)

T-test of mean Difference = 0 (vs. Not = 0): T-value = -2.51 (P-value = 0.016, $p < 0.05$).

Table 6-16. TREATMENT GROUP: Paired T-test and CI for log White - log Black.

	N	Mean	SD	SE Mean
log White	38	2.1253	0.4013	0.0651
log Black	38	2.0391	0.35	0.0568
Difference	38	0.0862	0.1521	0.0247

95% Confidence Interval for Mean Difference: (0.0362, 0.1361)

T-test of mean Difference = 0 (vs. Not = 0): T-value = 3.49 (P-value = 0.001, $p < 0.05$).

- Results from T-test for the **REFERENCE GROUP** (fireman, $n=38$) revealed that mean log error scores in white background ($\log E_w=1.5418$) are significantly (S) different of log error scores in black background ($\log E_b=1.6296$), and with negative signal, thus:
Log White – Log Black = -0.0878 (SD=0.2152), or **$\log E_w < \log E_b$** , with 95% of confidence interval for mean difference (-0.1585, -0.0170).
- Results from T-test for the **TREATMENT GROUP** (patients with diabetic retinopathy, $n=38$) revealed that mean log error scores in white background ($\log E_w=2.1253$) are significantly (S) different of log error scores in black background ($\log E_b=2.0391$), and with positive signal, thus:
Log White – Log Black = 0.0862 (SD=0.1521), or **$\log E_w > \log E_b$** , with 95% of confidence interval for mean difference (0.1521, 0.0247).

From the paired T-test, it was possible to affirm that **the colour vision in the reference group is significantly different in white and black backgrounds ($p=0.016$)**, and **these firemen presented higher error scores in black background**.

Furthermore, **the colour vision in the treatment group is also significantly different in white and black backgrounds ($p=0.001$)**, and **these patients with diabetic retinopathy presented higher error scores in white background**.

6.6. Personalized $\text{SrAl}_2\text{O}_4:\text{Ce}^{3+}, \text{Dy}^{3+}, \text{Eu}^{2+}$ colour emission

In this topic, the colour vision performed in white and black backgrounds was investigated for the visibility of photoluminescent materials, namely for the colour emission of $\text{SrAl}_2\text{O}_4:\text{Ce}^{3+}, \text{Dy}^{3+}, \text{Eu}^{2+}$ photoluminescent material. Figure 6-13 shows a schema of the photopic colour vision of this material in the UV-VIS region, in white and black backgrounds.

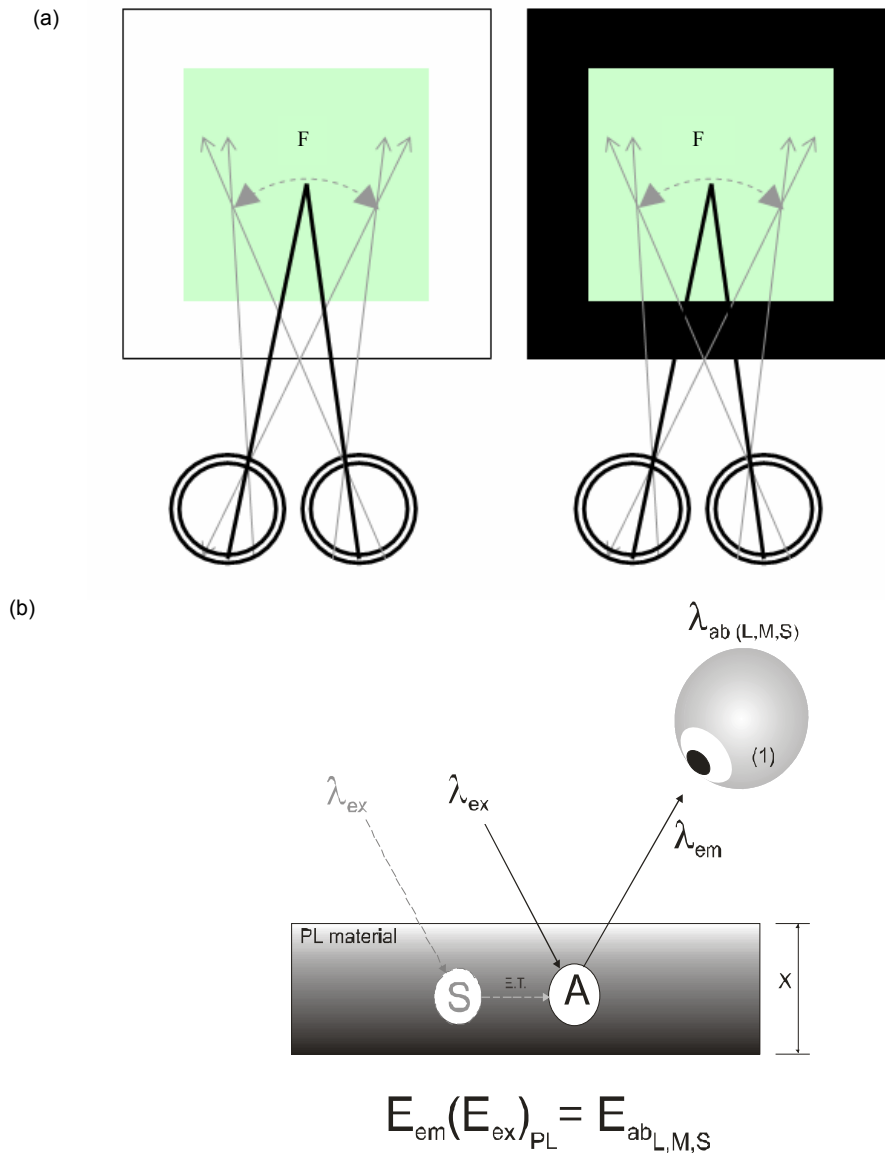


Figure 6-13. Photopic colour vision of a photoluminescent material (light emitting after excitation): a) diagram of comparative diagnoses of a binocular test of the retinal biofunctionality *in space* between white (light) and black (dark) backgrounds to be used as an estimative of visibility in darkness, valid on the first 10 minutes of PL visibility, while the photoreceptors cells are still hyperpolarized in response to illumination, and processing the colour signal; b) biofunctionality of retinal cells in function of the excitation source ($\lambda_{\text{ex}}_{\text{PL}}$), energy transfer (E.T.) and emission by a sensitizer (S) or activator (A) that produces the PL light emission ($\lambda_{\text{em}}_{\text{PL}}$). The photon energy emitted by luminescent centres in the UV-VIS region must be detected by the human eye cells with biofunctionality for long-, middle- and short- wavelengths ($\lambda_{\text{abs L, M, S}}$).

Some points that were exploited in this study on the medical equipment:

- (1) testing the biofunctionality of photoreceptors cells in presence of illumination "*in space*" is applied to the threshold of depolarization of the photopic retinal cells, while beginning the PL emission, in analogy to the visibility of static scenarios from a white (light) → black (dark) backgrounds, Figure 6-13a; the colour vision is used in a visual memory, instantly, during the decision making processes of evacuation in emergencies: all results are validated for the first 10 minutes of PL visibility;
- (2) extrapolation of the colour vision tests to attribute a "safety factor" for the limit of visibility of the human eye ($>0.032 \text{ mcd/m}^2$) in personalized PL materials; the PL features depending of the atomic excitation (λ_{ex}) and emission (λ_{em}) ought to present visible wavelength emissions in highest colour sensitivity regions of the human eyes, in values of $\lambda_{\text{em}} < 555 \text{ nm}$ (Purkinje Effect) — the corresponding biofunctionality of retinal cells for these wavelengths may be personalized for a sight quality from light signal (λ_{abs} L, M, S), Figure 6-13b.

Supported in the results obtained from the statistical analysis, which comprised the superior mean quality on the colour vision in black background for treatments, these personal data are, herein, used for the personalization of PL materials, according to the method described in Section 6.3.

Factor:	personalization of PL materials;
Function:	emergency signalling (at 0 lux);
Optical emission:	UV-VIS, ranging 555-485 nm ($\lambda_{\text{em}} < 555 \text{ nm}$, Purkinje Effect);
PL material:	$\text{SrAl}_2\text{O}_4:\text{Ce}^{3+}, \text{Dy}^{3+}, \text{Eu}^{2+}$;
Specific emission:	525 nm (C35);
End users:	38 patients with diabetic retinopathy;
Biometric data:	colour vision from FM100-HUE (log error scores from C31 to C53).
Data analysis:	ANOVA, T-test and Pearson correlation coefficients.

Specific analysis for personalization was made from C31 to C53 colours vision of treatments of patients with diabetic retinopathy ($n=38$) from black background diagnoses, Table 6-17. **The mean error score (Table 6-17a) for the C35 was 4.36842 ($SD=2.30$), corresponding to the light emission of $\text{SrAl}_2\text{O}_4:\text{Ce}^{3+}, \text{Dy}^{3+}, \text{Eu}^{2+}$ at 525 nm, with an excellent colour vision quality in the FM100-HUE scale (see chapter 2, Table 2-6, p.25). The mean of log error scores also resulted in excellent quality on the colour vision (Table 6-17b).**

Pearson correlation coefficients (r) between the C35 colour vision and C31, C33, C37, C38, C40, C41, C42, C50, and C51 were identified ($p < 0.05$), Table 6-18. Pearson coefficients from log error scores revealed slight correlations between the C35 colour vision with C32, C33, C34, C36 and C37 ($p < 0.05$). Medium positive correlations ($0.70 > r > 0.50$) were identified from log error scores between C35 with C31 ($r=0.6383$), or C38 ($r=0.5185$), or C40 ($r=0.5984$), or C41 ($r=0.6376$), assume that PL materials with light emission in the respective wavelength regions are correlated to the excellent colour contrast sensitivity of $\text{SrAl}_2\text{O}_4:\text{Ce}^{3+}, \text{Dy}^{3+}, \text{Eu}^{2+}$ at 525 nm from treatments.

Table 6-17. Descriptive statistics of the treatment group for colour vision from (C31) to (C53), in black background.

(a) Error scores:

	N	Mean	SD	Sum	Min	Max
C31	38	4,55263	2,85409	173	2	15
C32	38	4,07895	1,60036	155	2	8
C33	38	5,57895	3,60654	212	2	15
C34	38	4,39474	2,30791	167	2	10
C35	38	4,36842	2,54071	166	2	14
C36	38	3,92105	1,80662	149	2	9
C37	38	4,05263	2,21722	154	2	12
C38	38	3,84211	1,65262	146	2	8
C39	38	3,63158	1,85153	138	2	10
C40	38	3,42105	1,83997	130	2	8
C41	38	3,68421	3,03231	140	2	13
C42	38	3,26316	2,53286	124	2	13
C43	38	3,18421	2,03822	121	2	12
C44	38	2,52632	0,76182	96	2	5
C45	38	2,71053	1,27147	103	2	8
C46	38	2,92105	0,9693	111	2	5
C47	38	3,81579	2,77883	145	2	14
C48	38	3,89474	2,62822	148	2	14
C49	38	4,18421	4,23534	159	2	22
C50	38	3,97368	2,60443	151	2	13
C51	38	3,94737	3,49476	150	2	23
C52	38	3,97368	2,22379	151	2	12
C53	38	4,47368	2,77768	170	2	13

(b) Log-transformed error scores:

	N	Mean	SD	Sum	Min	Max
C31	38	0,59904	0,21756	22,76356	0,30103	1,17609
C32	38	0,57861	0,16996	21,98716	0,30103	0,90309
C33	38	0,67554	0,24137	25,67042	0,30103	1,17609
C34	38	0,59538	0,19812	22,62458	0,30103	1
C35	38	0,58505	0,21259	22,23203	0,30103	1,14613
C36	38	0,55387	0,18356	21,04717	0,30103	0,95424
C37	38	0,55521	0,20099	21,09783	0,30103	1,07918
C38	38	0,54484	0,19009	20,70386	0,30103	0,90309
C39	38	0,51639	0,18903	19,62264	0,30103	1
C40	38	0,48576	0,19693	18,45879	0,30103	0,90309
C41	38	0,48234	0,2414	18,32899	0,30103	1,11394
C42	38	0,44419	0,21619	16,87925	0,30103	1,11394
C43	38	0,44777	0,20156	17,01519	0,30103	1,07918
C44	38	0,38624	0,11571	14,67717	0,30103	0,69897
C45	38	0,40209	0,15172	15,27923	0,30103	0,90309
C46	38	0,44412	0,13587	16,87639	0,30103	0,69897
C47	38	0,51621	0,21565	19,6158	0,30103	1,14613
C48	38	0,52696	0,21896	20,02463	0,30103	1,14613
C49	38	0,52336	0,25069	19,88782	0,30103	1,34242
C50	38	0,53542	0,22209	20,34598	0,30103	1,11394
C51	38	0,52466	0,21717	19,93709	0,30103	1,36173
C52	38	0,54478	0,21286	20,70182	0,30103	1,07918
C53	38	0,57934	0,24606	22,01498	0,30103	1,11394

Table 6-18. Pearson correlation coefficients from (C31) to (C53) in black background for treatment (log-transformed error scores).

	C31	C32	C33	C34	C35	C36	C37	C38	C39	C40	C41	C42	C43	C44	C45	C46	C47	C48	C49	C50	C51	C52	C53
C31	1,0000	0,4106	0,5103	0,5019	0,6383	0,2434	0,4024	0,4457	0,3644	0,5336	0,5818	0,4278	0,2578	0,0311	-0,0039	0,0541	0,3413	0,3387	0,4376	0,4001	0,3462	0,3625	0,1859
C31 Sig.	--	0,0105	0,0011	0,0013	0,0000	0,1409	0,0123	0,0051	0,0245	0,0006	0,0001	0,0074	0,1181	0,8529	0,9815	0,7470	0,0360	0,0387	0,0060	0,0128	0,0333	0,0253	0,2637
C32	0,4106	1,0000	0,7337	0,4153	0,3209	0,4884	0,3100	0,2647	0,5137	0,5370	0,4473	0,4246	0,3481	0,3028	0,0358	0,0611	0,1480	0,4539	0,4475	0,3524	0,2480	0,0710	0,2509
C32 Sig.	0,0105	--	0,0000	0,0095	0,0495	0,0019	0,0582	0,1082	0,0010	0,0005	0,0049	0,0079	0,0322	0,0646	0,8309	0,7156	0,3752	0,0042	0,0048	0,0300	0,1332	0,6720	0,1287
C33	0,5103	0,7337	1,0000	0,4005	0,3994	0,3202	0,3885	0,2669	0,4106	0,4885	0,4360	0,4185	0,3854	0,1066	0,2424	0,1736	0,3552	0,5368	0,3881	0,3647	0,3593	0,0597	0,3005
C33 Sig.	0,0011	0,0000	--	0,0127	0,0130	0,0500	0,0159	0,1053	0,0105	0,0019	0,0062	0,0089	0,0169	0,5242	0,1425	0,2973	0,0287	0,0005	0,0160	0,0244	0,0267	0,7220	0,0668
C34	0,5019	0,4153	0,4005	1,0000	0,3579	0,5230	0,2096	0,3821	0,5110	0,5272	0,4965	0,1930	0,1833	0,2193	-0,0668	-0,0331	0,4267	0,5014	0,1967	0,1705	0,3506	0,2822	0,2640
C34 Sig.	0,0013	0,0095	0,0127	--	0,0274	0,0008	0,2067	0,0179	0,0010	0,0007	0,0015	0,2456	0,2707	0,1859	0,6903	0,8438	0,0076	0,0013	0,2366	0,3060	0,0309	0,0793	0,1093
C35	0,6383	0,3209	0,3994	0,3202	1,0000	0,3273	0,3911	0,5185	0,3495	0,5984	0,6376	0,4630	0,1626	0,1523	-0,0337	-0,0287	0,0309	0,2757	0,2663	0,4015	0,4221	0,1958	0,2286
C35 Sig.	0,0000	0,0495	0,0130	0,0274	--	0,0449	0,0152	0,0009	0,0315	0,0001	0,0000	0,0034	0,3293	0,3613	0,8406	0,8640	0,8539	0,0939	0,1061	0,0125	0,0083	0,2387	0,1674
C36	0,2434	0,4884	0,3202	0,5230	0,3273	1,0000	0,3018	0,5613	0,6392	0,6400	0,4164	0,3255	0,1509	0,4173	-0,1798	-0,1705	0,0693	0,5284	0,3413	0,2154	0,2819	0,3266	0,3101
C36 Sig.	0,1409	0,0019	0,0500	0,0008	0,0449	--	0,0656	0,0002	0,0000	0,0000	0,0093	0,0482	0,3658	0,0091	0,2801	0,3063	0,6795	0,0006	0,0360	0,1940	0,0864	0,0454	0,0582
C37	0,4024	0,3100	0,3885	0,2096	0,3911	0,3018	1,0000	0,5828	0,3910	0,4314	0,6043	0,3582	0,3761	0,2848	0,1288	0,0805	0,2208	0,3047	0,4463	0,2839	0,1188	0,1622	0,1614
C37 Sig.	0,0123	0,0582	0,0159	0,2067	0,0152	0,0656	--	0,0001	0,0152	0,0069	0,0001	0,0272	0,0200	0,0831	0,4409	0,6311	0,1828	0,0629	0,0050	0,1094	0,4777	0,3308	0,3331
C38	0,4457	0,2647	0,2669	0,3821	0,5185	0,5613	0,5828	1,0000	0,5606	0,5836	0,5651	0,3462	0,1865	0,3082	-0,0687	-0,2477	0,0959	0,3963	0,3406	0,2594	0,2977	0,4300	0,1602
C38 Sig.	0,0051	0,1082	0,1053	0,0179	0,0009	0,0002	0,0001	--	0,0002	0,0001	0,0002	0,0332	0,2622	0,0598	0,6818	0,1338	0,5688	0,0138	0,0364	0,1158	0,0695	0,0071	0,3366
C39	0,3644	0,5137	0,4106	0,5110	0,3495	0,6392	0,3910	0,5650	1,0000	0,7557	0,5666	0,5758	0,5398	0,4789	-0,1533	0,0092	0,2568	0,5897	0,5336	0,3665	0,3970	0,3147	0,5021
C39 Sig.	0,0245	0,0010	0,0105	0,0010	0,0315	0,0000	0,0152	0,0002	--	0,0000	0,0002	0,0002	0,0002	0,0581	0,9563	0,1197	0,0001	0,0006	0,0236	0,0138	0,0543	0,0543	0,0013
C40	0,5336	0,5370	0,4885	0,5272	0,5984	0,6400	0,4314	0,5836	0,7557	1,0000	0,7595	0,7539	0,4849	0,4312	-0,1457	0,0587	0,0740	0,4592	0,4375	0,3764	0,3178	0,2004	0,4021
C40 Sig.	0,0006	0,0005	0,0019	0,0007	0,0001	0,0000	0,0069	0,0001	0,0000	--	0,0000	0,0000	0,0020	0,0069	0,3828	0,7262	0,6589	0,0037	0,0060	0,0199	0,0520	0,2276	0,0123
C41	0,5818	0,4473	0,4360	0,4965	0,6376	0,4164	0,6043	0,5651	0,5666	0,7595	1,0000	0,4917	0,3453	0,2748	-0,0807	-0,0805	-0,0290	0,4131	0,4505	0,3671	0,3330	0,1204	0,2057
C41 Sig.	0,0001	0,0049	0,0062	0,0015	0,0000	0,0093	0,0001	0,0002	0,0002	0,0000	--	0,0017	0,0337	0,0950	0,6301	0,6310	0,8629	0,0099	0,0045	0,0234	0,0410	0,4715	0,2153
C42	0,4278	0,4246	0,4185	0,1930	0,4630	0,3255	0,3582	0,3462	0,5758	0,7539	0,4917	1,0000	0,6502	0,4684	-0,2100	0,1391	0,1123	0,2266	0,2646	0,2273	0,0588	0,0922	0,3286
C42 Sig.	0,0074	0,0079	0,0089	0,2456	0,0034	0,0462	0,0272	0,0332	0,0002	0,0000	0,0017	--	0,0000	0,0030	0,2056	0,4048	0,5019	0,1713	0,1084	0,1699	0,7257	0,5818	0,0440
C43	0,2578	0,3481	0,3854	0,1833	0,1626	0,1509	0,3761	0,1865	0,5398	0,4849	0,3453	0,6502	1,0000	0,5430	-0,0005	0,3284	0,1970	0,1426	0,1630	0,0670	-0,0870	-0,0469	0,2372
C43 Sig.	0,1181	0,0322	0,0169	0,2707	0,3293	0,3658	0,0200	0,2622	0,0005	0,0020	0,0337	0,0000	--	0,0004	0,9978	0,0441	0,2359	0,3932	0,3282	0,6894	0,6034	0,7799	0,1517
C44	0,0311	0,3028	0,1066	0,2193	0,1523	0,4173	0,2848	0,3082	0,4789	0,4312	0,2748	0,4684	0,5430	1,0000	0,2486	0,3074	0,0336	0,2706	0,1155	0,0187	-0,0660	0,0761	0,2967
C44 Sig.	0,8529	0,0646	0,5242	0,1859	0,3613	0,0091	0,0831	0,0598	0,0024	0,0069	0,0950	0,0030	0,0004	--	0,1323	0,0605	0,8414	0,1003	0,4900	0,9112	0,6940	0,6498	0,0705
C45	-0,0039	0,0358	0,2424	-0,0668	-0,0337	-0,1798	0,1288	-0,0687	-0,1533	-0,1457	-0,0807	-0,2100	-0,0005	0,2486	1,0000	0,5463	0,1677	0,1017	0,1371	0,1343	0,0499	-0,0070	0,1384
C45 Sig.	0,9815	0,8309	0,1425	0,6903	0,8406	0,2801	0,4409	0,6818	0,3581	0,3828	0,6301	0,2056	0,9978	0,1323	--	0,0004	0,3143	0,5435	0,4117	0,4214	0,7860	0,9666	0,4073
C46	0,0541	0,0611	0,1736	-0,0331	-0,0287	-0,1705	0,0805	-0,2477	0,0092	0,0587	-0,0805	0,1391	0,3284	0,3074	0,5463	1,0000	0,3184	-0,0616	0,2104	0,2054	-0,1130	-0,1779	0,0766
C46 Sig.	0,7470	0,7156	0,2973	0,8438	0,8640	0,3063	0,6311	0,1338	0,9563	0,7262	0,6310	0,4048	0,0441	0,0605	0,0004	--	0,0514	0,7135	0,2048				

Figure 6-14 demonstrates the FM100-HUE results from the photopic retinal responses of treatment for a blue-green spectral region from (C53) to (C31) colour vision in black background. All mean values of the error-scores ranging within 485-555 nm were up to 10 in the FM100-HUE scale (excellent quality), excepting the C33.

The lowest (log) error score was detected for C44, and it may be considered the ideal region for emission of personalized PL materials for treatments in emergency signalling. The correlated spectral sensitivities for C36, C39, C40, C42 and C43 colours with the best colour vision of C44, suggest a personalization of other PL materials light emitting on the respective region at 495 nm.

Note that all mean values of the scores for colours from C31 to C53 (485-555 nm) resulted in excellent FM100-HUE quality and might be recommended for personalized approaches for these specific treatments.

Recently, scientific studies reveal that the personalization from specific diagnostics with a specialization domain and highly innovative solutions for small populations will be come commoner, but still more expensive [153]. More “prevalent” diseases are more significant for statistical studies, and specific subgroups may justify different personalized approaches.

Thus, the personalization from diagnostic of retinal cells of the end users must, for instance, be understood in personalized approach cost effectiveness most critically as a function of:

- (1) frequency of occurrence of uses of photoluminescent materials for the trial individuals with their specific attributes, i.e. diabetic retinopathy, in their respective conglomerate;**
- (2) cost of the colour vision tests, if applicable;**
- (3) incremental cost of “personalized photoluminescent materials” approach over “standard” approach, if applicable.**

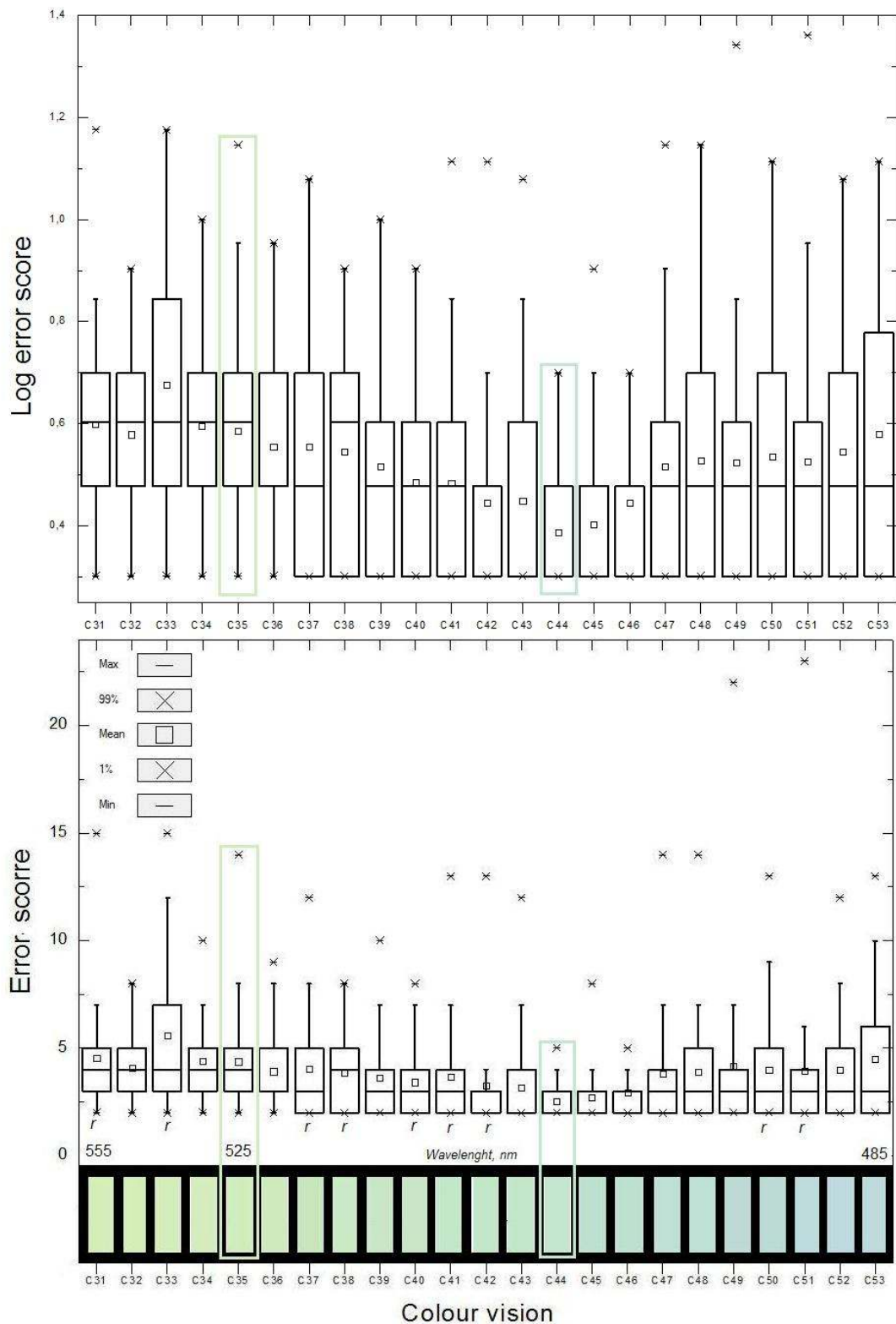


Figure 6-14. Biostatistics of retinal responses of treatments with diabetic retinopathy from (C31) to (C53) in the yellow-green-blue region (485-555 nm), in black background, for personalization of $\text{SrAl}_2\text{O}_4:\text{Ce}^{3+}, \text{Dy}^{3+}, \text{Eu}^{2+}$ in emergency, more specifically at 525 nm (C35).

6.7. Conclusion

This work provided the development and experimentation of a medical equipment to diagnose the photopic retinal biofunctionality from measurements of the colour vision through computational FM100-HUE test. The equipment showed to be efficient in the practice of ophthalmology, enabling the binocular examination of 85 individuals (170 diagnoses) in a time period of 38 days, which users/patients were located in different geographical regions.

Optimizing the visibility as a vital factor to save people in escape routes, the investigation was focused on the personalization of photoluminescent materials for emergency signalling. The diagnoses were obtained from examinations in 38 treatment-patients with diabetic retinopathy and 38 references-firemen ($N=76$). A biostatistical study was made through ANOVA (intergroup), T-test (intragroup) and Pearson correlations analysis.

Comparing the diagnoses obtained between white/black backgrounds by T-test, treatments presented lower log error scores in black background, as a better colour contrast sensitivity. Based in this result, a personalization of photoluminescent materials was made for this specific treatment group with diabetic retinopathy, for optimization of the luminescence visibility upon a black background.

The colour sensitivity on the UV-VIS region at about 555-485 nm revealed to be excellent in the FM100-HUE scale, with mean error scores up to 10. The best colour vision quality of treatments was C44 (~495 nm) as an ideal region for luminescence emission and detection by these end users. Correlated colours C36, C39, C40, C42 and C43 and their respective wavelengths might be personalized for the treatments, in emergency signalling, aiming to promote a higher autonomy during utilizations in escape routes.

The medical equipment may open new prospects in personalized approaches. However, considering the scientific limitations of this study in the Ophthalmology area, the equipment should, therefore, be further investigated, before it finds applications for the end users. ■

Chapter 7

Designing the photoluminescent-warning ceramic tiles for risk areas and emergency

The first two parts of this chapter describe the principles of Universal Design applied at projectual level for the development of multidisciplinary solutions in the scientific area of Architecture. *Photoluminescent-warning ceramic tiles for risk areas and emergency — PL-WCT* were designed, aiming at applying the $\text{SrAl}_2\text{O}_4:\text{Ce}^{3+}$, Dy^{3+} , Eu^{2+} nanomaterials in large scale for accessibility in emergency. The directives for the technical characteristics of the product, still defined at conceptual level, were supported by different data sources crossing transversal normatives of accessibility and luminescence. The third part of this chapter reports the results of a preliminary investigation on the assessability of thermal properties of $\text{SrAl}_2\text{O}_4:\text{Ce}^{3+}$, Dy^{3+} , Eu^{2+} , porcelain stoneware substrate, and transparent glass frit, as well as the evaluation of their compatibility when integrated into a multilayered system as that required to accomplish the planned PL-WCT. The results showed that the main technical solutions still remain to be solved through a more detailed approach in order to obtain the PL-WCT as a final product.

Key-words: luminescence, warning detectable tiles, ceramic, emergency, persons with disabilities.

PART I – DESIGNING FOR ACCESSIBILITY

This part of the chapter proposes the conceptual solutions for architectural applications of $\text{SrAl}_2\text{O}_4:\text{Ce}^{3+}$, Dy^{3+} , Eu^{2+} nanomaterials in a multisensorial system for accessibility in emergency.

7.1. Multisensory systems for accessibility

A brief description of the existing multisensory systems is presented, stating the available technologies for accessibility, namely the warning detectable tiles and photoluminescent products for safety.

7.1.1. Warning detectable tiles

Assistive technologies of floors to facilitate the mobility of people with deficiencies are in the common sense well known as “*warning detectable tiles*” [12], which are produced according specific international standardization [3-5]. In 2003, a utility model of ceramic floors with warning devices was developed in previous research [9], which makes up a system of signalling the conditions of access with tactile, visual and sound devices. Despite being doted by differentiated features for people with disabilities, including the use by blind and people with low vision, these tiles do not include the functionality to risk areas, in the dark in emergency, due to the absence of luminescent material.

Other tactile tiles have been used in Japan since 1967, namely started in Okayama City. Figure 7-1a

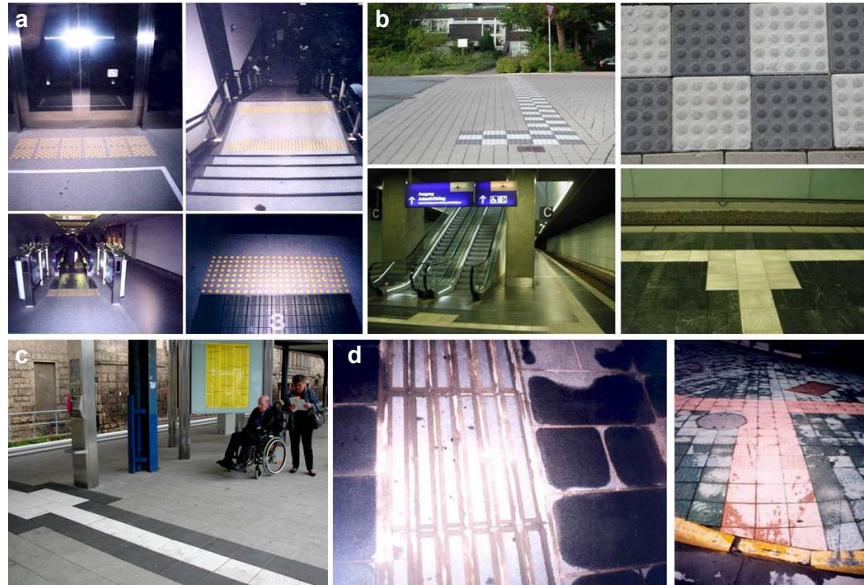


Figure 7-1. Warning detectable tiles applied in: a) Japan; b) and c) Germany; and d) China.

shows a type of tactile tile in Tokyo City, Japan. Detectable tiles in concrete (Figure 7-1b) and in ceramic material (Figure 7-1c) are used on the street, in Germany, evidencing the black background contrast. Guiding tiles, in metal and concrete, are also used in public spaces in China, Figure 7-1d. The main produced typologies are for alert and guide floors, in diverse materials, such as natural rock, vinyl, rubber, hardened metal, and with some peculiar forms.

7.1.2. Photoluminescent products for safety

In parallel to tactile tiles, photoluminescent (PL) floors started being developed since the decade of 1990, following the sprouting of innumerable materials, methods of preparation, products and devices with this property [13]. Several techniques support the manufacture and application of polymeric, metallic or ceramic artefacts with photoluminescence property. The PL products destined to the emergency signalling in pedestrian pathways are used in the floor (horizontal plain) as in the wall (plain vertical line). They offer a gamma of cryptograms of accessibility (e.g. PL tapes and paints, or other products which are applied in a secondary process), generally combined with a non-luminescent (inert) product installed on the egress route.

The labour required to combine the photoluminescent component with the non-luminescent product, however, still adds considerable cost because of a separate manufacturing step, i.e. the application of the photoluminescent material. No satisfactory products comprising an integral combination of luminescent and non-luminescent materials with said multisensory mechanisms have been disclosed so far, as discussed in the follow documents [13]:

U.S. Pat. N° 4,385,586 [13a] discloses a path-marking system employing a series of photoluminescent accessories. Each individual accessory has tactile characteristics of shape and surface contacts which indicate direction and distance to the nearest evacuation exit.

U.S. Pat. N° 4,801,928 [13o] shows an egress detection system including at least three electroluminescent lamps in a linear arrangement and circuitry for sequentially illuminating the lamps. Each lamp contains two sets of indicators in the form of arrows pointing in opposite directions. The arrows pointing toward one exit are illuminated in the case of sensed danger, and in the opposite direction, are illuminated in response to a second sensed danger.

U.S. Pat. N° 4,401,050 [13p] discloses a continuous adhesive transparent sheet having discontinuous phosphorescent arrows or other indicia protruding there from. The indicia is either formed within or attached to the adhesive sheet. If the indicia are formed within the sheet, the phosphorescent material is added in a secondary combining operation.

U.S. Pat. N° 2,169,657 [13q] discloses a woven floor covering made with yarn dyed with rhodamine, a substance which fluoresces when exposed to ultraviolet light. Another embodiment discloses a woven floor covering printed with fluorescent or ultraviolet light-sensitive pigments. In another embodiment, a floor covering is painted with fluorescent paint.

U.S. Pat. N° 2,387,512 [13r] discloses a photoluminescent adhesive tape with a layer of photoluminescent pigment which is protected from the atmosphere by a transparent film which does not interfere with the activation of the photoluminescent pigment on exposure to light. The product is continuous strip of non-luminescent material coextruded with photoluminescent material to form an integral product molecularly bonded. An emergency lighting system for an aircraft has photoluminescent strips mounted on the floor rather than a string of electrical lights.

7.2. Designing with $\text{SrAl}_2\text{O}_4:\text{Ce}^{3+}$, Dy^{3+} , Eu^{2+} nanomaterials

As seen previously, photoluminescent $\text{SrAl}_2\text{O}_4:\text{Ce}^{3+}$, Dy^{3+} , Eu^{2+} nanotubes, nanowires and core-shells materials have been investigated for applications in emergency (please see chapters 3, 4, 5 and 6). Their potential application was investigated in this chapter according to the principles of Universal Design, virtual modelling (CAD 2D/3D), architectural crafts and ceramic process, aiming at developing photoluminescent-warning ceramic tiles for emergency signalling.

Stages/limitations of photoluminescence application in ceramic tiles

This hypothesis stays yet in an early stage of development. An essential cornerstone was the utility model of ceramic floors with warning devices for handicapped and visual impairments proposed before [9]. Further extending the concept to photoluminescent-warning ceramic tiles [113] implies applying the phosphors materials in the reliefs of ceramic tiles. Achieving this target following a ceramic processing route requires matching the coefficients of thermal expansion of all material components involved, namely, the porcelain tile substrate, the low melting temperature glaze frit and the phosphors. This is challenging considering the differences in the thermal properties of these materials, as will be reported (Part III of this chapter). The schematics of the exploratory stages of such a product are drawn in Figure 7-2.

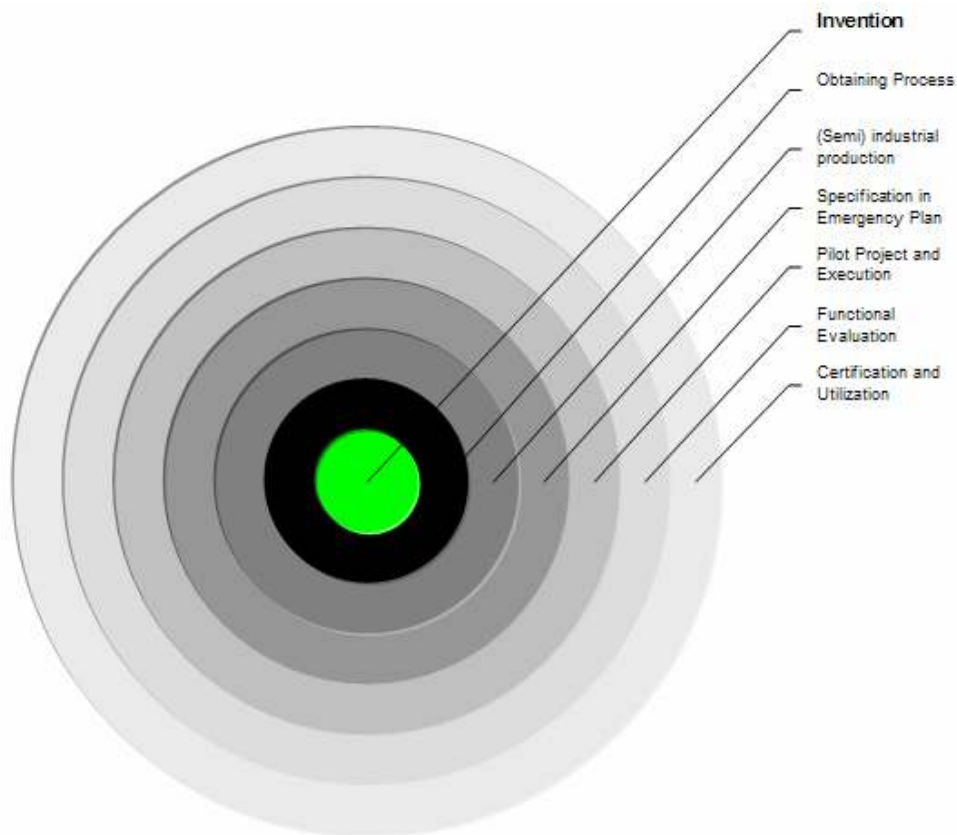


Figure 7-2. Stages of the exploratory application of $\text{SrAl}_2\text{O}_4:\text{Ce}^{3+}$, Dy^{3+} , Eu^{2+} nanomaterials on the development of the photoluminescent-warning ceramic tiles (PL-WCT).

7.3. PL-WCT — Photoluminescent-warning ceramic tiles [113]

The conceptual development of *PL-WCT— photoluminescent-warning ceramic tiles for risk areas and emergency of people with disabilities* [113] is described. Some typologies were designed with multisensory mechanisms and multifunctional properties (e.g. fire and water resistance), aiming at compensating the restrictions of mobility of people with disabilities, in emergencies, with the priority to help to save lives.

7.3.1. PL-WCT typologies

The PL-WCT (Table 7-1) are conceptually characterized by comprising multisensory mechanisms, through the follow functional combinations:

- a **ceramic substrate** for pedestrian traffic in escape routes;
- a **photoluminescent surface** for visualization of escape routes, in the dark;
- a **relief surface** with tactile signage and sonorous contrast between assistive devices (e.g. wheelchairs, canes, walkers);
- an **antimicrobial and antibacterial surface** to maintain immune health;
- a **photocatalytic self-cleaning surface**, optional, for antiseptic maintenance.

Figure 7-3 illustrates a general sight of four possible typologies of the photoluminescent-warning ceramic tiles, absorbing light in the clarity, and light-emitting in the dark, under the effect of persistent luminescence. When the relief surfaces are activated by the mechanism of persistent photoluminescence by long afterglow-in-the-dark emission of light after a source of excitation energy is removed, the related floors can emit light during hours (~12 h), allowing faster evacuation of people with deficiencies during the emergency situations, such as in absence of electricity or fire presence.

Table 7-1. Photoluminescent-warning ceramic tiles for risk areas and emergency [113].

Typologies	Function in risk areas and emergency
Crossing	Allows the simultaneous use of mobility aids for demarcation of a change of direction during the evacuation of areas of risk in the dark, preferably with the substrate produced in the colour representative of signalling (red), Figure 7-3, (a) and (b).
Stopped	Allows the simultaneous use of mobility aids for short stay in emergency equipment (e.g. fire extinguishers) for the evacuation of areas of risk in the dark, preferably with the substrate produced in the colour representative of signals (yellow), Figure 7-3, (c) and (d).
Directional (Connected)	Allows the simultaneous use of mobility aids for the demarcation of rapid evacuation routes in areas of risk in the dark, preferably with the inert substrate produced in the colour representative of signalling (green). The photoluminescent directional grooves are connected to each other forming continuous lines in the dark, Figure 7-3, (e) and (f).
Directional (Non-connected)	Allows the simultaneous use of mobility aids for the demarcation of rapid evacuation routes in areas of risk in the dark, preferably with the substrate produced in the colour representative of signalling (green). The photoluminescent directional grooves are forming independent discrete lines in the dark, Figure 7-3, (g) and (h).

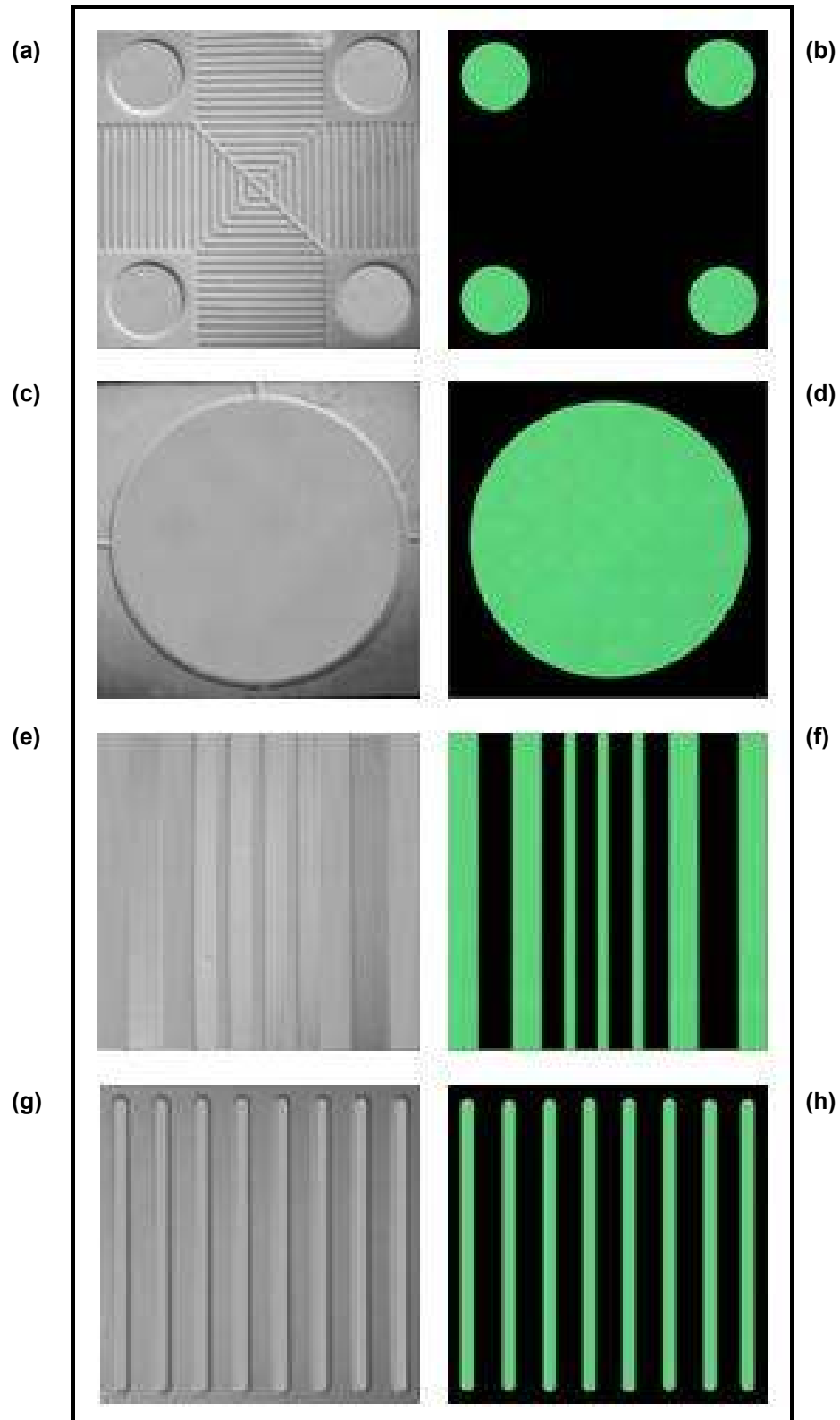


Figure 7-3. Typologies of multisensory photoluminescent-warning ceramic tiles comprising visual, sonorous and tactile contrast features, which may be functionalized with antibacterial, antimicrobial and self-cleaning surfaces, under D65-illuminant and upon afterglow-in-dark emission (0 lux) [113].

7.3.2. Transversal characterization in emergency

The transversal technical characteristics required for the tiles attending the current normatives and legislations, as described in Table 7-2. The normatives ANSI ICC/A117 [3], ADAAG 4.29 [4], and ISO-TC/173 [5] are specific about facilities and accesibility of persons with disabilities, while the DIN 67510 [14] and PSPA [16] are specific for photoluminescent materials and products.

Table 7-2. Transversal characterization of the photoluminescent-warning ceramic tiles, predicted after exposition to illuminance >25 lux, for 10 min.

PL-WCT typologies		International legislation
Type A Surface of PL-WCT Directional (Connected)	Width of the PL relief: 30 ± 0.5 mm Spacing between reliefs: 75 ± 0.5 mm	ANSI ICC/A117 [3] ADAAG 4.29 [4] ISO-TC/173 [5] DIN 67510 [14] PSPA [16]
Type B Surface of PL-WCT Directional (Non-Connected)	Width of the PL relief: 30 ± 0.5 mm Spacing between relief: 75 ± 0.5 mm	
Type C Surface of the PL-WCT Stopped	Diameter of the PL relief: 200-500 mm Unitary photoluminescent relief	
Type D Surface of the PL-WCT Crossing	Diameter of the PL relief: 30-100 mm Spacing between reliefs: 90-200 mm	
Luminescence performance (relief): Classes I, II or III Luminance on the afterglow lifetime (relief): > 1 h (above the limit of visibility of 0.3 mcd/m^2)		DIN 67510 [14] PSPA [16]
Visual contrast (relief reflectance and adjacent area): > 70%		
Tactile contrast (height of the relief): ~3 mm with anti-slip texture		
Coefficient of static friction (μ): 0.6 a 0.8 (<i>slip resistance</i>)		
Sound contrast (with the adjacent floor): includes aid for mobility		
Application in risk areas		
Level of risk I	Place with some natural light source, with emergency lighting system	DIN 67510 [14] PSPA [16]
Level of risk II	Places without natural light or regular busy periods in the dark or night, with emergency lighting system	
Level of risk III	Places with artificial lighting, or busy in regular periods in the dark or night, without emergency lighting system (evacuation routes)	

For practical applications in emergency, the height of reliefs without the PL layer is recommended to be of 5 mm [4], but the concept of PL-WCT here proposed goes beyond this limits and, accordingly, the height of the reliefs can vary between 3 and 12 mm [113].

7.3.3. Principles of Universal Design in emergency signalling

The PL-WCT were proposed to be functionalized with the persistent luminescence property, added to the relief surfaces, in accordance to the principles of Universal Design. The ergonomic aspects and legibility of these floors include individuals with physical deficiency or with reduced, temporary or permanent low mobility (including persons in post-surgery period, pregnant, obese, children patient, or people with special needs).

The Universal Design concerning the development of these tiles will enable higher degrees of autonomy and security on risk areas in emergency situations, attributing the benefits offered by these tiles to all users, as shown in Table 7-3.

Table 7-3. Evaluation of the photoluminescent-warning ceramic tiles based on the Principles of Universal Design for an emergency system [113].

Dark adapted emergency signalling system		
Equitable use	PL-WCT in lighting or darkness provides the same means of use for all users: identical whenever possible; equivalent when not. Avoid segregating or stigmatizing any users. Provisions for security and safety are equitable and available to all users in emergency. Make the design appealing to all users.	ADAAG 4.29 [4] ISO-TC/173 [5] DIN 67510 [14] PSPA [16] Universal Design
Tolerance for error	PL-WCT in lighting or darkness arranges elements to minimize hazards and errors in risk areas and emergencies. Provides warnings of hazards and errors. Provides fail safe features. Discourage unconscious action in tasks during emergencies that require vigilance and defines the preferential escape routes.	
Perceptible information	PL-WCT in lighting or darkness uses multisensory modes (visual, tactile, and sonorous) for redundant presentation of essential information in emergency. Provide adequate visual contrast between photoluminescent escape routes and its surroundings. Maximize "legibility" of essential information in risk areas and emergencies. Differentiates signal elements (directional, crossing, stopped) in ways that can be described (i.e., make it easy to give instructions or directions). Provides compatibility with multisensory devices used by people with sensory limitations in emergency.	
Size and space for approach and use	PL-WCT provides a clear directional line of sight in escape routes for any seated or standing user. Makes reach to all components comfortable for any seated (ex., in a wheelchair) or active users. Accommodates variations in foot and pace sizes during the tactile locomotion. Provides adequate space for the use of assistive devices or personal assistance in emergency escape routes.	
Flexibility in use	PL-WCT in lighting or darkness provides choice in methods of use. Accommodates right- or left-footed access and use. Facilitates the user's accuracy and precision in emergency. Provides adaptability to the user's pace, velocity and health condition during the evacuation in emergency.	
Simple and intuitive use	PL-WCT eliminates unnecessary complexity in emergency signals, attending user expectations and intuition. Accommodates a wide range of literacy and language skills. Arranges information in lighting or darkness consistent with its importance during emergency. Provides effective prompting and feedback during and after task completion.	
Low physical effort	PL-WCT allows user to maintain a neutral body position lighting or darkness. Uses reasonable operating forces in presence of fire or smoke. Minimizes repetitive actions and minimize sustained physical effort in emergency.	

7.4. PL-WCT sunlight energy upconversion and emission

The PL-WCT upconversion is a photoluminescent process converting lower levels of solar energy incident light to higher energy emitted light that occurs on the PL layer surfaces when applied in risk areas exposed to sunlight illumination. These surfaces are detailed for each typology in the following Figures 7-4, 7-5, 7-6 and 7-7.

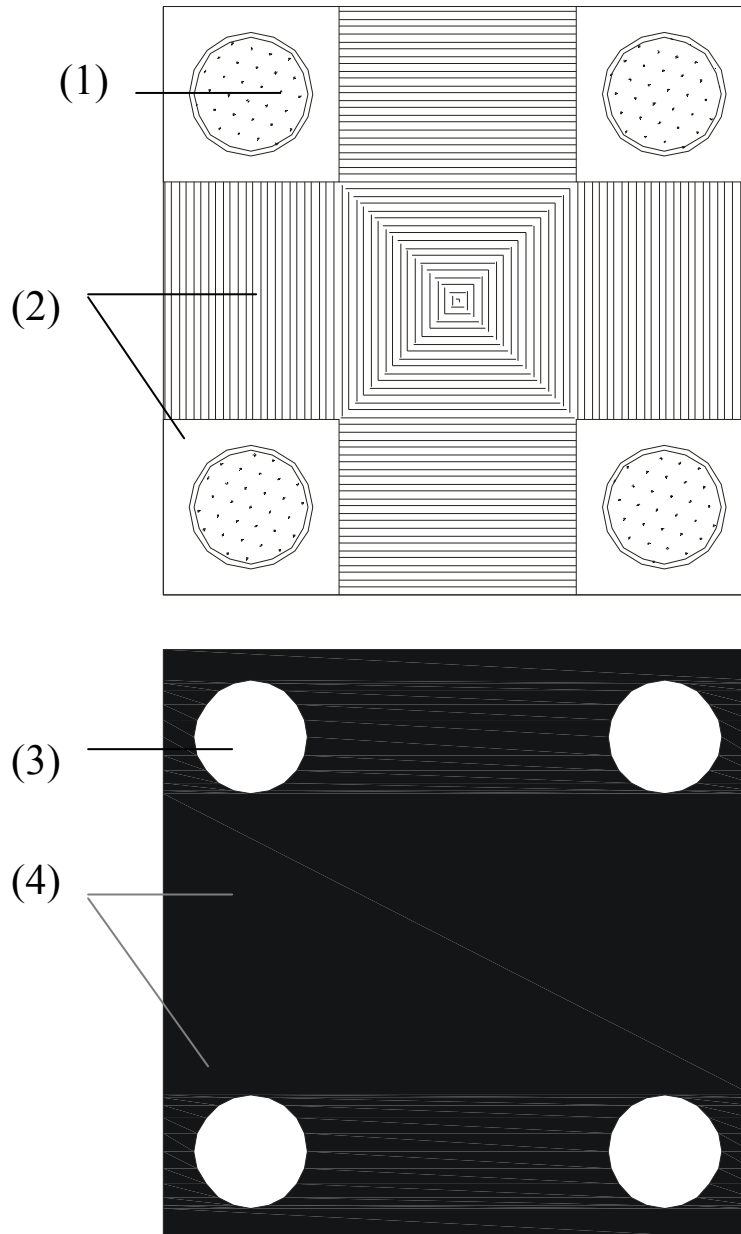


Figure 7-4. PL-WCT crossing tile under a solar exposition absorbing the sunlight energy on the photoluminescence relief surfaces (1) adjacent to non-luminescent (inert) surfaces (2); and under afterglow-in-dark (0 lux) by persistent luminescence upconversion and emission from relief surfaces (4) in contrast with dark surfaces (2).

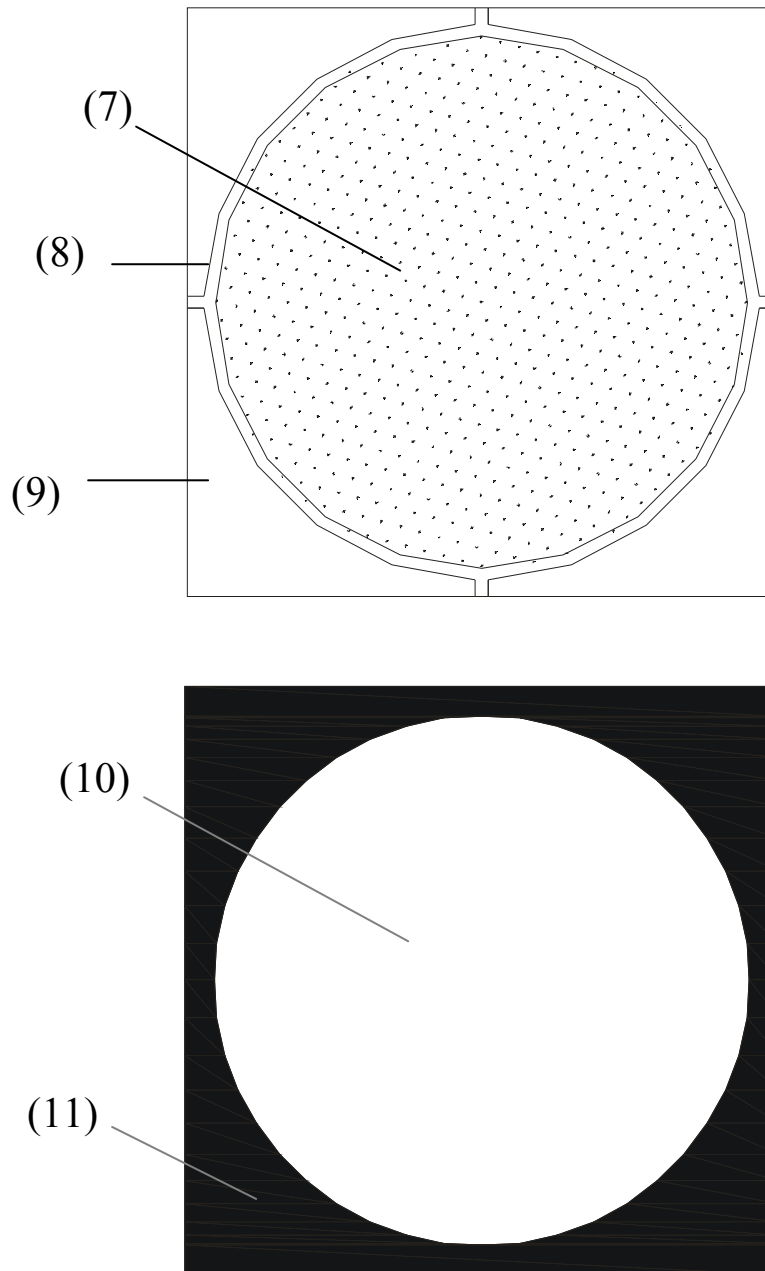


Figure 7-5. PL-WCT stopped tile under a solar exposition absorbing the sunlight energy on the photoluminescence relief surfaces (7) adjacent to non-luminescent (inert) surfaces (8) and (9); and under afterglow-in-dark (0 lux) by persistent luminescence upconversion and emission from relief surface (10) in contrast with dark surface (11).

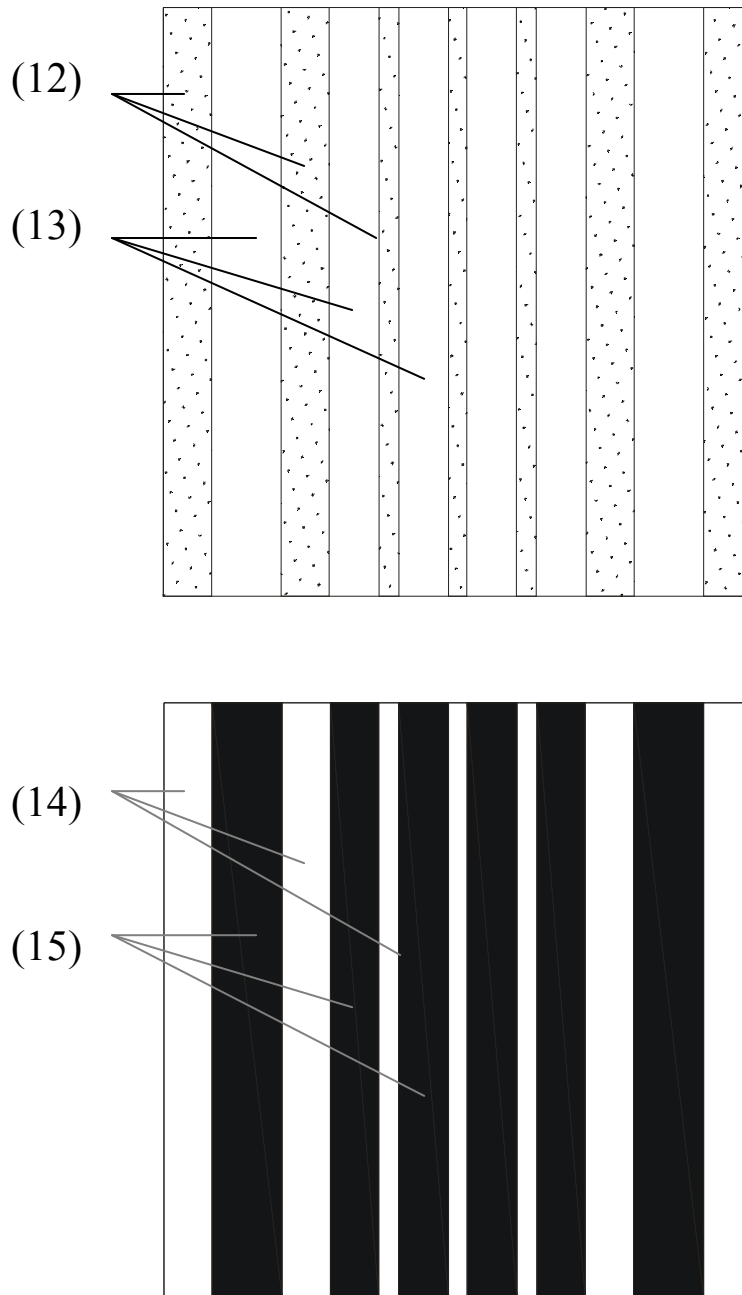


Figure 7-6. PL-WCT directional guiding tile (connected) under a solar exposition absorbing the sunlight energy on the photoluminescence relief surfaces (12) adjacent to non-luminescent (inert) surfaces (13); and under afterglow-in-dark (0 lux) by persistent luminescence upconversion and emission from relief surfaces (14) in contrast with dark surfaces (15).

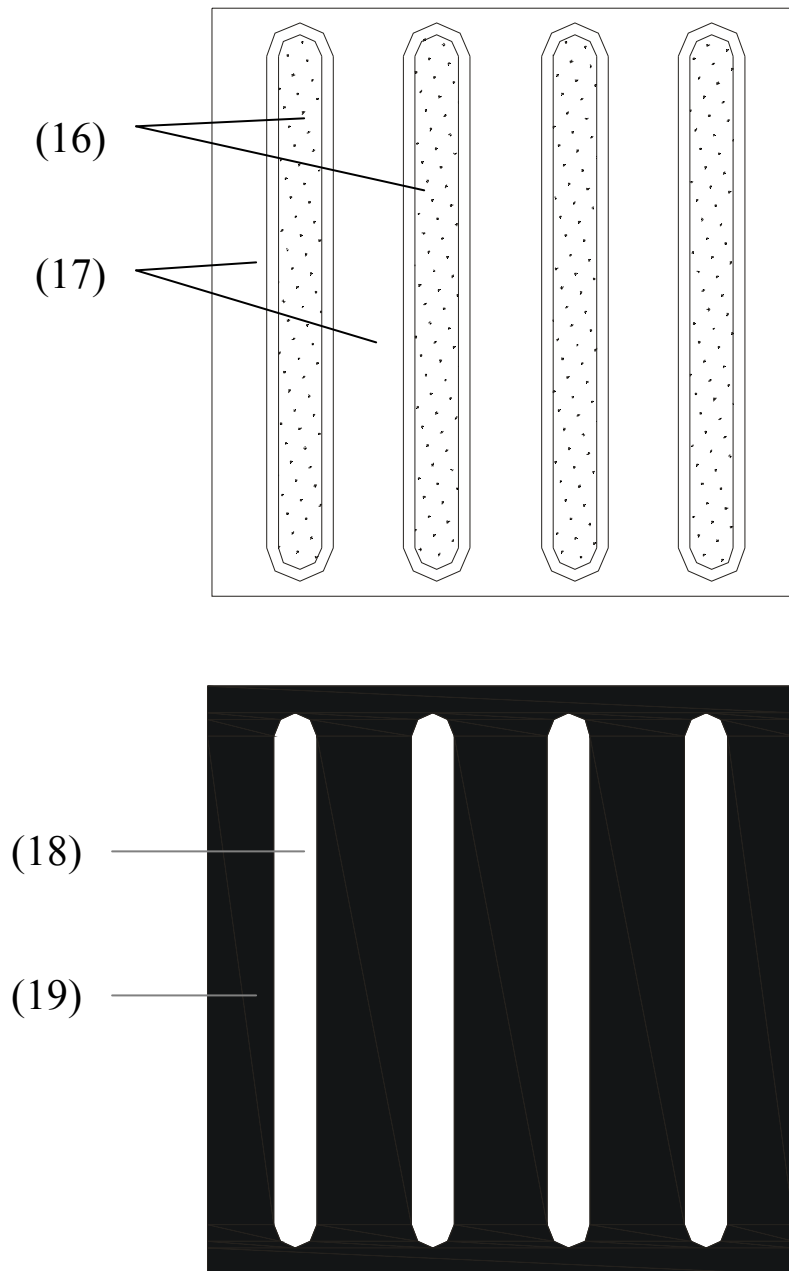


Figure 7-7. PL-WCT directional guiding tile (non-connected) under a solar exposition absorbing the sunlight energy on the photoluminescence relief surfaces (16) adjacent to non-luminescent (inert) surfaces (17); and under afterglow-in-dark (0 lux) by persistent luminescence upconversion and emission from relief surfaces (18) in contrast with dark surfaces (19).

7.5. PL-WCT architectural applications

The architectural applications of the PL-WCT might be useful in the pedestrian pathways, of interior or exterior spaces, with public or private uses, under natural or artificial illumination, lighting systems or absent (0 lux), activated or not for emergency illumination, in dark environments, in emergency.

These floor tiles are destined to the use in routes of evacuation, corridors, slopes and exits of emergency in general (e.g. in airports, train stations, industries, hospitals, health centres, etc.). Such floors also may contribute to order the architectural barriers (e.g. pillars, equipments), to signal conditions of access (e.g. staircases, corridors), including areas of short permanence with equipment (e.g. in front of the elevators, hydrants and fire extinguishers).

Figure 7-8 exemplifies an Emergency Plan by using the directional and crossing PL-WCT when its need change the direction on the evacuation process in escape route.

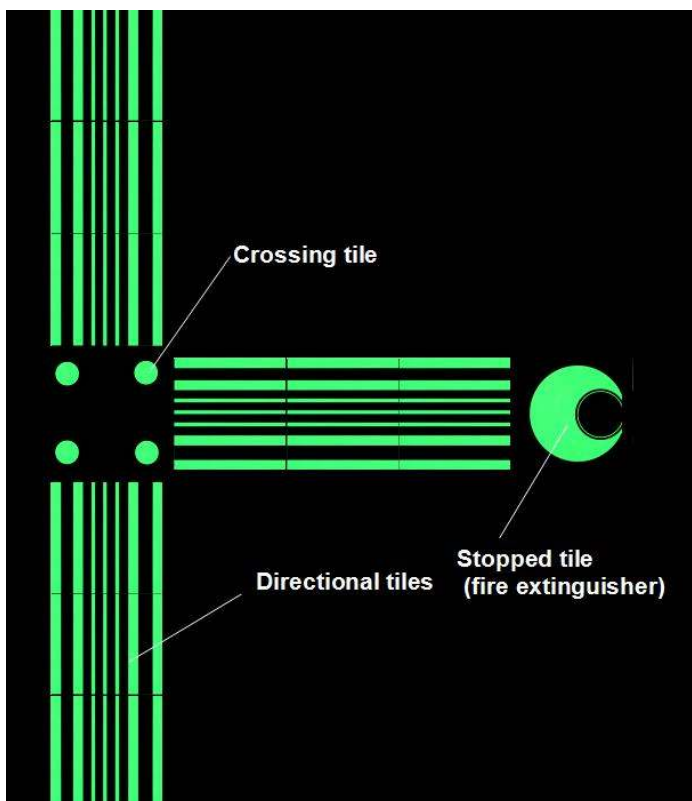


Figure 7-8. Example of a functional Emergency Plan using directional (connected), stopped and crossing tiles typologies combined in an escape route.

Such floor tiles are destined to pave the evacuation routes in Emergency Plan (Figure 7-8), in aerospace, maritime space, or earth space, in vertical-building (Figure 7-9), or horizontal-building (Figure 7-10 and 7-11) with signalized pedestrian pathways under risk conditions of severe or absent illumination.

Vertical-building evacuation in earth space

Empire State Building, New York City (US)

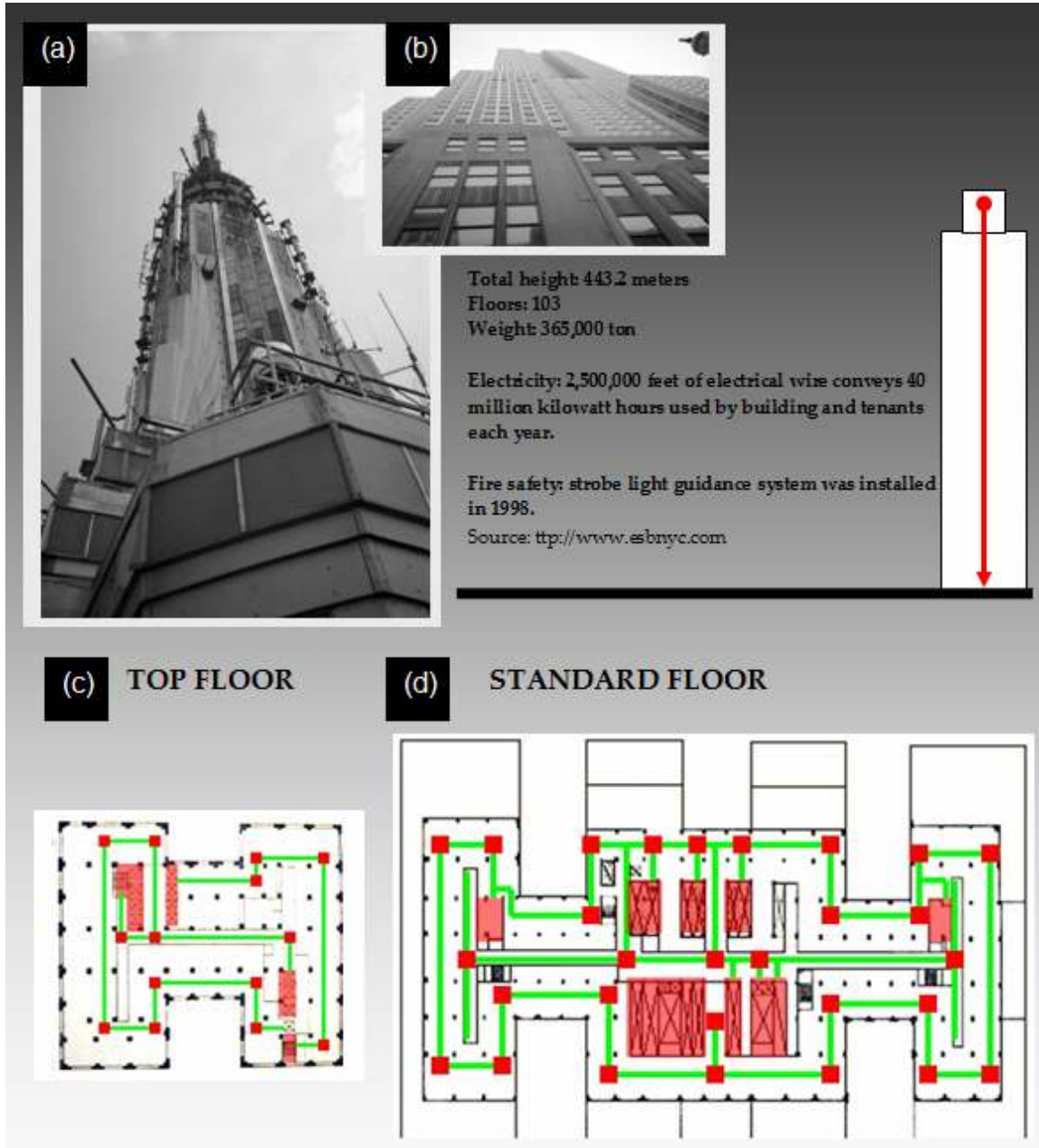


Figure 7-9. a-b) Top view and building plan of Empire State Building, New York City, US (2006). Schematic example of a functional dark adapted Emergency Plan: c) tower and d) standard floor plans for evacuation using the photoluminescent-warning ceramic tiles. This solution was planned based on the elemental circulation pathways. Not scaled (n/s). <http://www.safe-t-first.com/reference-standard-rs6-1.pdf>

Horizontal-building evacuation in earth space

University of Aveiro Library, Aveiro City (PT)

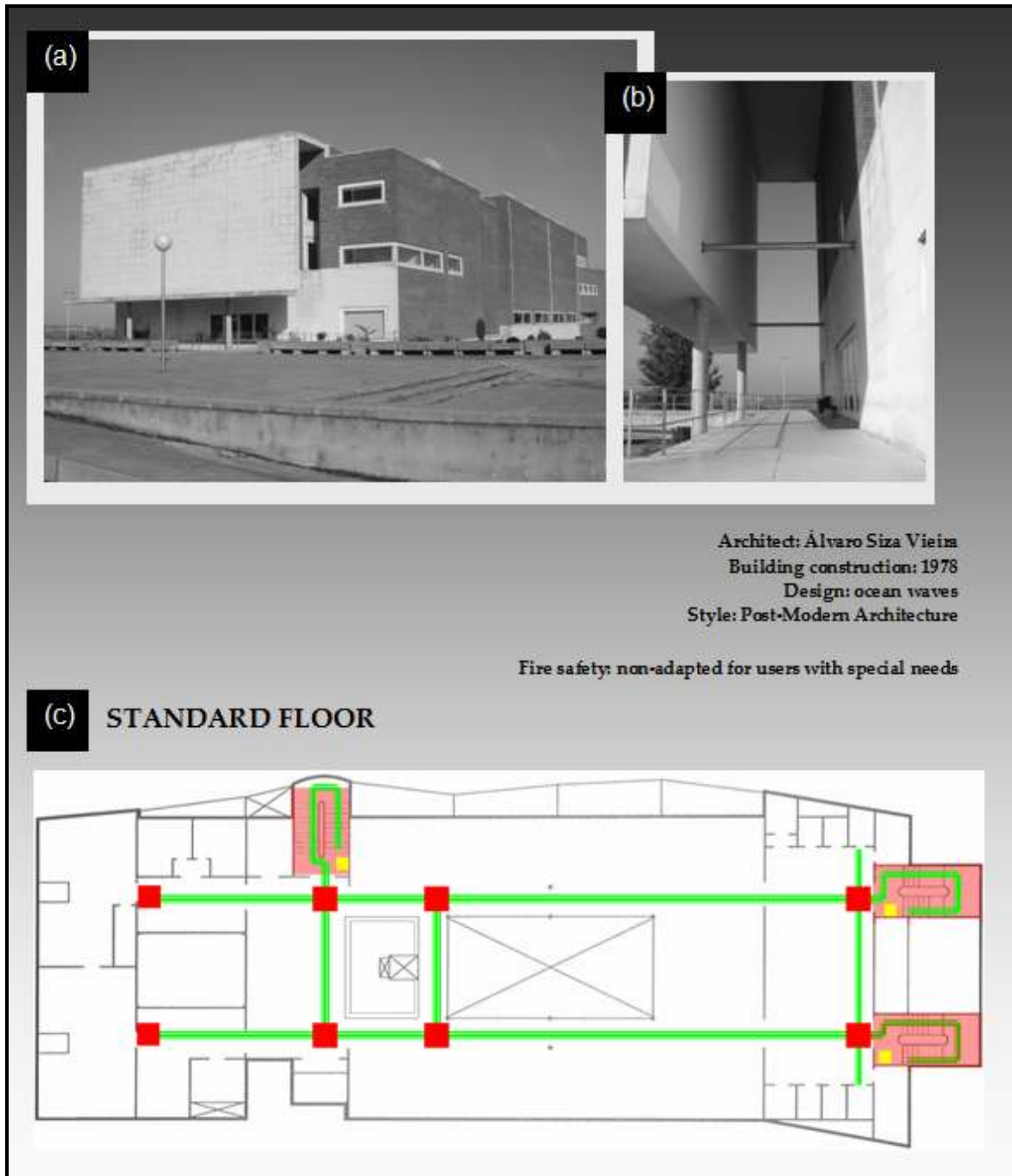


Figure 7-10. Example of a functional dark adapted Emergency Plan of the University of Aveiro Library for evacuation using the photoluminescent-warning ceramic tiles. The solution was planned based on the elemental circulation pathways [113]. Not scaled.

Horizontal-building evacuation in earth space

University of Aveiro Library, Aveiro City (PT)

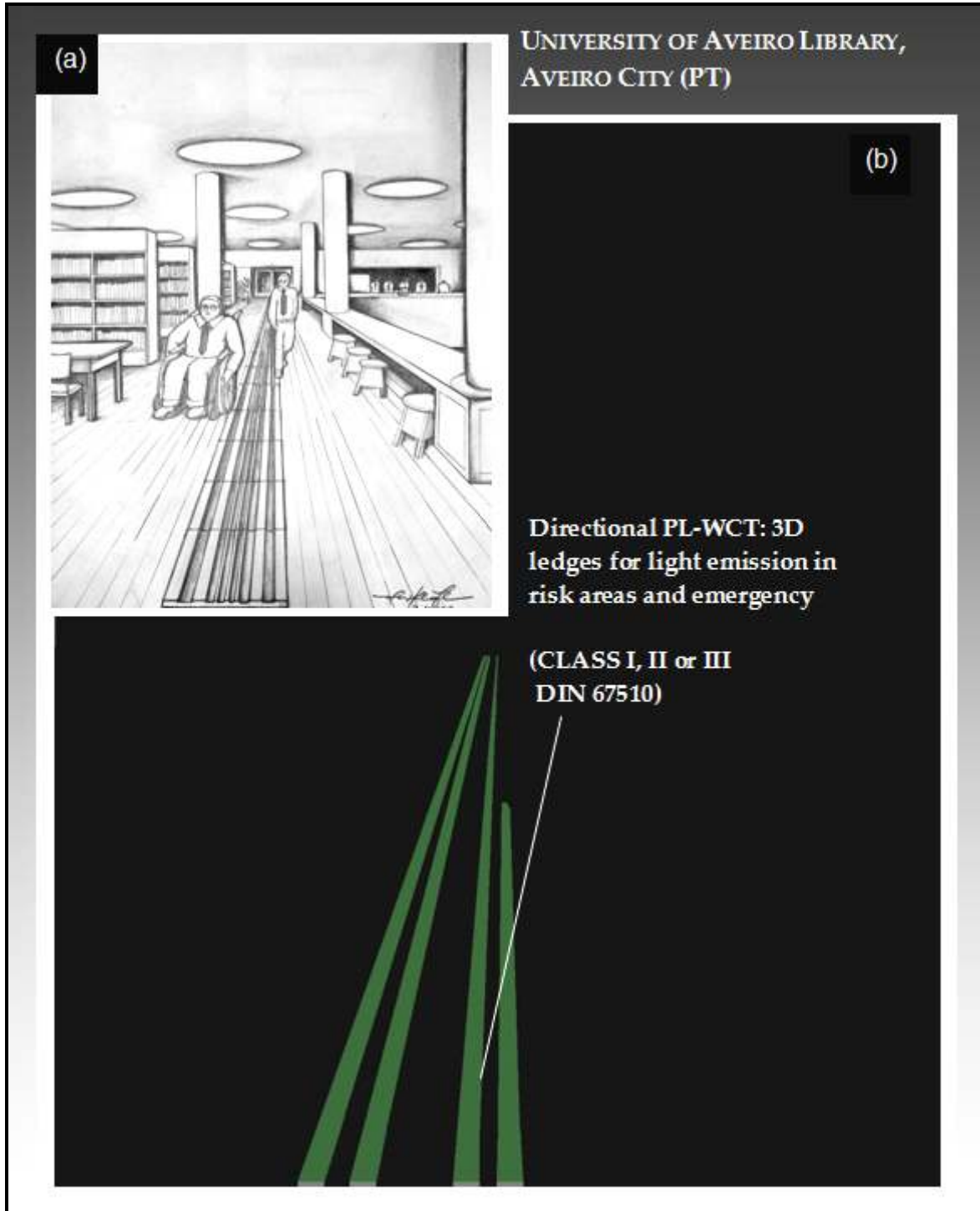


Figure 7-11. Example of a functional dark adapted Emergency Plan of the University of Aveiro Library for evacuation, using the photoluminescent-warning ceramic tiles [113]. The solution was planned based on the elemental circulation pathways. No scale.

PART II — MANUFACTURING PL-WCT

This part of the chapter concerns the design of the ceramic process to manufacture the PL-WCT. The steps proposed via sintered route are illustrated at a conceptual level. The materials mentioned in each section of the ceramic process in multilayered system are given as examples.

7.6. Ceramic process [113]

The processing routes attempted for obtaining small samples of the PL-WCT system are schematized in Figure 7-12:

- non-sintered route, from hydraulic cement-based formulations;
- sintered route, involving the use of traditional ceramic tiles formulations.

The PL-WCT systems may be enamelled with technical or natural finishing, polished or rectified to enhance the physical properties (optical, mechanical and morphological) to allow its use in areas of pedestrian traffic.

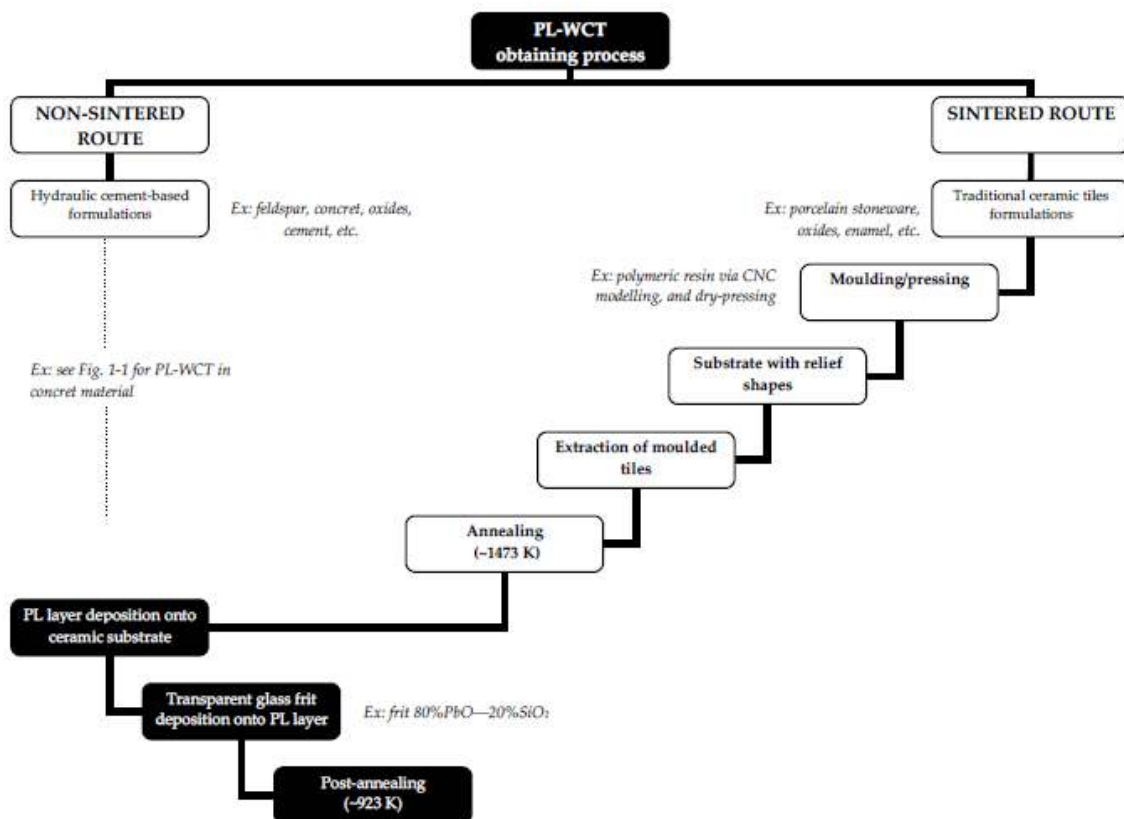


Figure 7-12. Processing routes attempted for preparing PL-WCT products.

The sintered route investigated in the thesis included the following basis steps: (i) filling the mould with the ceramic powder; (ii) pressing to obtain the substrate; (iii) firing the ceramic substrate at 1473 K; (iv) applying the photoluminescent layer onto the ceramic substrate; (v) applying the transparent glass frit onto PL layer; and (vi) post-annealing at 923 K.

7.6.1. Moulding and pressing the ceramic substrate

As referred before, an industrial porcelain stoneware formulation (65% SiO_2 —21% Al_2O_3 —14% alkali, source: *Eliane Ceramic Tiles S. A.*) was used as substrates for the PL-WCT. The extraction of the tiles is a critical step due to the reliefs. Figure 7-13 shows an example of polymeric moulds (400 mm x 400 mm) that could be used to consolidate the ceramic substrates (a), and to deposit the PL layer (b). At moment, only the prototyping of the substrate of these tiles was realized using semi-industrial models in porcelain stoneware material in the mould shown in Figure 7-13a [10].

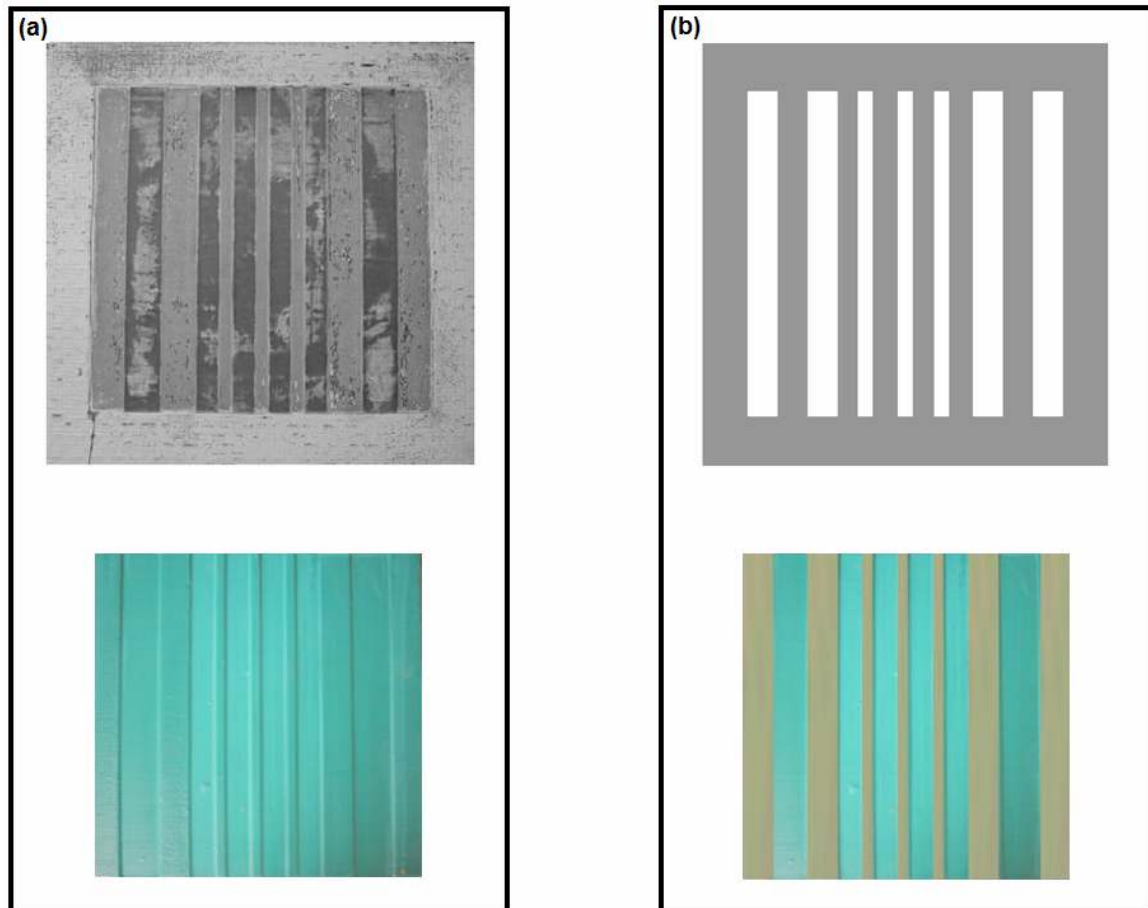


Figure 7-13. Examples of semi-industrial moulding: a) polymeric moulding of substrates [10]; b) design of a second moulding of PL layer and transparent glass frit.

7.6.2. Sintering of the ceramic substrate at 1473 K

The ceramic substrates were sintered at 1473 K, in a fast thermal cycle of 1 hour, remaining for 10 minutes at the maximum temperature, followed by natural cooling inside the furnace. The SEM microstructure of fracture surfaces of the sintered substrate is shown in Figure 7-14 with different magnifications. The morphological AFM features of the pellets' surface and the roughness are presented in Figure 7-15. It can be seen that the samples are rough, as expected from non-polished surfaces.

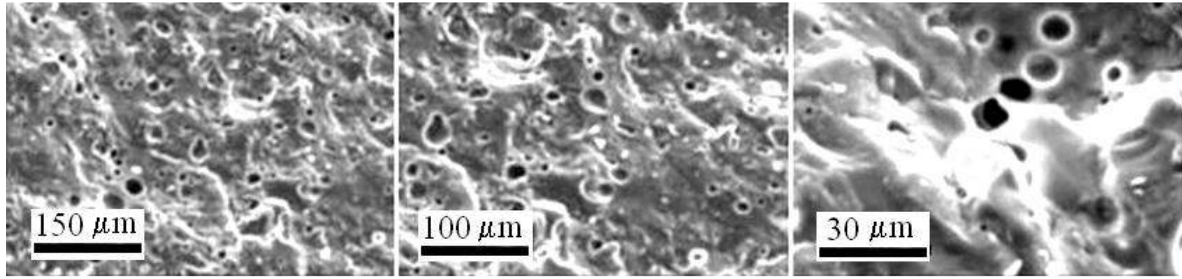


Figure 7-14. SEM images of porcelain stoneware substrate annealed at 1473 K. Opened porosity and roughness on the surface samples are showed and facilitate the interfacial adhesion of luminescent micro- and nano-particles layer in post-annealing conditions.

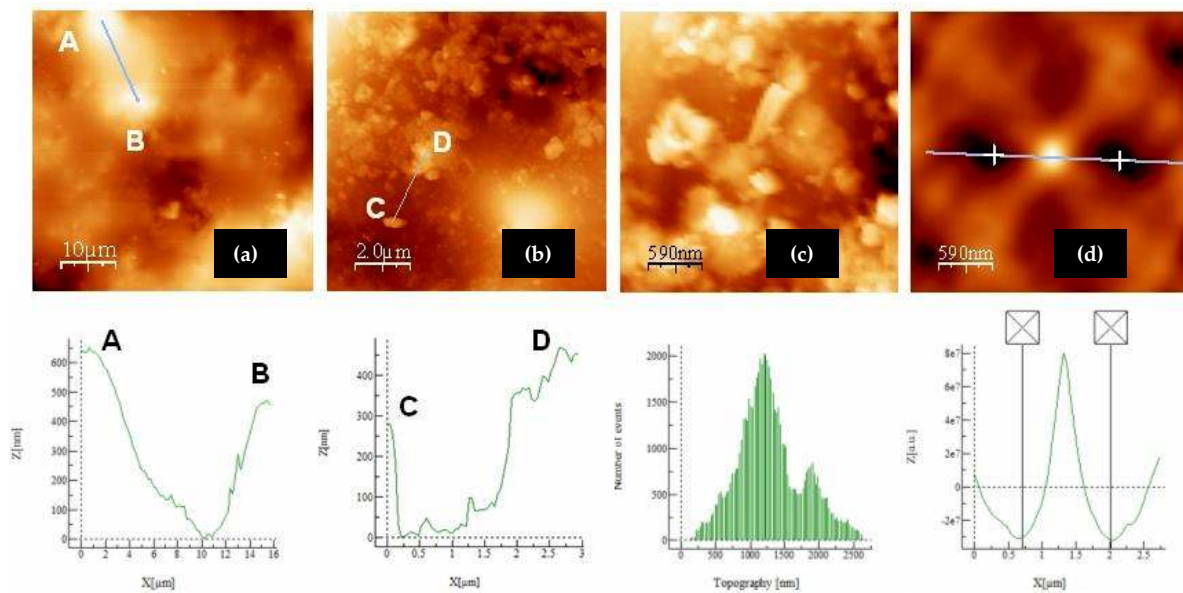


Figure 7-15. AFM morphology analysis of a porcelain stoneware substrate, annealed at 1473 K: a) and b) cross sections, with an average roughness of 2.7 μm (b); c) RMS= 4.7 μm , and surface area= 37.8 μm^2 ; d) self-correlation, with respective grain size = 15 nm.

7.6.3. Photoluminescent layer onto the ceramic substrate

The photoluminescent layer onto the ceramic substrates aims at obtaining a surface transmission light-emitting relief as schematized in Figure 7-16. For a multisensory efficiency, a relation of the total height of the photoluminescent relief (h_L) is proposed:

$$h_L = f + x + s' \quad (7-1)$$

$$12 \geq h_L \geq 3 \text{ mm} \quad (7-2)$$

where f is the thickness of the transparent glass-frit, x is the thickness of the photoluminescent layer, always $> 1 \text{ mm}$ for a better luminous efficiency [23f], and s' is the height of the substrate relief. The s'' corresponds to the planar substrate thickness.

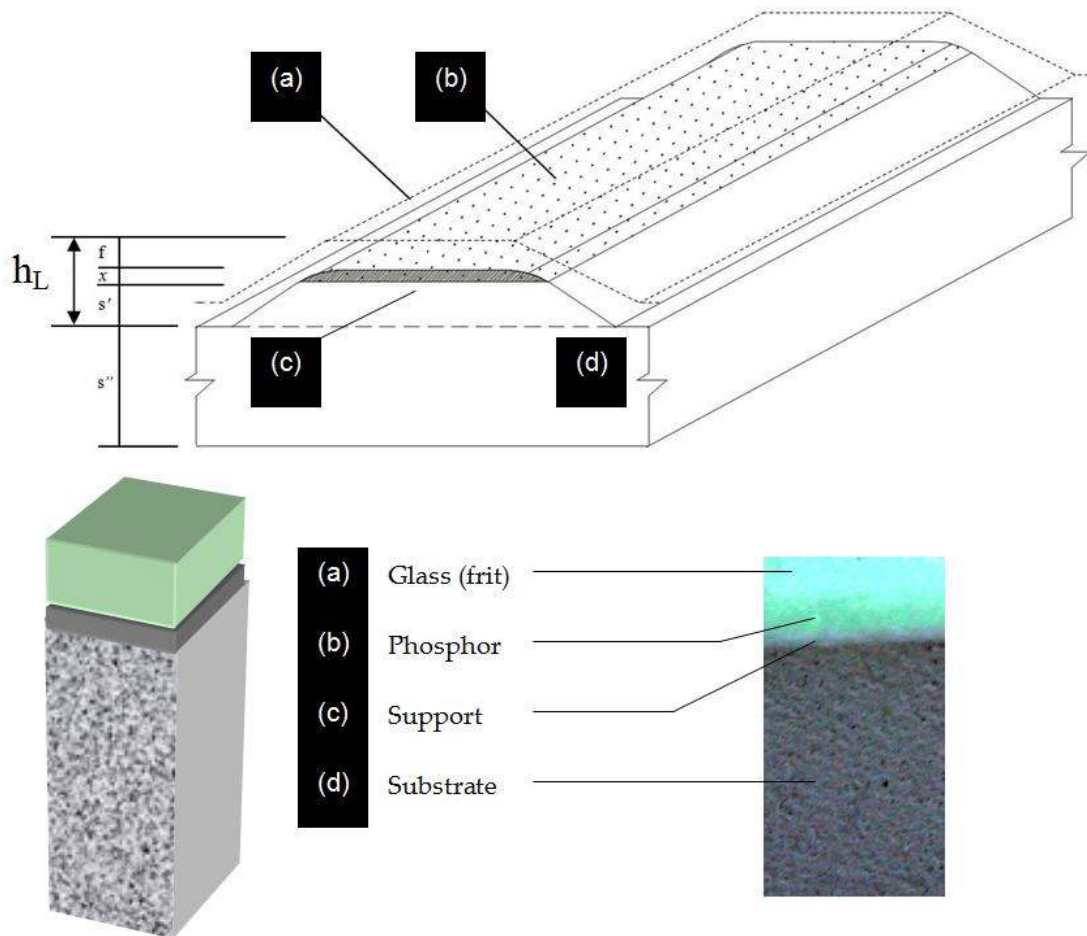


Figure 7-16. Surface transmission light-emitting reliefs: a) transparent glass frit (e.g. PbO-based); b) photoluminescent material (e.g. $\text{SrAl}_2\text{O}_4:\text{Ce}^{3+}$, Dy^{3+} , Eu^{2+} nanotubes, nanowires, nanorods or core-shells); c) support; and d) ceramic substrate (e.g. porcelain stoneware).

The following pigments too can be used on the PL layer (b) in Figure 7-16:

- a) Zinc sulphite ($\text{ZnS}:\text{Cu}$);
- b) Calcium sulphite ($\text{CaS}:\text{Bi}$);
- c) Strontium sulphite ($\text{CaSrS}:\text{Bi}$);
- d) Calcium aluminate co-doped with lanthanide ions (e.g. $\text{CaAl}_2\text{O}_4:\text{Eu}^{2+}$, Ln);
- e) Barium aluminate co-doped with lanthanide ions (e.g. $\text{BaAl}_2\text{O}_4:\text{Eu}^{2+}$, Ln);
- f) or a combination thereof.

7.6.4. Transparent glass frit deposition onto photoluminescent layer

The need of a frit with low melting temperature ($T_m \leq 923$ K) to avoid the phase transformation of PL materials severely restricted the selection of the composition of the transparent enamel layer.

7.6.5. Post-annealing at 923 K

A second heat treatment (post-annealing) at 923 K is required after depositing the photoluminescent and transparent glass frit layers.

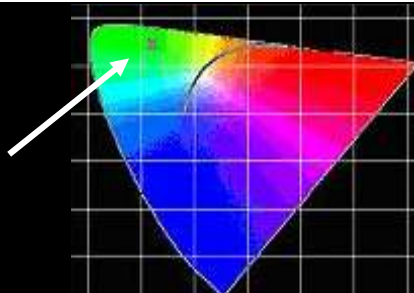



7.6.6. Predicting the technical characteristics of PL-WCT

A prediction of the technical characteristics of PL-WCT is described in Table 7-4 and 7-5 by a combination of $[\text{PbO}_{0.8}(\text{SiO}_2)_{0.2}]\text{-}[\text{SrAl}_2\text{O}_4:\text{Ce}^{3+}, \text{Dy}^{3+}, \text{Eu}^{2+}]\text{-}[(\text{SiO}_2)_{0.65}\text{-}(\text{Al}_2\text{O}_3)_{0.21}\text{-}(\text{alkalis})_{0.14}]$.

Table 7-4. Prediction of technical characteristics of the PL-WCT in multilayered system.

Transparent glass frit (ball-milled)								
Composition	Density [g/cm ³]	Temperature, K						
		TG	Sint _i	TR	T _{sealed}	Sint _f	1/2-sphere	1/3-sphere
80% PbO 20% Al ₂ O ₃	5,85	708	778	826	843	893	1053	1073
Phosphor (monoclinic)								
Composition	Host lattice			Lanthanide activators (Ln)			PL emission	
	Sr	Al	O	Ce	Dy	Eu	525 nm	> 10 h
ICP-MS [ppm]	370300	303940	-	9980	13186	7223		
Porcelain ceramic enamel (sintered at 1473 K)								
Composition	Density [g/cm ³]	Porosity	R _{FLEXION}	R _{ANTI-SLIP}	Rupture force, [N]	Water absorption [%]	Trial parameters	
			[N/mm ²]					
65% SiO ₂ 21% Al ₂ O ₃ 14% alkalis*	2.37	2-8 %	> 25	> 0.4 > 0.75	1600	< 0.1	Thickness 9 mm Size 400 x 400 mm	
	R _A [μm]	R _{MAX} [μm]	R _Z [μm]	P _C [cm ⁻¹]	R _{ABRASION}			
	1.69	14.00	11.10	65	≤ 150			

Table 7-5. Colour appearance of photoluminescent reliefs and inert substrate surfaces.

Luminescent surfaces (reliefs)							
Atomic excitation [nm]	Colour emission		Integral			Radiance [μW/cm ²]	Luminance [cd/m ²]
	U	V	X	Y	Z		
λ _{max1} = 320nm	0.1207	0.5480	0.2746	0.5541	0.1710	9,5664	41,3613
Colour appearance after end excitation (0 lux)							
Non-luminescent surfaces (ceramic substrate)							
PL-WCT typologies	λ _{max} [nm]	R _{max} [%]	Colour coordinates CIEL*a*b*			Colour appearance	
			L* (D65)	a* (D65)	b* (D65)	During light excitation (D65)	After end excitation (0 lux)
Crossing	720	45,07	58	13	13	 Red	Dark
Stopped	740	65,00	70	14	42	 Yellow	
Directional	740	40,33	43	-9	0	 Green	

PART III – MULTILAYERED SYSTEM

This third part presents the results of the preliminary experiments performed aiming at evaluating the thermal properties of the different materials involved in the multilayered system. As referred above, manufacturing of PL-WCT, in a multilayered system via sintered route requires a good match of the coefficients of thermal expansion of all material components, namely, the porcelain tile substrate, the low melting temperature glaze frit and the phosphor. If significant differences exist, then new approaches involving the design of intermediate layers to bridge the different multilayers will be required. However, such a detailed study is out of the scope of the present thesis and will be presented as further work to be conducted in the future.

7.7. Photoluminescent multilayered system

The preliminary experiments realized to evaluate the feasibility of manufacturing the PL-WCT in a PL-multilayered system via sintered route are described as follows.

7.7.1. Samples preparation

Materials. As mentioned in 7.6.4, a low melting temperature ($T_m \leq 923$ K) frit was selected for the transparent enamel layer to avoid the phase transformation of PL materials. Such low melting temperature frits are usually rich in PbO [154], an oxide that also produces enamels with superior surface finish. On the other hand, PbO raises potential toxicity concerns. To balance the properties, the application of the frit layer is restricted only to relief areas and its application will be made after firing the porcelain tiles covered or not with high temperature melting glazes. The relief areas will then be covered with the photoluminescent materials, which in turn will be glazed with a low melting temperature frit and the multilayered system fired in a second firing process step. For this purpose, a transparent glass frit, 80% PbO—20% SiO₂, was chosen. The luminescent SrAl₂O₄:Ce³⁺, Dy³⁺, Eu²⁺ baseline material and (SiO₂)_{0.65}-(Al₂O₃)_{0.21}-(alkalis)_{0.14} ceramic substrate composition were studied in a multilayered system covered by the transparent glass frit.

Experimental. For the dilatometric study, rectangular probes with dimensions of 5x5x15 mm were prepared from the porcelain paste and the transparent glass frit and fired at 1473 K and at 923 K, respectively. For the multilayered samples preparation, cylindrical pellets ($\phi = 10$ mm, height ~3 mm) of porcelain stoneware paste were consolidated using an applied pressure of ~490 MPa to closely simulate the processing conditions used at industrial scale (500 kgf/m²) for consolidating porcelain stoneware tiles with anti-slip and high pedestrian traffic resistance properties. The sintered pellets of the ceramic substrates were then successively coated with layers of the photoluminescent material and of the transparent glass frit 80% PbO—20% SiO₂. Attempts were also made to coat the ceramic substrates with a mixed composition layers of 50 wt.% photoluminescent material + 50 wt.% of the transparent glass frit.

7.7.2. Thermal behaviour of the PL-multilayered system

Dilatometric experiments were separately performed for each of the different materials involved in the multilayered system, namely, $[\text{PbO}_{0.8}\text{-(SiO}_2\text{)}_{0.2}]$, $[\text{SrAl}_2\text{O}_4\text{:Ce}^{3+}, \text{Dy}^{3+}, \text{Eu}^{2+}]$, and $[(\text{SiO}_2)_{0.65}\text{-(Al}_2\text{O}_3)_{0.21}\text{-(alkalis)}_{0.14}]$ to evaluate the thermal behaviour and the potential mismatches between their thermal expansion coefficients (TEC). The dilatometric curves (1) and (4) were performed on green glass frit and ceramic substrate samples, respectively, to assess their densification behaviour in Figure 7-17. It is clear that accentuated shrinkages have occurred after about 750 K and 1250 K, respectively, being consistent with the expected behaviour for the materials. Figure 7-17 suggests that a reasonable match seems to exist between the frit and the photoluminescent material. This is somewhat confirmed from the value of TEC for the

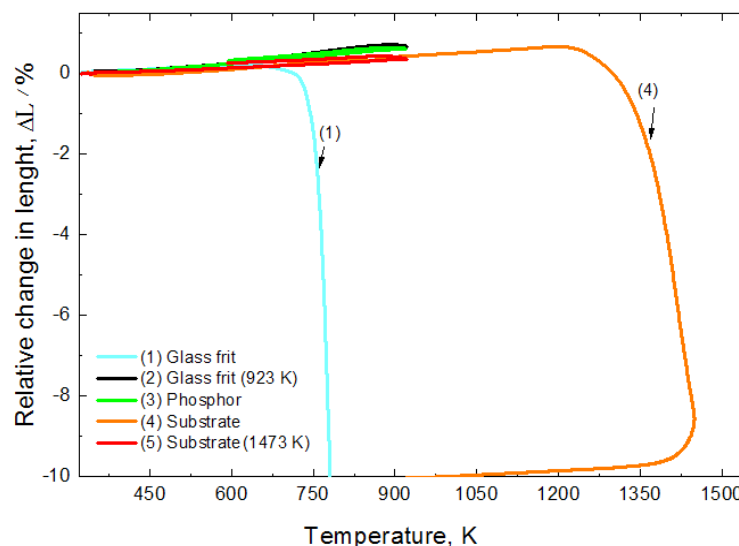


Figure 7-17. Dilatometric curves of different materials for a multilayered system of PL-WCT via sintered route.

frit $[(10.0 \pm 0.1) \times 10^{-6} \text{ K}^{-1}$, between 323–573 K], as given by the supplier, and that calculated for the α -monoclinic phase of SrAl_2O_4 sintered at 1723 K $[(9.5 \pm 0.1) \times 10^{-6} \text{ K}^{-1}$, between 350–940 K] [155]. As a matter of fact, a good bonding was observed between the $\text{PbO}_{0.8}(\text{SiO}_2)_{0.2}$ frit and the $\text{SrAl}_2\text{O}_4\text{:Ce}^{3+}, \text{Dy}^{3+}, \text{Eu}^{2+}$ phosphor. However, these TEC values are significantly different from that measured for the sintered ceramic substrate $[(7.9 \pm 0.1) \times 10^{-6}$, between 300–673 K]. These differences resulted in a lack of adhesion between the monolithic frit/phosphor bilayer and the ceramic substrate, confirming the predicted difficulties in making up the multilayered system. Such large differences between the TECs of these materials, curves (2) and (3), and that of sintered ceramic substrate, curve (5), can probably be mitigated by using intermediate engobe layers with a gradient in the TEC in order to make the consecutive layers compatible, as suggested below.

7.7.3. Alternative solutions for the PL-multilayered system

As seen above, the most critical issue in the fabrication of a multilayered system comprising all the component materials tested in the frame of this study is related to the (mis)match of the TECs of the different materials. Based on the results presented before (Figure 7-17) it is clear that further efforts need to be made in order to accomplish this objective through an exhaustive detailed study of

the intermediate layer compositions. The possible strategies for the production of the PL-WCT are proposed as follows:

- (I) **gradient of engobe materials:** formation of a gradient in multilayered system minimizing the different dilatometric behaviours, specifically between the photoluminescent layer and the ceramic substrate;
- (II) **ceramic substrate with higher dilatometric coefficient:** substitution of the porcelain stoneware by another ceramic material, namely with a dilatometric curve nearest of the PbO-SiO₂ transparent glass frit and SrAl₂O₄:Ce³⁺, Dy³⁺, Eu²⁺ phosphor, already experimented would also be helpful, although this approach alone has a limited capability to solve the entire problem;
- (III) **super-high temperature resistant epoxy and silicone composition:** utilization of a super-high temperature sealant for adhesion of the PbO-SiO₂ transparent glass frit—SrAl₂O₄:Ce³⁺, Dy³⁺, Eu²⁺ phosphor with the ceramic substrate up to temperatures as high as 589 K (e.g. type of sealant used in aerospace industry requires heat cure [156]); it includes high strength structural adhesive which retains good physical strength properties even after prolonged exposure to unfavorable environmental conditions;
- (IV) **glasses in the SnO-ZnO-P₂O₅ (SZP) ternary system:** potential replacements to PbO-SiO₂ transparent glass frit for low temperature, sealing applications to eliminate the harm of Pb to human body and environment; or selecting other frits with lower Pb contents, such as PbO-TeO₂-SiO₂, PbO-ZnO-B₂O₃ or PbO-ZnO-SiO₂ frits for low temperature (< 773 K) [154].

7.8. Conclusion

PL-WCT— Photoluminescent-warning ceramic tiles for risk areas and emergency of people with disabilities were conceptually designed, including relief surfaces that emit light for long duration, which luminescence property is activated with minimum illuminance of 25 lux. The PL reliefs were projected to comprise directional and circular shapes and height from 3 to 12 mm. SrAl₂O₄:Ce³⁺, Dy³⁺, Eu²⁺ materials might be applied in the PL layer, but the need of a low melting temperature frit severely restricted the choice to a PbO-rich (80% PbO—20% SiO₂) transparent glass frit to cover the PL layers. The application of SrAl₂O₄:Ce³⁺, Dy³⁺, Eu²⁺ nanomaterials should be further investigated, in terms of multilayered materials via sintered route at semi-industrial scale, followed of an architectural Pilot Project, before its application as a safety product. ■

Chapter 8

General Conclusion

This transversal thesis aimed to develop a solution to resolve a serious problem of public security and social inclusion of people with disabilities in emergency situations, prospecting the property of persistent luminescence in escape routes. Some derivative problems were approached in the specific area of Materials Science and Engineering: (1) develop multifunctional luminescent nanomaterials; (2) reach the requirements in afterglow-in-the-dark emergency signalling application; (3) potential applications in vivo. The integrated solution of $\text{SrAl}_2\text{O}_4:\text{Ce}^{3+}$, Dy^{3+} , Eu^{2+} nanotubes, nanowires, and core-shells, and their personalized colour vision in black background, even by a critical trial group with diabetic retinopathy, supported their application in photoluminescent-warning ceramic tiles for risk areas and emergency — this facility is accessible for all persons with disabilities.

8.1. Conclusion

The luminescent SrAl₂O₄:Ce³⁺, Dy³⁺, Eu²⁺ baseline material, as-received in shape of micro- and nano-particles obtained by solid-state reaction, was used to produce novel one-dimensional structures in shape of nanotubes, nanowires, nanorods and core-shells.

Luminescent SrAl₂O₄:Ce³⁺, Dy³⁺, Eu²⁺ nanotubes were synthesized by post-annealing process of the precursor particles from 573 to 1473 K, more specifically within the range of 1273-1473 K. Planar (linear and lamellar) lattice defects and unstable dangling bonds favoured the rolling up mechanism of formation of the tubular structure during the thermal treatment.

Luminescent SrAl₂O₄:Ce³⁺, Dy³⁺, Eu²⁺ nanowires and nanorods were developed by an ultrasonic method of synthesis by grinding, ultrasonification (3 MHz) and post-annealing (373 K). Self-assembled nanowires were identified and might find applications as biosensors.

Luminescent core-shells of SrAl₂O₄:Ce³⁺, Dy³⁺, Eu²⁺@TiO₂ nanotubes were developed by decomposition of Na₂TiO₃ to create a TiO₂ coating layer covalently bonded with insaturated ions on the phosphor surface. This encapsulation process and derived products increase the range of functionalities of luminescent materials that can be used in emergency applications, with the encapsulated materials presenting the following characteristics:

- water resistance (≈4 h);
- fire resistance (≈923 K);
- persistent luminescence;
- photocatalytic antimicrobial and antibacterial properties;
- biocompatibility.

The photocatalytic luminescent core-shell nanoprobe also might be utilized in formulations of vaccines, as biomaterials and biosensors.

Luminescence colour emission of SrAl₂O₄:Ce³⁺, Dy³⁺, Eu²⁺ nanotubes, nanowires and core-shells was personalized in the UV-VIS wavelength region from 485-555 nm. These nanomaterials are visually accessible for the personalized colour vision of a trial group (p<0.05). The personalization was made through using a **BIO-UV-VIS Telemedical Workstation—ophthalmic equipment** for the diagnostic of retinal cells focusing in the visibility as vital factor. The personalization involved the acquisition of biometric data from retinal diagnostic tests with the end users for photopic colour vision biofunctionality in white/black backgrounds. The retina cell responses were obtained from individuals with diabetic retinopathy (treatment group, n=38), in comparative diagnoses from voluntary fireman (reference group, n=38), and their biostatistical differences were analyzed by ANOVA, T-test and Pearson correlation analysis. The colour emissions of nanomaterials from 485-555 nm examined in diabetic trials, corresponding to the colour vision (C31-C53), resulted in error-scores up to 10 (FM100-HUE scale). The best colour

vision quality of treatments was C44 as an ideal region for luminescence emission at 495 nm and visual detection of PL materials for these specific end users. For this quality visibility, these nanomaterials with blue-green luminescence emissions might be, for example, personalized for this specific trial group for application in emergency signalling in a conglomerate spatial building. This equipment (cabinet) should be further investigated for the practice of ophthalmic telemedicine and personalized approaches.

Photoluminescent-warning ceramic tiles for risk areas and emergency — PL-WCT were conceptually created on a novel application for persistent luminescent $\text{SrAl}_2\text{O}_4:\text{Ce}^{3+}$, Dy^{3+} , Eu^{2+} nanomaterials. Such floors were designed with light emitting features through a variety of photoluminescent reliefs that make them dopted with a multisensory system, in three-dimensional (3D) tiles, as following described:

- **visual contrast:** the photoluminescent materials emit light in the dark, in contrast to the adjacent surface inert;
- **tactile constrast:** the relief surfaces with height between 3 and 12 mm are detectable in contrast with the mobility aid;
- **sonorous contrast:** the shapes of reliefs emit sound in contrast with the mobility aid.

These contrastant surfaces of paving enable people with disabilities to carry out evacuation, in emergency situations, in the dark. The persistent photoluminescence (> 10 h) allows its use in the absence of electricity, in darkness; in a timely enough for the evacuation process with integrity and safety.

In conclusion, $\text{SrAl}_2\text{O}_4:\text{Ce(III)}$, Dy, Eu nanotubes, nanowires and core-shells were developed with persistent luminescence property for emergency signalling applications, including persons with different types and degrees of disabilities — meeting the functional requirements of critical visibility, fire and water resistance, to save lives in emergencies, after the activation of the afterglow phenomenon. This facility was designed for to be accessible for persons with disabilities in emergency, and may be useful to solve a problem of social inclusion in public security.

A multidisciplinary outlook was presented, which may help on the development of novel nanomaterials with analogous formula $M_{(1-x-y)}\text{Al}_2\text{O}_4:\text{Ce}_x$, Ln_y (M is Be, Mg, Ca, Sr, Ba, or a combination thereof), and find applications in luminescence.

8.2. Perspectives for future works in related fields

Combining multidisciplinary researches from areas of Nanoscience, Materials Science and Engineering, Chemistry and Solid-State Physics, it is suggested the investigation of nanomaterials with analogous formula $M_{(1-x-y)}Al_2O_4:Ce_x, Ln_y$ (M is Be, Mg, Ca, Sr, Ba, or a combination thereof), comprising the follow experiments:

- ❖ Synthesis, characterization and application of luminescent nanoparticles, nanowires, nanorods, nanotubes and core-shells;
- ❖ Examination of the intercrystalline distal-effect on the afterglow phenomenon to other luminescent materials;
- ❖ Influence of other lanthanide co-doping and further characterization of the sono-, thermal-, quimio-, cathode-, piezo- and photo-luminescence properties;
- ❖ Application of luminescent nanostructures in optical devices;
- ❖ The findings of this work may enable scaling up the production of photoluminescent-warning ceramic tiles and photoluminescent materials.

In the field of Medicine, Biology and Rehabilitation, the following topics might be pursued:

- ❖ Experiment of the medical equipment in ophthalmologic telemedicine by diagnostic of the biofunctionality of retinal cells from visual acuity test (Snellen);
- ❖ Development of ophthalmologic biomaterials and devices incorporating luminescent nanomaterials;
- ❖ Development of a multimedia software for visual personalization for different trial groups, namely focused on the accessibility of persons with disabilities;
- ❖ Investigation of the persistent luminescence property from nanomaterials as contrastant probe for optical imaging in vitro and in vivo.

It is also suggested the development of theoretical and practical researches in the follow topics:

- ❖ Design of novel products and solutions with persistent luminescence property for signalling applications;
- ❖ Project of Emergency Plan with photoluminescent materials and products, with detailed solutions for accessibility.

The nanotube, core-shell, nanowire and nanorod-shaped phosphors from the field of nanoscience were designed for applications in photoluminescent signalling. Extrapolating this specific field, these nanomaterials, with different formulations, might be correlated with the property of superconductivity and persistent luminescence. This correlation is attributed from the mechanisms of energy transfer of the electrons in the emission, not yet explored. ■

Bibliography

- [1]. EUROSTAT – European Commission Statistical Committees: a) Population and Social Conditions, **2009**, Luxembourg; b) 2010: A Europe Accessible for All, Report from the Group of Experts set up by the European Commission, **2003**, 27, In: http://www.polis-ubd.net/UserFiles/File/EU_Access2010_Report-1.pdf.
- [2]. UNESCO – United Nations for Education, Science and Culture Organization, UN Agency citing WHO – World Health Organization: people with disabilities, *UNESCO Program - Bildung for Kinder in Not*, **2006**.
- [3]. ANSI – American National Standard Institute, ANSI ICC/A117.2-1998 Accessible and Usable Buildings and Facilities, Falls Church, VA: International Code Council, **2003**.
- [4]. ADAAG - Americans with Disabilities Act Accessibility Guidelines for Buildings and Facilities, ADAAG 4.29, **1991**. In: <http://www.access-board.gov/adaag>.
- [5]. ISO – International Organization for Standardization, ISO/TC 173, Assistive products for persons with disability, **1999**.
- [6]. J. TAVARES, E. MARTINS, M. DISCHINGER, N. K. ZURBA, Pilot Project of Technical Solutions for Urban Accessibility of Handicapped People and Elaboration of Municipal Law Facilities N^o. 2.153.784, Institute of Urban Planning of Florianopolis, *IPUF*, **1998**, Brazil.
- [7]. M. DISCHINGER, N. K. ZURBA, Accessibility in Historical Centre of Florianopolis, Technical Report of the Institute of Urban Planning of Florianopolis, *IPUF*, **1998**, Brazil.
- [8]. N. K. ZURBA, M. DISCHINGER, Accessibility in Public Urban Spaces, *IV Proc. ENEPEA*, **1998**, 1, 33-4.
- [9]. N. K. ZURBA, Ceramic tiles with warning devices for people with disabilities, *Appl. Patent*, **2003**, MU83026479, MU84004142, Brazil.
- [10]. N. K. ZURBA, Methodology of the Design Process and Classification of Floor Tiles for Accessibility Applied in Porcelain Stoneware Material, Master Dissertation Mat. Sc. Eng., *UFSC*, **2003**, Federal University of Santa Catarina, Brazil, 106p.
- [11]. ELIANE CERAMIC TILES, Arqtec Tactile Ceramic Tiles, **2007**, Brazil, in: <http://www.eliane.com/doc/download/Catalogo/arqtec.pdf>.
- [12]. For tactile floors and devices for people with disabilities, see: a) B. L. BENTZEN, T. L. NOLIN, R. D. EASTON, L. DESMARAI, P. A. MITCHELL, Detectable warnings: safety and negotiability on slopes for persons who are physically impaired. Project Action, National Easter Seal Society, U.S. Department of Transportation, Federal Transit Administration, Volpe National Transportation Systems Center, **1994**; b) US2421171, **1947**; c) US4715743, 1987; d) US5328293, 1994; e) US5626094, 1997; f) US6025773, **2000**; g) US6499421, **2002**; h) US6499910, **2002**; i) US6694652, **2004**; j) US6785992, **2004**; k) US6951435, **2005**; l) US6971818, **2005**; m) US6964244, **2005**; n) US7001103, **2006**.
- [13]. For recent developments of PL materials and products for safety, see, for example, the patent documents: a) US4385586, **1983**; b) US5103608, **1992**; c) US5779919, **1998**; d) US5904017, **1999**; e) US0021436, **2001**; f) US6233857, **2001**; g) US6237266, **2001**; h) US6375864, **2002**; i) US6875989, **2002**; j) US0051379, **2003**; k) US6627315, **2003**; l) US6696126, **2004**; m) US6841785, **2005**; n) ES200400027, **2004**; o) US4801928; p) US4401050; q) US2169657; r) US2387512; s) WO2005028399, **2005**.
- [14]. DIN - Deutsches Institut für Normung e.V., DIN 67510, German Industrial Standard: Photoluminescent pigments and products; escape route system, **2004**.
- [15]. NASA – National Aeronautics and Space Administration, NASA's Space Operations Mission Directorate – Photoluminescent System for International Space Station (ISS), *Scientific and Technical Information*, **2004**, Washington DC, US. In: <http://www.nasa.gov/station>.
- [16]. PSPA – Photoluminescent Safety Products Association. British Association of Normalization of Photoluminescent Products and Materials: a) PSPA Standard 002, Art. 3.2. Special Needs, **1997**; b) PL Standard: Emergency Way finding Guidance Systems, Guide to the Use of Photoluminescent Safety Markings, **2008**; c) Guide to the Use of Photoluminescent Safety Markings, Part 1: Egress Markings in Stairwells, **2008**. In: <http://www.pspa.org.uk>.
- [17]. L. Q. MINH, W. STREK, T. K. ANH, K. YU, Luminescent Nanomaterials, *J. Nanomat.*, **2007**, 48312.
- [18]. C. FELDMANN, T. JUSTEL, C. R. RONDA, P. J. SCHMIDT, Inorganic luminescent materials: 100 years of research and application, *Advanc. Funct. Mat.* **2003**, 13, 7, 511–516.

- [19]. A. S. EDELSTEIN, R. C. CAMMARATA, *Nanomaterials: Synthesis, Properties and Applications*, Taylor & Francis, UK, **1998**.
- [20]. B. R. RATNA, A. D. DINSMORE, ET AL., *Nanophosphors: synthesis, properties and application*, *Proceed. ICSTDP*, **1999**, 295
- [21]. Products for rehabilitation of people with disabilities, see: N. K. ZURBA in *UNESCO Symposium, Workshop and Exhibition Toys for Rehabilitation*: a) Humanism by (Bio)Materials – An Introduction for Accessibility and Rehabilitation, *Deutschen UNESCO-Kommission*, Bielefeld, Deutschland, **2006**; b) Universal Design in Toys, UNESCO Toys for Children’s Rehabilitation, Symposium presentation, *Chinese and Deutschen UNESCO-Kommissions*, Anji, China, **2003**; c) Designing for Handicapped People, *CONALMEX and Deutschen UNESCO-Kommission*, Mexico City, Mexico, **1998**.
- [22]. Rehabilitation centre, see N. K. ZURBA in UNESCO Spielkulturen, A. HEINZELMANN, C. SONNTAG, R. ELBRACHT (Editors), *Deutschen UNESCO-Kommission, Wissen Media Verlag*, **2007**, 1, 12. ISBN 978-3-577-10200-1. In: <http://www.unesco.de>.
- [23]. Afterglow phenomenon, see: a) J. KAPLAN, A New Afterglow Phenomenon, *Phys. Rev.* **1940**, 57, 662-662; b) H. G. JENKINS, J. N. BOWTELL, R. W. STRONG, Afterglow Phenomena in Argon-Nitrogen Mixtures at Pressures Close to Atmospheric, *Nature*, **1949**, 163, 401-402, DOI:10.1038/163401a0; c) *Astronomy & Astrophysics*, **2001**, 379, L39-L43; d) R. SAGAR, Another Indian optical observation of a gamma-ray burst afterglow from UPSO, *Current Science*, **2000**, 78, 5; e) C. C. KANG, R. S. LIU, J. C. CHANG, B. J. LEE, Synthesis and Luminescent Properties of a New Yellowish-Orange Afterglow Phosphor $Y_2O_3:Sr^{2+}, Mg$, *Chem. Mater.*, **2003**, 15, 3966-3968; f) S. SHIONOYA, W. M. YEN, Phosphor Handbook, *CRC Press*, **1998**.
- [24]. Population and legal postulations, see: a) INE – National Institute of Statistic, Portugal, **2001**; b) UNITED NATIONS, Convention on the Rights of Persons with Disabilities and Additional Protocol, New York, **2006**; c) UNITED NATIONS, Standard Rules on the Equalization of Opportunities for Persons with Disabilities; d) DECISION N° 771/2006/EC OF THE EUROPEAN PARLIAMENT: 2007 European Year of Equal Opportunities for All, **2006**; e) IBGE - Brazilian Institute of Geography and Statistics, **2000**; f) LAW N° 9/1989 OF MAY 2, Portugal: Law for Prevention, Rehabilitation and Integration of People with Disabilities, **1989**; g) DECREE-LAW N° 123/1997 OF 22 MAY, Portugal: People with disabilities and access to public buildings, public roads and public amenities, **1997**; h) RESOLUTION OF THE COUNCIL OF MINISTERS N° 9/2007 OF 17 JANUARY, and DECREE-LAW 163/2006 OF 8 AUGUST, Portugal: PNPA - National Plan for the Promotion of Accessibility, **2006**; i) DGS - Directorate General of Health of the Ministry of Health, Portugal, **2001**.
- [25]. Luminescence and lanthanides, see: a) V. P. GRIBKOVSKII, Academy of Sciences of Belarus, Minsk, *Luminescence of Solids*, D. R. VIJ (Editor), *Plenum Press*, **1998**; b) X. CHEN, G. LI, Y. SU, X. QIU, L. LI, Z. ZOU, Synthesis and room-temperature ferromagnetism of CeO_2 nanocrystals with nonmagnetic Ca^{2+} doping, *Nanotechnology*, **2009**, 20, 115606, DOI: 10.1088/0957-4484/20/11/115606; c) G. BALDUCCI, M. S. ISLAM, J. KASPAR, P. FORNASIERO, M. GRAZIANI, Reduction process in CeO_2 -MO and CeO_2 - M_2O_3 mixed oxides: a computer simulation study, *Chem. Mater.*, **2003**, 15, 3781-3785; d) Handbook of Chemistry and Physics, 78th Ed., **1998**; e) H. E. HEIDEPRIEM, D. EHRT, *Opt. Mater.*, **2000**, 15, 7.
- [26]. H. C. ASPINALL, Chemistry of the f-block elements, *Overseas Publishers Association (OPA)*, Netherlands, **2001**, ISBN 90-5699-333-X.
- [27]. a) S. Hüfner, Optical spectra of transparent rare earth compounds, 1st Ed., *Academic Press*, New York, **1978**; b) Handbook of Chemistry and Physics, 78th Edition, **1997**; c) B. G. WYBOURN, Spectroscopic properties of rare earths, *Interscience*, New York, **1965**; d) C. TANG, Y. BANDO, D. GOLBERG, R. MA, Cerium phosphate nanotubes: synthesis, valence state and optical properties, *Angew. Chem. Int. Ed.* **2004**, 44, 4, 576-579.
- [28]. Seculit, Fabricant of $ZnS:Cu$ and $SrAl_2O_4$ co-doped phosphors.
- [29]. a) T. MATSUZAWA, Y. AOKI, N. TAKEUCHI, Y. MURAYAMA, A new long phosphorescent phosphor with high brightness $SrAl_2O_4:Eu^{2+}, Dy^{3+}$, *J. Electrochem. Soc.*, **1996**, 143, 2670–2673; b) Y. H. LIN, Z. T. ZHANG, F. ZHANG, Z. L. TANG, Q. Y. CHEN, Preparation of the ultrafine $SrAl_2O_4:Eu, Dy$ needle-like phosphor and its optical properties, *Mater. Chem. Phys.*, **2000**, 65, 103.
- [30]. a) T. AITASALO, P. DEREN, J. HÖLSA, H. JUNGNER, J. C. KRUPA, M. LASTUSAARI, J. LEGENDZIEWICZ, J. NIITTYKOSKI, W. STREK, Persistent luminescence phenomena in materials doped with rare earth ions, *J. Solid-state Chem.*, **2003**, 171, 114–122; b) J. HÖLSA, H. JUNGNER, M. LASTUSAARI, J. NIITTYKOSKI, Persistent luminescence of Eu^{2+} doped alkaline earth aluminates $MA_2O_4:Eu^{2+}$, *J. Alloys Comp.* **2003**, 354, 326–330.
- [31]. S. H. M. POORT, W. P. BLOKPOEL, G. BLASSE, Luminescence of Eu^{2+} in barium and strontium aluminate and gallate. *Chem. Mater.*, **1995**, 7, 1547-1551.

- [32]. W. S. SHI, H. YAMADA, K. NISHIKUBO, H. KUSABA, C. N. XU, Novel structural behavior of strontium aluminate doped with europium, *J. Electrochem. Soc.*, **2004**, *151*, 5, H97-100.
- [33]. Z. FU, S. ZHOU, S. ZHANG, Study on optical properties of rare-earth ions in nanocrystalline monoclinic SrAl_2O_4 : Ln (Ln= Ce^{3+} , Pr^{3+} , Tb^{3+}), *J. Phys. Chem. B*, **2005**, *109*, 14396–14400.
- [34]. A. DOUY, M. CAPRON, Crystallisation of spray-dried amorphous precursors in the $\text{SrO}-\text{Al}_2\text{O}_3$ system: a DSC study, *J. Eur. Ceram. Soc.* **2003**, *23*, 2075–2081.
- [35]. B. N. OKERIYA, D. S. TSAGARESHVILI, G. G. GVELESYANI, Enthalpy and heat capacity of strontium aluminate at high temperatures, *F. Techn. Div. AFB Ohio*, **1972**.
- [36]. a) A. M. ABAKUMOV, O. I. LEBEDEV, L. NISTOR, G. VAN TENDELOO, S. AMELINCK, The ferroelectric phase transition in tridymite type BaAl_2O_4 studied by Electron Microscopy, *Phase Trans.*, **2000**, *71*, 2, 143–160; b) Y. L. CHANG, H. I. HSIANG, Phase evolution during formation of SrAl_2O_4 from SrCO_3 and $\alpha\text{-Al}_2\text{O}_3/\text{AlOOH}$, *J. Am. Ceram. Soc.*, **2007**, *90*, 9, 2759–2765.
- [37]. Aluminates: a) K. R. S. PREETHI, C. H. LU, J. THIRUMALAI, R. JAGANNATHAN, T. S. NATARAJAN, N. U. NAYAK, I. RADHAKRISHNA, M. JAYACHANDRAN, D. C. TRIVEDI, SrAl_4O_7 : Eu^{2+} nanocrystals: synthesis and fluorescence properties, *J. Phys. D: Appl. Phys.* **2004**, *37*, 2664-2669; b) A. NAG, T. R. N. KUTTY, The mechanism of phosphorescence of $\text{SrAl}_{2-x}\text{B}_x\text{O}_4$ ($0 < x < 0.2$) and $\text{Sr}_4\text{Al}_{14-x}\text{B}_x\text{O}_{25}$ ($0.1 < x < 0.4$) co-doped with Eu^{2+} and Dy^{3+} , *Mat. Res. Bull.* **2004**, *39*, 331-342; c) S. H. HAN, Y. J. KIM, Luminescent properties of Ce and Eu doped $\text{Sr}_4\text{Al}_{14}\text{O}_{25}$ phosphors, *J. Opt. Mat.* **2005**, *28*, 6-7, 626-630; d) T. TAKEDA, K. TAKAHASHI, K. UHEDA, H. TAKIZAWA, T. ENDO, Crystal structure and luminescence properties of $\text{Sr}_2\text{Al}_6\text{O}_{11}$: Eu^{2+} , *J. Japan Soc. Powder Metal.* **2002**, *49*, 12, 1128-1133; e) J. S. CHOI, S. H. BAEK; S. G. KIM, S. H. LEE, H. L. PARK, S. I. MHO, T. W. KIM, Y. H. HWANG, Energy transfer between Ce^{3+} and Eu^{2+} in $\text{SrAl}_{12}\text{O}_{19}$: Ce_xB_3 , $\text{Eu}_{0.012}$ ($x = 0.01-0.09$), *Mat. Res. Bull.* **1999**, *34*, 4, 551-556; f) C. YUESHENG, Z. PING, Z. ZHENTAI, Eu^{2+} and Dy^{3+} co-doped $\text{Sr}_3\text{Al}_2\text{O}_6$ red long-afterglow phosphors with new flower-like morphology, *J. Phys. B: Phys. Cond. Matt.* **2008**, *403*, 21-22, 4120-4122; g) R. W. HYLAND JR, J. P. QUINTENZ, B. T. DUNVILLE, G. SUBRAHMANYAM, Photoluminescent Alkaline Earth Aluminate and Method for Making the Same, *US6969475 Appl. Patent*, **2005**, *11*, 29; h) C. ZHAO, D. CHEN, Y. YUAN, M. WU, Synthesis of $\text{Sr}_4\text{Al}_{14}\text{O}_{25}$: Eu^{2+} , Dy^{3+} phosphor nanometer powders by combustion processes and its optical properties, *Mater. Science Eng. B* **2006**, *133*, 1-3, 200-204.
- [38]. L. WANG, Y. ZHU, Preparation of nano-sized SrAl_2O_4 using an amorphous hetero-nucleus complex as a precursor, *J. Alloys Comp.*, **2004**, *370*, 276–280.
- [39]. M. L. RUIZ-GONZÁLEZ, J. M. GONZÁLEZ-CALBET, M. VALLET-REGI, E. CORDONCILLO, P. ESCRIBANO, J. B. CARDA, M. MARCHAL, Planar defects in a precursor for phosphor materials: $\text{SrAl}_{2-x}\text{B}_x\text{O}_4$ ($x < 0.2$), *J. Mater. Chem.*, **2002**, *12*, 1128–1131.
- [40]. F. MASSAZZA, Diagram phase of $\text{SrO}-\text{Al}_2\text{O}_3$ system, *La chimica e l'industria – XLI*, **1959**, *2*, 108-115.
- [41]. O. KNACKE, O. KUBASCHEWSKI, K. HESSELMANN, Thermochemical Properties of Inorganic Substances, *Springer Verlag*, 2nd, **1991**, I-II.
- [42]. J. J. LANDER, Polymorphism and anion rotational disorder in the alkaline earth carbonates, *J. Chem. Phys.*, **1949**, *17*, 892–0.
- [43]. P. ESCRIBANO, M. MARCHAL, M. L. SANJUÁN, P. A. GUTIÉRREZ, B. JULIÁN, E. CORDONCILLO, Low-temperature synthesis of SrAl_2O_4 by a modified sol-gel route: XRD and Raman characterization, *J. Solid-state Chem.*, **2005**, *178*, 6, 1978–1987.
- [44]. C. BEAUGER, Elaboration, Caractérisation et Modélisation des Phénomènes de Luminescence du Monoaluminate de Strontium Dope à l'Europium et au Dysprosium SrAl_2O_4 :Eu, Dy, Doctoral Thesis, *Inst. Nat. Polytechnique Grenoble*, **1999**, 47-87.
- [45]. A. NAG, T. R. N. KUTTY, Role of B_2O_3 on the phase stability and long phosphorescence of SrAl_2O_4 : Eu, Dy, *J. Alloys Comp.*, **2003**, *354*, 221–231.
- [46]. ASTM – American Society for Testing and Materials: a) ASTM E 2030 Guide for Recommended Uses of Photoluminescent (Phosphorescent) Safety Markings, **2004**; b) ASTM E 2072-00 Standard Specification for Photoluminescent (Phosphorescent) Safety Markings, **2004**; c) ASTM E 2073 Test Method for Photopic Luminance of Photoluminescent (Phosphorescent) Markings, **2004**; d) ASTM E 12.13 Standard for Photoluminescent Safety Markings, **2004**.
- [47]. ISO – International Organization for Standardization: a) ISO 3864-1 Graphical Symbols – Safety colours and safety signs – Part 1: Design principles for safety signs in workplaces and public areas, **2002**; b) ISO 7010 Graphical Symbols – Safety colours and safety signs – Safety signs used in workplaces and public areas, **2003**; c) ISO/TC 145 16069 Graphical Symbols – Safety colours and safety signs – Safety way guidance systems (SWGS), **2004**; d) ISO 17398 Safety colours and safety signs – Classification, performance and durability of safety signs, **2004**.

- [48]. New York City Building Code: a) Reference Standard 0RS 6-1 Photoluminescent exit path markings, as required by Local Law 26 of 2004, New York City Building Code § 27-383 (b), **2005**; b) Reference Standard RS 6-1A Additional Standards as Required by Reference Standard RS 6-1 Photoluminescent Exit Path Markings, **2005**.
- [49]. AFNOR – Association Française de Normalisation, PR NF X08-050 Systèmes de sécurité photoluminescents. — Partie 2: définition des produits et équipements de sécurité photoluminescents, Norme Française (valid from July 25, 2008), **2003**.
- [50]. Brazilian and Portuguese standards: a) Brazilian Standard NBR-9050: Acessibility to buildings, equipment and the urban environment, **2004**; b) DL 441/91; c) DL 141/91; d) 1456-A/95; e) DL 64/1990; f) NP 4386 Equipment for fire protection and fire fighting, **2001**; g) NP 3992, Fire protection and safety signs, **1999**.
- [51]. F. R. ZOLESSI, L. POGGI, C. J. WILKINSON, C. CHIEN, W. A. HARRIS, Polarization and orientation of retinal ganglion cells in vivo, *Neural Develop.*, **2006**, *10*, 1186.
- [52]. J. NEITZ, M. NEITZ, J. C. HE, S. K. SHEVELL, Trichromatic color vision with only two spectrally distinct photopigments, *Nature Neurosc.*, **1999**, *2*, 884-888.
- [53]. J. POKORNY, V. SMITH, Chromatic discrimination in the visual neurosciences, *MIT Press*, **2003**, *1*, 1930, 908-923.
- [54]. A. TOUFEEQ, Specifying colours for colour vision testing using computer graphics, *Eye Nature*, **2004**, *18*, 1001-1005.
- [55]. W. F. GANONG, *McGraw-Hill*, **2005**, *22*, 148-168, 928.
- [56]. W. H. XIONG, E. C. SOLESSIO, K. W. YAU, An unusual cGMP pathway underlying depolarizing light response of the vertebrate parietal-eye photoreceptor, *Nature Neurosc.* **1998**, *1*, 359-365. DOI: 10.1038/nn0998_359.
- [57]. CIE – Commission International de l'Eclairage (International Commission on Illumination), CIE 69, Methods of Characterizing Illuminance Meters and Luminance Meters, **1987**.
- [58]. J. C. MAIDA, C. K. BOWEN, C. D. WHEELWRIGHT, B. LYNDON, Photometric evaluation of photoluminescent materials for multi-egress guidance placards lighting environment test facility, *NASA/TM*, **2005**, 213165
- [59]. Purkinje effect, see: a) H. B. BARLOW, Purkinje shift and retinal noise, *Nature*, **1959**, *179*, 255-256. DOI:10.1038/179255b0; b) Y. GRAND, Optique Physiologique, *Éditions de la Revue d'Optique*, Paris, **1950**; c) D. I. POMERANTZ, J. R. CANNON, The Purkinje Effect in luminance measurements of Air Force Phosphorus, *Radiation and Nuclear Chemistry*, Aeronautical Systems Div. Wright-Patterson AFB OH.
- [60]. J. READ, L. CLEMENTS, Disabled People and European Human Rights: A Review of the Implications of the Human Rights Act 1988 for Disabled Children and Adults in the United Kingdom, *Paperback*, **2003**.
- [61]. WHO – World Health Organization: a) Prevention of blindness from diabetes mellitus: report of a WHO consultation in Geneva, Switzerland, **2006**, ISBN 9789241547123; b) Prevention of Blindness and Deafness, WHO/PBL/97.61, WHO consultation in Geneva, Switzerland, **1997**, *1*; c) Blindness and Visual Disability: part 2: Major Causes Worldwide, Fact Sheet N° 143, WHO consultation in Geneva, Switzerland, **1997**; d) Global initiative for the elimination of avoidable blindness, World Health Organization Programme for the Prevention of Blindness and Deafness, WHO consultation in Geneva, Switzerland, **1997**; e) The costs of diabetes, Fact Sheet N° 236, WHO consultation in Geneva, Switzerland, **1999**.
- [62]. Incidences of ophthalmic diseases, see: a) H. JÄGLE, E. ZRENNER, H. KRASTEL, W. HART, in: Clinical Neuro-Ophthalmology - A Practical Guide: Dyschromatopsias Associated with Neuro-Ophthalmic Disease, *Springer Berlin Heidelberg*, **2007**, 71-85, DOI: 10.1007/978-3-540-32708-0, ISBN 978-3-540-32706-6; b) D. YORSTON, High-Volume Surgery in Developing Countries, *Cambridge Ophthalmol. Symp. Eye* **2005**, *19*, 1083–1089, DOI:10.1038/sj.eye.6701966; c) S. B. SMITH, in: Ophthalmology Research: Retinal Degenerations, *Humana Press*, **2007**, Totowa, NJ; d) P. P. LEE, Z.W. FELDMAN, J. OSTERMANN, ET AL., Longitudinal rates of annual eye examinations of persons with diabetes and chronic eye diseases, *Ophthalmol.*, **2003**, *110*, 1952-1959; e) J. TRÄGER, H. C. KIM, N. HAMPP, Two-photon treatment, *Nature Photonics*, **2007**, *1*, 509-511; f) E.T. CUNNINGHAM JR., T. M. LIETMAN, J. P. WHITCHER, Blindness: a global priority for the twenty-first century, *Bull. WHO*, **2001**, *79*, 180; g) S. RESNIKOFF, R. PARARAJANSEGARAM, Blindness prevention programmes: past, present, and future, *Bull. WHO*, **2001**, *79*, 222-226; h) B. THYLEFORS, Avoidable blindness, *Bull. WHO*, **1999**, *77*, 453.
- [63]. Retinopathy: a) D. MCCULLEY, Death to Diabetes: The 6 Stages of Type 2 Diabetes Reference and Reversal, *BookSurge*, **2005**, ISBN 0977360741; b) D. ANDREANI, Diabetic complications: early diagnosis

- and treatment, University of Michigan, *Wiley Medical Publication*, **1987**, 312p., ISBN 0471916781; c) NEI – U.S. National Eye Institute, Diabetic retinopathy, *Nat. Inst. Health*, **2009**, in: <http://www.nei.nih.gov>; d) NSC – U.K. National Screening Committee, Department of Health, Social Services and Public Safety, In: <http://www.nsc.nhs.uk>; e) H. C. CHEN, Classification and Diagnosis of Diabetic Retinopathy, in: *Vascular Complications of Diabetes: current issues in pathogenesis and treatment*, by R. DONNELLY, J. JONAS (Editors), *Blackwell Publishing*, **2002**; f) O. P. BÛSTERVELD (Editor), Diabetic Retinopathy, *Informa Health Care*, **2000**, ISBN 1853176257; g) S. SAXENA, S. JALALI, T. A. MEREDITH, N. M. HOLEKAMP, D. KUMAR, Management of diabetic retinopathy, *Indian J. Ophthalmol.*, **2000**, *48*, 321-330; h) H. R. TAYLOR, J. E. KEEFE, World blindness: a 21st century perspective, *Br. J. Ophthalmol.*, **2001**, *85*, 261-266.
- [64]. Colour vision and diabetes: a) S. J. PARK, S. R. FERNANDEZ, L. TAPLIN, Evaluation and correlation of color discrimination abilities, *MCSL- Munsell Color Sc. Lab*, **2000**; b) F. M. E. EWING, I. J. DEARY, M. W. J. STRACHAN, B. M. FRIER, Seeing beyond retinopathy in diabetes: electrophysiological and psychophysical abnormalities and alterations in vision, *Endocrine Reviews*, **1998**, *19*, 4, 462-476; c) J. ZANEN, Introduction a l'etude de dyschromatopsias retiniennes contrales asquises, *Bull Soc Belge Ophthal.*, **1953**, *103*, 3–148; d) D. FARNSWORTH (Editor) The Farnsworth-Munsell 100 Hue Test Manual, *Munsell Color Co.*, **1957**, Baltimore, MD; e) K. J. HARDY, C. FISHER, P. HEATH, D. H. FOSTER, J. H. B. SCARPELLO, Comparison of colour discrimination and electroretinography in evaluation of visual pathway dysfunction in aretinopathic IDDM patients, *Br J Ophthalmol*, **1995**, *79*, 35–37; f) K. J. HARDY, J. LIPTON, M. O. SCASE, D. H. FOSTER, J. H. B. SCARPELLO, Detection of colour vision abnormalities in uncomplicated type 1 diabetic patients with angiographically normal retinas, *Br J Ophthalmol*, **1992**, *76*, 461–464; g) P. LOMBRIL, G. CATHELIN, P. GERVAIS, N. THIBULT, Abnormal color vision and reliable self-monitoring of blood glucose, *Diabetes Care*, **1984**, *7*, 318–321; h) M. S. ROY, C. MCCULLOCH, A. K. HANNA, C. MORTIMER, Colour vision in long-standing diabetes mellitus. *Br J Ophthalmol*, **1984**, *68*, 215–217; i) G. H. BRESNICK, R. S. CONDIT, M. PALTA, K. KORTH, A. GROO, S. SYRJALA, Association of Hue Discrimination Loss and Diabetic Retinopathy, *Arch Ophthalmol.*, **1985**, *103*, 1317–1324; j) P. A. ASPINALL, P. R. KINNEAR, L. J. P. DUNCAN, B. F. CLARKE, Prediction of diabetic retinopathy from clinical variables and color vision data, *Diabetes Care*, **1983**, *6*, 144–148; k) D. G. THOMPSON, F. HOWARTH, I. S. LEVY, Colour blindness: a hazard to diabetics, *Lancet*, **1978**, *1*, 44; l) K. GRAHAM, C. M. KESSON, H. B. KENNEDY, J. T. IRELAND, Relevance of colour vision and diabetic retinopathy to self-monitoring of blood glucose, *Br Med J*, **1980**, *281*, 971–973; m) P. R. KINNEAR, P. A. ASPINALL, R. LAKOWSKI, The diabetic eye and colour vision, *Trans Ophthal Soc UK*, **1972**, *92*, 69–78; n) G. L. TRICK, R. M. BURDE, M. O. GORDON, J. V. SANTIAGO, C. KILO, The relationship between hue discrimination and contrast sensitivity deficits in patients with diabetes mellitus, *Ophthalmology*, **1988**, *95*, 693–698; o) P. LOMBRIL, P. GERVAIS, G. CATHELIN, Prediction of diabetic retinopathy from color vision data, *Diabetes Care*, **1983**, *6*, 621–622; q) M. S. ROY, R. D. GUNKEL, M. J. PODGOR, Color vision defects in early diabetic retinopathy, *Arch Ophthalmol*, **1986**, *104*, 225–228.
- [65]. a) J. M. BURNFIELD, C. M. POWERS, Biomechanics of ambulation, in: *Metrology of pedestrian locomotion and slip resistance* by M. I. MARPET, M. A. SAPIENZA (Editors), ASTM International, Committee F13 on Safety and Traction for Footwear, **2002**; b) D. C. KERRIGAN, M. K. TODD, U. D. CROCE, Gender differences in joint biomechanics during walking: normative study in young adults, *American J. Phys. Med. Rehabilitation*, **1998**, *77*, 2-7; c) J. E. HIMANN, D. A. CUNNINGHAM, P. A. RECHNITZER, D. H. PATERSON, Age-related changes in speed of walking, *Med. Sc. Sports and Exercise*, **1998**, *20*, 2, 161-166; d) A. D. MOSS, N. E. FOWLER, V. L. TOLFREY, A telemetry-based velocometer to measure wheelchair velocity, *J. Biomechanics*, **2003**, *36*, 2, 253-257; NFFA – National Fire Protection Association: e) NFFA 170 Standard for Fire Safety and Emergency Symbols, **2006**; f) NFFA 101 Life Safety Code, **2006**; g) A. MILLONIG, G. GARTNER, A multi-method approach to the interpretation of pedestrian spatio-temporal behaviour, in: *Pedestrian and Evacuation Dynamics* by W. W. F. KLINGSCH, C. ROGSCH, A. SCHADSCHNEIDER, M. SCHRECKENBERG (Editors), *Springer Berlin Heidelberg*, **2008**, 563-568, DOI: 10.1007/978-3-642-04504-2_50.
- [66]. AFM, see: a) G. BINNIG, C. QUATE, G. GERBER, *Phys. Rev. Lett.* **1986**, *56*, 930; b) W. A. DUCKER, T. J. SENDEN, R. M. PASHLEY, *Nature* **1991**, *353*, 239; c) W. A. DUCKER, T. J. SENDEN, R. M. PASHLEY, *Langmuir* **1992**, *8*, 1831; d) D. SARID, *Scanning Force Microscopy*, Oxford Series in Optical and Imaging Sciences, *Oxford University Press*, New York, **1991**.
- [67]. Electron microscopy, see: a) G. I. GOLDSTEIN, D. E. NEWBURY, P. ECHLIN, D. C. JOY, C. FIORI, E. LIFSHIN, *Scanning electron microscopy and X-ray microanalysis*, *Plenum Press*, New York, **1981**; b) D. GOLBERG in *Electron Microscopy of Nanotubes*, Z. L. WANG, C. HUI (Editors), *Kluwer Academic*, **2003**.
- [68]. Other techniques, see: a) D. P. SHOEMAKER, C. W. GARLAND, J. W. NIBLER, *Experiments in Physical Chemistry*, 6th ed., *McGraw-Hill*, New York, 389-397; b) J. R. FERRARO, K. NAKAMOTO, *Introductory Raman Spectroscopy*, *Academic Press*, **1994**; c) J. A. KONINGSTEIN, *Introduction to the Theory of the Raman Effect* (D. Reidel) **1972**; d) D. A. LONG, *Raman Spectroscopy*, *McGraw-Hill*, **1977**; e) MALVERN INSTRUMENTS, Zetasizer: Principles of Operation, *Manual MAN N^o. 0152*, **1996**, 1.1; f) E. CORDONCILLO,

- B. J. LOPEZ, M. MARTÍNEZ, M. L. SANJUÁN, P. ESCRIBANO, New insights in the structure–luminescence relationship of Eu:SrAl₂O₄, *J. Alloys Compoun.* **2009**, *484*, 1-2, 18, 693-697; g) Y. C. KIM, H. H. PARK, J. S. CHUN, W. J. LEE, Compositional and structural analysis of aluminum oxide films prepared by plasma-enhanced chemical vapor deposition, *Thin Solid Films*, **1994**, *237*, 1-2, 57-65.
- [69]. S. IJIMA, *Nature*, **1991** (London), *354*, 56.
- [70]. For the hydrothermal synthesis of SrAl₂O₄ nanotubes and nanorods, see: C. YE, Y. BANDO, G. SHEN, D. GOLBERG, Formation of crystalline SrAl₂O₄ nanotubes by a roll-up and post-annealing approach, *Angew. Chem. Int. Ed. Wiley-VCH Verlag GmbH & Co. KGaA, Weinheim*, **2006**, *118*, 5044–5048.
- [71]. U. K. GAUTAM, S. R. C. VIVEKCHAND, A. GOVINDARAJ, G. U. KULKARNI, N. R. SELVI, C. N. R. RAO, Generation of onions and nanotubes of GaS and GaSe through laser and thermally induced exfoliation, *J. Am. Chem. Soc.*, **2005**, *127*, 3658.
- [72]. F. ZHANG, Y. WAN, T. YU, F. ZHANG, Y. SHI, S. XIE, Y. LI, L. XU, B. TU, D. ZHAO, Uniform nanostructured arrays of sodium rare-earth fluorides for highly efficient multicolor upconversion luminescence, *Angew. Chem. Int. Ed. Wiley-VCH Verlag GmbH & Co. KGaA, Weinheim*, **2007**, *46*, 7976–7979.
- [73]. For the co-precipitation synthesis of SrAl₂O₄:Eu²⁺, Dy³⁺ nanotubes, see: B. CHENG, H. LIU, M. FANG, Y. XIAO, S. LEI, L. ZHANG, Long-persistent phosphorescent SrAl₂O₄:Eu²⁺, Dy³⁺ nanotubes, *Chem. Commun.*, **2009**, DOI: 10.1039/b818057a.
- [74]. N. K. ZURBA, Luminescent beryllium, magnesium, calcium, strontium and barium aluminate nanotubes doped with cerium (III) and co-doped with other lanthanide ions, M_(1-x-y)N₂O₄:Ce_x, Ln_y, *Appl. Patent*, PCT/104486, **2009**.
- [75]. N. K. ZURBA, I. BDIKIN, A. KHOLKIN, D. GOLBERG, J. M. F. FERREIRA, Intercrystalline distal-effect on the afterglow phenomenon in photoluminescent SrAl₂O₄:Eu²⁺, Dy³⁺, Ce³⁺ nanotube growth, *Nanotechnology* **2010**, *21*, 32, 325707, DOI:10.1088/0957-4484/21/32/325707.
- [76]. For synthesis and optical features of SrAl₂O₄:Eu²⁺, Dy³⁺ see, for example, a) I. C. CHEN, T. M. CHEN, Sol-gel synthesis and the effect of boron addition on the phosphorescent properties of SrAl₂O₄:Eu²⁺, Dy³⁺ phosphors, *J. Mater. Res.* **2001**, *16*, 3, 644-651; b) Z. L. FU, S. H. ZHOU, Y. N. YU, S. Y. ZANG, Combustion synthesis and luminescence properties of nanocrystalline monoclinic SrAl₂O₄:Eu²⁺, *Chem. Phys. Lett.* **2005**, *416*, 4-6:381; c) H. SONG, D. CHEN, Combustion synthesis and luminescence properties of SrAl₂O₄:Eu²⁺, Dy³⁺, Tb³⁺ phosphor, *J. Lumin.* **2007**, *22*, 6, 554-558; d) H. CHANDER, D. HARANATH, V. SHANKER, P. SHARMA, Synthesis of nanocrystals of long persisting phosphor by modified combustion technique, *Cornell Univ. Lib.* **2007**, arXiv.org, 0405110; e) Y. SUN, G. QIU, X. LI, S. ZHANG, C. YAN, X. ZHANG, Synthesis of SrAl₂O₄:Eu²⁺, Dy³⁺ phosphor by the coupling route of microemulsion with coprecipitation method, *J. Rare Metals*. **2006**, *25*, 6, 615-619; f) C. H. LU, S. Y. CHEN, C. H. HSU, Nanosized strontium aluminate phosphors prepared via reverse microemulsion route, *Mat. Sc. Eng.* **2007**, *140*, 3, 218-221; g) J. GENG, Z. WU, Synthesis of long afterglow SrAl₂O₄:Eu²⁺, Dy³⁺ phosphors through microwave route, *J. Mat. Synthesis Proc.* **2002**, *10*, 5, 245-248; h) X. LI, Y. QU, X. XIE, Z. WANG, R. LI, Preparation of SrAl₂O₄:Eu²⁺, Dy³⁺ nanometer phosphors by detonation method, *Mat. Lett.* **2006**, *60*, 29-30, 3673-3677; i) T. PENG, L. HUAJUM, H. YANG, C. YAN, Synthesis of SrAl₂O₄:Eu, Dy phosphor nanometer powders by sol-gel process and its optical properties, *Mat. Chem. Phys.*, **2004**, *85*, 1, 68-72; j) G. XIUJUAN, C. YONGJIE, X. LINJIU, Y. CHANGHAO, Synthesis of long afterglow photoluminescent materials Sr₂MgSi₂O₇:Eu²⁺, Dy³⁺ by sol-gel method, *J. Rare Earths*, **2005**, *23*, 3, 292-294; k) B. FARIDNIA, M. M. K. MOTLAGH, A. MAGHSOUDIPOUR, Optimising synthesis conditions for long lasting SrAl₂O₄ phosphor, *P. Res. Technol.*, **2007**, *36*, 4, 216-223; l) H. YAMADA, W. S. SHI, K. NISHIKUBO, C. N. XU, Determination of the crystal structure of spherical particles of SrAl₂O₄:Eu prepared by the spray method, *J. Electrochem. Soc.*, **2003**, *150*, E251-E254.
- [77]. a) E. NAKAZAWA, Y. MURAZAKI, S. SAITO, Mechanism of the persistent phosphorescence in Sr₄Al₁₄O₂₅:Eu and SrAl₂O₄:Eu codoped with rare earth ions, *J. Appl. Physics*. **2006**, *100*, 11, 113113-113113-7; b) F. CLABAU, X. ROCQUEFELTE, S. JOBIC, P. DENIARD, M-H. WHANGBO, A. GARCIA, T. LE MERCIER, Mechanism of phosphorescence appropriate for the long-lasting phosphors Eu²⁺-doped SrAl₂O₄ with co-dopants Dy³⁺ and B³⁺, *Chem. Mater.*, **2005**, *17*, 3904; c) J. DONGDONG, W. XIAO-JUN, W. JIA, W. M. YEN, Temperature dependent photoconductivity of Ce³⁺ doped SrAl₂O₄, *J. Lumin.*, **2005**; d) P. DORENBOS, Absolute location of lanthanide energy levels and the performance of phosphors, *J. Lumin.*, **2007**, *122-123*, 315-317; e) J. DONGDONG, W. XIAO-JUN, W. JIA, W. M. YEN, Trapping processes of 5d electrons in Ce³⁺ doped SrAl₂O₄, *J. Lumin.*, **2007**, *122-123*, 311-314; f) F. PELLÉ, T. AITASALO, M. LASTUSAARI, J. NIITYKOSKI, J. HÖLSÄ, Optically stimulated luminescence of persistent luminescence materials, *J. Lumin.*, **2006**, *119-120*, 64-68; g) K. KATO, I. TSUTAI, T. KAMIMURA, F. KANEKO, K. SHINBO, M. OHTA, T. KAWAKAMI, Thermoluminescence properties of SrAl₂O₄:Eu sputtered films with long phosphorescence, *J. Lumin.*, **1999**, *82*, 3, 213-220.
- [78]. G. BLASSE, B. C. GRABMARIER, Luminescent Materials, *Springer-Verlag*, Berlin, **1994**.

- [79]. NEMOTO & Co., LTD., Phosphorescent Phosphor, *Eur. Patent*, **1996**, EP0622440B1.
- [80]. D. P. STUMBO, S. A. EMPEDOCLES, F. LEON, J. W. PARCE, Artificial dielectrics using nanostructures, *Appl. Patent*, **2005**, US7365395.
- [81]. Nanowires/nanorods: a) TANA ET AL, Morphology-dependent redox and catalytic properties of CeO₂ nanostructures: nanowires, nanorods and nanoparticles, *Catal. Today* **2009**, DOI:10.1016/j.cattod.2009.02.016; b) K. B. ZHOU, X. WANG, X. M. SUN, Q. PENG, Y. D. LI, *J. Catal.*, **2005**, 229, 206; c) H. X. MAI, L. D. SUN, Y. W. ZHANG, R. SI, W. FENG, H. P. ZHANG, H. C. LIU, C. H. YAN, *J. Phys. Chem. B*, **2005**, 109, 24380; d) C. PAN, D. ZHANG, L. SHI, J. FANG, *Eur. J. Inorg. Chem.*, **2008**, 15, 2429; e) N. BUGAYEVA, J. ROBINSON, *Mater. Sci. Technol.*, **2007**, 23, 237; f) K. B. ZHOU, Z. Q. YANG, S. YANG, *Chem. Mater.*, **2007**, 19, 1215; g) W. Q. HAN, L. J. WU, Y. M. ZHU, *J. Am. Chem. Soc.*, **2005**, 127, 12814.
- [82]. P. SHARMA, D. HARANATH, H. CHANDER, S. SINGH, Green chemistry-mediated synthesis of nanostructures of afterglow phosphor, *Appl. Surf. Sci.*, **2008**, 254, 4052–4055.
- [83]. a) E. M. ELSSFAH, A. ELSANOUSI, J. ZHANG, H. S. SONG, CHENGCUN TANG, Synthesis of magnesium borate nanorods, *Mater. Lett.*, **2007**, 61, 22, 4358-4361; b) R. MA, Y. BANDO, T. SATO, *Appl. Phys. Lett.*, **2002**, 81, 3467; c) J. ZHANG, J. LIN, H. S. SONG, E. M. ELSSFAH, S. J. LIU, J. J. LUO, X. X. DING, C. TANG, S. R. QI, *Mater. Lett.*, **2006**, 60, 3292; d) Y. LI, Z. FAN, J. LU, R. P. H. CHANG, *Chem. Mater.*, **2004**, 16, 2512; e) R. Z. MA, Y. BANDO, D. GOLBERG, *Angew. Chem.*, **2003**, 42, 1836.
- [84]. a) S. A. HILDERBRAND, F. SHAO, C. SALTHOUSE, U. MAHMOOD, R. WEISSLEDER, Upconverting luminescent nanomaterials: application to in vivo bioimaging, *Chem. Commun.*, **2009**, 4188–4190; b) P. L. A. M. CORSTJENS, S. LI, M. ZUIDERWIJK, K. DARDOS, W. R. ABRAHMS, R. S. NIEDBLA, H. J. TANKE, *IEEE Proc. Nanobiotechnol.*, **2005**, 152, 64; c) K. KUNIGAS, H. PAKKILA, T. UKONAHO, T. RANTANEN, T. LOVGREN, T. SOUKKA, *Clin. Chem. (Washington, D. C.)*, **2007**, 53, 145; d) Z. Chen, H. Chen, H. Hu, M. Yu, F. Li, Q. Zhang, Z. Zhou, T. Yi, C. Huang, *J. Am. Chem. Soc.*, **2008**, 130, 3023; e) T. Rantanen, M. L. Jarvenpaa, J. Vuojola, K. Kuningas, T. Soukka, *Angew. Chem., Int. Ed.*, **2008**, 47, 3811; f) S. N. MISRA, M. A. GAGNANI, I. DEVI, R. S. SHUKLA, Biological and clinical aspects of lanthanide coordination compounds, *Bioinorg. Chem. Appl.*, **2004**, 2, 3-4, 155-192; g) Q. L. CHERMOUT, C. CHANEAC, J. SEGUIN, et. al, Nanoprobes with near-infrared persistent luminescence for in vivo imaging, *Proc. Nat. Ac. Sc. USA*, **2007**, 104, 9266-9277; h) E. SOINI, N. J. MELTOLA, A. E. SOINI, J. SOUKKA, J. T. SOINI, P. E. HÄNUIREN, Two photon fluorescence excitation in detection of biomolecules, *Biomech. Soc. Trans.*, **2000**, 28, 70-74; i) T. SOUKKA, K. KUNINGAS, T. RANTANEN, V. HAASLAHTI, T. LÖVGREN, Photochemical characterization of up-converting inorganic lanthanide phosphors as potential labels, *J. Fluoresc.*, **2005**, 15, 4, 513-528; j) R. E. BAILEY, A. M. SMITH, S. NIE, Quantum dots in biology and medicine, *Physica E* **2004**, 25, 1, 1-12; k) M. BRUCHEZ JR, M. MORONNE, P. GIN, S. WEISS, A. P. ALIVISATOS, Semiconductor nanocrystals as fluorescent biological labels, *Science*, **1998**, 281, 5385, 2013-2016; l) C. FELDMANN, T. JÜSTEL, C. R. RONDA, P. J. SCHMIDT, Inorganic luminescent materials: 100 years of research and application, *Adv. Funct. Mat.*, **2003**, 13, 7, 511-516.
- [85]. For correlation about persistent luminescence and superconductivity, see: a) D. JIA, ET AL, Green phosphorescence of CaAl₂O₄:Tb³⁺, Ce³⁺ through persistence energy transfer, *Appl. Phys. Lett.*, **2002**, 80, 9, 1535-1537; b) D. JIA ET AL, Persistent energy transfer in CaAl₂O₄:Tb³⁺, Ce³⁺, *J. Appl. Phys.*, **2003**, 93, 148-152; c) J. HÖLSÄ, T. LAAMANEN, M. LASTUSAARI, M. MALKAMÄKI, J. NIITTYKOSKI, P. NOVAK, Synchrotron radiation spectroscopy of rare earth doped persistent luminescence materials, *Rad. Phys. Chem.*, **2009**, 78, 10, 1, S11-S16; d) C. M. LIEBER, P. YANG, Nanorod-superconductor composites: a pathway to materials with high critical current densities, *Science* **1996**, 273, 1782-1879, DOI: 10.1126/science.273.5283.1836.
- [86]. a) W. M. YEN, D. J. JIA, W. WEIYI, X. J. WANG, Long persistent phosphors and persistent energy transfer technique, *Appl. Patent*, **2005**, US6953536; b) BE134745; c) US3294696.
- [87]. J. LIU, Z. WU, G. MENG, P. PENG, Z. CHEN, Z. ZHAN, P. LIAO, Preparation method of multicenter zinc aluminate nanometer pipe, *Appl. Patent*, **2008**, CN101319388.
- [88]. Y. HE, J. A. WANG, W. F. ZHANG, X. B. CHEN, Z. H. HUANG, Q. W. GU, Colour electroluminescence with end light-emitting from ZnO nanowire/polymer film, *J. Phys.: Conf. Ser.*, **2009**, 152, 12-54.
- [89]. J. UPENDRA, L. J. SUNG, Large-scale, surfactant-free, hydrothermal synthesis of lithium aluminate nanorods, *Inorg. Chem.*, **2007**, 46, 8, 3176-3184.
- [90]. G. ZHU, X. ZOU, Y. SU, J. CHENG, M. WANG, Direct synthesis of straight SiO₂ nanorods, *J. Phys.: Conf. Ser.*, **2009**, 152, 12-13.
- [91]. N. PINNA, M. G. WILLINGER, K. WEISS, J. URBAN, R. SCHLOGL, Local structure of nanoscopic materials: V₂O₅ nanorods and nanowires, *Nano Letters* **2003**.
- [92]. C. A. MIRKIN, L. QIN, S. PARK, L. HUANG, S. W. CHUNG, Multicomponent nanorods, *Appl. Patent*, **2008**, US7422696.

- [93]. F. T. JOHN, M. J. NAUGHTON, R. A. FARRER, Method of fabricating nanowires and electrodes having nanogaps, *Appl. Patent*, **2007**, WO040558.
- [94]. T. HYEON, J. PARK, Method of synthesizing nanorods by reaction of metal-surfactant complexes, *Appl. Patent*, **2005**, US0214190.
- [95]. D. B. MITZI, C. B. MURRAY, D. V. TALAPIN, Method for fabricating an inorganic nanocomposite, *Appl. Patent*, **2007**, US0160747.
- [96]. L. T. ROMANO, J. M. HAMILTON, Methods for nanowire growth, *Appl. Patent*, **2008**, US7344961.
- [97]. a) V. J. TEUNIS, V. P. LIESBETH, Optical nanowire biosensor based on energy transfer, US196239, 2007; b) B. YOSHIO; Z. Y. CHUN, Boron nitride nanowire and method of manufacturing the same, *Appl. Patent*, **2005**, JP075656; c) T. MIRKOVIC ET AL, Hinged nanorods made using a chemical approach to flexible nanostructures, *Nature Nanotech.* **2007**, 565-569, DOI:10.1038/nnano.2007.250.
- [98]. C. M. LIEBER, P. YANG, Metal oxide nanorods, *Appl. Patent*, **1999**, US5897945.
- [99]. N. K. ZURBA, J. M. F. FERREIRA, Ultrasonic method of synthesis of luminescent aluminate nanowires and nanorods doped with cerium (III) and nanostructured composites, *Prov. Appl. Patent* 105107, **2010**.
- [100]. F. CLABAU, X. ROCQUEFELTE, S. JOBIC, P. DENIARD, M. H. WHANGBO, A. GARCIA, T. LE MERCIER, *Chem. Mater.*, **2005**, *17*, 3904.
- [101]. T. AITASALO, J. HÖLSÄ, H. JUNGNERD, ET AL., *J. Lumin.*, **2001**, *94*, 59.
- [102]. Y. H. LIN, Z. T. ZHANG, Z. L. TANG, ET AL., *Mater. Chem. Phys.*, **2001**, *70*, 156.
- [103]. C. K. CHANG, D. L. MAO, J. F. SHEN, ET AL., *J. Alloys Compd.*, **2003**, *348*, 224.
- [104]. Y. H. LIN, Z. T. ZHANG, Z. L. TANG, *Mater. Lett.*, **2001**, *51*, 14.
- [105]. Y. H. LIU, H. DING, CHIN, *J. Inorg. Chem.*, **2001**, *17*, 181.
- [106]. D. VAN, M. DEBRA, Tintable luminescent paint, *Appl. Patent*, **2002**, US6359048.
- [107]. C. Y. LI, S. B. WANG, J. SU, CHIN, *J. Lumin.*, **2002**, *23*, 233.
- [108]. H. T. PU, F. Y. SU, J. WANG, *Plastic Ind.* **1998**, *26*, 113.
- [109]. C. P. YANG, Y. YONG, C. ZHU, L. CHONG, Effect of hydrolysis on the stability of SrAl₂O₄:Eu²⁺, Dy³⁺, *J. Portland*, **2004**, *32*, 09.
- [110]. P. VIOLANTE, A. VIOLANTE, J. M. TAIT, Morphology of nordstrandite, *Clays Miner.*, **1982**, *30*, 6, 431-437.
- [111]. NISHIO, NAOKI, KAMIMOTO ET AL, Coating for phosphor particles, *Appl. Patent*, **1999**, US5856009.
- [112]. BECHTEL, HELMUT, CZARNOJAN ET AL, Aluminate phosphor with a polyphosphate coating, *Appl. Patent*, **1999**, US5998047.
- [113]. N. K. ZURBA, M. FERNANDES, E. O. B. LEITE, M. C. FREDEL, Photoluminescent-warning ceramic tiles for risk areas and emergency of people with special needs, *Appl. Patent*, **2007**, PT103915.
- [114]. a) G. A. PARKS, *Chem. Rev.*, **1965**, *65*, 2, 177-98; b) X. LÜ, Silica encapsulation study on SrAl₂O₄:Eu²⁺, Dy³⁺ phosphors, *Mater. Chem. Phys.*, **2005**, *93*, 526-530.
- [115]. L. DONG, W. GEN, Organic encapsulation on SrAl₂O₄:Eu²⁺, Dy³⁺ phosphors and its characterization, *Appl. Chem.*, **2005**, *22*, 6.
- [116]. X. LÜ, M. ZHONG, W. SHU, Q. YU, X. XIONG, R. WANG, Alumina encapsulated SrAl₂O₄:Eu²⁺, Dy³⁺ phosphors, *Powder Techn.* **2007**, *177*, 83-86.
- [117]. C. GUOA, L. LUAN, D. HUANG, Q. SUB, Y. LV, Study on the stability of phosphor SrAl₂O₄:Eu²⁺, Dy³⁺ in water and method to improve its moisture resistance, *Mater. Chem. Phys.*, **2007**, *106*, 268-272.
- [118]. S. WU, S. ZHANG, Y. LIU, J. YANG, The organic ligands coordinated long afterglow phosphor, *Mater. Lett.*, **2007**, *61*, 3185-3188.
- [119]. S. ZHANG, S. WU, J. YANG, Polymer grafted alkali earth aluminate phosphor through coordination bond, *Appl. Patent*, **2007**, US0221886.
- [120]. S. YU, P. PI, X. WEN, J. CHENG, Z. YANG, Preparation and luminescence of SrAl₂O₄:Eu²⁺, Dy³⁺ phosphors coated with maleic anhydride, *Can. J. Chem. Eng.*, **2008**, *86*, 02.
- [121]. Y. ZHU, M. ZHENG, J. ZENG, Y. XIAO, Y. LIU, Luminescence enhancing encapsulation for strontium aluminate phosphors with phosphate, *Mater. Chem. Phys.*, **2009**, *113*, 721-726.
- [122]. F. GAO, Z. XIONG, H. XUE, Y. LIU, Improved performance of strontium aluminate luminous coating on the ceramics surface, in *F: Functional Ceramics*, F19.105, **2008**, Chinese Academy of Sciences.

- [123]. N. SUN, L. YING-LIANG, H. LANGHUAN, C. WENXIN, Study of preparation and photocatalytic properties of new type compounded material $\text{CaAl}_2\text{O}_4:\text{Eu}^{2+}$, Dy^{3+} coated by TiO_2 , *Chem. Mater. Const.*, **2004**, *20*, 06.
- [124]. Y. WANG, H. LI, Photocatalytic properties of $\text{CaAl}_2\text{O}_4:\text{Eu}^{2+}$; Dy^{3+} coated with TiO_2 without light source, in *10th Intern. Symp. Eco-Mater. Proc. Des.*, ISEPD, **2009**, China.
- [125]. J. B. ZHONG, D. MA, Z. Y. HE, J. Z. LI, Y. Q. CHEN, Sol-gel preparation and photocatalytic performance of $\text{TiO}_2/\text{SrAl}_2\text{O}_4:\text{Eu}^{2+}$, Dy^{3+} toward the oxidation of gaseous benzene, *Sol-Gel Sci. Technol.*, **2009**, DOI: 10.1007/s10971-009-2003-5.
- [126]. A. FUJISHIMA, K. HONDA, *Nature*, **1972**, *238*, 37.
- [127]. D. BAHNEMANN, D. BOCKELMANN, R. GOSLICH, *Solar Energy Mater.*, **1991**, *24*, 594.
- [128]. D. BLAKE, J. WEBB, C. TURCHI, K.K. MARGRINI, *Solar Energy Mater.*, **1991**, *24*, 584.
- [129]. P. STORY, B. HANEGAN, *Appl. Patent*, **1990**, WO99013606.
- [130]. L. LUO, L. MIAO, S. TANEMURA, M. TANEMURA, Photocatalytic sterilization of TiO_2 films coated on Al fiber, *Mater. Science Eng. B*, **2008**, *148*, 183–186.
- [131]. S. RANA, J. RAWAT, M. M. SORENSON, R. D. K. MISRA, Antimicrobial function of Nd^{3+} -doped anatase titania-coated nickel ferrite composite nanoparticles: a biomaterial system, *Acta Biomat.* **2006**, *2*, 4, 421-432.
- [132]. Z. HUA, Y. LIU, L. DONG, S. WAN-GEN, DAI, Encapsulation study on strontium aluminate pigment, *Guangzhou Chem. Ind.*, **2004**, *32*, 04.
- [133]. I. YUSUKE, X. CHAO-NAN, Visible light transparent stress luminescent composite material, water resistant stress luminescent inorganic particle and their manufacturing process and applications, *Appl. Patent*, **2005**, JP2005320425.
- [134]. T. MAYER, S. A. YAMANAKA, J. ZIEBA, Color-shifting pigments and foils with luminescent coatings, *Appl. Patent*, **2000**, US6565770.
- [135]. J. SHERMAN, Nanoparticulate titanium dioxide coatings, and process for the production and use thereof, *Appl. Patent*, **2000**, US6653356.
- [136]. C. C. GYUN, P. I. U, Y. J. SU, Y. W. TAE, Strontium aluminate phosphor and light emitting diode using the strontium aluminate phosphor with strontium barium silicate, *Appl. Patent*, **2004**, KR20040082543.
- [137]. YONETANI, T. KOBE-SHI, HYOGO-KEN, Phosphorescent article, *Appl. Patent*, **1995**, EP0704510.
- [138]. H. MAAS, A. CURRAO, G. CALZAFERRI, Encapsulated lanthanides as luminescent materials, *Angew. Chem. Int. Ed.*, **2002**, *41*, 14, 2495–2497.
- [139]. J. INO, H. FUKUCHI, Luminescent-film-coated product, *Appl. Patent*, **2007**, US7279236.
- [140]. S. OGATA, Molded product having photocatalytic function, *Appl. Patent*, **2000**, US6074748.
- [141]. P. D. GALLO, G. ETCHEGOYEN, T. CHANTIER, Catalytic membrane layer, *Appl. Patent*, **2006**, US0127656.
- [142]. K. L. LURVEY ET AL, Medical fluid access device with antiseptic indicator, *Appl. Patent*, **2008**, US0021381.
- [143]. N. K. ZURBA, J. M. F. FERREIRA, Encapsulation process of luminescent beryllium, magnesium, calcium, strontium and barium aluminates doped with cerium (III) encapsulated with TiO_2 , *Appl. Patent*, **2009**, P1104801.
- [144]. M. KARMAOUI, M. G. WILLINGER, L. MAFRA, T. HERNTRICH, N. PINNA, A general nonaqueous route to crystalline alkaline earth aluminate nanostructures, *Nanoscale*, **2009**, *1*, 1-7, DOI: 10.1039/b9nr00164f.
- [145]. N. K. ZURBA, J. M. F. FERREIRA, Luminescent antibacterial dental paste based in aluminates doped with cerium (III) encapsulated with TiO_2 , *Appl. Patent*, **2009**, Div. P1104801.
- [146]. N. K. ZURBA, M. FERNANDES, G. BARRA, M. C. FREDEL, Study of bioceramics with ophthalmologic applications, *Proc. Bras. Cer. Cong.*, **2005**, *49*, 17-01.
- [147]. N. K. ZURBA, M. FERNANDES, E. O. B. LEITE, A. NOGUEIRA, P. T. FIADEIRO, M. C. FREDEL, Method of personalization of materials by diagnosis of biofunctionality of retinal photoreceptor cells *in space* and biomedical equipment, *Appl. Patent*, **2008**, P1103919.
- [148]. M. Rodgers, R. Hodges, J. Hawkins, W. Hollingworth, S. Duffy, M. McKibbin, M. Mansfield, R. Harbord, J. Sterne, P. Glasziou, P. Whiting, M. Westwood, Colour vision testing for diabetic retinopathy: a

- systematic review of diagnostic accuracy and economic evaluation, *Health Technology Assessment*, **2009**, 13, 60.
- [149]. G. L. Ong, L. G. Ripley, R. S. B. Newsom, A. G. Casswell, Assessment of colour vision as a screening test for sight threatening diabetic retinopathy before loss of vision, *Br. J. Ophthalmol.*, **2003**, 87, 747-752, DOI:10.1136/bjo.87.6.747.
- [150]. R. Wong, J. Khan, T. Adewoyin, S. Sivaprasad, G. B. Arden, V. Chong, The ChromaTest, a digital color contrast sensitivity analyzer for diabetic maculopathy: a pilot study, *BMC Ophthalmology*, **2008**.
- [151]. AFNOR – Association Française de Normalisation, AFNOR NF EN ISO 15197, In Vitro Diagnostic Test Systems - Requirements for Blood-Glucose Monitoring Systems for Self-Testing in Managing Diabetes Mellitus, **2004**.
- [152]. a) L. KESSEL, A. ALSING, M. LARSEN, Diabetic versus non-diabetic colour vision after cataract surgery, *Br. J. Ophthalmol.*, **1999**, 83, 9, 1042-1045; b) D. B. HENSON, R. V. NORTH, Dark adaptation in diabetes mellitus, *Br. J. Ophthalmol.*, **1979**, 68, 8, 539-541; c) M. MÄNTYJÄRVI, Colour vision and dark adaptation in diabetic patients after photocoagulation, *Acta Ophthalmol.*, **1989**, 67, 2, 113-118; d) N. DRASDO, Z. CHITI, D. R. OWENS, R. V. NORTH, Effect of darkness on inner retinal hypoxia in diabetes, *The Lancet*, **2002**, 359, 9325, 2251-2253; e) Z. NING, D. WEIMING, W. JIAXIN, P. J. CLAUDE, Simulating human visual perception in nighttime illumination, *Tsinghua Sc. Techn.*, **2009**, 14, 1, 133-138. ISSN all1007-0214/19/21.
- [153]. a) H. LI, Telemedicine and Ophthalmology, *Survey Ophthalmol.*, **1999**, 44, 1, 61-72; b) F. ROYO in: Personalized Medicine, Fourth Annual Workshop on the Business-Government Interface, *MIT Portugal Program, Center for Neuroscience and Cell Biology, Biocant*, **2010**.
- [154]. Low temperature frit: a) V. V. GOLUBKOV, V. N. BOGDANOV, A. Y. PAKHNIN, V. A. SOLOVYEV, E. V. ZHIVAEVA, V. O. KABANOV, O. V. YANUSH, S. V. NEMILOV, A. KISLIUK, M. SOLTWISCH, D. QUITMANN, Microinhomogeneities of glasses of the system PbO-SiO₂, *J. Chem. Phys.*, **1999**, 110, 10, 4897-4906, DOI: 10.1063/1.478375; b) T. TAKAISHI, M. TAKAHASHI, J. JIN, T. UCHINO, T. YOKO, Structural study on PbO-SiO₂ glasses by X-ray and neutron diffraction and ²⁹Si MAS NMR measurements, *J. Amer. Ceram. Soc.*, **2005**, 88, 6, 1591-1596(6); c) The study on partial heat properties of SnO-ZnO-P₂O₅ glasses, *Glass & Enamel*, **2006**, 2.
- [155]. A. A. YAREMCHENKO, V. V. KHARTON, A. A. VALENTE, A. L. SHAULA, F. M. B. MARQUES, J. ROCHA, Mixed conductivity and electrocatalytic performance of SrFeO_{3-δ}-SrAl₂O₄ composite membranes, *Solid State Ionics* **2006**, 177, 2285-2289.
- [156]. Super-high temperature sealant: Master Bond Sealant EP125 100/50, in: <http://www.directindustry.com/prod/master-bond/sealant-adhesive-for-aerospace-17407-198184.html>.
- [157]. Glossary, see the follow sources: a) EPEDOO - Emergency Procedures for Employees with Disabilities in Office Occupancies, Federal Emergency Management Agency, United States Fire Administration; b) ATBCB - U.S. Architectural & Transportation Barriers Compliance Board, Lawrence W. Roffee, Washington DC, 20004-1111; c) Technical Assistance on Accessibility Issues & the ADA; d) PCEPWD - President's Committee on Employment of People with Disabilities Maggie Roffee, Program Manager 1331 Washington, DC 20004; e) JAN - Job Accommodation Network, Anne E. Hirsh West Virginia University P. O. Box 6080 918 Chestnut Ridge Road, Suite 1 Morgantown, West Virginia 26506-6080; f) NFPA - National Fire Protection Association Learn Not To Burn Foundation Sharon Gamache, Executive Director P. O. Box 9101 Batterymarch Park Quincy, Massachusetts 02269-9101; g) NEMA - National Electrical Manufacturers Association Malcolm E. O'Hagan, President 2101 L Street, NW, Suite 300 Washington, DC 20037 voice 202-457-8400; h) AEMA - Accessibility Equipment Manufacturers Assn. Terry Nevins-Buchholtz, Administrative Assistant P. O. Box 51784 2445 South Calhoun Road New Berlin, Wisconsin 53151, An affiliate of PCEPWD; i) EPVA - Eastern Paralyzed Veterans Association Buffalo Regional Office Brian Black, New York; j) NAD - National Association of the Deaf Nancy; k) SHHH - Self Help for Hard of Hearing People; l) TDI - Telecommunications for the Deaf, Incorporated Alfred Sonnenstrahl, Executive Director 8719 Colesville Rd, Suite 300 Silver Spring, Maryland 20910; m) NFB - National Federation of the Blind, Patricia Maurer, Coordinator, Community Relations, 1800, Johnson Street Baltimore, Maryland 21230-4998; n) ACB - American Council of the Blind Oral Miller, National Representative, 1155, 15th Street, NW, Suite 720, Washington, DC; o) PSPA [16]; p) NDC - National Council on Disabilities, Effective Emergency Management: Making Improvements for Communities and People with Disabilities, Washington DC, **2009**, 510.

Glossary

Activator is an ionic impurity in a host material which acts as a luminescent centre, also called dopant.

ADA Americans with Disabilities Act.

Afterglow is a general emission of light after a source of excitation energy is removed, usually by phosphorescence.

Anti-Stokes is a material which converts low energy light to high energy light by photoluminescence, also called up-converter.

Aphasia is an absence or impairment of the ability to communicate through speech, writing or signs.

Area of Refuge or Area of Rescue Assistance is an area that has direct access to an exit, where people who are unable to use stairs may remain temporarily in safety to await further instructions or assistance during emergency evacuation.

Asthma is a complex disease which causes obstruction of the respiratory system.

Back Pain can be caused by congenital conditions, disease or injury, but for the millions of people affected by this condition the key element is always the same, pain.

Blind/Blindness is a range of vision impairments from the inability to distinguish light and dark to a loss of part of the visual field or the inability to see detail (see definition: visually impaired).

Braille "Perkins Braille" is an all-purpose Braille writer.

Buddy System is the system of assigning the appropriate individual(s) to assist in the evacuation of persons with disabilities.

Candela is unit of luminous intensity.

Cane as used by the blind individual, the cane is a natural extension of the arm and hand and is used as an "information gathering" device (to locate familiar landmarks) for the purpose of establishing a clear path of travel. The conventional two-point touch system: the cane is moved from side to side in an arcing motion. The width of the arc is usually two inches to either side of the shoulders. As the cane touches to the left, the right foot should be forward. The cane tip touches in the opposite direction of the leading foot.

Cascading are multiple absorption/emission cycles in a material where the emission from one cycle is matched to the absorption of the next.

Cathodoluminescence is luminescence where the initial energy comes from fast moving electron bombardment, such as on a television screen or computer monitor.

Cerebrovascular Accident (CVA) is a localized brain damage due to a ruptured blood vessel in the brain; commonly called a stroke.

Cerebral Palsy is a non-progressive disorder of the brain, results from damage to the nervous system at birth or in the first hours or days of life; not a disease.

Charging is the excitation of a phosphorescent material, usually by incident light.

Chemiluminescence is luminescence where the initial energy comes from chemical reactions, such as phosphorous burning in oxygen.

Chronic Obstructive Pulmonary Disease (COPD) includes the diseases of chronic bronchitis and emphysema.

Closed Circuit TV Magnifier (CCTV) consists of television camera which takes the picture of the printed page and a television monitor which displays image in enlarged form.

Correlated Colour Temperature is the colour of white light sources, the temperature of the black body radiator which produces the chromaticity most similar to the light source. Unit: Kelvin temperature, K.

Critical Language is a terminology that must be avoid as unacceptable and/or insulting to persons with disabilities.

Daylight Fluorescence (DF) is fluorescence where the emission is in the visible spectrum.

Deaf/Deafness is a range of auditory impairments, from a total lack of sensitivity to sound to reduced sensitivity to certain sound frequencies.

Deutanopia the colour receptors (cones) in the eyes of people with deutanopia are not sensitive to medium wavelengths (i.e. greens).

Diabetic Retinopathy is a damage to blood vessels in the retina, caused by diabetes.

DIN 67510 Part 1 is a specification describing afterglow performance in a standard way, in the form (a/b - c - d - e), where "a" is afterglow brightness in mcd/m² after 10 minutes, "b" is afterglow brightness after 60 minutes, "c" is the decay period in minutes to 0.3 mcd/m², "d" is excitation colour code, "e" is emission colour code. Parts 2 and 3 refer to in situ testing of photoluminescent items.

Dog Guide is a dog that has been specially trained to assist people who are blind, physically disabled or hearing-impaired.

Dopant is an ionic activator commonly used in inorganic phosphors.

Electroluminescence (EL) is luminescence where the initial energy comes from electric fields, usually alternating.

Epilepsy is a condition characterized by occasional seizures. A small fraction of those with epilepsy are photosensitive. Seizures can be triggered by flashing lights.

Excited state is a condition of a charged phosphor before emission.

Exercise Induced Bronchospasm (EIB) is a form of asthma.

Finger spelling when no sign language exists for a thought or concept, the word can be spelled out using the American Manual Alphabet.

Fluorescence is a very fast absorption and emission of photons where there is no appreciable afterglow. No electron spin inversion is involved.

Flux (light) is luminous intensity, usually of a light source, per unit solid angle. Unit: lumen.

Guide Dog is a proprietary name for a dog guide.

Handicapped is a human condition that may be attributed to a person with disability. Critical Language.

Hearing Impaired is a scale of hearing impairment ranges from mild hearing loss to profound deafness, the point at which the individual receives no benefit from aural input. Many hard-of-hearing persons are able to use residual hearing effectively with the assistance of hearing aids (HA) or other sound-amplification devices, often augmented by lip reading. Hearing aids amplify background noises as well as voices, so noise caused by emergency conditions (alarm bells, people shouting, sirens, etc.) may rise to an uncomfortable level for the person with the hearing impairment.

Head Pointer is a stick or rod which is attached to a person's head with a head band so that by moving the head, an individual can perform tasks that would ordinarily be performed by hand or finger movement.

Hemiplegia is a disability resulting from a CVA which involves some degree of muscle weakness and motor skill loss on one side of the body.

Illuminant A, B, C is an incandescent illumination in the range 380 nm to 770 nm, respectively 2856 K (yellow), 4874 K (mean noontime sunlight), and 6774 K (average daylight, blue).

Illuminant D is daylight illumination defined from 300-830 nm, designated with a two digit subscript to describe Correlated Colour Temperature, e.g. D65 indicates 6500 K, close to Illuminant C.

Illumination is a luminous flux, usually of incident light. Units: lux or lumens per square metre.

Infrared is a part of the electromagnetic spectrum immediately less energetic than visible light, ranging from around 700 nanometres to 10 microns wavelength.

Interpreter is a professional who assists a deaf person in communicating with hearing people who cannot sign.

Intersystem Crossing is a transfer from one molecular angular momentum state to another by electron spin inversion.

Killing is a quenching.

Learning Disability is an individual who may have difficulty recognizing or being motivated to act in an emergency. These individuals may also have difficulty in following anything other than a few simple instructions.

Light Output is the quantum efficiency multiplied by amount of absorbed radiation.

Little People is a general term for persons of short stature who are less than 4' 10" or whose height is significantly below average.

Low Level Signage/ Floor Proximity Exit Signs are usually placed between 6" to 8" above the floor, a supplement to the required exit sign. The required exit signs are usually located over the exits or near the ceiling, the first place to become obscured by smoke.

Low Vision can be moderate to severe vision impairment which includes difficulty in reading without magnification and seeing fine detail. Some persons with low vision may be considered legally blind.

Lumen is one unit of light flux. One lumen equals the flux emitted into a solid angle by a point source of one candela.

Luminance is the brightness, usually of a surface, e.g. luminous intensity per unit area. Unit: candelas per square metre, usually expressed in millicandelas per square metre (mcd/m^2).

Luminescence is an emission of light from a substance unaccompanied by heat.

Luminophor is a luminescent material.

Luminous Directional Reflectance is a reflectance of a surface in given directions of illumination and view. The ratio of the brightness of a surface to the brightness that an ideally diffusing, perfectly white surface would have if illuminated in the same way. Units: none.

Luminous Intensity is a fundamental unit derived from black body radiation at set conditions in a given direction. Unit: candela.

Luminous Efficiency (L) is a luminous flux emitted by a source, per unit of power consumed. Unit: lumens per Watt.

Lux is an unit of illuminance, lumens per square metre. In imperial units, one foot-candle is approximately 10 lux.

Means of Egress an accessible means of egress is one that complies with these following guidelines: a continuous and unobstructed way of exit travel from any point in a building or facility to a public way. A means of egress comprises vertical and horizontal travel and may include intervening room spaces, doorways, hallways, corridors, passageways, balconies ramps, stairs, enclosures, lobbies, horizontal exits, courts and yards. Areas of refuge or evacuation elevators may be included as part of accessible means of egress.

Mobility Impaired employees with mobility impairments can vary in the degree of assistance that they require. The degree of impairment can range from walking with a slow gait (thus requiring more time to exit), to walking with a mobility aid such as a cane, crutches and/ or braces, to the wheelchair user.

Monitors/Wardens are terms used to identify the different assignments made in the Occupant Emergency Plan. For example, the duties of the Monitor could include assisting with the coordination of the evacuation of their floor or unit, identifying people with disabilities who require special assistance and coordinating assignment of "buddies" or assistants to stay with them.

Mouth Wand is a rod with a tooth grip that is held in the mouth and used to perform tasks that would normally be performed by hand.

Munsell Colour System is a colour space that defines colours based on three dimensions: hue, value (lightness) and chroma (colour purity or colourfulness).

Nystagmus is an uncontrolled movement of the eye also noticeable by (characteristic) head tilt because it helps the person get a better focus on an object, thereby to see better.

Optical Character Reader Device that can be scanned over a printed page, reading the text aloud through a voice synthesis system. These may also have provision for reading directly from a computer disk containing a word processor file.

Optically Active is a (a) luminescent, or (b) able to change the polarity of incident light during reflection.

Opticon Device to enable a blind person to "read," consisting of a camera that converts print into an image of letters which are then produced via vibrations onto the finger.

Paraplegia is an impairment or loss of motor and/or sensory function in the thoracic, lumbar or sacral segments of the spinal cord, affecting trunk and legs.

Phakic Eye is an eye that still possesses its natural crystalline lens.

Phosphor is a substance exhibiting the property of phosphorescence.

Phosphorescence is a slower absorption and emission of photons where afterglow is usually apparent, involving electron spin inversion allowing absorbed energy to be trapped for a period before being released as photons.

Photoluminescence is luminescence where the energy comes from incident light, includes fluorescent and phosphorescent processes.

Post Polio Syndrome this affects individuals who have recovered from polio. The symptoms include an increase in muscle weakness and an increase in respiratory weakness. Usually necessitates use of a wheelchair.

Protanopia the colour receptors (cones) in the eyes of people with protanopia are not sensitive to long wavelengths (i.e. reds).

Quadriplegia (see tetraplegia).

Quantum Yield (q) is the ratio of energy emitted by a luminescent substance to that absorbed, expressed as a percentage or decimal part of unity. Units: none.

Quenching is the loss of luminescent emissions to absorbing centres, or the addition of an agent to do this, also called killing.

Radiant Efficiency is the ratio of emitted luminescent power to power absorbed from exciting radiation.

Radioluminescence (RL) is luminescence where the initial energy comes from radioactive decay, e.g. as with tritium. Products relying on RL are also called self emitters.

Resonance Radiation is a fast fluorescence with no internal loss of energy.

Saturation is the charging of a phosphorescent material to maximum.

Scintillator is a photoluminescent material with absorption at very low wavelengths, e.g. gamma- or X-rays.

Screening is a health service in which members of a defined population, who do not necessarily perceive that they are at risk of a disease or its complications, are asked a question or offered a test to identify those individuals who are more likely to be helped than harmed by further tests or treatment.

Seeing Eye Dog is a proprietary name for dog guide.

Seizure is an involuntary muscular contraction, a brief impairment or loss of consciousness, etc., resulting from a neurological condition, such as epilepsy.

Service Animal is a trained dog or other animal that provides assistance to a person who is blind, deaf or mobility impaired. The animal can be identified by the presence of a harness or backpack.

Self Emitter is a radioluminescent material.

Sign Language means of communication used by persons who are deaf.

Snellen is a scale used to measure visual acuity. This has now been superseded by the development of the LogMAR scale.

Speech Disorder is a limited or difficult speech patterns or without speech.

Stokes Shift is the difference in wavelength peaks between absorption and emission curves in photoluminescent materials, positive where wavelength increases, negative where wavelength decreases. Unit: nanometres.

Tactile Signage is signs or labels with Braille, raised letters or textured patterns that can be read tactilely by persons with visual impairments.

Tetraplegia is an impairment or loss of motor and/or sensory function in the cervical segments of the spinal cord, affecting arms, trunk and legs.

Text Telephone is equipment that includes teletypewriters (TTY) and employs interactive graphic communications through transmission of coded signals across the standard telephone network.

Thermoluminescence (TL) is luminescence where heat energy triggers emission of photons from internal energy previously stored.

Triboluminescence (TB) is a short lived luminescence caused by the violent breaking of chemical bonds, often associated with frictional forces.

Tritanopia is an insensitivity to short wavelengths (i.e. blues).

Ultraviolet is a part of the electromagnetic spectrum immediately more energetic than visible light, ranging from approximately 100 nanometres (VUV) to 400 nanometres (UVA) wavelength.

Upconversion is a photoluminescent process converting lower energy incident light to higher energy emitted light, also called anti-Stokes.

Visual Acuity is the limit of spatial visual discrimination, commonly measured using letter or other geometric forms. Two of the scales used to measure visual acuity are the Snellen and LogMAR scales.

Visually Impaired a person with vision impairment may be totally or legally blind. Legally blind implies that a person may be able to differentiate between light and dark or see very large objects, but may not be able to see anything clearly enough to depend on their vision in an emergency situation. This can also include persons with low vision who can see well enough to walk but cannot read without magnification.

Wardens are persons assigned as coordinators of emergency actions by occupants of a single floor or part of a floor of a building.

Warning is a message sent to alert those at potential risk and designed to motivate them to take protective action. ■

ANNEX I

Solid state synthesis of strontium aluminates via $(\text{SrO}-\text{Al}_2\text{O}_3)\cdot\text{B}_2\text{O}_3$ system

Strontium aluminate materials were prepared by solid-state reactions. Some independent factors of the host lattices crystallization, such as thermo chemical performance of the reagents and the effects of boron flux addition are reported. A number of balanced compositions on the $(\text{SrO}-\text{Al}_2\text{O}_3)\cdot\text{B}_2\text{O}_3$ system using a phase diagram were studied. The elucidation of the thermodynamic features of the crystallization was commenced with measurements of XRD, DTA, TG, SEM and HR-TEM analysis.

Key-words: solid-state reactions, thermodynamic, enthalpy, strontium aluminate, host lattice, crystallization.

Introduction. The synthesis of SrAl_2O_4 host lattice crystallization is here investigated by the traditional solid state method under a catalyst boric acid addition. Stoichiometric mixtures, 1:1 molar ratio of SrCO_3 and $\alpha\text{-Al}_2\text{O}_3$, adding catalyst concentrations of 0.5 mol% (B1) and 1.0 mol% (B2) H_3BO_3 were investigated. The dried (323 K, 3 h) powders mixtures were planetary ball-milled. The as obtained powder mixtures were compacted (200 MPa) into cylindrical pellets, which were heat treated in alumina crucibles under air atmosphere at 1473 K and 1573 K, for 3 and 10 h. The annealed samples were grinded/deagglomerated using an agate mortar for characterization.

Materials. SrCO_3 (Aldrich; 99%, orthorhombic) and $\alpha\text{-Al}_2\text{O}_3$ (Alcoa), were used as received (Figure Al-1). Boric acid, H_3BO_3 (Aldrich, 99.99%), was added in convenient quantity as a fluxing agent to the mixture. Powder materials present particles size distributions from 0.5 to 2.3 μm (SrCO_3) and from 0.4 to 3.5 μm (Al_2O_3), measured by Coulter, LS Fraunhofer PIDS.

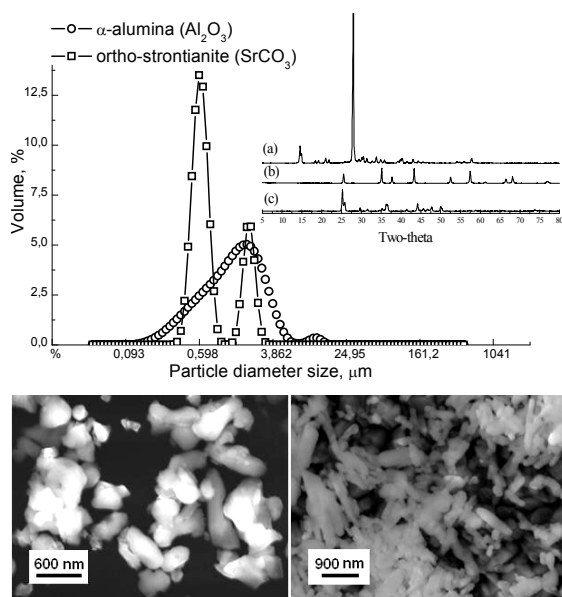
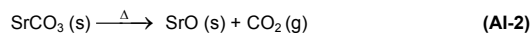


Figure Al-1. Particles size distributions of SrCO_3 and $\alpha\text{-Al}_2\text{O}_3$ powders. In detail: X-ray patterns of a) H_3BO_3 , b) $\alpha\text{-Al}_2\text{O}_3$ and c) ortho- SrCO_3 . SEM images of powders d) $\alpha\text{-Al}_2\text{O}_3$ and e) SrCO_3 reagents.

The solid-state chemical reactions between SrCO_3 and Al_2O_3 reagents to form SrAl_2O_4 (SA) are described by Equations (Al-1), (Al-2) and (Al-3):



The weight-loss due to thermal decomposition of SrCO_3 with release of CO_2 is an essential step to get free SrO to react with Al_2O_3 . Considering one mole of SrCO_3 (147.63 g), the reaction products after complete thermal decomposition will be one mole of SrO (103.63 g) and one mole of CO_2 (44 g) that is released to the atmosphere (Eq. Al-2). So, $\Delta m_{\text{SrCO}_3}(\%) = (44/147.63) \times 100 = 29.8\%$. This theoretical value of the strontianite weight-loss is coherent with the TG curve obtained during the experimental SrCO_3 decomposition process indicated on the thermogram (Δm_{SrCO_3}), Figure Al-2.

Furthermore, the DTA of SrCO_3 from Figure Al-2 revealed the follow features:

- **endothermic peak with a maximum at 1203 K:** attributed to the phase transformation from orthorhombic to hexagonal structure of SrCO_3 ; this polymorphic transformation of SrCO_3 structure occurs by the rotational disorder transition of the anion group at a certain temperature, in agreement value reported in literature [41-42]; the phase transformation results in an increase of crystal symmetry and volumetric expansion [34];
- **endothermic peak with a maximum at 1423 K:** attributed to thermal decomposition of SrCO_3 with the release of $-\text{CO}_2(\text{g})$;
- **exothermic peak centred at 1440 K:** due to the crystallization of SrO ;
- **endothermic peak centred at 1533 K:** probably due to any remaining decarbonisation, since it is concomitant with a small weight loss.

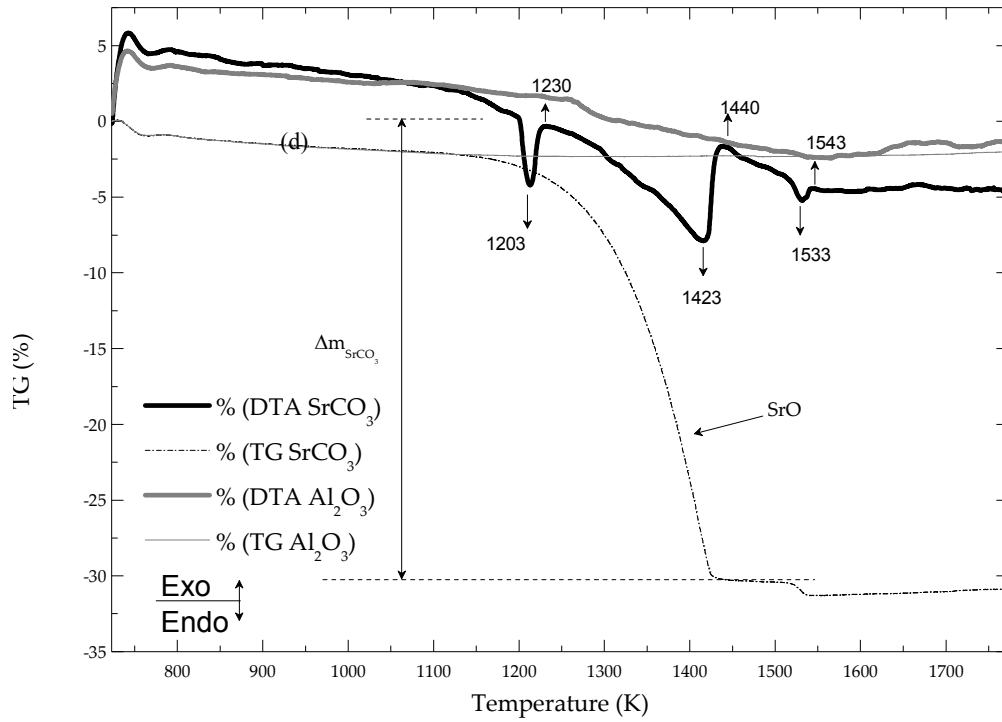


Figure AI-2. DTA and TG in Argon atmosphere at temperatures still 1773 K. Thermograms of separated SrCO₃ and Al₂O₃ reagents.

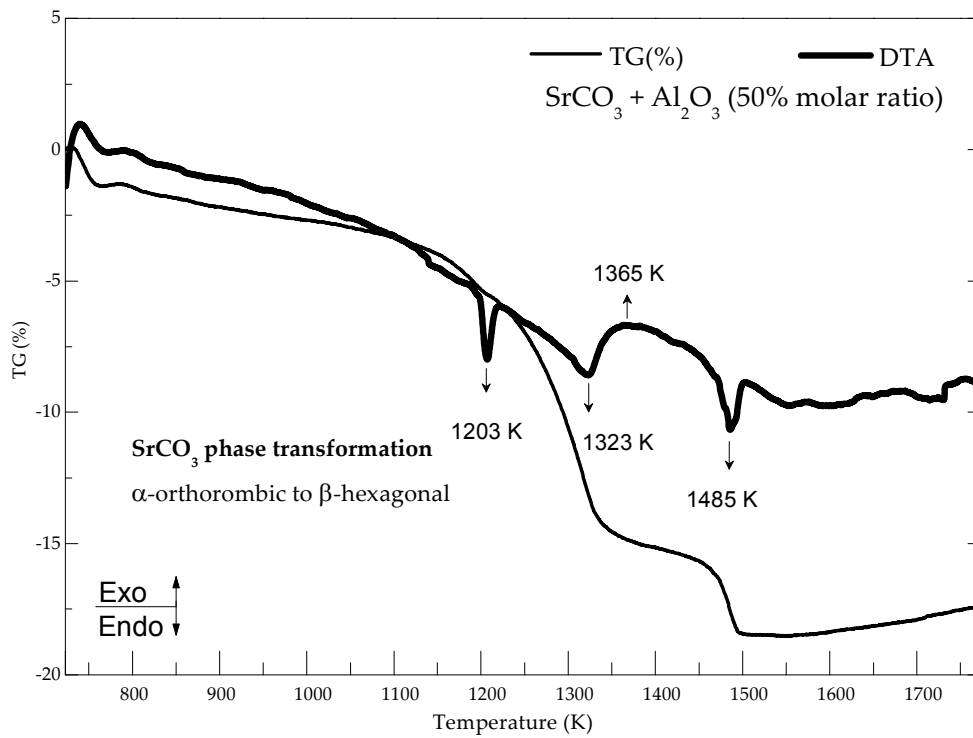


Figure AI-3. DTA and TG in Argon atmosphere at temperatures still 1773 K. b) thermogram of SrCO₃—Al₂O₃ (50% molar ratio).

The thermal analysis of SrCO₃—Al₂O₃ mixture (50% molar ratio) is presented in Figure AI-3. It can be seen that the powders mixture underwent thermal effects similar to those observed for SrCO₃ component alone, which tended to appear at somewhat lower temperatures, suggesting that the chemical reaction in the SrCO₃—Al₂O₃ system is partially preceded by the decomposition of SrCO₃. The DTA curve exhibits the following characteristics:

- **endothermic peak with a maximum at 1203 K:** also observed for the SrCO₃ alone, assigned to its phase transformation from orthorhombic to hexagonal structure. The interfacial reaction between SrCO₃ and Al₂O₃ and the formation of SrAl₂O₄ at temperatures below that of SrCO₃ phase transformation (~1203 K) requires activation energy of 130 kJ/mol for the carbonate decomposition [34]. At temperatures > 1203 K, the crystallization of SrAl₂O₄ is dominated by diffusion of Al³⁺ ions into the SrCO₃ lattice co-existent with free SrO, and the activation energy for the carbonate decomposition decreases.
- **endothermic peak with a maximum at 1323 K:** attributed to thermal decomposition of SrCO₃ with the release of —CO₂ (g), thus occurring about 100°C below and being less deep in comparison to the single SrCO₃ component. This suggest the occurrence of a concomitant exothermic reaction due to the formation of strontium aluminates, in such a way that the heat released is consumed in the thermal decomposition of SrCO₃;
- **broad exothermic band with a maximum at 1365 K:** due to the formation of crystalline strontium aluminates;
- **endothermic peak with a maximum at 1485 K:** due to the second decomposition step of SrCO₃. The maximum weight loss is observed at about 1500 K.

According *Chang-Hsiang* [36b], the activation energy for SrCO₃ decomposition is significantly influenced by the calcination temperature, while the nature of alumina precursor, i.e. α-Al₂O₃ or γ-Al₂O₃, presents a secondary factor. The α-alumina used in this work might be obtained, for instance, from gibbsite (→ χ-Al₂O₃ → κ-Al₂O₃ → α-Al₂O₃) or boehmite (→ γ-Al₂O₃ → δ-Al₂O₃ → θ-Al₂O₃ → α-Al₂O₃) routes. The very shallow thermal effects observed with further

increasing temperature suggest that the progresses towards the formation of more stable strontium aluminates are slow, as expected from diffusion controlled synthesis reactions. The theoretical enthalpies for the formation of SrAl₂O₄ host lattice are given by Equations (AI-4) to (AI-8).

$$\Delta_{\text{r}} H^{\circ} (T_0) = \sum_i \nu_i \Delta_{\text{f}} H_i^{\circ} (T_0) \quad \text{AI-4}$$

$$\Delta_{\text{r}} S^{\circ} (T_0) = \sum_i \nu_i S_i^{\circ} (T_0) \quad \text{AI-5}$$

$$\Delta_{\text{r}} H^{\circ} (T) = \Delta_{\text{r}} H^{\circ} (T_0) + \int_{T_0}^T \sum_i \nu_i C_{\text{p}i} (T) dT \quad \text{AI-6}$$

$$\Delta_{\text{r}} S^{\circ} (T) = \Delta_{\text{r}} S^{\circ} (T_0) + \int_{T_0}^T \sum_i \nu_i \frac{C_{\text{p}i} (T)}{T} dT \quad \text{AI-7}$$

$$\Delta_{\text{r}} G^{\circ} (T) = \Delta_{\text{r}} H^{\circ} (T) - T \Delta_{\text{r}} S^{\circ} (T) \quad \text{AI-8}$$

Where:

$\Delta_{\text{r}} H^{\circ} (T)$ = standard enthalpy change;

$\Delta_{\text{r}} S^{\circ} (T)$ = standard entropy change;

$\Delta_{\text{r}} G^{\circ} (T)$ = standard Gibbs energy change;

ν_i = stoichiometric coefficient of the compound;

C_{p} = heat capacity at constant pressure;

T = absolute temperature;

for initial (i) reactants or final (f) products.

The enthalpies of SrCO₃—Al₂O₃ reactions were studied from room temperature to about 1503 K (Figure AI-4). The enthalpy changes confirmed that solid-state synthesis is favoured over 1300 K leading to the formation of better defined single phases from a direct reaction between SrO and Al₂O₃ (Equation AI-3).

The enthalpy of the solid-state synthesis attends the Hess Law, which states that the enthalpy change is independent of the route by which the reaction is achieved. The thermodynamic approach depends only on the initial and final stages of enthalpies. Standard enthalpy values ($\Delta_{\text{f}} H^{\circ} (T)$) are positive for the Equations (AI-1) and (AI-2) as endothermic reactions, and negative for Equation (AI-3) as an exothermic reaction, according the standards enthalpies reported elsewhere by [41], [42] and [44].

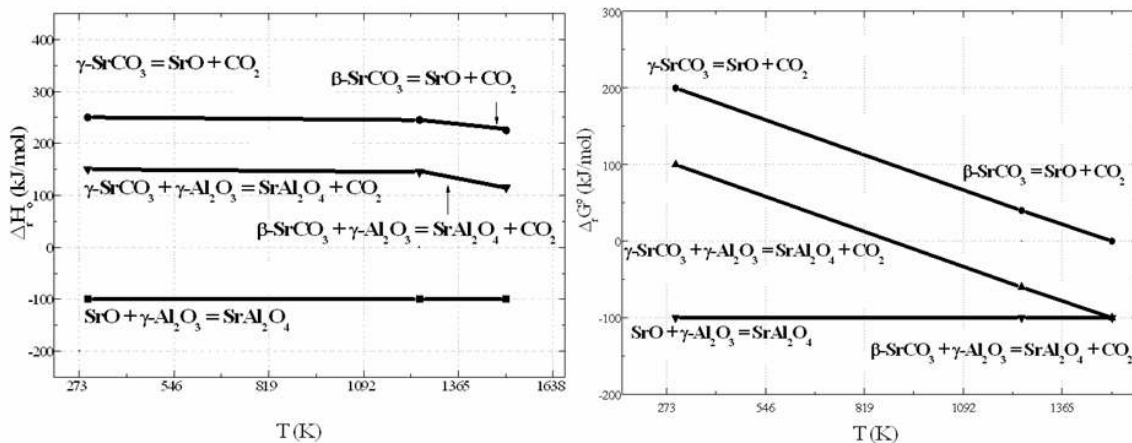


Figure AI-4. Thermodynamic properties of the SrCO₃—Al₂O₃ reactions from room temperature to about 1503 K: a) changes of the enthalpies; b) standard molar of free enthalpies [42, 44]. Data converted in Kelvin temperature.

Thermodynamic equilibrium is obtained decreasing the enthalpy of the SrO, in accordance with the Equations from (AI-9) to (AI-10):

$$\Delta_r G(T) = -RT \ln \frac{K(T)}{Q(T,P,\xi)} = \Delta_r G^0(T) + RT \ln Q(T,P,\xi) \quad (\text{AI-9})$$

$$\Delta_r G(T) = \Delta_r G^0(T) + RT \ln \prod_i a_i^{v_i} \quad (\text{AI-10})$$

$$\Delta_r G(T) = \Delta_r G^0(T) + RT \ln \frac{P_{\text{CO}_2}}{p^0} \quad (\text{AI-11})$$

Where:

R = gas constant;

T = absolute temperature;

K = equilibrium constant;

Q = heat transfer.

P = pressure;

ξ = degree of the advancement of the reaction;

$\Delta_r G^0(T)$ = standard Gibbs energy change;

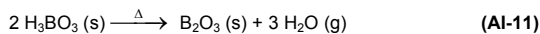
Π_i = chemical potential in the standard state of the component i;

a_i = activity of the compound;

v_i = stoichiometric coefficient of the compound.

The thermodynamic activities on the SrO—Al₂O₃ system within the temperature range of 1473-1573 K were determined using the FactSage 5.5 software in Integrated Thermodynamic Databank System (ITDS). Theoretical reactivity of reagents to obtain Sr aluminates by stoichiometric solid state reaction among the constituents indicates that the activity degree of (SrO)(Al₂O₃) and primary Al₆Sr arrangements are superior at 1473 than at 1573 K. Increasing the thermal energy, the activity of O₃Al₂-Al₂O₃ also is highest. Atoms in position of Al1 and Al4 are isoactives at 1473-1573 K, and in position of Al2 and Al3 have higher activity degrees at 1573 K. The activities of Sr-free ions are higher at 1573 K. Analogously, a catalyst boron-doped with B³⁺ ions on the Al³⁺ substitutional system are enabled to produce an activity degree to form tetrahedral BO₄ in the AlO₄ framework preferentially at 1573 K, upon the higher ionic activity of Al³⁺ free ions. At 1473 K, B³⁺ ions have a tendency to form B₄Sr, before the formation of the BO₄ tetrahedra.

Boron doping replacing Al³⁺ ions generates distortions in the Al-framework and reduces the temperature required for the formation of the crystalline phases [45]. In these boric acid containing systems, the decomposition into B₂O₃ occurs in a first stage with the release of constitutional water at temperatures below 673 K, according to Equation (AI-11).



Experimentally, the XRD patterns reveal that SrAl₂O₄ was formed, in conjunction with Sr₃Al₂O₆, upon holding the sample for 3 h at 1473 K in free (Figure AI-5a) and pressed (Figure AI-5b) powders. An increase of the intensity of Sr₃Al₂O₆ peaks was evidenced for the sample containing the highest amount of boron, and under the thermal treatment of recrystallization for 10 h (Figure AI-5b). At the second stage of chemical interaction, there was the occurrence of mixed borate melt with intermediate compounds, which enhanced

the diffusion phenomena thus, leading to an overall acceleration of the formation process of SrAl₂O₄, Sr₃Al₂O₆ and Sr₃B₂O₆, as described in Equations from (AI-12) to (AI-15).

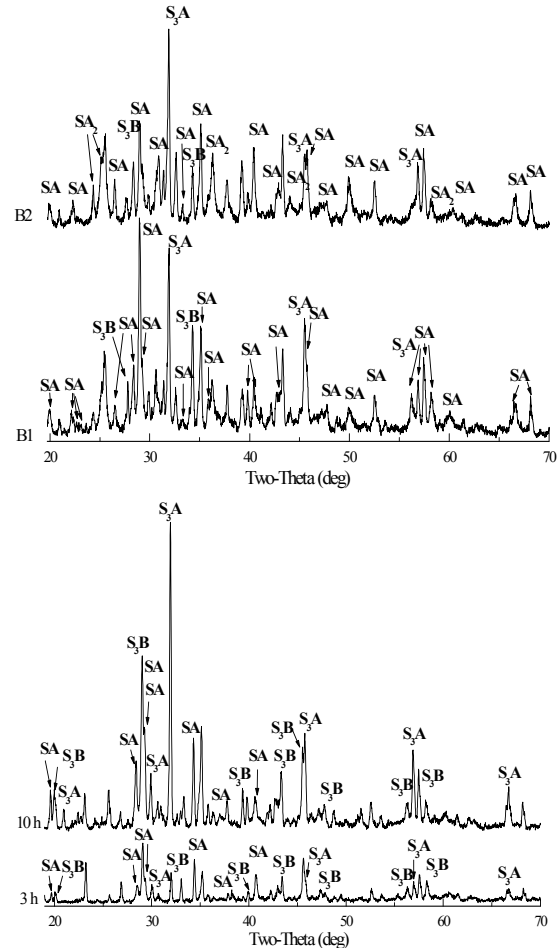
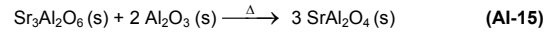
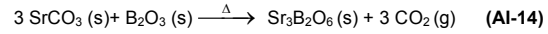
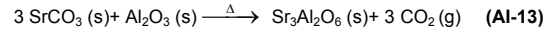
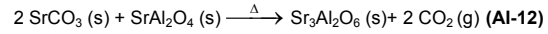
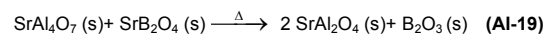
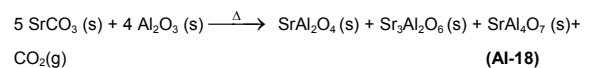
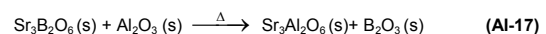
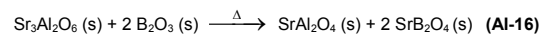


Figure AI-5. Effect of boron addition on X-ray diffraction profiles of samples annealed at 1473 K: a) B1 and B2 for 3 h, SrAl₂O₄ (SA), SrAl₄O₇ (SA₂), Sr₃Al₂O₆ (SA₃), and Sr₃B₂O₆ (S₃B); and b) B1 for 3 and 10 h, SrAl₂O₄ (SA), Sr₃Al₂O₆ (SA₃), and Sr₃B₂O₆ (S₃B).

In boron containing samples, the strontianite can be involved in cyclic borate reactions forming Sr₃Al₂O₆ and SrAl₂O₄ as major phases in successive reactions that might occur during the formation of these phases as described in Equations from (AI-16) to (AI-19). Note that when the boron oxide is reacting, intermediary strontium borates are formed.



TEM image of the micro and nano-particles (SrAl_2O_4 , $\text{Sr}_3\text{Al}_2\text{O}_6$ and $\text{Sr}_3\text{B}_2\text{O}_6$) obtained by increasing the annealing time to 10 h are showed in Figure AI-6. The respective SAED pattern (Figure AI-6b) of the region indicated in Figure AI-6c reveals a nanostructure with spacing parameters of about 0.5×0.8 nm. This result is a possible SrAl_2O_4 detection, in agreement with the unit-cell parameters of the monoclinic structure ($a = 5.1607$, $b = 8.822$, $c = 8.4424$, $\beta = 93.415$, space group $P2_1$). EDX analysis comprised the boron atoms doping the structure replacing Al^{3+} sites (Figure AI-6d).

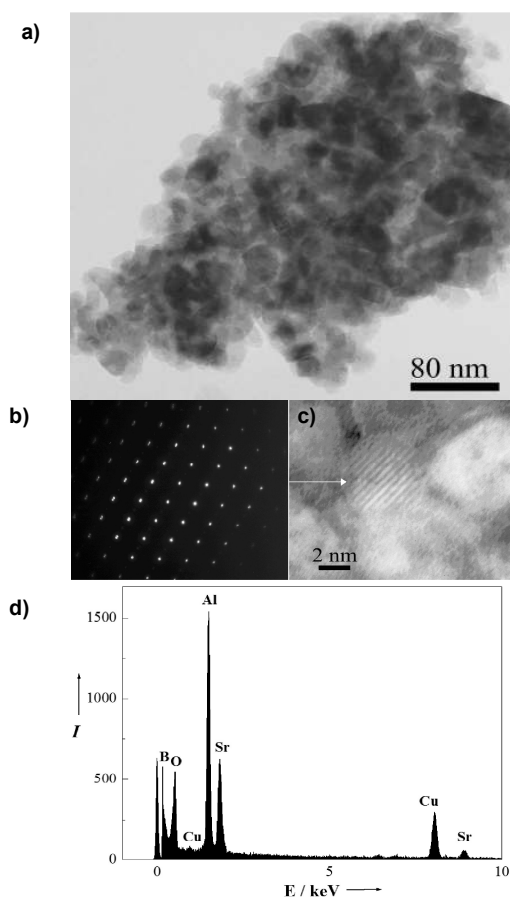


Figure AI-6. a) TEM of crystalline host lattice sample (SrAl_2O_4 , $\text{Sr}_3\text{Al}_2\text{O}_6$, and $\text{Sr}_3\text{B}_2\text{O}_6$) obtained by pressing at 200 MPa and annealing at 1573 K for 10 h, and the respective b) SAED pattern of the c) indicated region; d) EDX analysis revealing boron atoms doping the crystal structure.

In the phosphor industry, the solid-state synthesis carried out within the temperature range of 1473-1573 K using a catalyst boron-doping revealed to be an effective route to prepare large-scale micro- and nano-particles of Sr-aluminates. ■

ANNEX II

Optical characterization of 13 commercial phosphors

Table AII-1. Part I – Optical features of commercial phosphors under illuminance of Xenon lamp, 150 W, 500 lux.

Colour appearance	Atomic excitation [nm]	Colour emission		Integral			Radiance [$\mu\text{W}/\text{cm}^2$]	Luminance [mcd/m^2]
		u	v	x	y	z		
Yellow-Green N1	$\lambda_{\text{control}} = 300\text{nm}$	0.1960	0.5454	0.2696	0.5465	0.1830	18,7	79,9848
		0.1197	0.5453	0.2699	0.5463	0.1830	18,3	78,3760
		0.1198	0.5457	0.2704	0.5476	0.1820	18,0	77,1078
	$\lambda_{\text{UV-dark}} = 360\text{nm}$	0.1199	0.5472	0.2722	0.5523	0.1750	36,0	155,4660
		0.1200	0.5472	0.2724	0.5521	0.1750	35,6	153,9363
		0.1202	0.5472	0.2728	0.5520	0.1750	35,2	152,1167
	$\lambda_{\text{max } 1} = 320\text{nm}$	0.1201	0.5472	0.2726	0.5519	0.1750	28,1	121,6369
		0.1201	0.5473	0.2727	0.5521	0.1750	27,7	119,6633
		0.1203	0.5474	0.2732	0.5524	0.1740	27,4	118,6898
Yellow-Green N2	$\lambda_{\text{control}} = 300\text{nm}$	0.1212	0.5466	0.2740	0.5492	0.1760	5,2849	22,6511
		0.1218	0.5455	0.2738	0.5450	0.1810	5,3565	22,6931
		0.1215	0.5461	0.2739	0.5474	0.1780	5,2540	22,4516
	$\lambda_{\text{UV-dark}} = 360\text{nm}$	0.1200	0.5483	0.2737	0.5557	0.1700	17,1	74,4864
		0.1199	0.5484	0.2735	0.5561	0.1700	17,1	74,1778
		0.1200	0.5484	0.2737	0.5560	0.1700	16,90	73,2735
	$\lambda_{\text{max } 1} = 320\text{nm}$	0.1207	0.5480	0.2746	0.5541	0.1710	9,5664	41,3613
		0.1205	0.5482	0.2743	0.5548	0.1700	9,3403	40,5954
		0.1206	0.5484	0.2748	0.5555	0.1690	9,2949	40,4255
Yellow-Green N3	$\lambda_{\text{control}} = 300\text{nm}$	0.1212	0.5456	0.2728	0.5461	0.1810	5,3848	22,9536
		0.1214	0.5457	0.2734	0.5461	0.1800	5,3848	22,9536
		0.1218	0.5456	0.2739	0.5454	0.1800	5,3848	22,9536
	$\lambda_{\text{UV-dark}} = 360\text{nm}$	0.1209	0.5474	0.2743	0.5521	0.1730	13,7	59,5571
		0.1208	0.5476	0.2743	0.5528	0.1720	13,7	59,5571
		0.1209	0.5477	0.2746	0.5528	0.1720	13,5	58,4533
	$\lambda_{\text{max } 1} = 320\text{nm}$	0.1213	0.5476	0.2753	0.5521	0.1720	8,7643	37,9883
		0.1216	0.5473	0.2754	0.5510	0.1730	8,7303	37,7527
		0.1213	0.5475	0.2752	0.5521	0.1720	8,6425	37,4024
Yellow-Green N4	$\lambda_{\text{control}} = 300\text{nm}$	0.1177	0.5459	0.2667	0.5497	0.1830	10,2	43,6094
		0.1179	0.5455	0.2666	0.5484	0.1840	10,2	43,6304
		0.1177	0.5458	0.2666	0.5494	0.1840	10,2	43,5655
	$\lambda_{\text{UV-dark}} = 360\text{nm}$	0.1174	0.5476	0.2680	0.5556	0.1760	22,6	97,6143
		0.1174	0.5475	0.2680	0.5553	0.1760	22,5	96,9808
		0.1173	0.5476	0.2677	0.5555	0.1760	22,6	97,865
	$\lambda_{\text{max } 1} = 320\text{nm}$	0.1176	0.5472	0.2680	0.5542	0.1770	16,0	68,9567
		0.1177	0.5474	0.2682	0.5547	0.1770	16,1	69,4164
		0.1175	0.5472	0.2679	0.5543	0.1770	16,0	69,2076
Yellow N5	$\lambda_{\text{control}} = 300\text{nm}$	0.1096	0.5572	0.2635	0.5955	0.1410	14,0	62,5579
		0.1106	0.5571	0.2655	0.5943	0.1400	12,2	54,2850
		0.1109	0.5570	0.2658	0.5936	0.1400	12,0	53,6149
	$\lambda_{\text{UV-dark}} = 360\text{nm}$	0.1181	0.5573	0.2802	0.5879	0.1310	25,2	114,5903
		0.1180	0.5574	0.2802	0.5886	0.1310	25,2	114,9117
		0.1181	0.5574	0.2805	0.5883	0.1310	25,2	114,5536
	$\lambda_{\text{max } 1} = 320\text{nm}$	0.1122	0.5582	0.2697	0.5967	0.1330	19,6	88,1479
		0.1125	0.5582	0.2704	0.5965	0.1330	19,3	86,6712
		0.1126	0.5581	0.2705	0.5960	0.1330	19,1	85,9923
$\lambda_{\text{max } 2} = 430\text{nm}$	0.0996	0.5663	0.2535	0.6402	0.1060	24,2	112,4876	
	0.0996	0.5665	0.2537	0.6413	0.1050	24,2	112,7334	
	0.0993	0.5666	0.2531	0.6418	0.1050	24,2	112,5481	
Blue-Green N6	$\lambda_{\text{control}} = 300\text{nm}$	0.1024	0.3979	0.1475	0.2547	0.5970	22,0	38,9665
		0.1027	0.3981	0.1480	0.2549	0.5970	22,1	39,1052
		0.1025	0.3981	0.1477	0.2550	0.5970	22,2	39,3377
	$\lambda_{\text{UV-dark}} = 360\text{nm}$	0.0848	0.4437	0.1411	0.3281	0.5300	41,2	101,0139
		0.0847	0.4420	0.1411	0.3291	0.5290	41,4	101,9454
		0.0846	0.4441	0.1409	0.3289	0.5300	41,8	102,6596
Blue-Green N7	$\lambda_{\text{control}} = 300\text{nm}$	0.1016	0.3986	0.1468	0.2558	0.5970	33,0	58,7133
		0.1017	0.3986	0.1468	0.2559	0.5970	33,0	58,7920
		0.1014	0.3989	0.1466	0.2562	0.5970	32,7	58,4041
	$\lambda_{\text{UV-dark}} = 360\text{nm}$	0.0844	0.4439	0.1406	0.3286	0.5300	54,6	133,8888
		0.0841	0.4449	0.1405	0.3305	0.5290	55,1	136,0466
		0.0839	0.4449	0.1402	0.3304	0.5290	55,4	136,7913
	$\lambda_{\text{max } 1} = 280\text{nm}$	0.1056	0.3886	0.1481	0.2423	0.6090	21,8	36,1392
		0.1070	0.3854	0.1487	0.2381	0.6183	21,3	34,5490
		0.1071	0.3852	0.1488	0.2377	0.6130	21,0	34,1090

Table AII-1. Part II - Optical features of commercial phosphors under illuminance of Xenon lamp, 150 W, 500 lux.

Colour appearance	Atomic excitation [nm]	Colour emission		Integral			Radiance [$\mu\text{W}/\text{cm}^2$]	Luminance [mcd/m^2]
		u	V	x	y	z		
Blue N8	$\lambda_{\text{control}} = 300\text{nm}$	0.1380	0.2879	0.1510	0.1401	0.7080	24,0	29,3853
		0.1381	0.2876	0.1511	0.1398	0.7090	24,5	29,9386
		0.1381	0.2872	0.1509	0.1395	0.7090	24,5	29,9805
	$\lambda_{\text{UV-dark}} = 360\text{nm}$	0.1246	0.3248	0.1485	0.1721	0.6790	25,0	39,1449
		0.1243	0.3262	0.1486	0.1734	0.6778	25,3	39,8105
		0.1242	0.3260	0.1485	0.1732	0.6780	25,2	39,7498
	$\lambda_{\text{max } 1} = 280\text{nm}$	0.1347	0.3007	0.1516	0.1504	0.6980	19,0	23,7337
		0.1359	0.2971	0.1517	0.1474	0.7000	18,7	22,8337
		0.1361	0.2969	0.1519	0.1473	0.7000	18,6	22,7509
	$\lambda_{\text{max } 2} = 325\text{nm}$	0.1504	0.2468	0.1512	0.1102	0.7380	30,9	32,8292
		0.1502	0.2471	0.1511	0.1105	0.7380	31,1	33,0905
		0.1500	0.2473	0.1510	0.1106	0.7380	31,1	33,1887
Purple N9	$\lambda_{\text{control}} = 300\text{nm}$	0.1951	0.1104	0.1540	0.0387	0.8070	20,9	8,8634
		0.1953	0.1107	0.1542	0.0388	0.8070	20,9	8,9040
		0.1955	0.1102	0.1542	0.0386	0.8070	21,0	8,9028
	$\lambda_{\text{UV-dark}} = 360\text{nm}$	0.1944	0.1135	0.1542	0.0400	0.8050	21,2	9,2933
		0.1943	0.1137	0.1541	0.0401	0.8050	21,2	9,3106
		0.1943	0.1132	0.1540	0.0399	0.8060	21,2	9,2557
	$\lambda_{\text{max } 1} = 260\text{nm}$	0.1954	0.1115	0.1545	0.0392	0.8060	8,54	3,6668
		0.1957	0.1112	0.1546	0.0390	0.8060	8,1424	3,4758
		0.1956	0.1121	0.1547	0.0394	0.8050	8,0988	3,4905
Orange N10	$\lambda_{\text{control}} = 300\text{nm}$	0.2965	0.5445	0.5266	0.4299	0.0430	32,0	116,2720
		0.2961	0.5445	0.5261	0.4300	0.0430	31,8	115,6465
		0.2960	0.5445	0.5260	0.4301	0.0430	31,9	115,7402
	$\lambda_{\text{UV-dark}} = 360\text{nm}$	0.2743	0.5452	0.5014	0.4429	0.0550	33,8	124,2767
		0.2744	0.5451	0.5014	0.4428	0.0550	33,9	124,5278
		0.2742	0.5451	0.5012	0.4429	0.0550	33,8	124,3036
	$\lambda_{\text{max } 1} = 350\text{nm}$	0.2725	0.5450	0.4990	0.4436	0.0570	33,6	124,0512
		0.2726	0.5450	0.4991	0.4435	0.0570	33,8	124,7798
		0.2724	0.5451	0.4990	0.4437	0.0570	33,6	124,0414
	$\lambda_{\text{max } 2} = 450\text{nm}$	0.3704	0.5437	0.6035	0.3937	0.0020	39,1	138,2148
		0.3706	0.5436	0.6035	0.3935	0.0030	40,0	136,2097
		0.3705	0.5436	0.6035	0.3936	0.0020	41,0	139,4847
	$\lambda_{\text{max } 3} = 530\text{nm}$	0.3818	0.5426	0.6126	0.3869	0.0000	33,1	110,4565
		0.3815	0.5426	0.6124	0.3871	0.0000	32,9	110,1012
		0.3816	0.5426	0.6124	0.3870	0.0000	33,7	112,7047
Orange N11	$\lambda_{\text{control}} = 300\text{nm}$	0.2895	0.5328	0.4999	0.4089	0.0910	5,3253	16,8772
		0.2894	0.5335	0.5008	0.4103	0.0880	5,2559	16,7538
		0.2890	0.5331	0.4999	0.4098	0.0900	5,2762	16,8348
	$\lambda_{\text{UV-dark}} = 360\text{nm}$	0.3020	0.5376	0.5217	0.4127	0.0650	9,093	28,41
		0.3026	0.5379	0.5228	0.4131	0.0640	9,6873	30,1011
		0.3026	0.5384	0.5237	0.4142	0.0620	9,6455	30,0593
	$\lambda_{\text{max } 1} = 340\text{nm}$	0.2933	0.5370	0.5109	0.4157	0.0730	13,9	44,5942
		0.2927	0.5368	0.5098	0.4155	0.0740	14,0	45,0085
		0.2926	0.5367	0.5095	0.4153	0.0750	14,0	44,8179
Red N12	$\lambda_{\text{control}} = 300\text{nm}$	0.4427	0.5316	0.6478	0.3457	0.0060	12,2	24,1642
		0.4429	0.5318	0.6484	0.3460	0.0050	12,1	23,9985
		0.4429	0.5316	0.6480	0.3457	0.0060	12,1	23,9935
	$\lambda_{\text{UV-dark}} = 360\text{nm}$	0.4441	0.5274	0.6419	0.3388	0.0190	5,757	10,6254
		0.4457	0.5280	0.6442	0.3392	0.0160	5,7493	10,6104
		0.4461	0.5283	0.6451	0.3396	0.0150	5,734	10,5905
	$\lambda_{\text{max } 1} = 460\text{nm}$	0.4467	0.5329	0.6532	0.3463	0.0000	23,0	45,5964
		0.4460	0.5330	0.6528	0.3468	0.0000	23,0	45,5723
		0.4465	0.5329	0.6532	0.3464	0.0000	23,0	45,8506
Red N13	$\lambda_{\text{control}} = 300\text{nm}$	0.2777	0.5362	0.4913	0.4216	0.0870	15,6	48,76
		0.2759	0.5366	0.4898	0.4234	0.0860	15,3	47,934
		0.2747	0.5365	0.4881	0.4237	0.0880	15,3	47,9552
	$\lambda_{\text{UV-dark}} = 360\text{nm}$	0.2614	0.5369	0.4726	0.4314	0.0960	20,8	66,2726
		0.2617	0.5370	0.4732	0.4315	0.0950	20,8	66,1899
		0.2620	0.5370	0.4736	0.4314	0.0950	20,9	66,5837
	$\lambda_{\text{max } 1} = 325\text{nm}$	0.2544	0.5376	0.4649	0.4366	0.0980	19,9	64,2873
		0.2543	0.5375	0.4647	0.4365	0.0980	20,2	65,0336
		0.2542	0.5375	0.4644	0.4365	0.0990	20,0	64,5872
	$\lambda_{\text{max } 2} = 460\text{nm}$	0.4242	0.5348	0.6375	0.3572	0.0050	20,8	51,6129
		0.4273	0.5344	0.6396	0.3555	0.0040	20,9	50,9838
		0.4251	0.5349	0.6385	0.3570	0.0040	21,0	51,635

Table AII-2. Optical emission of commercial phosphors under illuminance of Xenon lamp, 150 W, 500 lux.

<p>Figure AII-1. N1 Yellow-green emission spectra of SrAl₂O₄ host co-doped with lanthanide ions.</p>	<p>Figure AII-8. N8 Blue emission spectra of a host co-doped with Ce³⁺ and Dy³⁺: a) λ_{ex} = 300 nm (control); b) λ_{ex} = 360 nm (UV-lamp); c) λ_{ex} = 280 nm (max.1); and d) λ_{ex} = 325 nm (max.2).</p>
<p>Figure AII-2. N2 Yellow-green emission spectra of SrAl₂O₄ host co-doped with lanthanide ions.</p>	<p>Figure AII-9. N9 Purple emission spectra of a mixture of CaAl₂O₄, CaAl₄O₇ and Ca₂Al₂O₆ host lattices lanthanide co-doped: a) λ_{ex} = 300 nm (control); b) λ_{ex} = 260 nm (max.); c) λ_{ex} = 360 nm (UV-lamp).</p>
<p>Figure AII-3. N3 Yellow-green emission spectra of SrAl₂O₄ host co-doped with lanthanide ions.</p>	<p>Figure AII-10. N10 Orange emission spectra of a mixture of CdS and other hosts co-doped with lanthanide ions: a) λ_{ex}=340 nm; b) λ_{ex}=360 nm (UV-lamp); c) λ_{ex}=350 nm (max.1); d) λ_{ex} = 450 nm (max.2); and e) λ_{ex} = 530 nm (max.3).</p>
<p>Figure AII-4. N4 Yellow-green emission spectra of SrAl₂O₄ host co-doped with lanthanide ions.</p>	<p>Figure AII-11. N11 Orange emission spectra: Y₂O₃:Eu, Ln³⁺ co-doped: a) λ_{ex} = 300 nm (control); b) λ_{ex} = 360 nm (UV-lamp); c) λ_{ex} = 340 nm (max.).</p>
<p>Figure AII-5. N5 Yellow emission spectra of a mixture of SrAl₂O₄ and Y₂O₃ host lattices co-doped with lanthanide ions</p>	<p>Figure AII-12. N12 Red emission spectra of a host doped with lanthanide ions: a) λ_{ex} = 300 nm (control); b) λ_{ex} = 360 nm (UV-lamp); c) λ_{ex} = 460 nm (max.).</p>
<p>Figure AII-6. N6 Blue-green emission spectra of a mixture of Sr₄Al₁₄O₂₅ and MAI₂O₄ co-doped with lanthanide ions.</p>	<p>Figure AII-13. N13 Red emission spectra of a mixture of strontium/calcium aluminates materials co-doped with lanthanide ions: a) λ_{ex} = 300 nm (control); b) λ_{ex} = 360 nm (UV-lamp); c) λ_{ex} = 325 nm (max.1); d) λ_{ex} = 460 nm (max.2).</p>
<p>Figure AII-7. N7 Blue-green emission spectra: Sr₄Al₁₄O₂₅ co-doped with lanthanide ions.</p>	

ANNEX III

Ophthalmologic test (chapter 6)

Information Sheet:



UNIVERSIDADE DE AVEIRO

DEPARTAMENTO DE ENGENHARIA CERÁMICA E DO VIDRO
3810-193 AVEIRO (Portugal)

Sub-Projecto de Validação Científica a desenvolver no Hospital Infante Dom Pedro no âmbito de um Protocolo com a Universidade de Aveiro para a realização das actividades de Bolsa de Doutoramento

CONSENTIMENTO INFORMADO Nº. _____

Eu, abaixo assinado, paciente do Sector de Oftalmologia do Hospital Infante Dom Pedro de Aveiro, declaro o consentimento para a participação do Grupo de Tratamento, para a utilização dos meus dados clínicos (idade, índice glicémico, acuidade visual, histórico clínico em geral) e para a realização de TESTE OFTALMOLÓGICO FARNSWORTH-MUNSELL 100-HUE, no âmbito de um Protocolo com a Universidade de Aveiro, com o objectivo de contribuir para a investigação científica aplicada no estudo de doenças oftalmológicas e desenvolvimento de novos produtos para pessoas com deficiências.

(Paciente – Grupo de Tratamento)


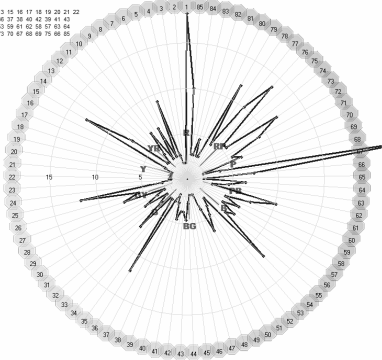
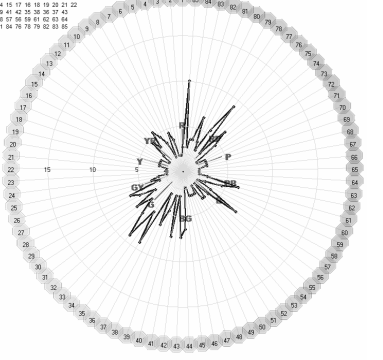
(Doutoranda – Examinador)

Aveiro, ____ de _____ de 2009.

ANNEX III

Ophthalmologic test (chapter 6)

Questionnaire/interview with data collection:

 <p>FICHA DE TESTE OFTALMOLÓGICO FARNSWORTH-MUNSELL 100-HUE Visual Acuity and Colour Vision Test 1.01</p> <p>Departamento de Engenharia Cerâmica e do Vidro Doutorado em Ciência e Engenharia de Materiais/Biomateriais</p>		<p>Data:</p> <p>Arquivo: HDI_p026.doc</p> <p>Examinador:</p>	
PERFIL DO PACIENTE:			
Nome:		Idade: 71	Glicemia: 135
a) Presença de doença corneana, intra-ocular ou trauma?	catarata		OE
b) Submetido alguma cirurgia correctiva?	Sim (catarata)		
c) Usou lentes de contacto ou outro biomaterial?	IOL	Olho direito	Olho esquerdo
GRUPO DE TESTE: Retinopatia diabética			
Grupo A		Grupo B	
<input type="checkbox"/> Visão com 2 olhos normais e não-usuário de biomaterial	<input type="checkbox"/> Visão normal		<input type="checkbox"/> Visão subnormal
	<input type="checkbox"/> Usuário de biomaterial		<input type="checkbox"/> Não-usuário de biomaterial
	<input type="checkbox"/> B1 (auxilia na visão)	<input type="checkbox"/> B2 (não auxilia na visão)	
	<input type="checkbox"/> LIO catarata	<input type="checkbox"/> Orbital biocerâmico de anoftalmo	
	<input type="checkbox"/> Lente de contacto	<input type="checkbox"/> Orbital polietileno poroso de anoftalmo	
	<input type="checkbox"/> Lente anti UVA e UVB	<input type="checkbox"/> Prótese acrílica	
<input type="checkbox"/> Óculos com grau dióptrico	<input type="checkbox"/> Outro:		
FOTOMETRIA DE TESTE			
Luz Natural		Luz Artificial	
<input checked="" type="checkbox"/> Luz do dia (S)		<input checked="" type="checkbox"/> Fluorescente (F) <input type="checkbox"/> Mercúrio (C) <input type="checkbox"/> Halógena Tungsténio (L)	
		Escala: 2000-20000	
		Lux: 730	Foot-candle:
		Horário: 09:30	Local: HDI
Retinal diagnostic:			
<p>Note: These results have not been saved</p> <p>Score: 318</p> <p>Tray 1 01 02 03 04 05 06 07 08 09 10 11 12 13 14 15 16 17 18 19 20 21 22</p> <p>Tray 2 23 24 25 26 27 28 29 30 31 32 33 34 35 36 37 38 39 40 41 42</p> <p>Tray 3 43 44 45 46 47 48 49 50 51 52 53 54 55 56 57 58 59 60 61 62 63 64</p> <p>Tray 4 65 66 67 68 69 70 71 72 73 74 75 76 77 78 79 80 81 82 83 84</p> <p>Tray 5 85 86 87 88 89 90 91 92 93 94 95 96 97 98 99 100</p>  <p>Edt</p> <p style="text-align: center;">White background</p>		<p>Note: These results have not been saved</p> <p>Score: 178</p> <p>Tray 1 01 02 03 04 05 06 07 08 09 10 11 12 13 14 15 16 17 18 19 20 21 22</p> <p>Tray 2 23 24 25 26 27 28 29 30 31 32 33 34 35 36 37 38 39 40 41 42</p> <p>Tray 3 43 44 45 46 47 48 49 50 51 52 53 54 55 56 57 58 59 60 61 62 63 64</p> <p>Tray 4 65 66 67 68 69 70 71 72 73 74 75 76 77 78 79 80 81 82 83 84</p> <p>Tray 5 85 86 87 88 89 90 91 92 93 94 95 96 97 98 99 100</p>  <p>Edt</p> <p style="text-align: center;">Black background</p>	

ANNEX IV



IOPscience | [Login](#) | [Create account](#) | [Athens/Institutional login](#)

Nanotechnology



[Home](#) | [Search](#) | [Collections](#) | [Journals](#) | [About](#) | [Contact us](#) | [My IOPscience](#)

Intercrystalline distal-effect on the afterglow phenomenon in photoluminescent SrAl₂O₄:Ce(III), Ln nanotube growth

Author
Nadia Khaled Zurba¹, Igor Bdkin¹, Andrei Kholkin¹, Dmitri Golberg² and José M F Ferreira¹

Affiliations
¹ Centre for Research in Ceramic and Composite Materials (CICECO), Ceramic and Glass Engineering Department, University of Aveiro,  3810193 , Aveiro, Portugal
² International Centre for Materials Nanoarchitectonics (MANA), National Institute for Materials Science (NIMS), Tsukuba 3050044, Ibaraki, Japan

E-mail
f2698@ua.pt | golberg.dmitri@nims.go.jp

Journal
Nanotechnology  [Create an alert](#)  [RSS this journal](#)

Issue
Volume 21, Number 32

Citation
Nadia Khaled Zurba *et al* 2010 *Nanotechnology* **21** 325707
doi: 10.1088/0957-4484/21/32/325707

Intercrystalline distal-effect on the afterglow phenomenon in photoluminescent
 $\text{SrAl}_2\text{O}_4:\text{Ce(III)}, \text{Ln}$ nanotube growth

This article has been downloaded from IOPscience. Please scroll down to see the full text article.

2010 Nanotechnology 21 325707

(<http://iopscience.iop.org/0957-4484/21/32/325707>)

View [the table of contents for this issue](#), or go to the [journal homepage](#) for more

Download details:

IP Address: 68.227.216.3

The article was downloaded on 22/07/2010 at 02:33

Please note that [terms and conditions apply](#).

Intercrystalline distal-effect on the afterglow phenomenon in photoluminescent SrAl₂O₄:Ce(III), Ln nanotube growth

Nadia Khaled Zurba¹, Igor Bdikin¹, Andrei Kholkin¹, Dmitri Golberg² and José M F Ferreira¹

¹ Centre for Research in Ceramic and Composite Materials (CICECO), Ceramic and Glass Engineering Department, University of Aveiro, 3810193, Aveiro, Portugal

² International Centre for Materials Nanoarchitectonics (MANA), National Institute for Materials Science (NIMS), Tsukuba 3050044, Ibaraki, Japan

E-mail: f2698@ua.pt (N K Zurba) and golberg.dmitri@nims.go.jp

Received 9 March 2010, in final form 19 May 2010

Published 21 July 2010

Online at stacks.iop.org/Nano/21/325707

Abstract

We report a new method for the synthesis of photoluminescent SrAl₂O₄:Ce³⁺, Dy³⁺, Eu²⁺ nanotubes, PL-SNT:Ce(III), Ln, using solid-state reaction and post-annealing approach. This new optical nanotubular structure was characterized by HRTEM, SEM, AFM, EDX, steady-state and time-resolved PL spectroscopy. A series of f–f and f–d-transitions with light emission in structured bands peaking at 488 nm arising from the polymorphism of the host lattice was correlated with an intercrystalline distal-effect on the afterglow phenomenon.

 Online supplementary data available from stacks.iop.org/Nano/21/325707/mmedia

(Some figures in this article are in colour only in the electronic version)

1. Introduction

Since the identification of carbon nanotubes (CNTs) [1], one-dimensional inorganic nanotubes have extensively been investigated to meet the demands of science and nanotechnology. The formation of some inorganic nanotubes was suggested to occur by a curving and seaming process of lamellar structures formed after heat treatment [2]. In this way, metal oxide strontium aluminate (SrAl₂O₄) nanotubes have been obtained via hydrothermal synthesis by rolling-up and post-annealing approach [3]. This efficient SrAl₂O₄ host material for persistent luminescence has a ~6.5 eV bandgap in the α -monoclinic structure. The high-temperature phase with β -hexagonal structure is obtained via a phase transition at ~923 K.

Rare-earth ions with divalent/trivalent cations, such as Eu²⁺ (1.20 Å), Dy³⁺ (1.17 Å) and Ce³⁺ (1.03 Å), can substitute for Sr²⁺ ions (1.21 Å) [3] in the crystal lattice with possible charge compensations during luminescence.

Luminescent nanorod- and nanotube-shaped phosphors, including those co-doped with Eu²⁺ and Dy³⁺, have already been prepared [4, 5], but thereof changes on the persistent afterglow luminescence are not explainable to polymorphism at nanoscale. Furthermore, a Ce³⁺ co-doped strontium aluminate nanotube product has not yet been reported.

Herein, we report a new method for the synthesis of photoluminescent SrAl₂O₄:Ce³⁺, Dy³⁺, Eu²⁺ nanotubes, PL-SNT:Ce(III), Ln, via post-annealing the precursor micro- and nanoparticles synthesized through a solid-state reaction [6] from SrCO₃, Al₂O₃, Ce₂O₃, Dy₂O₃ and Eu₂O₃. The effects of the post-annealing approach on the relevant afterglow phenomenon were investigated. In contrast to the cetyltrimethylammonium bromide (CTAB)/*n*-butanol/water medium reaction usually used for formation of SrAl₂O₄ nanotubes derived by hydrothermal or co-precipitation methods, which require pH adjustments by adding urea [3, 4], the emphasis here was put on direct solid-state chemistry of PL-SNT:Ce(III), Ln. Obtaining the nanotubes without

Table 1. Chemical composition of the nanotube growth system, as determined by ICP-MS and EDX Bruker AXS Microanalysis, and an oxide mixture template measured by XRF.

Ionic function	SrAl ₂ O ₄ :Ce ³⁺ , Dy ³⁺ , Eu ²⁺						
	Host lattice (SrAl ₂ O ₄)			Lanthanide (co)activators (Ln)			
	Sr	Al	O	Eu		Dy	Ce
<i>K</i> ^a	2	3	1, 2	2	3	3	3
V	Sr ²⁺	Al ³⁺	O ²⁻	—	—	—	—
f ↔ f	—	—	—	—	Eu ³⁺ (F6)	Dy ³⁺ (F9)	—
f ↔ d	—	—	—	Eu ²⁺ (F7)	—	—	Ce ³⁺ (F1)
ICP-MS (ppm)	370 300	303 940	—	7223	—	13 186	9980
EDX (wt%)	46.43	14.49	32.45	1.57	—	0.82	2.78
	Ceramic template						
Oxides	SiO ₂	Al ₂ O ₃	Fe ₂ O ₃	Na ₂ O	K ₂ O	TiO ₂	Other
XRF (wt%)	65.80	21.21	0.61	3.82	1.81	1.71	10.03

^a *K* is the number of e⁻ transferred per mole from/to an oxidant or reductant in the balanced half-reaction, i.e. the valence state under spin changing.

a catalyst is the main advantage of the new solid-state method, which only requires a second heat treatment under temperatures below 1473 K. A combination of SiO₂, Al₂O₃ and alkali oxides was used as a thin phosphor layer template for an overgrowth system towards applications in photoluminescent ceramic devices. The advances from this multidisciplinary study concerning the PL-SNT:Ce(III), Ln are relevant comparable to the analogous formula M_(1-x-y)Al₂O₄:Ce_x, Ln_y (M = Be, Mg, Ca or Ba) product investigations related to the aluminate nanotube-shaped phosphors having several important applications in nanotechnology.

2. Experimental details

The new solid-state reaction method was used for the synthesis of SrAl₂O₄:Ce³⁺, Dy³⁺, Eu²⁺ nanotubes from a stoichiometric mixture of SrCO₃, Al₂O₃, Eu₂O₃, Dy₂O₃, and Ce₂O₃ powders (table 1). The powder mixture was annealed at about 1573 K in a reductive atmosphere to obtain the as-synthesized particles (Source: Lanxi Minhui Photoluminescent Co., Ltd, Minhui Zhejiang, China). Post-annealing was carried out at 573–1473 K for 1 h in an air atmosphere using a Termolab[®] furnace. A combination of SiO₂, Al₂O₃ and alkali oxides was used as a thin phosphor layer template for a nanocrystal/nanotube overgrowth system. Mechanical deposition and dry-pressing of single as-synthesized nanoparticles on templates (Source: Eliane S.A., Cocal do Sul, Brazil) into 0.10 and 0.25 g pellets were performed using a US Craver Laboratorial Press (490 MPa).

The phase purity of SrAl₂O₄:Ce³⁺, Dy³⁺, Eu²⁺ and evolution of crystal structures were measured by XRD on as-synthesized nanoparticles at 300 K and on post-annealed samples up to 1473 K, derived from the solid-state route (see supplementary data available, figure S1 available at stacks.iop.org/Nano/21/325707/mmedia). XRD patterns indicate an α -monoclinic phase in the temperature range from 573 to 973 K (space group *P*₂₁, *a* = 0.8447 nm, *b* = 0.8816 nm, *c* = 0.51639 nm, and β = 93.428°), changing

predominantly to a β -hexagonal phase of SrAl₂O₄ above 1073 K (space group *P*₆₃, *a* = 0.89260 nm, *c* = 0.84985 nm and *V* = 0.58639 nm³) during the nanotube growth. The high phase purity of SrAl₂O₄:Ce³⁺, Dy³⁺, Eu²⁺ products is well evidenced from the XRD patterns, but the yield of single phase nanotube could not be quantified from the polycrystalline system.

SEM images were recorded on a HITACHI SU-70 microscope with an accelerating voltage of 4 kV (a working distance of 4.9 mm). TEM and HRTEM images were recorded on PHILIPS CM-200 FEG and HITACHI H9000 microscopes, in conjunction with EDX using a Bruker AXS Microanalysis system. AFM in tapping mode was performed in a Multimode Nanoscope IIIA, DI (resonance frequency of 330 kHz, scanning speed 3 μ m s⁻¹) using a PPP-NCHR cantilever (Nanosensors). Photoluminescence afterglow spectra were obtained at room temperature using a TRIAX 320 monochromator coupled to a Hamamatsu R928 photomultiplier. Steady-state measurements used a Xe lamp (450 W), and TRE spectroscopy used a Xe–Hg laser (pulse of 6 μ s).

3. Results and discussion

3.1. Lattice defects and rolling-up mechanism

Initially, the α -monoclinic SrAl₂O₄:Ce³⁺, Dy³⁺, Eu²⁺ nanoparticles that present multifunctional piezo-, thermo-, sono-, electro- and long afterglow photoluminescence were characterized by transmission electron microscopy (TEM). The nanotube morphology was not observed at this stage (figure 1). Figure 1(a) reveals isotropically distributed crystallographic linear defects. A lamellar anisotropic distribution is also observed in figure 1(b). This asymmetry is coherent with the formation of nanotubes by a rolling mechanism [3]. Continuous post-annealing of α -monoclinic nanoparticles was carried out within a temperature range of host phase transformation, i.e. from 573 to 1473 K. A structural polymorphism of SrAl₂O₄:Ce³⁺, Dy³⁺, Eu²⁺ occurs during the

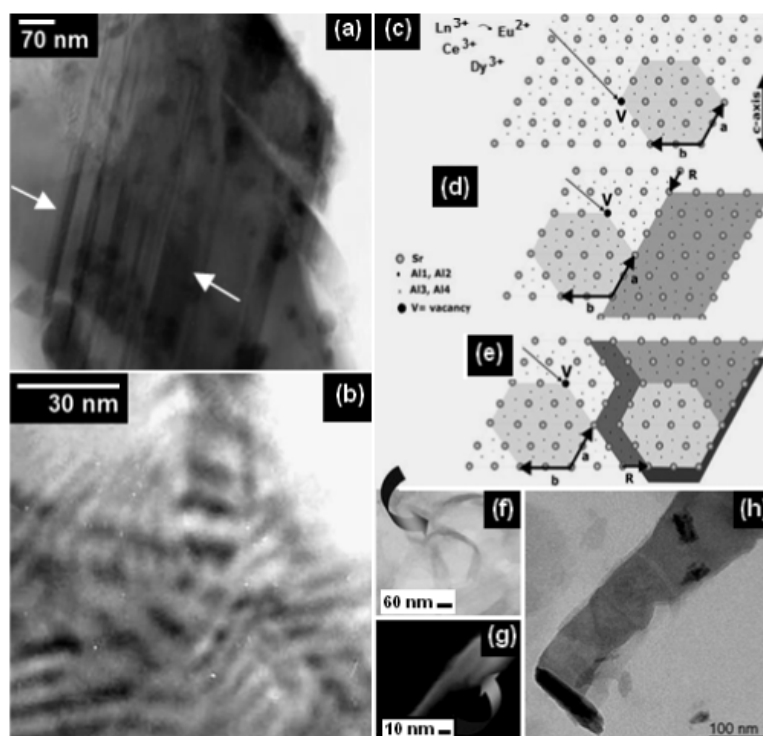


Figure 1. TEM image of a precursor α -monoclinic $\text{SrAl}_2\text{O}_4:\text{Ce}^{3+}, \text{Dy}^{3+}, \text{Eu}^{2+}$ isolated nanoparticle with linear lattice defects (arrowed) having (a) isotropic distribution, and (b) anisotropic lamellar distribution; (c)–(h) crystallographic arrangement and rolling-up mechanism of (α, β) phases \rightarrow γ -nanotube transition under a solid-state synthesis and post-annealing at 1473 K.

crystallographic arrangement from $\alpha \rightarrow (\beta \rightarrow \gamma)$ phases produced by post-annealing (see supplementary data, figures S1–5 available at stacks.iop.org/Nano/21/325707/mmedia). Reticular displacement vectors were originated during the β -hexagonal crystal growth from linear displacement defects present in the α -phase (figures 1(c)–(e)), and in which a hexagonal structure exhibits the light emission polarized along the c -axis. Continuing to increase the thermal energy, a planar roll-up is evidenced comprising the roll-up mechanism of a nanotube due to unstable dangling bonds [2, 3], figures 1(f)–(h).

3.2. Luminescent nanotube growth

Unusually, such treatment initiated $\text{SrAl}_2\text{O}_4:\text{Ce}^{3+}, \text{Dy}^{3+}, \text{Eu}^{2+}$ rolling-up and a successful formation of γ -nanotubes is commenced at ~ 1273 – 1473 K. The nanotubes of 90 nm in diameter and 650 nm in length are shown in TEM and SEM micrographs, figure 2. A substantial mesoporosity is noted, that has been produced due to O^{2-} vacancies involving typical defects at the 2d sites [8, 9] (because all samples were post-annealed in an air atmosphere). Energy dispersive x-ray (EDX) spectroscopy indicates the presence of rare-earth elements in all heat-treated samples, figure 2(b). The values found are coherent with the literature with respect to an Al/O atom ratio in the tetrahedra $[\text{AlO}_4]$ that can accept substitutional Sr^{2+} ions in open channels of the reticular crystals. The selected area electron diffraction (SAED) pattern in conjunction with the HRTEM image along the $[1\bar{1}0]$ zone axis reveals that a nanotube is well crystalline, as shown in figure 2(c).

3.3. Intercrystalline distances

Preferential one-dimensional growth was verified by tapping-mode atomic force microscopy (AFM), as depicted in figure 3(a). A grain size of ~ 1 – $3 \mu\text{m}$ and roughness RMS = 180 nm are seen in figure 3(b). Correlation between the layer periods with a height for different grains is seen in figure 3(b). The average intercrystalline distances correspond to the lattice vectors of 80 and 500 nm in figure 3(c), as additionally verified by the A–B cross-section profiles in figure 3(d). The intercrystalline layer thickness and the height of the samples range from 50 to 250 nm and from 80 to 900 nm, respectively, in cross-sectional profiles in figure 3(e). The polymorphism induced an increase of intercrystalline distances for high-temperature phases, measured by AFM cross-sections (see supplementary data, figure S5 available at stacks.iop.org/Nano/21/325707/mmedia).

3.4. Photoluminescence modifications from polymorphism

Figure 4(a) shows the steady-state photoluminescence spectroscopy of β -hexagonal and γ -nanotube products obtained by the post-annealing. We analysed emissions by excitation at 253, 300, 360, 392.5 and 463 nm, under a series of f–f and f–d transitions. The materials emit in large and thin bands, peaking significantly at ~ 488 nm. This is assigned to the 5d electronic excited states of Ce^{3+} ions, intra- $4f^1$ transitions [$^2\text{F}_{5/2} \rightarrow ^2\text{F}_{7/2}$], in overlap with Dy^{3+} ions, [$^4\text{F}_{9/2} \rightarrow ^6\text{H}_{15/2}$], and possible emission shifts from $4f^6 5d^1$ to the $4f^7$ configuration of Eu^{2+} ions. In the region of 600–680 nm,

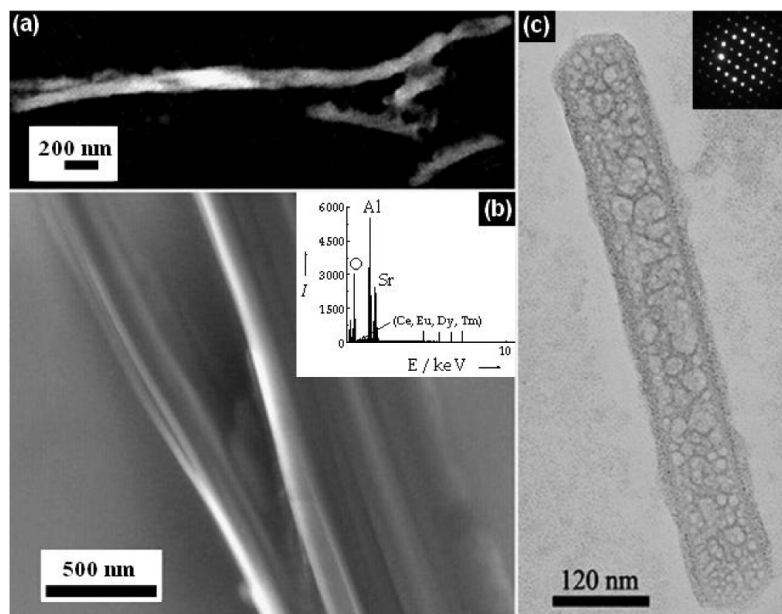


Figure 2. SEM and TEM images of PL-SNT:Ce(III), Ln obtained by solid-state synthesis and post-annealing at: (a) 1273 K; (b) 1473 K, with EDX spectrum of the nanotube as inset; (c) a nanotube and its SAED pattern recorded along the $[1\bar{1}0]$ zone axis.

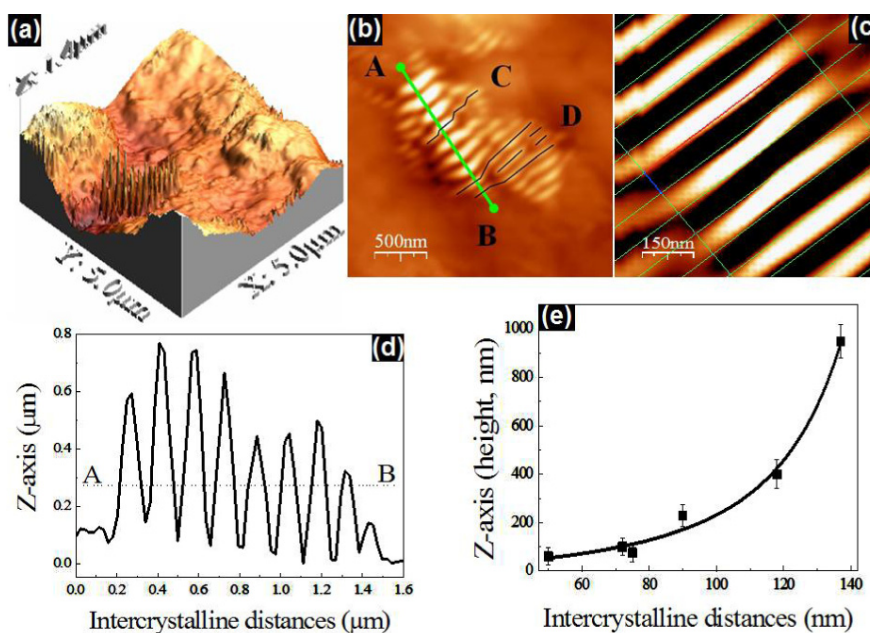


Figure 3. AFM analysis of $\text{SrAl}_2\text{O}_4:\text{Ce}^{3+}, \text{Dy}^{3+}, \text{Eu}^{2+}$ in a $5 \mu\text{m} \times 5 \mu\text{m}$ scanning area: (a) morphology of an oriented thin structure; (b) A–B cross-section; (c) host lattice vectors; intercrystalline distances (d) along the A–B line; and (e) versus height.

the thin emission lines have been assigned to the lanthanides in excited states and recombination of Eu^{3+} ions, intra- $4f^6$ transitions [$^5D_0 \rightarrow ^7F_{0-4}$] peaking in different points of UV-region from 600 to 700 nm, and Dy^{3+} ions peaking at 578 nm intra- $4f^9$ transitions [$^2F_{15/2} \rightarrow ^6F_{11/2}$] and [$^6H_{15/2} \rightarrow ^4M_{15/2} + ^6P_{7/2}$]. Compared to the long-lived luminescence of α -monoclinic structures [6–8], the afterglow decay curves of the PL-SNT:Ce(III), Ln and β -hexagonal phase structures reveal a reduction of the lifetime (τ). This phenomenon was not found in previous luminescence studies, and is shown in detail in figure 4(b).

3.5. Intercrystalline distal-effect on the afterglow phenomenon

The alteration on the relaxed excited states in time-resolved emission (TRE) spectra (figure 5) acquired at different starting delay times confirms a change in the ‘full width at half maximum’, FWHM, from precursor particles in figure 5(a) and a peak at ~ 488 nm, figures 5(b)–(e), and also comprises a reduction on the lifetime scale ($\tau < 10^{-8}$ s) due to polymorphism. Herein, a correlation between the changes in the afterglow phenomenon and the polymorphism is attributable to an ‘intercrystalline distal-effect’, d , defined

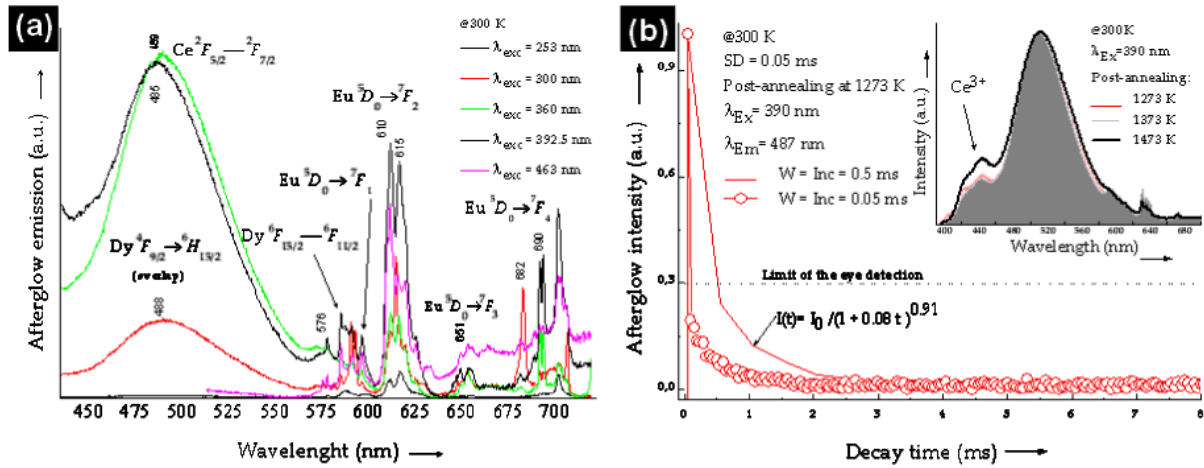


Figure 4. Afterglow phenomenon for polymorphic PL-SNT:Ce(III), Ln and β -hexagonal phase under post-annealing: (a) photoluminescence emission (1473 K) after excitation at 253, 300, 360 392.5 and 463 nm showing a series of f–f and f–d transitions; (b) decay time curves; in detail: emission spectra of a product onto templates post-annealed at 1273, 1373 and 1473 K, where the large bands correspond to the Ce^{3+} electronic transitions in the host lattice.

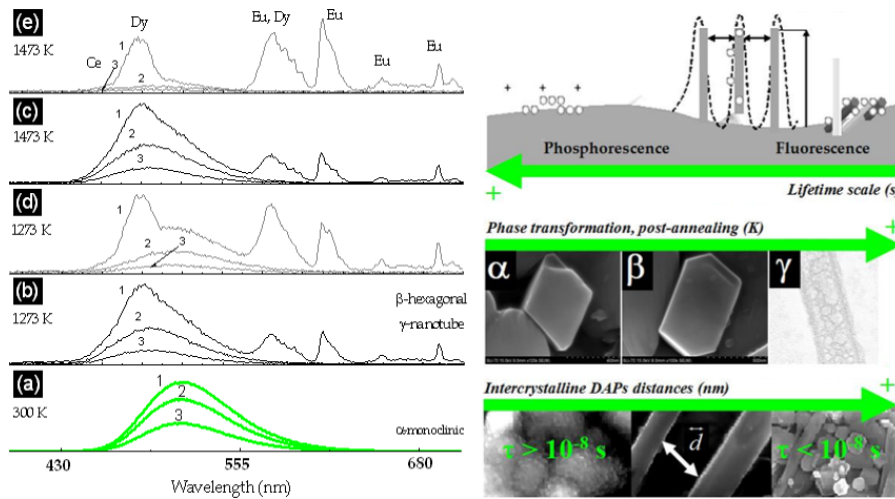


Figure 5. TRE spectra by excitation at 360 nm: (a) α -monoclinic; (b)–(d) PL-SNT:Ce(III), Ln and β -hexagonal phase structures by post-annealing at 1273 K. Starting delays of (1) 0.05 ms, (2) 50.00 ms and (3) 200.00 ms, using an integration window of 20.00 ms. Schematic representation of the intercrystalline distal-effect on the afterglow phenomenon performed for polymorphic structures.

as a geometrical influence of the host lattice structure (morphology, size, shape, distance and distribution of crystals). The intercrystalline parameter prevails over the interatomic distance between the donor and acceptor pairs (DAPs) in the dependence of the recombination time [9], because the spatial limitation for energy transfer is far larger in β - γ structures. Attributing d to the nanoscale, the lifetime scale changes with respect to the afterglow phenomenon along with the equation (1):

$$1/\tau(d) = [1/\tau(0)] \exp(-2d/a_B) \quad (1)$$

where τ is the lifetime, d is the intercrystalline distance between the donor and the acceptor of n th pairs, and a_B is the Bohr radius of the impurity. This provides the DAPs intercrystalline relation for the lifetime scale changes during the host phase transformation. The total charges

in the afterglow phenomenon produced by a stable phase transformation for a luminescent material should be constant, and are defined as in equation (2):

$$1/\tau(d) \rightarrow \text{constant}. \quad (2)$$

The crystallographic stabilization results in a constant value dependent of the intercrystalline distance. Experimentally, the DAPs distances were not addressed before as a nanoscale factor under the afterglow phenomenon. Owing to the dependence of transition probabilities on intercrystals, the DAP luminescence spectrum can be deformed and shifted toward short wavelengths. Also an emission intensity is varied during crystal phase transformation.

Qualitative performance of $SrAl_2O_4:Ce^{3+}, Dy^{3+}, Eu^{2+}$ polymorphs during the afterglow phenomenon reveals an increase of $d_{(\alpha-\alpha)} < d_{(\beta-\gamma)} < d_{(\beta-\beta)}$ distal series by the

host phase transformation, α -monoclinic, elucidating an old concept of the alterations from the phosphorescence to the fluorescence [8, 9]. The energy transferred between DAPs has been strongly reduced by the weak interaction between these luminescent centres with a physical limitation for electrons (de)trapping and (re)combining during the spatial separation of DAPs after host phase transformation to PL-SNT:Ce(III), Ln and β -hexagonal structures in post-annealed conditions.

4. Conclusion

In conclusion, polymorphism under the SrAl₂O₄:Ce³⁺, Dy³⁺, Eu²⁺ nanotube growth affected by host phase transformations in post-annealed conditions led to a reduction on the lifetime photoluminescence emission. This was attributed to the intercrystalline distal-effect as a physical limitation for electrons (de)trapping and (re)combining due to spatial separation of DAPs for polymorphic β - γ phases (figure 5). This work concerning the afterglow phenomenon of PL-SNT:Ce(III), Ln in a multidisciplinary outlook should be further deepened, considering that it may find applications in biosensors, *in vivo* imaging, and in thin film transistors.

Acknowledgments

We kindly acknowledge the CICECO Laboratory, namely the Physics Department for taking PL spectra, Dmitri Kiselev for AFM probing, and Dr Marc-Georg Willinger for a TEM support. SEM images were acquired in a SU-70 microscope (FCT/REDE/1509/RME/2005). This work was supported by the Ministry of Science, Technology and Higher Education of Portugal under a Doctoral Fellowship of the Research Institute of the University of Aveiro (BDUA/f2698/2006-2010).

References

- [1] Iijima S 1991 *Nature* **354** 56
- [2] Gautam U K, Vivekchand S R C, Govindaraj A, Kulkarni G U, Selvi N R and Rao C N R 2005 *J. Am. Chem. Soc.* **127** 3658
- [3] Ye C, Bando Y, Shen G and Golberg D 2006 *Angew. Chem.* **118** 5044–8
- [4] Cheng B, Liu H, Fang M, Xiao Y, Lei S and Zhang L 2009 *Chem. Commun.* **8** 944–6
- [5] Zhang F, Wan Y, Yu T, Zhang F, Shi Y, Xie S, Li Y, Xu L, Tu B and Zhao D 2007 *Angew. Chem. Int. Edn* **46** 7976–9
- [6] Chen I C and Chen T M 2001 *J. Mater. Res.* **16** 644–51
- Fu Z L, Zhou S H, Yu Y N and Zang S Y 2005 *Chem. Phys. Lett.* **416** 381
- Song H and Chen D 2007 *J. Lumin.* **22** 554–8
- Chander H, Haranath D, Shanker V and Sharma P 2007 *Cornell Univ. Lib. arXiv.org* 0405110
- Sun Y, Qiu G, Li X, Zhang S, Yan C and Zhang X 2006 *Rare Metals* **25** 615–9
- Lu C H, Chen S Y and Hsu C H 2007 *Mater. Sci. Eng.* **140** 218–21
- Geng J and Wu Z 2002 *J. Mater. Synt. Proc.* **10** 245–8
- Li X, Qu Y, Xie X, Wang Z and Li R 2006 *Mater. Lett.* **60** 3673–7
- Preethi K R S, Lu C H, Thirumalai J, Jagannathan R, Natarajan T S, Nayak N U, Radhakrishna I, Jayachandran M and Trivedi D C 2004 *J. Phys.* **37** 2664–9
- Peng T, Huajum L, Yang H and Yan C 2004 *Mater. Chem. Phys.* **85** 68–72
- Haiyan D, Gengshen L and Jiayue S 2007 *J. Rare Earths* **25** 19–22
- Escribano P, Marchal M, Sanjuan M L, Alonso-Gutierrez P, Julian B and Cordoncillo E 2005 *J. Solid State Chem.* **178** 1978–87
- Faridnia B, Motlagh M M K and Maghsoudipour A 2007 *Prog. Res. Technol.* **36** 216–23
- Yamada H, Shi W S, Nishikubo K and Xu C N 2003 *J. Electrochem. Soc.* **150** E251–4
- [7] Shi W S, Yamada H, Nishikubo K, Kusaba H and Xu C N 2004 *J. Electrochem. Soc.* **151** H97–100
- [8] Nakazawa E, Murazaki Y and Saito S 2006 *J. Appl. Phys.* **100** 113113
- Clabau F, Rocquefelte X, Jobic S, Deniard P, Whangbo M H, Garcia A and Mercier T 2005 *Chem. Mater.* **17** 3904–12
- Jia D, Wang X J, Jia W and Yen W M 2006 *J. Lumin.* **119** 55–8
- Dorenbos P 2007 *J. Lumin.* **122** 315–7
- Jia D, Wang X J, Jia W and Yen W M 2007 *J. Lumin.* **122** 311–4
- Pellé F, Aitasalo T, Lastusaari M, Niittykoski J and Hölsä J 2006 *J. Lumin.* **119** 64–8
- Kato K, Tsutai I, Kamimura T, Kaneko F, Shinbo K, Ohta M and Kawakami T 1999 *J. Lumin.* **82** 213–20
- [9] Gribkovskii V P 1998 *Luminescence of Solids* ed D R Vij (Minsk: Academy of Sciences of Belarus) pp 1–43 (New York: Plenum)